DOCTOR OF PHILOSOPHY

Hall Potential Mapping of Conducting Ferroelectric Domain Walls

Campbell, Michael

Award date:
2017

Awarding institution:
Queen's University Belfast

Hall Potential Mapping of Conducting Ferroelectric Domain Walls

Thesis submitted for the degree of

Doctor of Philosophy

in the

Faculty of Engineering and Physical Sciences

by

Michael Patrick Campbell MSci

School of Mathematics and Physics

Queen's University Belfast

September 2017

Abstract

The phenomenon of distinct conductivity at certain ferroelectric domain walls has the potential to revolutionise nanoelectronics. Existing as the interfaces between adjacent regions of differently orientated electric polarisation, domain walls can be written, displaced and erased within the bulk by locally applied electric fields. Complete control over their local carrier properties would allow analogues of semiconducting devices to be dynamically written, effectively supplanting modern printed circuit design. However, despite a growing array of ferroelectric materials found to exhibit domain wall conductance, the most fundamental carrier measurements have not been performed, with neither local carrier types, mobilities or densities explicitly determined for any domain wall system.

This thesis details the development of a scanning probe microscopy technique that allows the Hall potential developed within a conducting domain wall to be spatially mapped, with nanoscale resolution. A rudimentary measurement on the macroscale, inducing and recording the Hall potential within a material of known dimensions discloses the local carrier type, density and mobility in a single measurement. The approach discussed herein allows this foundational characterisation technique to be applied to the nanoscale geometry of ferroelectric domain walls.

Throughout this text an emphasis is placed on the more pragmatic aspects of the technique, with the hope this work may expedite future implementation. Correspondingly, the initial approach of Hall measurement via scanning voltage microscopy is discussed though ultimately it proved incompatible with the characteristically high resistivity of ferroelectric materials.

The Hall potential developed within conducting domain walls was imaged by its influence on an intermittent-contact atomic force microscopy topography profile. Studying $YbMnO_3$ single crystals, the enhanced conduction at tail-to-tail charged domain walls was confirmed to be facilitated by p-type carriers. Order of magnitude calculations were made for the local carrier density and mobility. An upper estimate for the carrier density of ~ $1x10^{16}$ cm^{-3} was obtained, a substantial four orders of

magnitude below that required for complete screening of the local divergence in polarisation. The estimated carrier mobility of ~ 60 $cm^2V^{-1}s^{-1}$ is lower than that for p-type silicon of equivalent carrier density, but sufficiently high to suggest an absence of lattice coupling as occurs for conduction via small polarons.

The technique was developed further by utilising dual pass kelvin probe force microscopy (KPFM) to map the topographic and electrostatic signal in isolation, facilitating direct measurement of the Hall potential. It is demonstrated that the quantitative accuracy of KPFM can be maintained under applied magnetic field and surface potential maps of a $ErMnO_3$ single crystal are presented for a range of magnetic and electric field states, conveying distinct domain wall contrast at both tail-to-tail and head-to-head walls. Due to time constraints, work beyond initial calibration and proof of concept mapping is not presented and further investigations into local carrier properties using KPFM Hall measurements are currently ongoing.

Lastly, the thesis leaves Hall effect measurement and discusses the complementary matter of accurately measuring the conductance of an individual domain wall. Despite orders of magnitude increase conductance in comparison to the ferroelectric bulk, the absolute conductance of domain walls is objectively low with the majority of studies reporting currents in the picoamp range. To isolate the minute driven current amongst background current sources, the alternating polarity method was employed wherein bias is applied in a low frequency square wave and a weighted moving average applied to the sampled current, acting as a basic impedance filter.

Here we investigate the dark conductance of a strongly charged head-to-head domain wall in congruent $LiNbO_3$ single crystal. Room temperature measurements exhibited strongly ohmic behaviour, while pronounced thermal activation was observed for temperatures above 70°C. The measured activation energy of 1.30 eV is consistent with that reported for diffusion of lithium vacancies in bulk, suggesting the local divergence in polarisation may be partially screened by ion vacancies which, immobile at room temperature, do not contribute to domain wall conduction until the thermally activated.

Publications and Conferences

Publications resulting from work in this thesis

M. P. Campbell, J. P. V McConville, R. G. P. McQuaid, D. Prabhakaran, A. Kumar and J. M. Gregg

Hall effect in charged conducting ferroelectric domain walls

Nature Communications **7**, 13764 (2016)

Publications resulting from work outside of this thesis

R. G. P. McQuaid, M. P. Campbell, R. W. Whatmore, A. Kumar and J. M. Gregg

Injection and controlled motion of conducting domain walls in improper ferroelectric Cu-Cl Boracite

Nature Communications **8**, 15105 (2017)

S. Prosandeev, I. I. Nuamov, H. Fu, L. Bellaiche, M. P. Campbell, R. G. P. McQuaid, L. Chang, A. Schilling, L. J. McGilly, A. Kumar and J. M. Gregg

Ferroelectric Vortices and Related Configurations

Nanoscale Ferroelectric and Multiferroics, 700-728

John Wiley & Sons 2016

Conferences

Poster Presentation

European Conference on Application of Polar Dielectrics (ECAPD) 2014

Domain wall conduction in ytterbium manganite

Vilnius, Lithuania

Oral Presentation

Deutsche Phsyikalische Gesellschaft (DPG) 2016

Conduction and diode behaviour in charged domain walls

Regensburg, Germany

Acknowledgements

Firstly, heartfelt thanks goes to my supervisor Marty Gregg for his constant guidance over the years and for expressing seemingly infinite patience in helping to fill the many gaps in my knowledge. His sincere enthusiasm in response to even the most incremental of data had an immeasurable influence on my own motivation, helping to maintain my morale when faced with the seeming perpetuity of the 'Hall experiment'. My secondary supervisor, Amit Kumar, was instrumental in the first year of my PhD as he spent countless hours in the lab, imparting his expertise on instrumentation and teaching me how to tinker with thousands of pounds worth of electronics without breaking anything (for the most part).

Thanks goes to every member of the research group for making the lab a legitimately enjoyable place to work. In particular those who, over the years, had the misfortune of sharing the office cubicle with me: Ray, Johnny, Alan, Jimmy, Matt and by proxy of how often I bothered him, Niall. As well as fielding an unending stream of physics questions (those deemed too basic for Marty) they provided endless craic and I don't think I made it through a single work day without laughter. Jimmy had the dubious honour of working on the Hall experiment and his contribution to the project cannot be understated. The work presented in the latter half of this thesis is as much his as it is mine.

I would like to thank my parents for their support throughout the PhD and, crucially, for never asking when I was going to graduate, even when three years turned to four.

Lastly, and most importantly I need to express my deepest gratitude to my partner MarieTherese. Over the past few years she has tolerated my majorly nocturnal sleep cycle and excessive work hours without complaint. She has supported me unquestionably, including my questionable decision to use what free time I had to prepare for and join a mountaineering expedition. She has made substantial sacrifices and I can honestly say I could not have done this without her.

Contents

Introduction and Motivation

Ferroelectric domain walls are interface structures separating regions of differently orientated electrical polarisation. The reversal of polarisation across the interface necessitates their structure be distinct from that of the bulk and as a consequence it has long been expected that they exhibit distinct functional properties[1–3]. Domain walls which display increased conductivity to that of the characteristically insulating ferroelectric bulk are of particular interest because of their possible applications in nanoelectronics. As the local polarisation within a ferroelectric material can be reoriented by a locally applied electrical field, these nanoscale channels can be written, moved and erased[4–9], opening the possibility of dynamic circuitry[10–12].

Since their original observation in $BiFeO_3$ by Seidel *et al.*[13], conducting domain wall research has grown rapidly and the phenomenon has now been seen in numerous material systems[7,14–22], with basic domain wall devices already demonstrated[4,23]. However, despite substantial interest, the mechanisms behind domain wall conduction remain poorly understood, with the most fundamental aspects of their conduction, carrier types, mobilities and densities, still undetermined. Such metrics are essential to determining the applicability of domain wall electronics: Are domain walls inherently metallic and hence limited to dynamic wiring or can they form semiconductor junctions and thus domain wall analogues of semiconducting devices can be patterned? While the former provides an additional degree of freedom to circuit design, the latter has the potential to replace circuits in their entirety.

By comparison, the carrier properties of the ubiquitous semiconductors silicon and germanium have been recorded with meticulous precision in an effort to exploit all available functionality[24–26]. The principal technique used in determining carrier properties in these materials is to induce and measure the Hall effect within a bulk sample[27,28]. Herein a current is driven through the material perpendicular to an applied magnetic field, resulting in charge carrier deflection and the development of a potential along the mutually orthogonal axis.

The utility of this technique is encapsulated by two simple expressions for the developed potential[29]:

$$V_{\mathrm{H}} = \frac{\mathbf{IB}}{qnt} = w\mu\mathbf{E}_x\mathbf{B}$$

Where V_{H} is the Hall voltage, **I** the driven current, **B** the applied magnetic field, $\mathbf{E}_x$ the lateral electric field, q the carrier charge, t sample thickness, w sample width and n and μ the carrier density and mobility. In essence, so long as the dimensions of the material are known, the dominant carrier type, density and mobility can be determined.

A major obstacle to Hall effect measurement at conducting domain walls is the pragmatic issue of sample size. Unlike bulk silicon which can be prepared in macroscopic dimensions for easy analysis, as interfacial structures, domain walls cannot be scaled beyond their innate nanoscale widths and consequently the traditional experimental approaches are inapplicable.

This thesis outlines the development of a scanning probe microscopy technique which allows the Hall potential developed within conducting ferroelectric domain walls to be spatially mapped with nanoscale resolution. As with any novel technique, optimisation is ongoing and, consequently, throughout the thesis an emphasis is placed on practical aspects of measurement and pathways for future improvement are discussed. Nonetheless, the efficacy of the technique was established and the Hall voltage within ferroelectric domain walls was successfully imaged, revealing local carrier type and providing values for carrier mobility and density. The measurements presented herein represent the first explicit characterisation of the carriers involved in conducting ferroelectric domain walls.

References

1. Vul, B. M., Guro, G. M. & Ivanchik, I. I. Encountering domains in ferroelectrics. *Ferroelectrics* **6,** 29–31 (1973).

2. Schmid, H. & Pétermann, L. A. Dielectric constant and electric resistivity of copper chlorine boracite, $Cu_3B_7O_{13}Cl$ (Cu-Cl-B). *Phys. Status Solidi* **41,** K147–K150 (1977).

3. Aristov, V. V., Kokhanchik, L. S., Meyer, K. P. & Blumtritt, H. Scanning electron microscopic investigations of peculiarities of the $BaTiO_3$ ferroelectric domain contrast. *Phys. Status Solidi* **78,** 229–236 (1983).

4. Whyte, J. R. *et al.* Sequential injection of domain walls into ferroelectrics at different bias voltages: Paving the way for 'domain wall memristors'. *J. Appl. Phys.* **116,** 66813 (2014).

5. McGilly, L. J., Yudin, P., Feigl, L., Tagantsev, a K. & Setter, N. Controlling domain wall motion in ferroelectric thin films. *Nat. Nanotechnol.* **10,** 145–50 (2015).

6. McGilly, L. J. *et al.* Velocity Control of 180° Domain Walls in Ferroelectric Thin Films by Electrode Modification. *Nano Lett.* **16,** 68–73 (2016).

7. McQuaid, R. G. P., Campbell, M. P., Whatmore, R. W., Kumar, A. & Gregg, J. M. Injection and controlled motion of conducting domain walls in improper ferroelectric Cu-Cl boracite. *Nat. Commun.* **8,** 15105 (2017).

8. Werner, C. S. *et al.* Large and accessible conductivity of charged domain walls in lithium niobate. *Sci. Rep.* 9862 (2017).

9. Vasudevan, R. K. *et al.* Domain wall conduction and polarization-mediated transport in ferroelectrics. *Adv. Funct. Mater.* **23,** 2592–2616 (2013).

10. Béa, H. & Paruch, P. Multiferroics: A way forward along domain walls. *Nat. Mater.* **8,** 168–169 (2009).

11. Catalan, G., Seidel, J., Ramesh, R. & Scott, J. F. Domain wall nanoelectronics. *Rev. Mod. Phys.* **84,** 119–156 (2012).

12. Meier, D. Functional domain walls in multiferroics. *J. Phys. Condens. Matter* **27,** 463003 (2015).

13. Seidel, J. *et al.* Conduction at domain walls in oxide multiferroics. *Nat. Mater.* **8,** 229–34 (2009).

14. Maksymovych, P. *et al.* Dynamic conductivity of ferroelectric domain walls in $BiFeO_3$. *Nano Lett.* **11,** 1906–1912 (2011).

15. Farokhipoor, S. & Noheda, B. Conduction through 71° Domain Walls in BiFeO3 Thin Films. *Phys. Rev. Lett.* **107,** (2011).

16. Guyonnet, J., Gaponenko, I., Gariglio, S. & Paruch, P. Conduction at domain walls in insulating $Pb(Zr_{0.2}Ti_{0.8})O_3$ thin films. *Adv. Mater.* **23,** 5377–5382 (2011).

17. Meier, D. *et al.* Anisotropic conductance at improper ferroelectric domain walls. *Nat. Mater.* **11,** 284–288 (2012).

18. Schröder, M. *et al.* Conducting domain walls in lithium niobate single crystals. *Adv. Funct. Mater*. **22,** 3936–3944 (2012).

19. Sluka, T., Tagantsev, A. K., Bednyakov, P. & Setter, N. Free-electron gas at charged domain walls in insulating $BaTiO_3$. *Nat. Commun.* **4,** 1808 (2013).

20. Stolichnov, I. *et al.* Bent Ferroelectric Domain Walls as Reconfigurable Metallic-Like Channels. *Nano Lett.* **15,** 8049–8055 (2015).

21. Benedek, N. A. & Fennie, C. J. Hybrid improper ferroelectricity: A mechanism for controllable polarization-magnetization coupling. *Phys. Rev. Lett.* **106,** 3–6 (2011).

22. Crassous, A., Sluka, T., Tagantsev, A. K. & Setter, N. Polarization charge as a reconfigurable quasi-dopant in ferroelectric thin films. *Nat. Nanotechnol.* **10,** 614–8 (2015).

23. Sharma, P. *et al.* Nonvolatile ferroelectric domain wall memory. *Sci. Adv.* **3,** e1700512 (2017).

24. Hull, R. in *Properties of Crystalline Silicon* 411–476 (INSPEC, 1999).

25. Ivanov-Schitz, A. K., Kireev, V. V, Mel'nikov, O. K., Chaban, N. G. & Schoonman, J. *Silicon Based Materials and Devices*. *Solid State Ionics* **10,**

26. Hull, R. & Bean, J. C. *Germanium Silicon: Physics and Materials*. (Academic Press, 1999).

27. Hall, E. H. On a New Action of the Magnet on Electric Currents. **2,** 287–292 (1879).

28. Hall, E. H. On the new action of magnetism on a permanent electric current. *Am. J. Sci.* **s3-20,** 161–186 (1880).

29. Popovic, R. S. in *Hall Effect Devices* 65–67 (IOP Publishing, 2004).

1 Ferroelectricity and Domain Walls

1.1 The Ferroelectric State

Ferroelectric materials are defined by a native electric dipole moment that can be reoriented between non-volatile states upon application of an external electric field[1]. A non-centrosymmetric crystal symmetry is required to allow for spatial separation of the centres of positive and negative charge within the unit cell. Of the 32 crystallographic point groups, defined by distinct symmetry with respect to a point, 21 are non-centrosymmetric. All, bar one, non-centrosymmetric point groups express a linearly increasing dipole moment upon applying stress to deform the crystal structure, *i.e.* piezoelectricity. However, only a further 10 of these possess a unique polar axis under zero stress. Referred to as spontaneous polarisation, this material property is quantified as the electric dipole moment per unit volume. Spontaneous polarisation is temperature dependent, typically decreasing as increasing thermal disorder leads to reduced separation of the centres of net positive and negative charge. Hence these 10 are known as the pyroelectric point groups.

Due to the rotational symmetry of the native dipole, there exists an energetically degenerate pair of states that lie along the same polar axis. Representing the dipole by a polarisation vector, the states are of equivalent magnitude but opposite polarisation direction. When the component of an external electric field parallel to the polar axis is antialigned with the electric dipole and of requisite magnitude, the polarisation vector will switch states to reduce the energetic cost. For some pyroelectric materials the requisite electric field, termed the coercive field, exceeds the point at which the crystal undergoes structural breakdown. Ferroelectrics are a sub-section of pyroelectrics in which the electric polarity can be switched reversibly between stable states. Depending on structure, a ferroelectric can have more than one polar axis allowing for multiple polarisation states. The hierarchy of electrical classification for point groups is summarised in Figure 1.1.

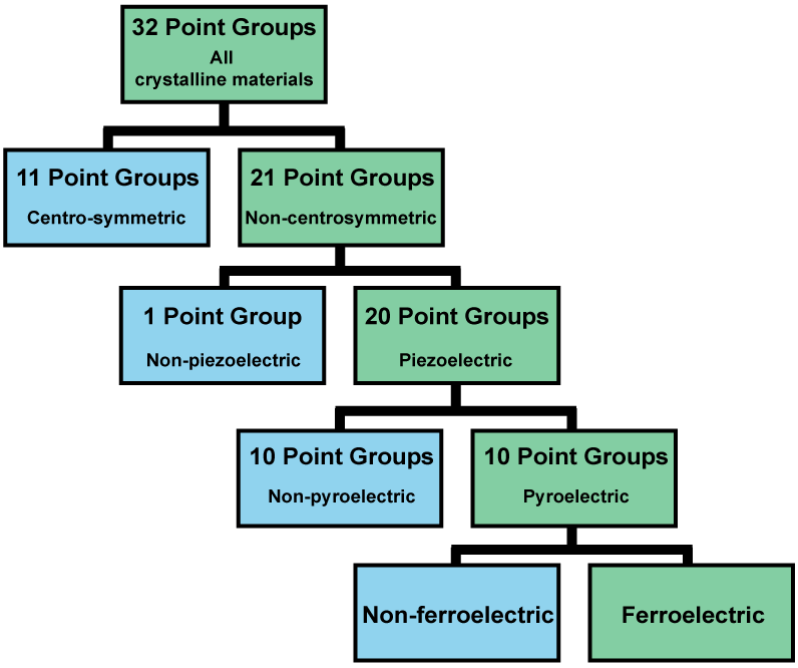

Figure 1.1 Hierarchy of the 32 crystallographic point groups, structured by their electric properties. The green panels corresponding to the sub-sections of which ferroelectric crystals are a member.

Native polarity results in a bound surface charge density of alternate sign on opposing crystal faces, which establishes a depolarising electric field anti-aligned with the polarisation vector. Unlike the magnetic counterpart, the depolarising field indicative of electric polarity cannot be observed outside the crystal as it is typically screened by aggregation of free charges within the crystal or the surrounding medium. Dynamic variation of the spontaneous polarisation, with temperature or external electric field, leads to observable changes in the bound and screening charge densities and it is from the change in charge developed across the crystal that the polarisation vector can be indirectly probed.

Plotting the change in polarisation as a function of applied field reveals that, for a ferroelectric, the response is hysteretic in nature *i.e.* a non-linear response dependent on the initial state. This exhibition of a persistent memory is analogous to magnetisation loops observed in ferromagnetic materials and is from where ferroelectrics derive their name. An ideal polarisation hysteresis loop is presented in Figure 1.2 and annotated to convey how several parameters inherent to ferroelectric behaviour can be determined from a hysteresis measurement.

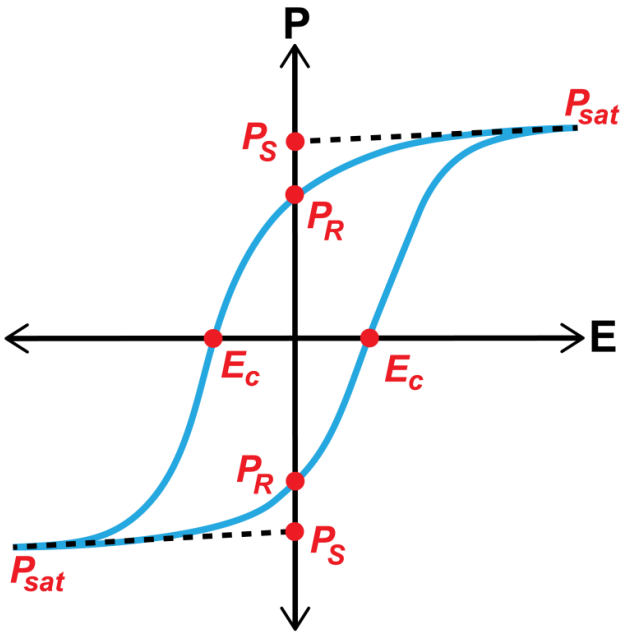

Figure 1.2 Sketch of an ideal ferroelectric hysteresis loop obtained when plotting polarisation P against applied electric field E. The values of spontaneous polarisation P_s, remnant polarisation P_R, coercive field E_C and saturation polarisation P_{sat} are obtained from the cross over points marked in red.

The coercive field, E_C, is defined by the field needed to zero the polarisation vector and the maximum polarisation value which can be induced is the saturation polarisation, P_{sat}. While ideally the polarisation value recorded at zero field would be the spontaneous polarisation, P_s, in reality it is a lower value than that theoretically predicted, termed remnant polarisation, P_R. Discrepancy between the two values arises as in practice, for a given crystal, the entirety of the constituent unit cells are not in the same ferroelectric state. Surface interactions and pinning defects within the crystal lattice may induce a directional favourability in adjacent unit cells, undermining the energetic degeneracy of ferroelectric states. Aligned under a strong electric field, upon reduction of the field these domains will revert to the favoured orientation, reducing the net polarisation vector. The spontaneous polarisation can be inferred from the hysteresis loop by extrapolating the linear behaviour near saturation back to obtain a maximum zero field polarisation for a uniformly aligned ferroelectric.

This indirect empirical determination is used as a pragmatic definition of spontaneous polarisation for a given material. Theoretical calculation of spontaneous polarisation is nontrivial as defining a singular discrete unit cell and taking it's polarisation as representative of the response of the bulk as a whole, while conceptually convenient, is an approximation which fails to accurately model the continuous nature of the charge density throughout the bulk[2]. For a given crystal lattice, differing subsets of the periodic structure may be defined as the unit cell, each with differing values of polarisation dependant on the subsection of the periodic charge distribution that they encapsulate[3].

A modern theory of polarisation has been expounded[3–6] wherein the value of polarisation is calculated for all possible unit cells within a polar lattice and each compared to the equivalent unit cell in the non-polar lattice for the high symmetry phase of the same material. While the local value of polarisation varies, the change in polarisation is found to be equal across all possible unit cells, thus a singular value for spontaneous polarisation is obtained not from a discrete unit cell but by considering all values of local polarisation that comprise the bulk as a whole. To accurately model the continuous nature of the charge density, the polarisation is not calculated via a classical ionic model but rather quantum mechanically, wherein the polarisation is ultimately represented by the phase of the periodic electronic wave function. The resultant general expression follows the form of a 'Berry phase'[7] and hence is often referred to in literature as the Berry phase polarisation[3,4,6].

This quantum mechanical approach undeniably offers a rigorous model for polarisation, however, the conceptually simpler dipole interpretation elucidates empirically observed ferroelectric behaviour while remaining intuitive. Therefore, while it remains important to acknowledge the inadequacies, in most cases the experimentalist need only consider the discrete unit cell model.

Measurement of a hysteresis loop is considered indicative of ferroelectricity. However, similar plots can be obtained when the zero field polarity is a metastable state, such as is artificially induced in electrets[8], and even in total absence of a zero field polarity, such as in lossy dielectrics[9]. For the latter, a loop is obtained but it is visually distinct from a true hysteretic plot, typically lacking the concave sides and

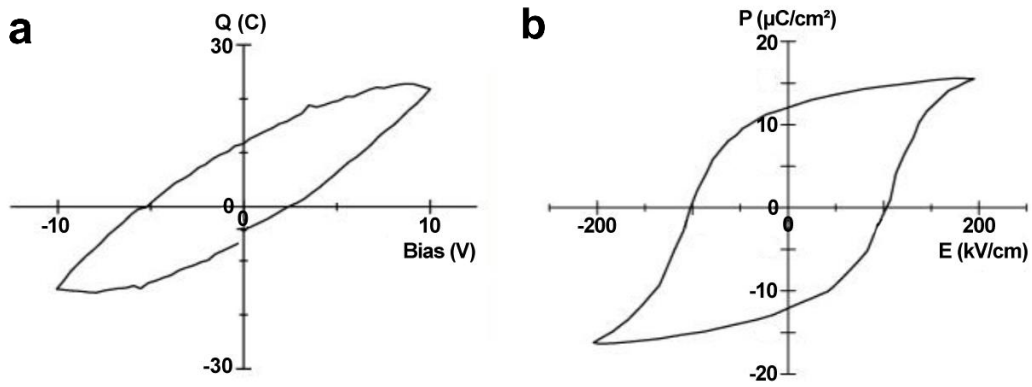

Figure 1.3 a Cigar shaped charge versus voltage loop measured from a lossy dielectric, a banana skin. **b** Ferroelectric hysteresis curve measured from ceramic $Ba_2NaNb_5O_{15}$. Figures adapted from [9].

pointed saturation features. The famous example[9] of a charge versus voltage loop measured from a banana skin in comparison to a true hysteresis curve from ferroelectric $Ba_2NaNb_5O_{15,}$ is presented in Figure 1.3. Knowledge of the sample history, exercising care to insure high quality electrical contacts and resolute inspection of the form of the loop are required to insure that true ferroelectric hysteresis has been observed.

1.2 Symmetry Breaking

Upon heating, the majority of ferroelectric materials undergo a structural transition to a higher symmetry phase with a non-polar point group. This paraelectric phase does not express a spontaneous polarisation. The temperature at which this transition occurs is known as the Curie temperature[10] (T_C) and the high symmetry. To discern the nature of the ferroelectric transition, the relationship between the symmetries and asymmetries of parent and daughter phases must be considered. Referring to asymmetries, the symmetries not expressed by a phase, may seem counter intuitive but it is important to note that while crystallographic point groups are defined by their symmetry it is the asymmetries that often result in interesting phenomena.

A key stone of symmetry theory, Curie's Principle[11,12] states that "*When certain effects show a certain asymmetry, this asymmetry must be found in the causes which give rise to them*". In other words, any transition from a high symmetry phase *G* to a

lower symmetry phase *F* must involve an additional parameter that expresses any asymmetry unique to *F*, to ensure that the asymmetries of the effect are present in the cause. Herein the action of this additional parameter (termed the order parameter) on the parent phase *G* represents the cause and the daughter phase *F* the effect.

It follows that concomitant to Curie's Principle is the requirement that all common symmetries of a cause are also common symmetries of its effect.[12] Therefore, the order parameter must also express any symmetry common between *F* and *G*. Using set theory notation we can state that for a general transition[13]:

$$F = G \cap H \tag{1.1}$$

Where *H* represents the group of symmetries expressed by the order parameter.

Returning to the ferroelectric case, the defining characteristic is the development of polarity across the phase transition. Therefore symmetry reduction from *G* to *F* as dictated by the form of the order parameter must ensure the formation of a native polarisation. A point group is defined as polar if the action of every symmetry operation of that group leaves two or more points of the crystal structure unmoved. The fixed nature of the points is essential for the crystal to have an invariant axis and thus a fixed directionality. Any symmetry operation that does not meet this definition is disallowed and cannot be present in *F*. Consequently, there is a discrete range of asymmetries that must be expressed by *F*, which are not expressed by *G*. In addition to being non-centrosymmetric, a polar point group may only have rotational symmetry in one plane and may not have a mirror plane horizontal to the polar axis[1].

The ferroelectric order parameter can hence be defined as one which introduces the asymmetries required for polarity. As these asymmetries are the origin of polarisation, this is equivalent to defining the order parameter as polarisation. To denote polarisation strictly, as in (1.1), the group of allowed symmetries, *H*, must be determined. Applying the required asymmetries to the point groups reveals the symmetry group ∞m *i.e.* allowing for mirror planes and infinite rotational symmetry in one axis[1,13]. Hence we can formally state that for a ferroelectric transition:

$$F = G \cap \infty m \tag{1.2}$$

Where ∞m has subgroups 1, 2, 3, 4, 6, m, mm2, 3m, 4mm and 6mm [13].

1.3 Thermodynamic description

To obtain a more quantitative understanding, the ferroelectric transition may be described by the reduction of thermodynamic potential, or free energy, of the system rather than reduction of symmetry. The central postulate of Landau-Ginzburg-Devonshire (LGD) theory[14,15] is that, within the vicinity of the phase transition, the free energy of a system can be expressed as a power series in the order parameter. The free energy may be a function of a range of thermodynamic variables including strain, temperature T, polarisation P and external electric field E.

Choosing the case of an unstrained, unpolarised crystal in absence of an external electric field to be zero energy, the free energy of the system can be written as:

$$\phi(P,T) = \frac{1}{2}\alpha P^2 + \frac{1}{4}\beta P^4 + \frac{1}{6}\gamma P^6 \tag{1.3}$$

Where temperature dependence is accounted for by coefficients α, β and γ. Odd powers are excluded so that the function is symmetrical about the origin, ensuring the free energy is not dependant on the sign of the polarisation. Here the power series is terminated at the 6th power for simplicity.

To account for application of an external electric field, an additional energy term is introduced that acts to reduce the free energy when polarisation and external field are aligned and increase the energy when they are anti-aligned.

$$\phi(P,T,E) = \frac{1}{2}\alpha P^2 + \frac{1}{4}\beta P^4 + \frac{1}{6}\gamma P^6 - E.P \tag{1.4}$$

The stable states of the system can be found by minimising the free energy function with respect to the polarisation:

$$\frac{\partial \phi}{\partial P}(P,T,E) = \alpha P + \beta P^3 + \gamma P^5 - E = 0 \quad (1.5)$$

Thus the electric field can be expressed in terms of the polarisation:

$$E = \alpha P + \beta P^3 + \gamma P^5 \quad (1.6)$$

Differentiating with respect to polarisation returns an expression for the inverse of the electric susceptibility, χ_E:

$$\frac{\partial E}{\partial P} = \alpha + 3\beta P^2 + 5\gamma P^4 = \frac{1}{\chi_E} \quad (1.7)$$

For the high temperature non-polar state ($P = 0$) we find:

$$\frac{1}{\chi_E} = \alpha \quad (1.8)$$

Following a Devonshire theory approach[15], it is assumed is that the temperature dependence is described fully by α, thus β and γ are constant in temperature, and that, near T_C, α varies linearly with temperature:

$$\alpha = \alpha_0(T - T_C) \quad (1.9)$$

Where α_0 is a temperature independent constant. Empirical investigations have revealed that the inverse susceptibility does indeed express linear behaviour near the transition temperature[16]. However, the sign reversal of the α coefficient is not universally observed at T_C. Therefore, α can be more strictly defined by:

$$\frac{1}{\chi_E} = \alpha_0(T - T_0) = \alpha \quad (1.10)$$

Where T_0 is the temperature at which $\chi_E \to \infty$. The form of (1.10) is analogous to the Curie-Weiss law for magnetic susceptibility[17] and hence T_0 is termed the Curie-Weiss temperature.

Substituting (1.10) into the original expression for the free energy (1.3) we find:

$$\phi(P,T) = \frac{1}{2}\alpha_0(T - T_0)P^2 + \frac{1}{4}\beta P^4 + \frac{1}{6}\gamma P^6 \qquad (1.11)$$

From (1.11) the form of the free energy of a ferroelectric system can be plotted as a function of polarisation at a range of temperatures T, defined in relation to T_0. Implicit in the Devonshire assumption of Curie-Weiss behaviour, T_0 is sufficiently near T_C for the inverse susceptibility to be within the linear regime, therefore for $T \gg T_0$ and $T \ll T_0$ the crystal is assumed to be in the high symmetry paraelectric and low symmetry ferroelectric phases respectively.

The majority of ferroelectric phase transitions fall into one of two cases[18]. Upon heating towards T_C the polarisation may decrease continuously or disappear discontinuously. In terms of free energy this corresponds to a discontinuity in the second and first differentials respectively, leading to the terms 'second order' and 'first order' phase transitions. Inspecting (1.11), α_0 is positive by construction and γ has been reported as positive for all known ferroelectrics[16]. Therefore, free energy behaviour across the transformation is dictated chiefly by the sign of β.

1.3.1 Second Order Phase Transition

The stable polarisation states of the system can be found by minimising the expression for the free energy with respect to P.

$$\frac{\partial \phi}{\partial P}(P,T) = \alpha_0(T - T_0) + \beta P^2 + \gamma P^4 = 0 \qquad (1.12)$$

In a second order transition, β is positive and thus real solutions for the polarisation can be obtained by simplifying the series expansion and considering only the two lowest order terms *i.e.* disregarding the influence of γ.

Solving for P we obtain two valid solutions:

$$P = 0 \qquad (1.13)$$

$$and\ \ P = \pm\sqrt{\frac{\alpha_0(T_0 - T)}{\beta}} \tag{1.14}$$

For temperatures greater than the Curie-Weiss temperature, $T > T_0$, (1.14) has no valid solutions, and thus the free energy has a single stable point at $P = 0$. Equivalently, $P = 0$ is the only solution at $T = T_0$. Below the Curie-Weiss temperature, $T < T_0$, the square root has real solutions and thus there are three stable points in the free energy, one at zero polarisation and two at equal and opposite non-zero values of polarisation. As a stable non-zero polarisation is not present until lowering the temperature through T_0, for a second order transition $T_0 = T_C$.

Taking the second derivative of free energy:

$$\frac{\partial^2 \phi}{\partial P^2}(P, T) = \alpha_0(T - T_C) + 3\beta P^2 \tag{1.15}$$

It is clear that the stable point at zero polarisation corresponds to a minimum and a maximum in the free energy for the high temperature ($T > T_C$) and low temperature phase, ($T < T_C$) respectively. Substituting (1.14) into (1.15), the non-zero polarisation states in the low temperature phase are confirmed to be minima in the free energy.

Therefore, the free energy transforms across the phase transition as follows: In the high temperature paraelectric phase ($T > T_C$) the free energy forms a single potential well, centred on zero polarisation (sketched Figure 1.4a). This persists for decreasing temperatures until the critical point of $T = T_C$, moving below the Curie temperature the system enters the low temperature ferroelectric phase ($T < T_C$) and the single potential well splits to form two minima that move to increasing polarisation magnitude, remaining symmetric about a maximum centred on zero polarisation. These equal and opposite energetic minima correspond to two energetically degenerate orientations of the spontaneous polarisation.

From (1.14), the spontaneous polarisation develops continuously across the phase transition as shown by plotting polarisation as a function of temperature, presented Figure 1.4b. Additionally, the electric susceptibility can be plotted across the transition: diverging towards infinity at the phase transition as shown in Figure 1.4c.

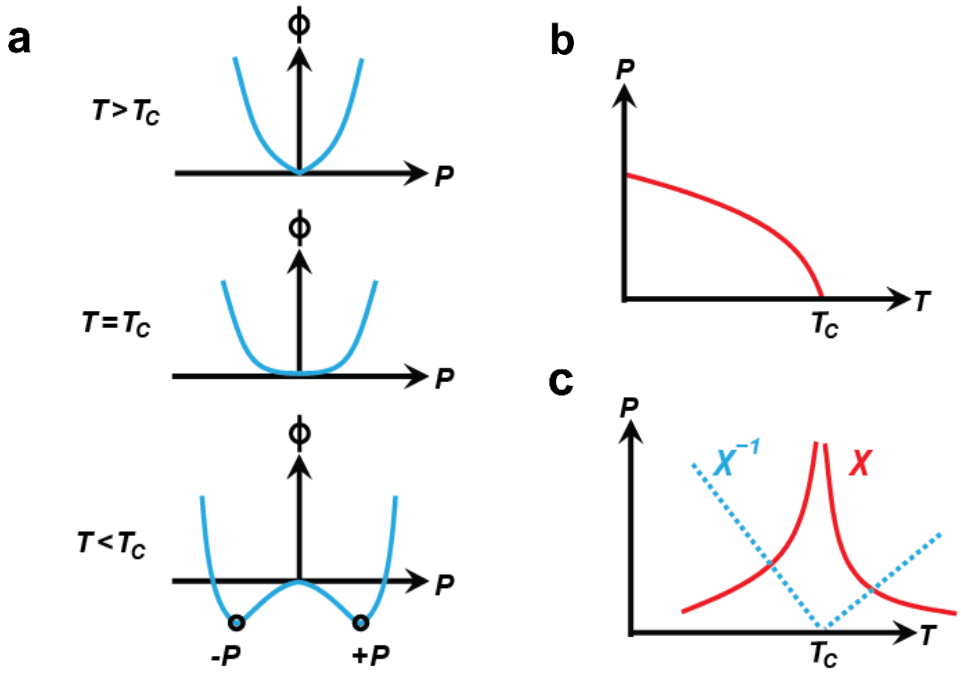

Figure 1.4 a Sketch of the development of the free energy, ϕ, in a second order phase transition as the system cools through the Curie temperature, T_c. **b** The polarisation, P, increases gradually upon cooling through T_c, expressing the continuous nature of a second order phase transition. **c** At T_C the electric susceptibility approaches infinity. Images adapted from [16] and [19].

1.3.2 First Order Phase Transition

In a first order transition, β is negative and it is clear the approximation made for the second order transition will no longer be effective: the higher order γ term in the free energy expression must be considered. Minimising the free energy with the higher order term included and solving for non-zero values of polarisation:

$$P^2 = \frac{-\beta \pm \sqrt{\beta^2 - 4\alpha_0\gamma(T - T_0)}}{2\gamma} \tag{1.16}$$

Attempts to solve directly result in complex expressions for P. Instead it is more instructive to consider the discontinuous nature which defines the first order transition. As the spontaneous polarisation develops discontinuously, (polarisation as function of temperature is sketched in Figure 1.5b), at the transition point there are simultaneously zero and non-zero solutions for the polarisation. Therefore when $T = T_C$ there must be energetically degenerate minima in the free energy both at $P = 0$ and for two non-zero polarisation values of equal magnitude. Taking the free energy expression (1.17) for $P = 0$ and the general non-zero case and equating:

$$\frac{1}{2}\alpha_0(T - T_0)P^2 + \frac{1}{4}\beta P^4 + \frac{1}{6}\gamma P^6 = 0 \tag{1.17}$$

$$\alpha_0(T - T_0) + \frac{1}{2}\beta P^2 + \frac{1}{3}\gamma P^4 = 0 \tag{1.18}$$

Equating (1.18) and (1.12) and solving for P yields:

$$P^2 = -\frac{3\beta}{4\gamma} \tag{1.19}$$

Substituting back into (1.12), and as we are considering the case when $T = T_C$:

$$T_C = T_0 + \frac{3\beta^2}{16\gamma\ \alpha_0} \tag{1.20}$$

Thus for a first order transition the Curie temperature is greater than the Curie-Weiss temperature ($T_C > T_0$). The significance of this is that there exists a temperature interval ($T_0 < T < T_C$) within which a stable polarisation has developed but $P = 0$ still represents a minimum in the free energy, as $(T - T_0)$ remains positive.

Therefore, the free energy transforms across the phase transition as follows: At temperatures far in excess of the Curie temperature ($T \gg T_C$) the free energy will express a single minimum at zero polarisation, representing the wholly paraelectric phase. However, as the temperature approaches the transition ($T > T_C$), the potential well will deform and express additional metastable minima, symmetric about the

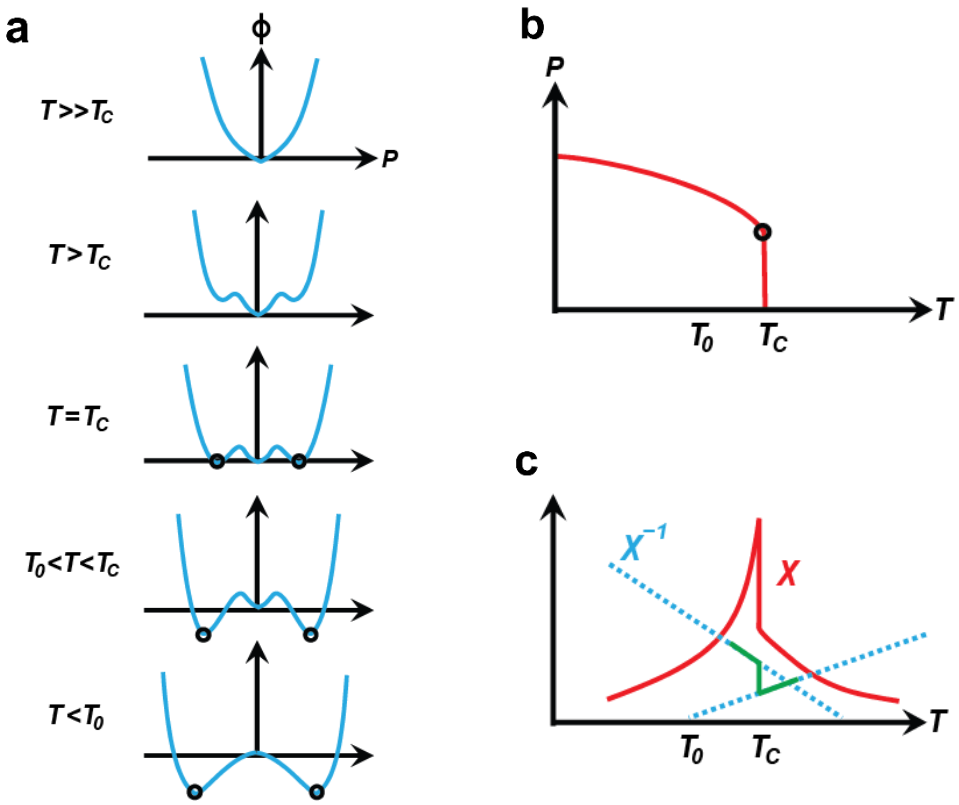

Figure 1.5 a Sketch of the development of the free energy, ϕ, in a first order phase transition as the system cools through the Curie temperature, T_C. **b** Discrete jump in the polarisation, P, at T_C corresponding to the coexistence of degenerate minima at both zero and non-zero values of polarisation. **c** Dotted lines plot the inverse of electric susceptibility , χ, for the low and high temperature phases. The discontinuous jump from one profile to the other at T_c, marked in green, corresponds to a spike in the susceptibility. Images adapted from [16] and [19].

origin, as sketched in Figure 1.5a. At $T = T_C$ the energetic favourability of the ferroelectric state is equivalent to the $P = 0$ minima, resulting in the discontinuously developed polarisation which defines a first order transition. Moving below T_C, the non-zero minima representing the ferroelectric state increase in stability and move to outward as the spontaneous polarisation develops. The stable point at $P = 0$ remains a minimum in the free energy until the Curie-Weiss temperature, below which it represents a maximum in the free energy ($T < T_0$).

In the paraelectric phase, $P = 0$ and thus the inverse of the electric susceptibility is given by (1.10) as for a second order transition. A complete expression of the electric

susceptibility in the ferroelectric phase requires solving (1.7) for the polarisation as defined in (1.16), which gives[18]:

$$\frac{1}{\chi_E} = 8\alpha_0(T_0 - T) + \frac{3\beta^2}{4\gamma} \tag{1.21}$$

Thus the predicted profile of the inverse susceptibility in the ferroelectric phase is linear, with a gradient eight times that of the paraelectric phase, with opposite sign. The change in electric susceptibility across the transition is sketched in Figure 1.5c. The two differing inverse susceptibility profiles no longer meet at zero, and rather the susceptibility changes discontinuously across the transition[16].

1.4 Improper Ferroelectricity

It is possible for polarity to develop across a phase transition where the symmetry reduction is not dictated by polarisation. Consider a general transition from a non-polar phase G to a lower symmetry phase F, as defined by (1.1), wherein the order parameter satisfies the expression:

$$H \subset \infty m \tag{1.22}$$

As H expresses all the asymmetries expressed by the polarisation order parameter, ∞m, a spontaneous polarisation will develop, fulfilling the definition of a ferroelectric transition. However, the polar phase F will express additional asymmetries, unique from G, that are not expressed by symmetry group ∞m. Using set theory notation:

$$F \subset (G \cap \infty m) \tag{1.23}$$

The reduction in symmetry from G to F is greater than required for development of a polarity *i.e.* F is not the 'maximal polar subgroup' of G. Therefore polarisation does not dictate the symmetry reduction and is not the order parameter for the transition. Rather the polarity develops as a by-product of the reduction in symmetry dictated by a separate order parameter with different transformation properties. In this situation

the low symmetry phase F, as defined by (1.23), is termed an 'improper ferroelectric', while (1.2) defines a proper ferroelectric[20].

In contrast to the proper ferroelectric where the complete set of symmetry operators was obtained, the symmetry description of the order parameter for an improper transition is comparatively open-ended; defined only as a subset. Significantly, (1.23) allows for the introduction of translational asymmetry across the transition, such that the order parameter does not have to correspond to a physical parameter macroscopically expressed by the crystal as a whole[21]. The lack of a macroscopic phenomenon to observe is in discord with the intrinsically phenomenological approach of LGD theory. Indeed, the wide range of theoretically allowed asymmetries of the order parameter make it significantly difficult to obtain a singular general free energy expression as was obtained for proper ferroelectrics. Despite this, the elegance of LGD theory is recovered by the work of Levanyuk and Sannikov[22], which considers just two general forms of the free energy expression which describe thermodynamic properties common amongst the improper ferroelectrics.

A key result is that an improper ferroelectric phase transition must have a multi-component order parameter. Consider a power series of a one-component order parameter, η, and the series must contain terms coupled with polarisation, P, as development of a polarisation is still a requirement. This allows for the linear coupled term, "ηP", where in polarisation and the order parameters have the equivalent transformation properties *i.e.* they are equally dominant in the symmetry reduction. In this case, the maximal polar subgroup can be obtained and the transition is proper. Thus an order parameter with at least two components (η, ξ), is required such that the order parameter is of different dimensionality for all coupling terms, for example $2\eta\xi P$ or $(\eta^2 - \xi^2)P$. Coupled terms linear in one component of the order parameter are disallowed. While the requirement is only for a multi-component order parameter, and indeed improper ferroelectrics with three or more component order parameters are allowed, Levanyuk and Sannikov have shown that most observed transformation behaviours can be conveyed by only considering a power series of two-components.

To facilitate a thermodynamic description as was presented for a ferroelectric transition, we consider one of the two general free energy expressions for an improper ferroelectric, as defined by Levanyuk and Sannikov[22]:

$$\begin{aligned}\phi = \ & \tfrac{1}{2}\alpha(\eta^2+\xi^2) + \tfrac{1}{4}\beta_1'(2\eta\xi)^2 + \tfrac{1}{4}\beta_2'(\eta^2-\xi^2)^2 + \tfrac{1}{6}\gamma(\eta^2+\xi^2)^3 \\ & + \frac{1}{8}\delta(2\eta\xi)^4 + \frac{1}{2}xP^2 + 2\alpha\eta\xi P - PE + \frac{1}{2}x'Q^2 + a'(\eta^2-\xi^2)Q\end{aligned} \tag{1.24}$$

On inspection the form of the free energy is similar to that of proper ferroelectrics, with expression (1.24) consisting of three main parts. The first part is a power series of the two component order parameter with a series of coefficients (α, β_1', β_2', γ and δ) analogous to the power series presented for proper ferroelectrics in (1.3). On comparison, the power series is terminated at a higher 6th order term as, unlike in proper ferroelectrics, the sign of the 6th order coefficient influences the minima of the potential. As before, the temperature dependence is accounted for by α while the remaining coefficients are taken to be temperature independent. The second part of the free energy expression is the terms added to describe the influence of a developed polarisation, again this could be expanded to a full power series but just the dominant coupled and uncoupled terms are included. The influence of an external electric field is accounted for by a $-PE$ term as it is in proper ferroelectrics. Finally the third main part is the inclusion of a general tensor component Q, necessary for the behaviour of (1.24) to account for empirically observed thermodynamic properties of improper ferroelectrics. Here x, x' and a' are more temperature independent coefficients.

The stable states of the system are found by minimising the free energy as stated in (1.24) with respect to the order parameter, a significantly more complex undertaking than as outlined previously for proper ferroelectrics. To facilitate calculation the authors restructured (1.24) by representing the two component order parameter by polar coordinates in the (η, ξ) plane[22], where in:

$$\eta = \rho\cos\varphi \qquad \xi = \rho\sin\varphi \tag{1.25}$$

Hence, the minima were found by solving for $\partial\phi/\partial\rho$, $\partial\phi/\partial\varphi$ and $\partial\phi/\partial P = 0$.

This system of partial differentials was found to have four different sets of solutions, one which corresponded to the high temperature phase and three distinct solution sets corresponding to three allowed low temperature phases. This correlates with the open ended symmetry definition of an improper ferroelectric transition as a subset of symmetries, as defined in (1.23), where the possible solutions of the free energy expression must allow for a greater range of distinct symmetries in the daughter phase. To continue presenting a thermodynamic description, the solutions for the high temperature phase and one of the low temperature phases are presented in (1.26) and (1.27) respectively[22].

$$\rho = 0, \qquad P = \frac{1}{x}E, \qquad Q = 0 \tag{1.26}$$

$$\rho^2 = \frac{1}{2\gamma}\left(-\left(\beta_1' - \frac{2\alpha^2}{x}\right) + \sqrt{\left(\beta_1' - \frac{2\alpha^2}{x}\right)^2 - 4\gamma\left(\alpha \mp \frac{2\alpha}{x}E\right)}\right) \tag{1.27}$$

$$\sin 2\varphi = \mp 1, \qquad P = \pm\frac{\alpha}{x}\rho^2 + \frac{1}{x}E, \qquad Q = 0$$

Presented in isolation, the solution set in (1.27) may appear somewhat obtuse, however, from inspection of these expressions we can deduce the form of the low temperature phase under zero applied electric field, *i.e.* when $E = 0$. There are two energetically degenerate polarisation states, of equal magnitude and opposite sign. The magnitude of the polarisation varies with temperature, as represented by the α term, and how the polarisation develops across the phase change is determined by the values of the temperature independent coefficients, as represented by ρ^2. The values for the order parameter which correspond to minima in the free energy are those which fulfil $\sin 2\varphi = \mp 1$, *i.e.* $\varphi = {}^{\pi}/_{4}, {}^{3\pi}/_{4}, {}^{5\pi}/_{4}$ and ${}^{7\pi}/_{4}$. Each of the four solutions correspond to an equivalent minimum in free energy and thus each of the four states for the order parameter are equally favourable. Consequently, moving from the high temperature non-polar phase to the low temperature phase, domains may form with the primary order parameter in one of four possible states and for each of these domains the spontaneous polarisation may be in one of two states.

Previously, for proper ferroelectrics, the change in the form of the free energy profile across the phase transition was depicted graphically by plotting free energy against

the order parameter, see Figures 1.4a and 1.5a. As in improper ferroelectrics the order parameter has two components, e.g η and ξ, the free energy profile is typically depicted by a contour plot in the (η, ξ) plane. The locations of the minima in the free energy for the initial high temperature phase, as defined by (1.26), and for the low temperature polar, as defined by (1.27), are conveyed in Figures 1.6a and 1.6b respectively.

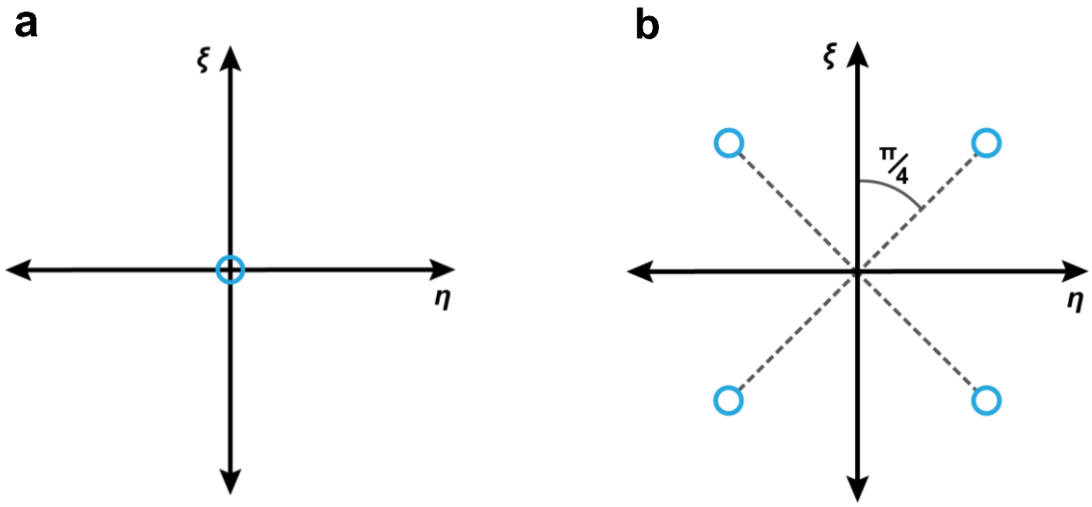

Figure 1.6 Plots depicting the position of minima in the free energy, in the (η, ξ) plane, with **a** and **b** corresponding to the phases described by (1.26) and (1.27) respectively. **a** In the high temperature nonpolar phase there is a single minimum centred on the origin. **b** The low temperature phase described by (1.27) has four energetically degenerate minima equidistant from the origin. These four minima correspond to four possible domain states for the order parameter. Figures **a**, **b** are adapted from [22].

The development of the polarisation in transition from Figure 1.6a to 1.6b cannot be inferred from the free energy profile as was done previously when discussing proper ferroelectrics. The depicted phase transition is valid whether the β coefficients are negative or positive, thus, the transition can be first or second order. It should be noted that the free energy profile depicted in Figure 1.6b is just one of the three allowed low temperature phases and that the differing solution sets can return free energy profiles with differing numbers of minima at differing positions. The many possible variations of how the polarisation may develop across the differing phase transitions, dependent on the differing coefficient values, are not presented here. For

a full analysis with plots analogous to Figures 1.4b and 1.5b, see the original work by Levanyuk and Sannikov[22].

The temperature dependence of the electric susceptibility across the phase transition can be found by taking the expression for polarisation in the solution sets and differentiating with respect to the applied electric field. For the low temperature phase, as defined by (1.27), calculation of the electric susceptibility is not trivial as a full solution requires substitution of the expression for ρ^2 into the expression for polarisation before differentiation. However, for the high temperature phase, as defined by (1.26), it's clear that the electric susceptibility is determined solely by a temperature independent coefficient.

Observation of a temperature independent electric susceptibility in the non-polar phase, often accompanied by an extremely weak peak at the transition on comparison to the pronounced peaks observed for a proper ferroelectric transition (see Figures 1.4c and 1.5c), is a convenient empirical indicator that distinguishes a proper ferroelectric from an improper ferroelectric. To demonstrate the distinct features of each profile, the temperature dependence of the measured dielectric constant in two improper systems, ammonium Rochelle salt and cobalt iodine boracite, are presented in Figure 1.7 alongside a proper ferroelectric, potassium di-hydrogen phosphate, for comparison[23–25]. The shape of the profile for the dielectric constant, ε, is equivalent that of the electric susceptibility, χ, as the quantities are related by the expression.

$$\chi = (\varepsilon - 1) \tag{1.28}$$

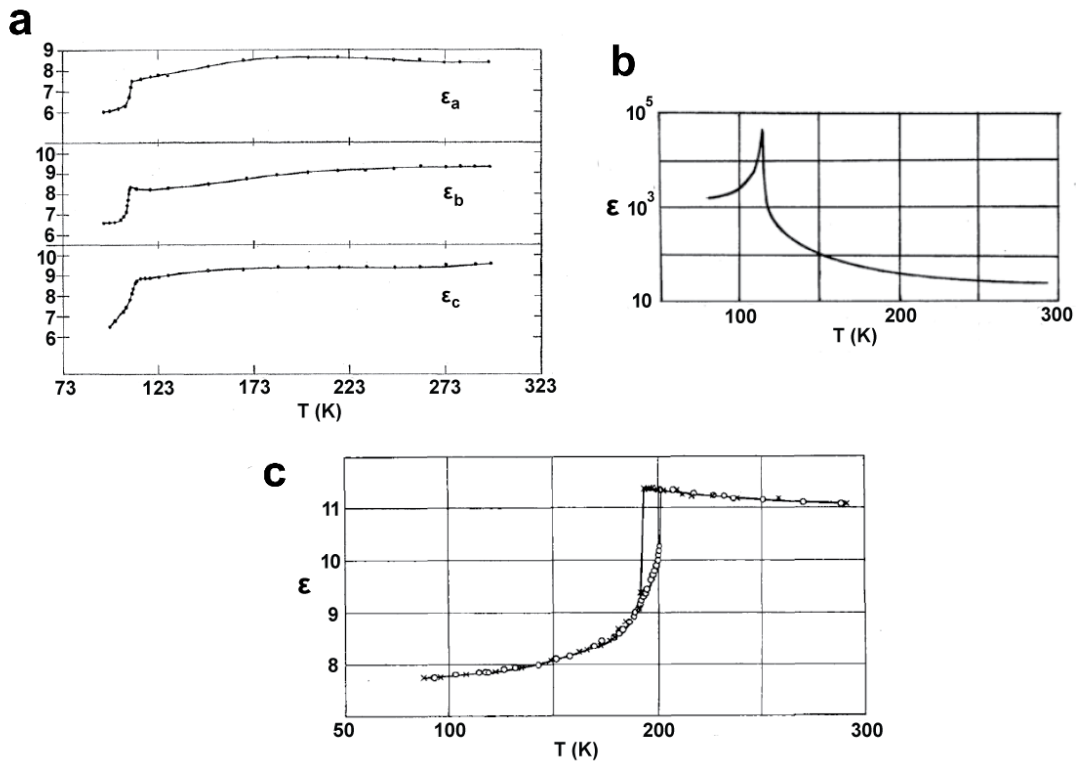

Figure 1.7 a Dielectric constant (ε_a, ε_b and ε_c measured along the a, b and c axes) of improper ferroelectric ammonium Rochelle salt across the Curie temperature. **b** Dielectric constant of the proper ferroelectric, potassium di-hydrogen phosphate, across the Curie temperature. **c** Dielectric constant of the improper ferroelectric cobalt idodine boracite (recorded at 800 Hz) across the Curie temperature. Neither of the improper systems, **a** and **c**, obey Curie-Weiss behaviour, conveyed by **b**, in the high temperature phase. Figures **a**, **b** and **c** adapted from [23], [24] and [25] respectively.

1.5 Ferroelectric Domains

In an ideal infinite crystal, such as is considered in LGD theory, the energetically favourable state is the entirety of the crystal aligned in the same polarisation direction. Structurally, polarisation has been defined discretely, by the dipole moment in individual unit cells of the material, and each polarisation vector has two possible, energetically degenerate, directional states. Upon cooling through T_C, the polarisation of each unit cell may develop in either direction with equivalent probability. Thus naively considering each unit cell individually, we would expect a random distribution throughout the material with equal proportions of each polarisation direction and no net polarisation. However, there are structural and

electrostatic contributions to the free energy which depend on the relative alignment of adjacent unit cells thus a purely random distribution is not favourable.

Typically a real crystal is observed to be divided into regions within which all unit cells are co-aligned but where the polarisation direction of adjacent regions is anti-aligned[26,27]. These opposing regions of uniform polarisation are called domains. The presence of domains in a real crystal, compared to an infinite one, can be understood by considering the effect of introducing surface boundaries. Consider a uniformly aligned, or monodomain, finite ferroelectric crystal as depicted in Figure 1.8a. The termination of the polarisation vector at a crystal boundary results in a bound surface charge with density proportional to the net polarisation. A depolarising electric field, anti-aligned to the polarisation, develops between the oppositely charged faces. As previously stated, once established the depolarising field may be screened by redistribution of free charges within the crystal or the surrounding medium.

However, the magnitude of the initially established depolarising field may be reduced if, across the phase transition, the crystal divides into two opposing domains, as shown in Figure 1.8b. This subdivision may be carried further, see Figure 1.8c, with the energetic cost of the depolarising field reducing as the spatial extension of the field reduces. As the dipole orientation depends on the structure of the unit cell, a change in polarisation direction requires a structural change between domains. The boundary regions between domains, across which this structural change occurs, are called domain walls. Subdivision of the crystal continues until the structural cost of forming domain walls is equivalent to the reduction in energy from reducing the depolarising field. Hence the energetically favoured domain distribution can be determined by considering an equilibrium between the polar and structural costs.

The initial calculations on the energetics of general domain formation were initially carried out by Landau and Lifschitz[28], before being formalised by Kittel[29] for ferromagnetic domains and the expressions later shown to hold valid for ferroelectrics, by Mitsui and Furuichi[30]. The generalised free energy, G, is stated in (1.29) for a finite crystal as a function of domain width, w.

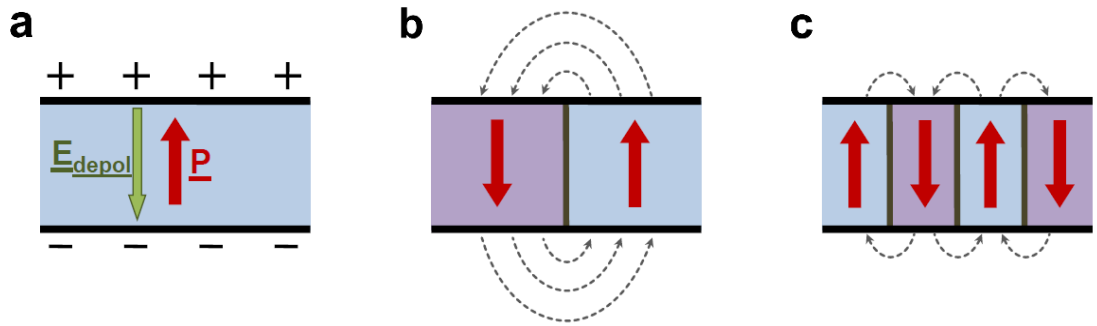

Figure 1.8 Schematic of how domain formation reduces the extent of the energetically costly depolarising field formed outside the crystal. **a** The monodomain state where opposing surface charges induce a maximal depolarising field. **b** Division into two antialigned domains states reducing the surface charge and resultant depolarising field. **c** Further domain formation leads to more complete surface charge compensation. Figures reprinted from [31].

$$G = Uw + \frac{\gamma t}{w} \tag{1.29}$$

The free energy component associated with the depolarising field is represented by a surface charge density, U, and scales proportionally with increased w while the domain wall energy per unit area, γ, decreases with increased w. In addition the domain wall area increases as the separation of the oppositely charged faces, t, (*i.e.* crystal thickness) increases.

To find the equilibrium domain distribution, the free energy is minimised with respect to w and rearranged:

$$w_{min} = \sqrt{t\frac{\gamma}{U}} \tag{1.30}$$

Referred to as the Landau-Lifschitz-Kittel (LLK) scaling law, (1.30) shows that the domain width grows proportionally to the square root of the material thickness. The scaling law assumes that the domain walls are of negligible width in comparison to the domain. Domains arranged as shown in Figure 1.8 are known as 180° 'stripe' domains and their associated domain walls are very narrow, with widths of the order of unit nanometres[32]. As a result, the assumption holds down to small values of t with the periodicity of 180° domains empirically verified to follow the LLK scaling

law down to ferroelectric material thickness of a few unit cells[33]. For comparison, ferromagnetic domain walls are much wider[29,32,34], on the order of hundreds of nanometres.

The different domain wall widths are a reflection of how each order parameter changes sign across the domain wall. In ferromagnetic domain walls, the exchange interaction dominates over crystal anisotropy and energetic cost is reduced when adjacent magnetic moments are aligned in parallel[35]. In addition, the order parameter, magnetisation, is quantised and cannot vary in magnitude. Hence ferromagnetic domain walls are typically Bloch and Neel type walls, shown in Figure 1.9a and 1.9b respectively, wherein the order parameter rotates continuously across the boundary to prevent adjacent antiparallel magnetic moments. All ferroelectric materials, as stated previously, are piezoelectric and the spontaneous polarisation strongly coupled with the lattice strain. This strong coupling disfavours rotation of polar axis and energetic cost is minimised when crystal anisotropy is reduced. As a result, ferroelectric domain walls are generally considered to exhibit Ising behaviour, sketched in Figure 1.9c, where the axis is fixed and instead the order parameter changes in magnitude across the boundary.

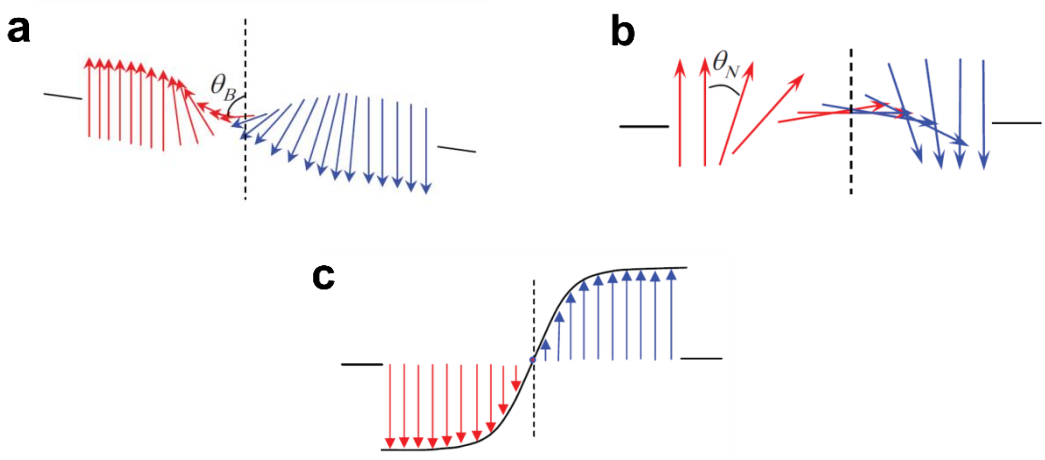

Figure 1.9 Bloch, **a**, and Neel, **b**, type domain walls commonly found in ferromagnets wherein the magnetisation inverts by a rotation through an angle, θ_B or θ_N, out of or in the plane of the wall respectively. **c** Ising type domain wall typically found in ferroelectrics wherein the magnitude of the polarisation decreases to zero before increasing with opposite sign. Schematics taken from [36].

Ferroelectric domain walls exhibiting a combination of Bloch, Neel and Ising behaviour have been predicted to occur with most research considering materials with a perovskite structure[36–38]. Calculations carried within a LGD model determined small non-axial components of the polarisation, corresponding to partial rotation, would be expected at 180° domain walls. Despite strong theoretical evidence, empirical verification of mixed behaviour walls has been elusive with the first observation in perovskites occurring only recently[39]. While no perovskite materials are under investigation in this thesis, partial Bloch behaviour has been similarly predicted to occur at 180° domain walls in lithium niobate[36,40].

1.5.1 Charged Domain Walls

Consider a domain wall that lies at an angle θ to the polarisation in a uniaxial crystal as depicted in Figure 1.10a. The off-axis wall ensures the uniaxial domains align such that positive or negative end of the dipoles meet at the domain wall, known respectively as a head-to-head or tail-to-tail wall configuration. As described above, the polarisation vector varies across the domain wall with Ising behaviour, depicted schematically and graphically for $\theta = 90°$ in Figures 1.10b and 1.10c respectively. However, unlike a parallel domain wall, the resultant polarisation vector field now has a non-zero divergence and, from Gauss' law for dielectric materials, this is equivalent to a local bound charge density[41], (1.31).

$$-\nabla \cdot P_n = \rho_b \tag{1.31}$$

Where, ρ_b is the bound charge density and $\nabla \cdot P_n$ is the divergence in the component of polarisation normal to the wall, P_n. For the general case depicted in Figure 1.10a, P_n is given by:

$$P_n = P \sin\theta \tag{1.32}$$

The bound charge at the domain wall results in a large depolarizing field that, if greater than the coercive field E_C, will cause the opposing domain to switch polarisation direction, effectively extinguishing the charged domain wall. The magnitude of the depolarising field, E_D, can be found by considering the change in electric displacement at the boundary[42], D.

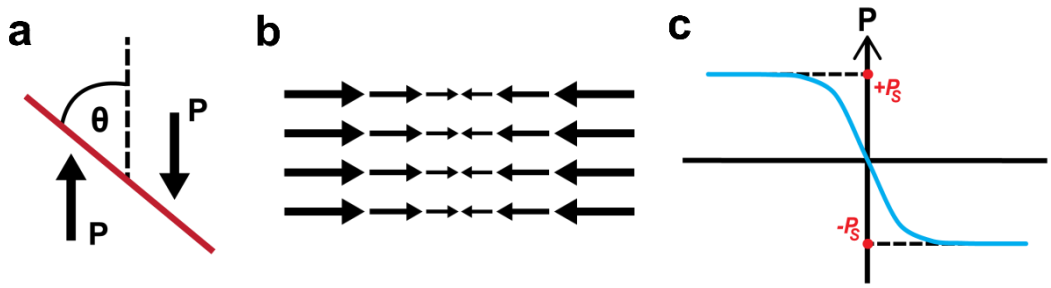

Figure 1.10 a Illustration of a head-to-head charged domain wall, where the wall is inclined at an angle θ relative to the polarisation axis. **b** Schematic representation of the Ising type polarisation reversal across a maximally charged head-to-head domain wall, conveying the divergence in the polarisation. **c** Qualitative graph plotting the polarisation, P, across the wall with a total difference of two times the spontaneous polarisation P_s.

$$D = \varepsilon_0 E + P_n \tag{1.33}$$

$$\nabla \cdot D = \nabla \cdot (\varepsilon_0 E + P_n) = \rho_f \tag{1.34}$$

Akin to P, which was the vector field due to the bound charge density, D is the vector field to the free charge density, ρ_f. E in this expression is the total electric field in the dielectric due to the combined charge density. The depolarising field is greatest in the case of an unscreened charged wall, *i.e.* when there is no free charge present at the boundary. By setting the free charge to zero we find:

$$\nabla \cdot (\varepsilon_0 E + P_n) = 0 \tag{1.35}$$

Assuming the charged wall exhibits complete Ising behaviour, with no out of plane change in polarisation, we can reduce the divergence to the one axis in which it changes:

$$\frac{\partial}{\partial \mathrm{x}} (\varepsilon_0 E + P_n) = 0 \tag{1.36}$$

$$\frac{\partial}{\partial \mathrm{x}} E = -\frac{\partial}{\partial \mathrm{x}} \left(\frac{P_n}{\varepsilon_0} \right) \tag{1.37}$$

Integrating both sides we find the depolarising field normal to the wall:

$$E_D = -\frac{P_n}{\varepsilon_0} \tag{1.38}$$

Often in literature (1.34) and (1.38) will be presented with ε_0 replaced by ε_b, representing 'background permittivity'[43,44]. This background permittivity is a useful fitting parameter[45] which accounts for the contribution to total polarisation from sources other than the unit cell centred electric dipole developed across the phase change, *i.e.* the traditionally defined spontaneous polarisation. In practice these "non-critical" sources of polarisation can be significant, and as such ε_b can be required to match experimental data with theory.

In the case of congruent lithium niobate[46] (P_s ~ 70 μCcm^{-2}) , using (1.38) we obtain a maximum depolarising field strength of ~ 7.9x10^7 Vmm^{-1}, which is three orders of magnitude larger than empirically determined values for the coercive field, E_C ~19 kVmm^{-1}[47]. Furthermore the depolarising field is of the same order of, or greater, than the dielectric strength[48] down to a minute 0.07° deviation from the polarisation axis. This test piece calculation conveys the substantial instability of an unscreened charge domain wall, even at small values of θ. Hence, for a charged domain wall to be stable, the bound charge must be mostly, if not completely, screened by free charges from the bulk.

From Figure 1.10c, it is clear that the change in polarisation across the wall is equal to twice the polarisation component normal to the wall. Therefore, for complete screening of the bound charge as defined by (1.31), the required charge density of free carriers at the wall is given by:

$$n = \frac{2P_n}{qd} \tag{1.39}$$

Where q is the charge an individual charge carrier and d the domain wall width. At room temperature ferroelectric materials, assuming undoped crystals with minimal fabrication defects, express large band gaps with low ionic mobility and, as such, q is taken to be the electronic charge. Indeed for the materials of study in this thesis,

$YbMnO_3$, $ErMnO_3$ and $LiNbO_3$, bulk conductivity is electronic with comparatively large activation energies measured for ionic conduction[49].

Ferroelectric materials are inherently insulating as a large free charge density would act to reduce polarisation and redistribute under external field to prevent a hysteretic response. In general the large spontaneous polarisation of a proper ferroelectric is complemented by a wide semiconductor band gap and consequently the intrinsic carrier density is insufficient to satisfy complete screening of bound charge as given by (1.39). Native charged domain walls rarely form in proper ferroelectrics and charged domain walls injected by application of local electric fields are unstable with short lifetimes: the unscreened depolarising field back switching the written wall. In recent years the increased interest in charged domain walls has led to the development of methods for stable formation including material doping[50], super-band gap illumination[51], pyroelectric switching[52–54] and strain engineering[55].

For the majority of techniques the crux is the same, providing additional sources of charge to screen the wall; at high temperatures additional carriers with large activation energies, immobile at room temperature, can aggregate at charged domain walls; appropriate dopant percentages increase bulk carrier density without detriment to the ferroelectricity; super-band gap illumination produces electron-hole pairs via photo-excitation.

A thermodynamic description of charged domain walls in proper ferroelectrics was formalised in an eminent publication by Gureev *et al.*[56] While not the first to apply LGD theory to the case of a charged domain wall[57], their approach considers a full range of screening regimes (linear / non linear, classical / degenerate), obtaining explicit expressions for the boundaries between each as a function of polarisation and bulk carrier density. The efficacy of the approach is conveyed by the simplicity of the resultant expressions for the domain wall energy in each screening regime.

For non-linear screening, via classical or degenerate electron gas, the wall energy W_{nl} is given by:

$$W_{nl} = \frac{2P_n}{q} E_g = nE_g \tag{1.40}$$

Where E_g is the band gap; the energetic cost is equal to the energy required to generate sufficient density of charge carriers to completely screen the wall.

For linear screening of a charged domain wall, by a classical or degenerate electron gas, the wall energy, W_l, is given by:

$$W_l = \frac{4}{3}|\alpha|{P_n}^2 \frac{d}{2} \tag{1.41}$$

Where α is the LGD coefficient and d is the domain wall width. From the polarisation profile in Figure 1.10c and (1.31) we can infer the screening charge density will be of a form similar to a normal distribution. Here the domain wall width is defined as the full width half maximum (FWHM) of the screening charge profile. Intuitively, Gureev *et al.* found that d was approximately twice the linear and non-linear Debye screening lengths for linear and nonlinear screening by a classical electron gas respectively. Consistently, d for charged domain walls with linear and nonlinear degenerate screening was on the order of the Thomas-Fermi lengths for linear and nonlinear media.

In the improper ferroelectrics, however, these expressions do not apply. As polarisation is not the primary order parameter, the increased electrostatic cost of forming a charged domain wall is secondary to facilitating the efficient reduction in order parameter across the boundary. Additionally, improper ferroelectric materials typically have significantly lower values of spontaneous polarisation compared to proper ferroelectrics, as the dipole moment forms as a by-product of symmetry reduction. Hence, the formation of native charged domain walls across the phase transition may be, on comparison, energetically favourable. The recent interest in charged domain walls has lead a resurgence in improper ferroelectrics research with an abundance of native charged domain walls observed in $Ca_3Ti_2O_7$ [58], $Cu_3B_7O_{13}Cl$ [55] and several members of the $RMnO_3$ family[59–62].

Significantly, the secondary weighting of the polarisation also typically corresponds to a large coercive field, as the electrostatic cost must overpower the cost in changing the primary order parameter. The large coercive field coupled with weak polarisation may result in reduction of the depolarising field below the coercive field with only partial screening of the charged domain wall. Therefore, in improper ferroelectric materials, the domain walls may stabilise at large values of θ despite a low free charge density in the bulk.

1.6 Domain Wall Conductance

Enhanced conductivity at charged domain walls was predicted in 1973 by Vul *et al.*[63] upon calculating the requisite density of aggregated screening carriers. Subsequent investigations into charged domain walls using surface etching and electron microscopy reported results characteristic of domain wall conductance[64–66]. Nonetheless increased conduction at ferroelectric domain walls was not directly observed until 2009 when Seidel *et al.* utilised conductive atomic force microscopy (c-AFM) to measure increased current on written walls in a $BiFeO_3$ thin film[67]. Unexpectedly, the increased conductivity corresponded to 180° uncharged domain walls.

This seminal work precipitated a surge in experimental and theoretical research into ferroelectric domain walls as discrete entities with functionality distinct from the bulk. Domain wall conductance brought with it the enticing possibility of a new class of reconfigurable nanoelectronic devices: an aspiration which has led to the growth of domain wall conductance into an internationally established field of research with strong ties to industry.

The following section summarises the key developments in conducting domain wall research, presenting and discussing the now numerous ferroelectric systems shown to exhibit domain wall conductance. This overview is not exhaustive, but merely aims to outline the current state of understanding, both over manipulation of conducting domain walls and the fundamental physics behind the enhanced conductivity.

Bismuth Ferrite, $BiFeO_3$

Room temperature $BiFeO_3$ is a rhombohedral ferroelectric with four distinct polarisation axes, lying along the psuedocubic <111> directions. The multiaxial structure leads to energetic minima for formation of domain walls with adjacent polarisation vectors meeting at 79°, 109° and 180°. All three wall types are uncharged with polarisation vectors either side of the wall meeting in a head-to-tail configuration. Seidel *et al.* reported enhanced conductivity at the 109° and 180° walls but no distinct conductivity was observed at 71° walls, piezoresponse force microscopy (PFM) and conductive AFM maps are shown in Figures 1.11a and 1.11b respectively[67].

High resolution transmission electron microscopy (HRTEM,) imaging of the 109° walls revealed a local increase in the normal component of polarisation, suggestive of locally increased carrier density. The observation was reinforced by subsequent density functional theory (DFT) calculations which considered the non-Ising structure of $BiFeO_3$ walls[68] and obtained a divergence in polarisation for each wall type[69]. Additionally, both studies predicted a local narrowing of the band gap due to structural distortions at the domain wall, with calculated reductions of approximately 0.2, 0.1 and 0.05 eV for 180°, 109° and 71° walls respectively. A combination of increased carrier density and decreased band gap was proposed as the source of domain wall conductance.

This work was expanded upon by Morozovska *et al.*, using LGD theory expressions for the Ising and Neel-type polarisation components to calculate the profile of screening carriers across each wall[70]. In agreement with [69] the calculated density of screening carriers was greatest for 180° and least for 71° walls. Bandgap narrowing was directly measured[71] at 109° and 71° domain walls using a combination of scanning tunnelling microscopy (STM) and scanning tunnelling spectroscopy (STS), with increased tunnelling current at 109° walls. In contrast to theory predictions and previous measurements, Farokhipoor *et al.* observed enhanced conductivity at 71° walls of the same magnitude as at 109° walls within the same film[72,73].

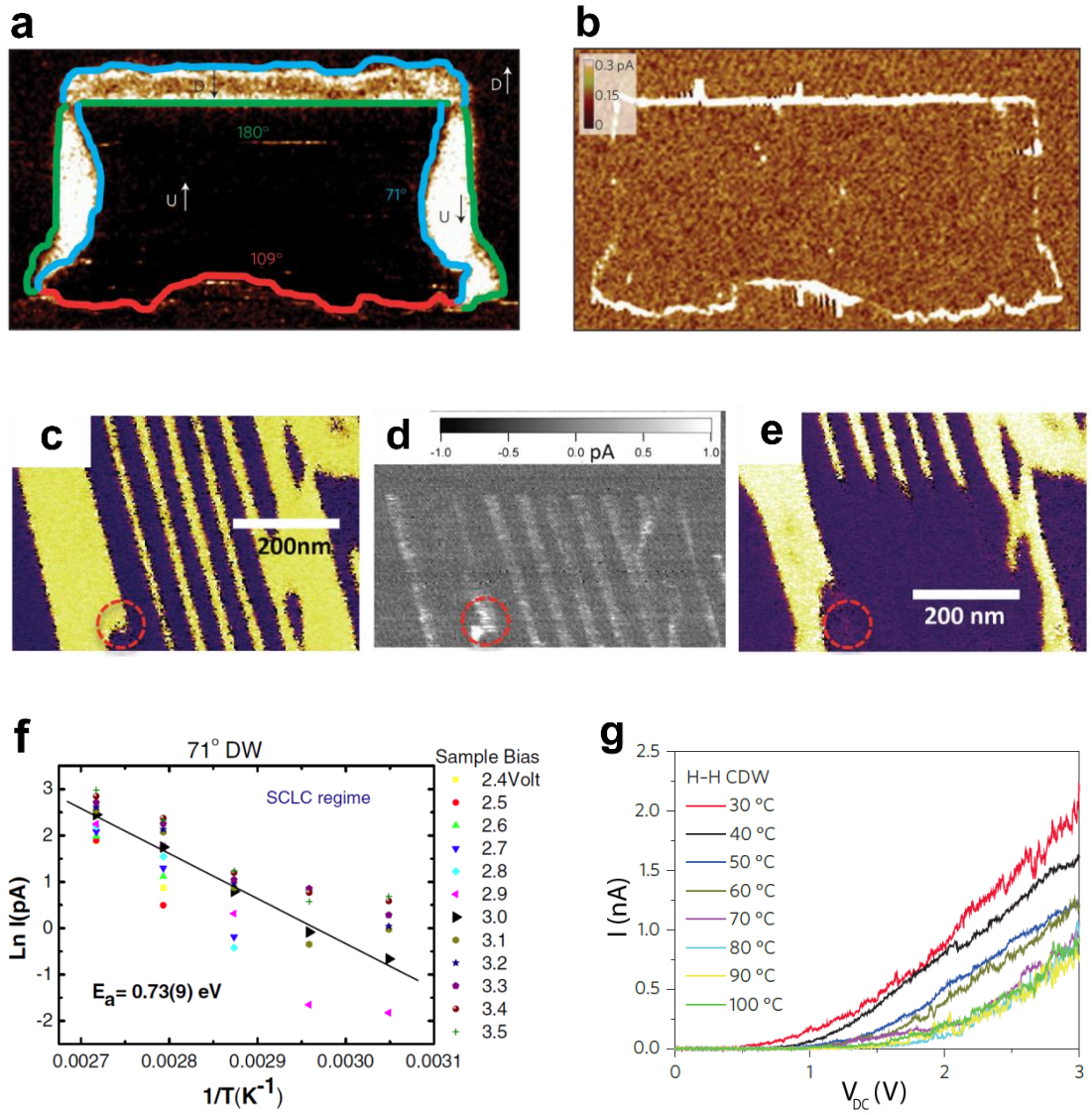

Figure 1.11 a Lateral PFM phase of a written domain pattern in $BiFeO_3$ thin film with three uncharged wall types 71°, 109° and 180°. **b** c-AFM map of the region in **a**, showing enhanced conduction at 109° and 180° domain walls. **c** PFM phase of an array of 71° domains. **d** The domains in **c** were erased with a applied bias and c-AFM measurement immediately recorded, showing a lingering conductive trace despite domain reversal. **e** Subsequent PFM phase map, confirming the domains were erased. **f** Thermally activated conductance observed at uncharged 71° walls. **g** Metallic conducting behaviour observed for charged head-to-head walls. Figures **a** and **b** reprinted from [67] **c**, **d** and **e** from [74], **f** from [72] and **g** adapted from [75].

Oxygen vacancies have been shown to play a crucial role with order of magnitude increased conductance observed for samples annealed in low oxygen pressures[76]. Temperature dependent studies revealed conductivity was thermally activated with

energies of 0.2-0.5 eV and 0.7 eV consistent with ionisation of independent[76] and clustered[72,73] oxygen vacancies respectively. Arrhenius behaviour at 71° walls presented in Figure 1.11f. In an influential study by Stolichnov *et al.*[74] the conductive traces of 109° walls were observed to persist temporarily after walls were erased by poling, shown in Figures 1.11c, 1.11d and 1.11e. This lingering conductivity strongly suggests mediation by defect aggregation as opposed to intrinsic carriers. Within $BiFeO_3$ oxygen vacancies act as electron donors and accordingly experimental studies[72–74] propose n-type conduction at the nominally uncharged walls, in conflict with the p-type carrier aggregation predicted by Morozovska *et al.* Recently p-type conduction was proposed for equivalent 180°, 109° and 71° walls in ceramic $BiFeO_3$, wherein screening was facilitated by an increase in the oxidation state of Fe at the walls relative to the bulk, Fe^{4+} and Fe^{3+} respectively[77].

Typical charged domain walls have also been written in $BiFeO_3$ thin films, where enhanced conductance was observed at head-to-head walls, tail-to-tail walls exhibited bulk conductance, suggesting conduction mediated by n-type carriers[75,78]. Significantly conductance was found to vary with wall angle, in agreement with theory predictions[56,79,80], with a maximum conductance (10^{-8} S) four orders of magnitude higher than at uncharged walls (~ 10^{-12} S). Temperature dependent investigation of the charged domain wall revealed metallic conductivity, presented Figure 1.11g, in contrast with the semiconducting behaviour observed on 71° walls.

Lead Zirconate Titanate, $PbZ_xTi_{x-1}O_3$

Shortly after the Seidel *et al.* paper was published, enhanced conductivity was observed in nominally uncharged 180° walls in $Pb(Zr_{0.2}Ti_{0.8})O_3$ thin films[81], data presented Figure 1.12a. Current against voltage (I/V) measurements at a range of temperatures revealed distinct semiconducting behaviour, data presented in Figure 1.12b. Akin to $BiFeO_3$, oxygen vacancy concentration was demonstrated as modulating domain wall conductance, with enhanced and bulk conductivity exhibited upon alternate vacuum annealing and ambient exposure respectively[82]. I/V measurements[83] during switching of 180° domains revealed a transient increase in conductance corresponding to temporary formation of head-to-head charged domain walls. The transient state was found to exhibit metallic temperature dependence,

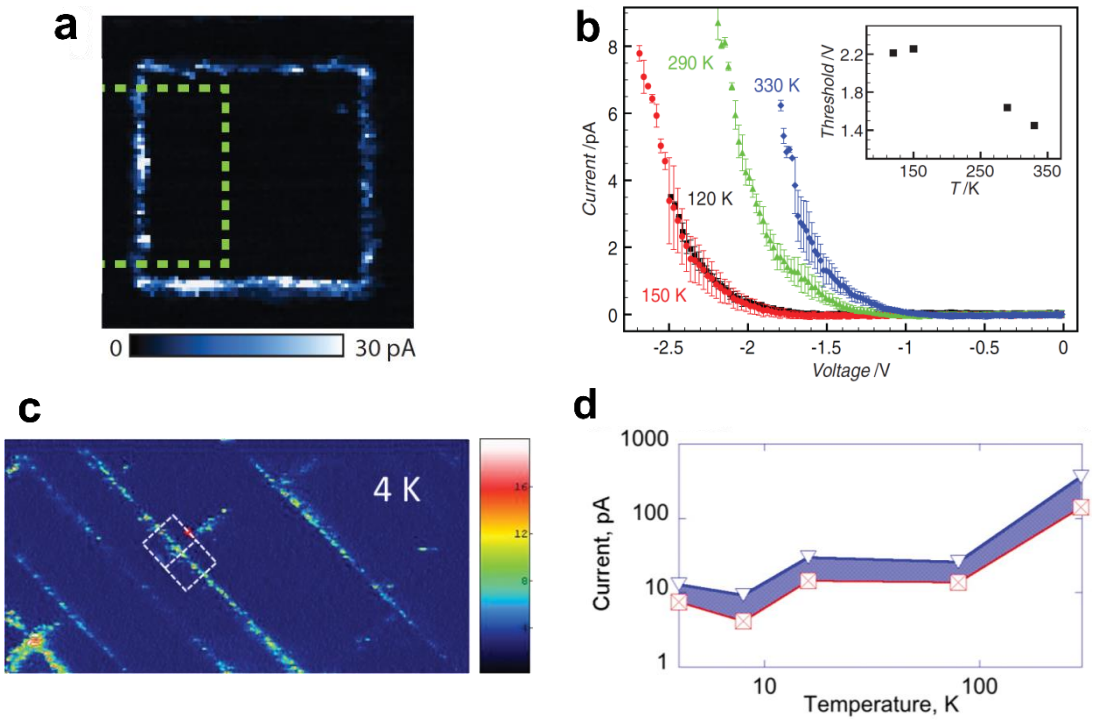

Figure 1.12 a c-AFM map of 180° domain pattern written into a $Pb(Zr_{0.2}Ti_{0.8})O_3$ thin film, measured under -1.5 V bias, conveying increased conductance at the uncharged domain walls. **b** I/V profile recorded at the uncharged 180° wall for a range of temperatures, revealing semiconducting behaviour. **c** c-AFM map of current measured at 4 K, under -7 V bias, for weakly charged domain walls, bent off their neutral position. Conductance at this extremely low temperature is strong indicator of intrinsic conductance. **d** In conflict to seemingly metallic behaviour presented in **c**, conductance of the weakly charged domain walls increased with temperature. Figures **a** and **b** reprinted from [81] and Figures **c** and **d** from [84].

contrary to the distinct semiconducting behaviour of 180° walls.

Stolichnov *et al.* used strain engineering to promote formation of narrow in-plane polarised stripe domains in a majority out-of-plane polarised film, generating head-to-tail 90° walls[84]. Observed domain wall conductance was attributed to substrate-strain induced bending of the walls, leading to local divergence in polarisation. Robust domain wall conductance was measured down to 4 K, c-AFM presented in Figure 1.10c, strongly indicative of metallic conductance. Notably, new 90° walls were mechanically written at 4 K and immediate domain wall conductance observed, verifying existence of an intrinsic conduction mechanism. Such "bent" charged domain walls display an inverse dependence on oxygen vacancy concentration to

180° walls, exhibiting enhanced conductance upon exposure to a high-pressure oxygen atmosphere[85]. In apparent conflict with the seemingly metallic 4 K measurements, domain wall current increased with temperature, data plotted in Figure 1.12d.

Recently increased conduction was reported along 180° domain walls in undoped single crystal $PbTiO_3$. Faraji *et al.* demonstrated increased conduction both for native domain walls and for domains formed under applied bias[86]. Notably, room temperature IV measurement revealed substantial wall conductance 4 to 5 orders of magnitude above the insulating bulk.

Lithium Niobate, $LiNbO_3$

Enhanced conductivity at charged domain walls in $LiNbO_3$ single crystals was indirectly observed by Aristov *et al.* in the 1980s[65]. Alternating electric-fields were applied during crystal growth to obtain periodic striped domains with alternating head-to-head and tail-to-tail domain walls. Imaging under scanning electron microscopy (SEM), voltage contrast was observed at head-to-head and tail-to-tail walls when the crystal surface was positively and negatively charged respectively. Aristov *et al.* predicted a sink for negative and positive charges at alternate walls and attributed the voltage contrast to locally increased conductivity. A continuation of the work by Kokhanchik and Irzhak, published in 2007, corroborated the assertion of domain wall conductance at tail-to-tail walls[87].

$LiNbO_3$ was chosen, as an archetypal uniaxial ferroelectric, as the material of study for a theoretical model by Eliseev *et al.*[79], which served to explain the relationship between local distribution of screening carriers and conductivity at charged domain walls. Enhanced conductivity was attributed to the aggregation of screening carriers, required to screen the depolarising field and stabilise the charged domain wall, resulting in an increase in the local carrier density. Following from relationship between screening density and wall angle, defined in (1.39), the domain wall conductance was found to increase as the wall angle θ increased from 0° to 90°.

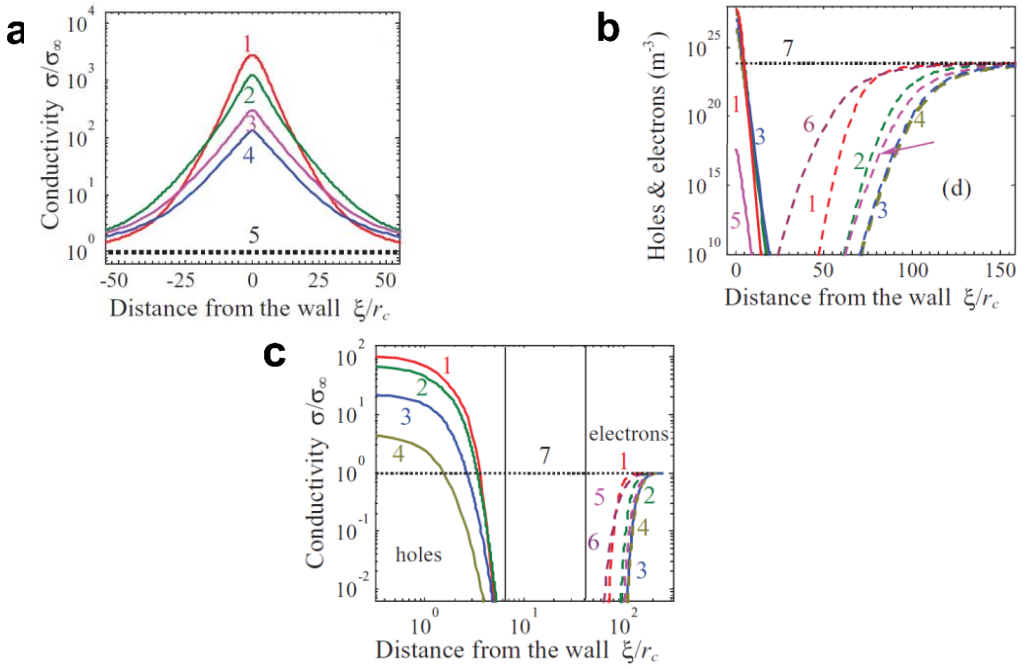

Figure 1.13 Carrier screening and conductivity models for charged domain walls within a n-type semiconducting bulk. **a** Conductivity profile across a head-to-head domain wall, relative to the bulk conductivity, for a range of wall angles. Curves 1 to 5 correspond to wall angles of $\theta = {}^{\pi}/_{2}, {}^{\pi}/_{6}, {}^{\pi}/_{20}, {}^{\pi}/_{40}$ and 0. **b** Carrier concentration at a tail-to-tail wall for a range of wall angles; solid and dashed lines corresponding to concentration of holes and electrons respectively. **c** Relative conductivity profile at a tail-to-tail wall for a range of wall angles; conveying a dual banded structure with an inner region of increased conductivity flanked by a band of decreased conductivity. Curves 1 to 7 correspond to wall angles of $\theta = {}^{\pi}/_{2}, {}^{\pi}/_{4}, {}^{\pi}/_{10}, {}^{\pi}/_{20}, {}^{\pi}/_{27}, {}^{\pi}/_{40}$ and 0. Figures reprinted from [79].

Also of note were the predicted differences in conductivity profiles between the head-to-head and tail-to-tail walls dependent on dominant bulk carrier type. $LiNbO_3$ is a wide band gap n-type semiconductor in bulk, though the authors state the outcomes can be equally applied to a p-type system by simply swapping the sign of charged domain wall and carrier in the discussion. Relative conductivity profile at head-to-head walls, plotted in Figure 1.13a, mirrored the normal distribution behaviour predicted by (1.31) for aggregation of screening carriers. Bound charge screening at tail-to-tail walls, presented in Figure 1.13b, has a more complex structure with majority screening facilitated by aggregation of ionized donors due to low bulk concentration of holes. Contribution from comparatively immobile donors to conductivity was deemed negligible, resulting in a dual band structure where a

narrow band of enhanced conductivity is flanked by an outer band wherein conductivity is decreased relative to the bulk, shown in Figure 1.13c.

Schroder *et al.* reported the first direct measurement of domain wall conductance, presenting c-AFM of increased current along head-to-head walls in Mg-doped congruent $LiNbO_3$ [50], PFM and corresponding c-AFM presented in Figures 1.14a and 1.14b. However, the enhanced conductance was only observed under super-band gap illumination indicating the conductance was mediated by the aggregation of generated photo-carriers. Charged domain walls were formed by poling along the c-axis, wherein the defect structure of the non-stoichiometric $LiNbO_3$ promoted marginal tilting of the domain walls. Mg-doping concentration did not have a direct effect on domain wall conductance. However, greater dopant concentration (0 to 5%) correlated with increased inclination of stable charged domain walls (θ = 0.006º to 0.225º), which exhibited increased conductance (10^{-14} to 10^{-12} S). A single strongly charged head-to-head domain wall, meandering with sections of θ = 90º, was produced by specialist thermal treatment of an undoped $LiNbO_3$ crystal[53,88]. Measured currents were significantly lower than expected, with a normalised conductance of 10^{-13} S.

The complete three dimensional profile of $LiNbO_3$ charged domain walls was imaged using Cherenkov second harmonic generation[89,90] (CSHG), revealing comparatively tortuous through-depth structure of the thermally treated strongly charged domain walls. Notably a charged domain wall was evidenced as folding upon itself, undergoing a continuous change through depth from head-to-head to tail-to-tail.

Recently, enhanced conductance has been reported at nominally uncharged 180º domain walls in $LiNbO_3$ thin films, without photoactive illumination[91,92]. Volk *et al.* deemed tilting of the domain wall within the 300 nm film thickness as negligible, and domain wall conductance was attributed to proposed existence of nanoscale kinks in the wall, as have been observed via HRTEM for 180º walls in single crystal $LiNbO_3$[93]. Conflictingly, Kämpfe and co-workers have presented phase field

simulations which predict tilted wall formation of up to 7° for a 100 nm film, suggesting a local divergence in polarisation [92].

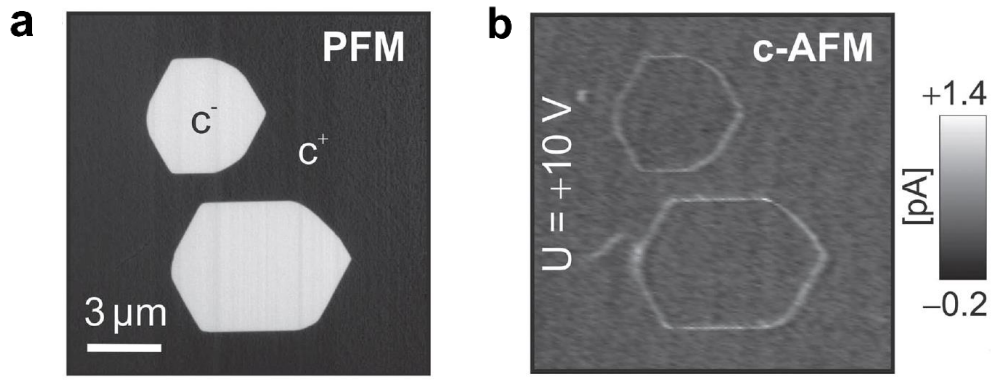

Figure 1.14 a Vertical PFM of oppositely polarised domains in 5% Mg doped $LiNbO_3$ crystal. The Mg dopant promotes slight tilting of the domain walls such that the walls are weakly charged in a head-to-head configuration. **b** c-AFM current map of the tilted walls recorded under super-bandgap illumination, showing locally increased conductance. Figures reprinted from [50].

Barium Titanate, $BaTiO_3$

$BaTiO_3$ is a tetragonal perovskite at room temperature, with multiple polarisation axes. Similarly to $LiNbO_3$, Aristov *et al.* observed voltage contrast at $BaTiO_3$ upon surface charging with SEM that was attributed to locally enhanced conductance[66]. Interestingly though, the contrast was observed at uncharged 90° head-to-tail walls.

In 2013 Sluka *et al.* utilised a frustrated poling technique[94], to generate an array of alternating head-to-head and tail-to-tail 90° walls in a $BaTiO_3$ single crystal. Charged domain walls were individually contacted with sputtered platinum electrodes, allowing for stable I/V characterisation of walls over large time scales (~10^5 s); beyond the capabilities of an AFM probe. Measured conductance for electrodes contacting head-to-head walls was five orders of magnitude greater than those without walls, ~10^{-8} and 10^{-13} S respectively, while zero change in conductance was measured at electrodes in contact with tail-to-tail walls. The recorded I/V profiles are presented in Figure 1.15a. Measurements taken over a narrow temperature range (10 to 50 °C) indicated metallic behaviour, suggesting an intrinsic conduction mechanism, are presented in Figure 1.15b.

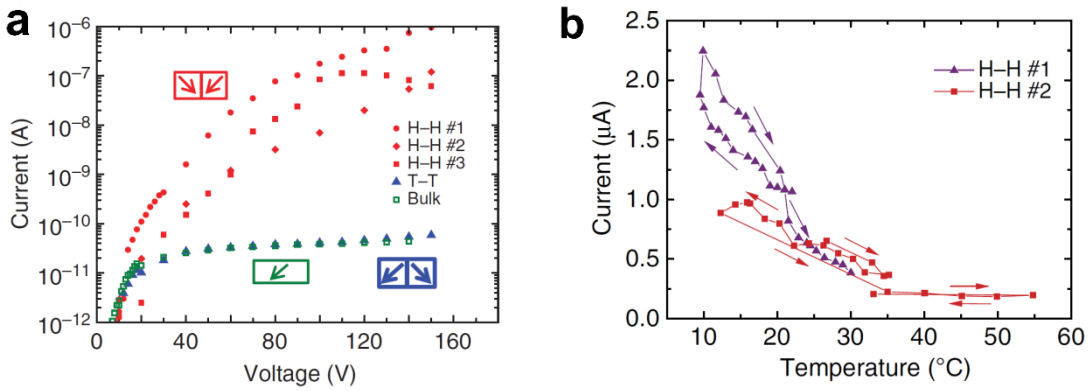

Figure 1.15 a Conductance profile for charged domain walls in $BaTiO_3$ single crystal, showing several orders of magnitude increased conductance at head-to-head (H-H) walls and bulk conductance for tail-to-tail (T-T) walls. **b** Temperature dependence of the head-to-head domain wall current, decreasing with increasing temperature, indicating metallic behaviour. Figures reprinted from [95].

Following the theoretical model set by Gureev *et al.*, this work represents the first experimental observation of a charged domain wall screening by a degenerate electron gas. The absence of enhanced conduction at tail-to-tail walls, due to a predicted degenerate hole gas, was attributed to a significant concentration of oxygen vacancies in the crystal facilitating screening without appreciably contributing to local conductivity.

Hexagonal Manganties, $RMnO_3$

The hexagonal manganites, $RMnO_3$ (R = Dy, Ho, Er, Tm, Yb, Lu, Y, Sc), are a family of improper ferroelectric materials that express a uniaxial polarisation at room temperature[96,97], with space group $P6_3cm$ [98,99]. The structural order parameter, dubbed trimerisation, results in three energetically equivalent structural distortions that couple with the two polarisation states, leading six energetically degenerate domain states[100,101]. Topologically this is realised by the formation of six-fold vertices, with a network of interconnecting domain walls meandering throughout the bulk, leading to a high density of charged domain walls[102,103]. The principal material of study throughout this thesis, the structure of $RMnO_3$ is discussed in full detail in section 5.1.

Meier *et al.* performed c-AFM measurements on the (100) face of single crystal $ErMnO_3$, presented Figure 1.16a, revealing increased and decreased conductance relative to the bulk at tail-to-tail and head-to-head domain walls respectively[59]. With reduced electrostatic weighting, the meandering path of individual domain walls may vary continuously from maximally head-to-head, through neutral to a maximally tail-to-tail orientation. This allowed dependence of domain wall conductance on wall angle, ϕ, to be investigated across a full 360° rotation, returning the relationship

$$G_{norm} \propto 2P \cos \phi \tag{1.42}$$

Where G_{norm} is domain wall conductance relative to the bulk conductance and ϕ = 0° and 180° for tail-to-tail and head-to-head walls respectively; verifying a direct relationship between divergence of polarisation, as defined by (1.31), and domain wall conductivity. The hexagonal manganites are p-type semiconductors in bulk[49], with insignificant ionic mobility at room temperature, and thus the increased and decreased conductance was attributed to the local aggregation and dispersion of holes at the tail-to-tail and head-to-head wall respectively.

I/V measurements of charged domain walls on the (110) face of a $HoMnO_3$ single crystal found that under positive bias both tail-to-tail and neutral walls exhibited increased conductance, with head-to-head walls insulating relative to the bulk[62]. While under large negative bias (-7 to -10 V) enhanced conductance was observed at all wall types, neutral, head-to-head and tail-to-tail. The authors focus their discussion on the behaviour observed under positive bias, proposing aggregation of holes, commenting that observed conductance at neutral walls may be due to local band gap reduction.

Choi *et al.* investigated z-cut (polarisation axis normal to the crystal face) samples of $YMnO_3$, reporting local reduction in conductance at neutral domain walls under sufficient bias[61]. Studies on the role of oxygen vacancies in $YMnO_3$ found that samples grown in an argon atmosphere displayed a highly distorted domain structure[104]. No distinct functionality was observed, but, upon poling under high

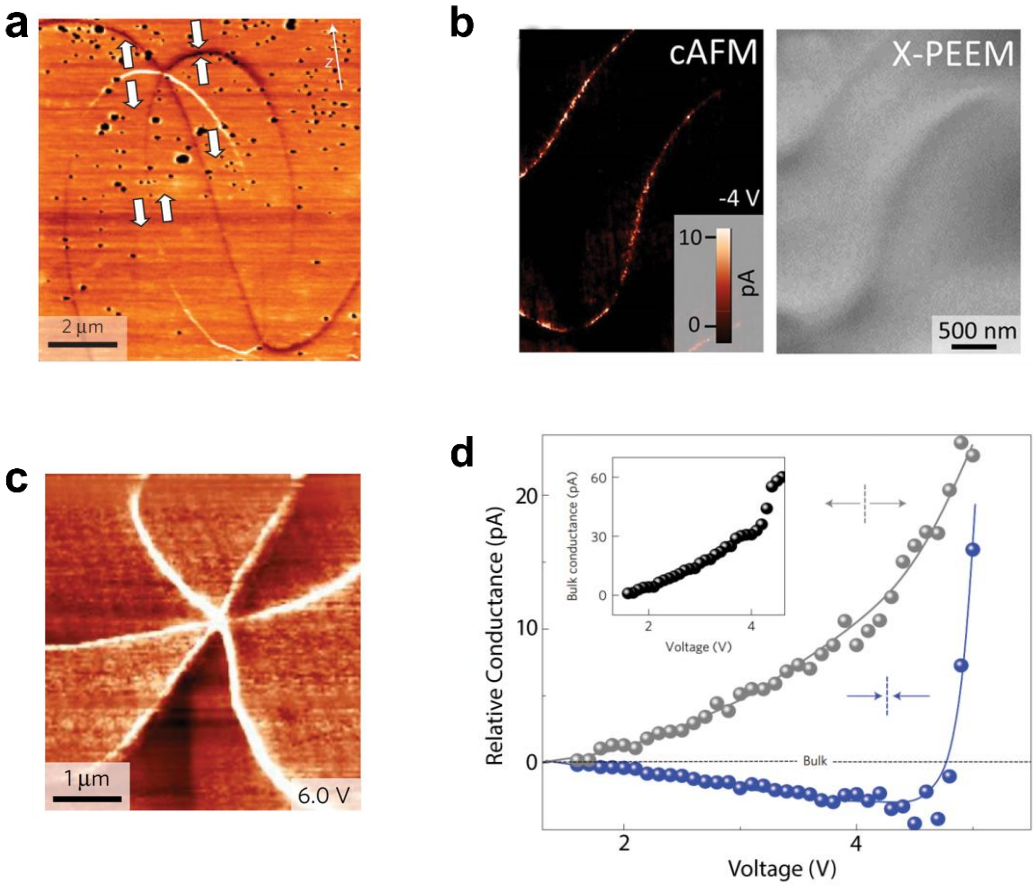

Figure 1.16 a c-AFM map of two six-fold vertices in $ErMnO_3$ single crystal, arrows indicate local polarisation direction, showing domain wall conductance varies with domain wall angle. Measurements show tail-to-tail and head-to-head walls express increased and decreased conductance relative to the bulk. **b** c-AFM and x-ray photoelectron emission microscopy (X-PEEM) images of the same area, verifying X-PEEM can map relative conductance. **c** c-AFM map of a vertex in $ErMnO_3$ conveying that under sufficient bias the typically insulating head-to-head walls may exhibit increased conductance relative to the bulk. **d** I/V profiles for tail-to-tail and head-to-head walls conveying relative conductance and the transition from below to above bulk conductance at head-to-head walls. Figure **a** reprinted from [59], **c** and **d** reprinted from [106] and **b** adapted from [105].

electric fields (80 kV/cm) domains redistributed to form a 180° stripe domain pattern, with enhanced conductance measured along the neutral domain walls.

Schaab *et al.* demonstrated control over domain wall conductance via acceptor (Ca^{2+}) doping of $ErMnO_3$ single crystals, increasing bulk p-type carrier concentration and facilitating aggregation of a greater density of mobile carriers for screening the tail-

to-tail walls[60]. Domain wall conductance increased with increased donor concentration, with 1% doping resulting in a factor 50 increase in conductance at tail-to-tail walls. Significantly, regardless of dopant level the ratio between wall and bulk conductance remained fixed. X-ray Photoelectron Emission Microscopy (XPEEM) of charged domain walls in $ErMnO_3$ single crystal found, with a methodology analogous to the SEM imaging of Artistov. *et al.*, that the energy of emitted secondary-electrons was determined by the local conductivity; thus facilitating non-contact imaging of domain wall conductance[105]. A comparison of X-PEEM and c-AFM measurements of the same conducting walls is presented in Figure 1.16b.

Most recently, in continuation of the work initiated by Meier *et al.*[59], Mundy *et al.* reported enhanced conduction along the previously insulating head-to-head walls[106], presented in Figure 1.16c. Performing I/V measurements via c-AFM, displayed in Figure 1.16d, for low bias the previously established behaviour was observed (increased and decreased conductance at tail-to-tail and head-to-head walls respectively) however approaching a threshold bias (4.8 V) the head-to-head wall transitioned gradually from more resistive to more conductive than the bulk. Electron energy spectroscopy (EELS) revealed an increased concentration of the lower valence Mn^{2+} state, compared to the predominant Mn^{3+}, at the head-to-head wall suggesting a locally increased electron density[106]. Additionally, the authors propose that due to the strong columbic repulsion experienced by the relevant manganese orbitals, coupling of the electrons with the lattice is energetically favourable thus suggesting conduction mediated by n-type polarons. Significantly this represents the first observation of domain wall conductance at a charged domain wall theoretically screened by minority carriers, as predicted by Eliseev *et al*[79].

Copper Chloride Boracite, $Cu_3B_7O_{13}Cl$

Cu-Cl boracite is an improper ferroelectric material wherein the symmetry reduction across the phase transition is dominated by structural shear of the unit cell from cubic to orthorhombic, resulting in formation of three equivalent polar axes[107]. Domain wall conductance in Cu-Cl boracite was speculated by Schmid and Pétermann in 1977 upon observing an order magnitude increase in bulk resistivity after poling[108].

McQuaid *et al.* presented the first direct measurements of domain wall conductance at native 90° charged domain walls, c-AFM measurements presented in Figure 1.17a, with tail-to-tail and head-to-head walls exhibiting increased and decreased conductance respectively[55]. In contrast to the meandering domain walls of $RMnO_3$, Cu-Cl boracite exhibits rectilinear domain walls of fixed angle and fixed conductance along their lengths. Notably, McQuaid and co-workers took advantage of the sheer strain nature of the primary order parameter by locally applying pressure near the transition temperature, facilitating the site-specific formation of conducting walls hundreds of microns in length.

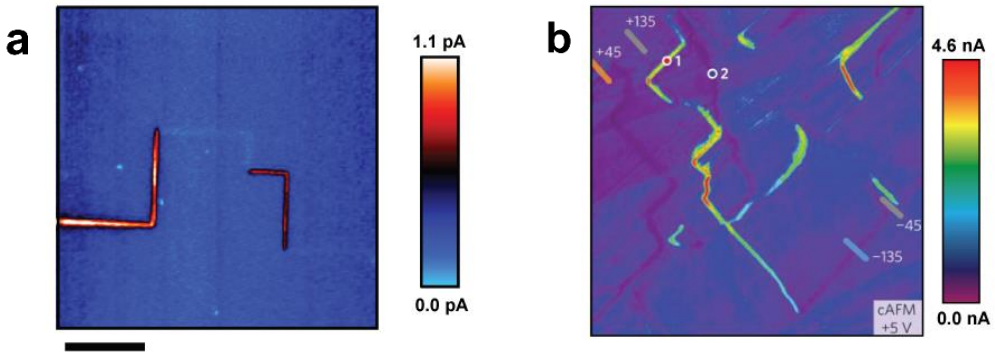

Figure 1.17 a c-AFM map of $Cu_3B_7O_{13}Cl$, recorded at -12 V, displaying increased and decreased conductance at tail-to-tail and head-to-head walls respectively. **b** c-AFM measurement of domain wall conductance at the native charged domain walls within oxygen deficient $Ca_{2.46}Sr_{0.54}Ti_2O_7$. Increased and decreased conductive traces correspond to head-to-head and tail-to-tail walls respectively Figure **a** reprinted from [55] and **b** adapted from [58].

$Ca_{2.46}Sr_{0.54}Ti_2O_7$

$Ca_3Ti_2O_7$ is one of a number of compounds predicted by Benedek *et al.* to exhibit the property of hybrid improper ferroelectricity[109]. Here the distinction from typical improper ferroelectricity is the polarisation develops from a combination of two nonpolar modes[110]. Oh *et al.*[58], reported the first measurement of switchable polarisation in intrinsic and strontium doped $Ca_3Ti_2O_7$ single crystals, with lateral PFM revealing an abundance of native charged domain walls with a range of wall angles, ($\pm$180°, $\pm$135°, $\pm$90° and $\pm$45°). Domain wall conduction was observed for oxygen deficient $Ca_{2.46}Sr_{0.54}Ti_2O_7$, c-AFM measurements presented in Figure 1.17b, with increased and decreased conductance relative to bulk at head-to-head and tail-

to-tail walls respectively. In agreement with theory and behaviour in other conducting charged domain wall systems, the conductance was found to scale proportionally with the divergence in polarisation normal to the wall.

Summary

From the above review there are a few general points which can be made on the current understanding of domain wall conductance:

i. Increased conductance has been observed for both charged and uncharged domain walls. While partial Bloch or Neel behaviour has been proposed to lead to a local divergence in polarisation at uncharged walls; observations of strong oxygen vacancy dependence, persistent conductive footprints and thermally activated conductance all support defect mediated conduction.

ii. The accepted model for domain wall conductance at charged domain walls is that the divergence in the polarisation normal to the wall generates a large depolarising field, which must be screened for the wall to stabilise. Assuming screening by free carriers, the local free carrier density at the wall is increased by several orders of magnitude relative to the bulk, resulting in a region of locally enhanced conductivity.

iii. Unlike the universally semiconducting behaviour observed at uncharged walls, temperature dependent studies on charged domain walls have revealed both metallic and semiconducting behaviours in different systems.

iv. Predominant tool for investigation is c-AFM, which allows for local conductance measurements at domain walls, however there is no established methodology for direct determination of local carrier densities and mobilities. To date the nature of the mobile carriers mediating the conduction (positive or negative, ionic or electronic) has only been inferred; through doping of the bulk and observing effect on domain wall conductance.

1.7 References

1. Lines, M. E. & Glass, A. M. in *Principles and Applications of Ferroelectrics and Related Materials* 8–15 (Oxford University Press, 2004).
2. Martin, R. M. Comment on calculations of electric polarization in crystals. *Phys. Rev. B* **9,** 1998–1999 (1974).
3. Spaldin, N. A. A beginners guide to the modern theory of polarization. *J. Solid State Chem.* **195,** 2–10 (2012).
4. King-Smith, R. D. & Vanderbilt, D. Theory of polarization of crystalline solids. *Phys. Rev. B* **47,** 1651–1654 (1993).
5. Resta, R., Posternak, M. & Baldereschi, A. Towards a quantum theory of polarization in ferroelectrics: The case of $KNbO_3$. *Phys. Rev. Lett.* **70,** 1010–1013 (1993).
6. Resta, R. & Vanderbilt, D. Theory of polarization: A modern approach. *Top. Appl. Phys.* **105,** 31–68 (2007).
7. Berry, M. V. Quantal Phase Factors Accompanying Adiabatic Changes. *Proc. R. Soc. A Math. Phys. Eng. Sci.* **392,** 45–57 (1984).
8. Eguchi, M. XX. On the permanent electret. *Philos. Mag. Ser. 6* **49,** 178–192 (1925).
9. Scott, J. F. Ferroelectrics go bananas. *J. Phys. Condens. Matter* **20,** 21001 (2007).
10. Kittel, C. in *Introduction to Solid State Physics* 113–114 (John Wiley & Sons, Ltd, 1954).
11. Curie, P. Sur la symétrie dans les phénomènes physiques, symétrie d'un champ électrique et d'un champ magnétique. *J. Phys. Théorique Appliquée* **3,** 393–415 (1894).
12. Ismael, J. Curie's Principle. *Synthese* **110,** 167–190 (1997).
13. Tagantsev, A., Cross, L. E. & Fousek, J. in *Domains in Ferroic Crystals and Thin Films* 32–35 (Springer New York, 2010).
14. Landau, L. D. On the theory of phase transitions. *Zh. Eks. Teor. Fiz.* **7,** 19–32 (1937).
15. Devonshire, A. F. XCVI. Theory of barium titanate. *London, Edinburgh, Dublin Philos. Mag. J. Sci.* **40,** 1040–1063 (1949).
16. Chandra, P. & Littlewood, P. B. A Landau primer for ferroelectrics. *Top. Appl. Phys.* **105,** 69–116 (2007).
17. Kittel, C. in *Introduction to Solid State Physics* 117–123 (John Wiley & Sons, Ltd, 1954).
18. Lines, M. E. & Glass, A. M. in *Principles and Applications of Ferroelectrics and Related Materials* 71–81 (Oxford University Press, 2004).
19. McQuaid, R. G. P. Domain Patterns and Domain Wall Dynamics in Small-Scale Ferroelectrics. (Queen's University Belfast, 2013).

20. Dvořák, V. Improper Ferroelectric Phase Transition in Rubidium Tri-Hydrogen Selenite. *Phys. Status Solidi* **51,** K129–K132 (1972).
21. Ishibashi, Y. & Takagi, Y. Improper Ferroelectric Phase Transitions. *Jpn. J. Appl. Phys.* **15,** 1621–1636 (1976).
22. Levanyuk, A. P. & Sannikov, D. G. Improper ferroelectrics. *Sov. Phys. Uspekhi* **17,** 199–214 (1974).
23. Jona, F. & Pepinsky, R. Dielectric Properties of Some Double Tartrates. *Phys. Rev.* **92,** 1577–1577 (1953).
24. Ishibashi, Y. & Takagi, Y. Improper ferroelectric phase transitions. *Jpn. J. Appl. Phys.* **15,** 1621–1636 (1976).
25. Smutný, F. & Fousek, J. Ferroelectric Transition in Co-I-Boracite. *Phys. status solidi* **40,** K13–K15 (1970).
26. Blattner, H., Kanzig, W., Merz, W. & H. Sutter. Domain structure of barium titanate crystals. *Helv. Phys. Acta.* **21,** 207–209 (1948).
27. Matthias, B. & Von Hippel, A. Domain structure and dielectric response of barium titanate single crystals. *Phys. Rev.* **73,** 1378–1384 (1948).
28. Landau, L. D. & Lifshitz, E. On the theory of the dispersion of magnetic permeability in ferromagnetic bodies. *Phys. Z. Sowjetunion* **8,** 153 (1935).
29. Kittel, C. Theory of the structure of ferromagnetic domains in films and small particles. *Phys. Rev.* **70,** 965–971 (1946).
30. Mitsui, T. & Furuichi, J. Domain structure of rochelle salt and KH_2PO_4. *Phys. Rev.* **90,** 193–202 (1953).
31. McGilly, L. J. Domain Topologies in Nanoscale Single-Crystal Ferroelectrics. (Queen's University Belfast, 2011).
32. Yudin, P. V., Gureev, M. Y., Sluka, T., Tagantsev, A. K. & Setter, N. Anomalously thick domain walls in ferroelectrics. *Phys. Rev. B - Condens. Matter Mater. Phys.* **91,** 60102 (2015).
33. Fong, D. D. Ferroelectricity in Ultrathin Perovskite Films. *Science.* **304,** 1650–1653 (2004).
34. Catalan, G., Seidel, J., Ramesh, R. & Scott, J. F. Domain wall nanoelectronics. *Rev. Mod. Phys.* **84,** 119–156 (2012).
35. Tagantsev, A., Cross, L. E. & Fousek, J. in *Domains in Ferroic Crystals and Thin Films* 271–292 (Springer New York, 2010).
36. Lee, D. *et al.* Mixed Bloch-Néel-Ising character of 180° ferroelectric domain walls. *Phys. Rev. B* **80,** 60102 (2009).
37. Marton, P., Rychetsky, I. & Hlinka, J. Domain walls of ferroelectric $BaTiO_3$ within the Ginzburg-Landau-Devonshire phenomenological model. *Phys. Rev. B - Condens.*

Matter Mater. Phys. **81,** 144125 (2010).

38. Hlinka, J. *et al.* Phase–field modelling of 180° 'Bloch walls' in rhombohedral $BaTiO_3$. *Phase Transitions* **84,** 738–746 (2011).
39. Wei, X.-K. *et al.* Néel-like domain walls in ferroelectric $Pb(Zr,Ti)O_3$ single crystals. *Nat. Commun.* **7,** 12385 (2016).
40. Scrymgeour, D. A., Gopalan, V., Itagi, A., Saxena, A. & Swart, P. J. Phenomenological theory of a single domain wall in uniaxial trigonal ferroelectrics: Lithium niobate and lithium tantalate. *Phys. Rev. B - Condens. Matter Mater. Phys.* **71,** 184110 (2005).
41. Grant, I. S. & Philips, W. R. in *Electromagnetism* 16–28 (John Wiley & Sons, Ltd, 2012).
42. Bednyakov, P. S., Sluka, T., Tagantsev, A. K., Damjanovic, D. & Setter, N. Formation of charged ferroelectric domain walls with controlled periodicity. *Sci. Rep.* **5,** 15819 (2015).
43. Tagantsev, A. K. Landau Expansion for Ferroelectrics: Which Variable to Use? *Ferroelectrics* **375,** 19–27 (2008).
44. Tagantsev, A. K. & Gerra, G. Interface-induced phenomena in polarization response of ferroelectric thin films. *J. Appl. Phys.* **100,** 51607 (2006).
45. Levanyuk, A. P., Strukov, B. A. & Cano, A. Background dielectric permittivity: Material constant or fitting parameter? *Ferroelectrics* **503,** 94–103 (2016).
46. Lines, M. E. & Glass, A. M. in *Principles and Applications of Ferroelectrics and Related Materials* 620–632 (Oxford University Press, 2004).
47. Peng, L.-H., Fang, Y.-C. & Lin, Y.-C. Polarization switching of lithium niobate with giant internal field. *Appl. Phys. Lett.* **74,** 2070 (1999).
48. Graham, R. in *Solids under High-Pressure Shock Compression* 87–89 (Springer New York, 1993).
49. Subba Rao, G. V., Wanklyn, B. M. & Rao, C. N. R. Electrical transport in rare earth ortho-chromites, -manganites and -ferrites. *J. Phys. Chem. Solids* **32,** 345–358 (1971).
50. Schröder, M. *et al.* Conducting domain walls in lithium niobate single crystals. *Adv. Funct. Mater.* **22,** 3936–3944 (2012).
51. Bednyakov, P., Sluka, T., Tagantsev, A., Damjanovic, D. & Setter, N. Free-Carrier-Compensated Charged Domain Walls Produced with Super-Bandgap Illumination in Insulating Ferroelectrics. *Adv. Mater.* **28,** 9498–9503 (2016).
52. Miyazawa, S. Ferroelectric domain inversion in Ti-diffused $LiNbO_3$ optical waveguide. *J. Appl. Phys.* **50,** 4599–4603 (1979).
53. Nakamura, K., Ando, H. & Shimizu, H. Ferroelectric domain inversion caused in

$LiNbO_3$ plates by heat treatment. *Appl. Phys. Lett.* **50,** 1413–1414 (1987).

54. Huang, L. & Jaeger, N. A. F. Discussion of domain inversion in $LiNbO_3$. *Appl. Phys. Lett.* **65,** 1763–1765 (1994).
55. McQuaid, R. G. P., Campbell, M. P., Whatmore, R. W., Kumar, A. & Gregg, J. M. Injection and controlled motion of conducting domain walls in improper ferroelectric Cu-Cl boracite. *Nat. Commun.* **8,** 15105 (2017).
56. Gureev, M. Y., Tagantsev, A. K. & Setter, N. Head-to-head and tail-to-tail 180° domain walls in an isolated ferroelectric. *Phys. Rev. B - Condens. Matter Mater. Phys.* **83,** 184104 (2011).
57. Fridkin, V. M. Ferroelectric Semiconductors. *Krist. und Tech.* **15,** (1980).
58. Oh, Y. S., Luo, X., Huang, F., Wang, Y. & Cheong, S. Experimental demonstration of hybrid improper ferroelectricity and the presence of abundant charged walls in $(Ca,Sr)_3Ti_2O_7$ crystals. *Nat. Mater.* **14,** 1–7 (2015).
59. Meier, D. *et al.* Anisotropic conductance at improper ferroelectric domain walls. *Nat. Mater.* **11,** 284–288 (2012).
60. Schaab, J. *et al.* Optimization of Electronic Domain-Wall Properties by Aliovalent Cation Substitution. *Adv. Electron. Mater.* **2,** 1500195 (2016).
61. Choi, T. *et al.* Insulating interlocked ferroelectric and structural antiphase domain walls in multiferroic $YMnO_3$. *Nat. Mater.* **9,** 253–8 (2010).
62. Wu, W., Horibe, Y., Lee, N., Cheong, S. W. & Guest, J. R. Conduction of topologically protected charged ferroelectric domain walls. *Phys. Rev. Lett.* **108,** 77203 (2012).
63. Vul, B. M., Guro, G. M. & Ivanchik, I. I. Encountering domains in ferroelectrics. *Ferroelectrics* **6,** 29–31 (1973).
64. Grekov, A. A., Adonin, A. A. & Protsenko, N. P. Encountering domains in SbSl. *Ferroelectrics* **13,** 483–485 (1976).
65. Aristov, V. V., Kokhanchik, L. S. & Voronovskii, Y. I. Voltage contrast of ferroelectric domains of lithium niobate in SEM. *Phys. Status Solidi* **86,** 133–141 (1984).
66. Aristov, V. V., Kokhanchik, L. S., Meyer, K. P. & Blumtritt, H. Scanning electron microscopic investigations of peculiarities of the $BaTiO_3$ ferroelectric domain contrast. *Phys. Status Solidi* **78,** 229–236 (1983).
67. Seidel, J. *et al.* Conduction at domain walls in oxide multiferroics. *Nat. Mater.* **8,** 229–34 (2009).
68. Kubel, F. & Schmid, H. Structure of a ferroelectric and ferroelastic monodomain crystal of the perovskite $BiFeO_3$. *Acta Crystallogr. Sect. B* **46,** 698–702 (1990).
69. Lubk, A., Gemming, S. & Spaldin, N. A. First-principles study of ferroelectric

domain walls in multiferroic bismuth ferrite. *Phys. Rev. B - Condens. Matter Mater. Phys.* **80,** 1–8 (2009).

70. Morozovska, A. N., Vasudevan, R. K., Maksymovych, P., Kalinin, S. V. & Eliseev, E. A. Anisotropic conductivity of uncharged domain walls in $BiFeO_3$. *Phys. Rev. B - Condens. Matter Mater. Phys.* **86,** 1–9 (2012).
71. Chiu, Y. P. *et al.* Atomic-scale evolution of local electronic structure across multiferroic domain walls. *Adv. Mater.* **23,** 1530–1534 (2011).
72. Farokhipoor, S. & Noheda, B. Conduction through 71° Domain Walls in $BiFeO_3$ Thin Films. *Phys. Rev. Lett.* **107,** 127601 (2011).
73. Farokhipoor, S. & Noheda, B. Local conductivity and the role of vacancies around twin walls of (001)-$BiFeO_3$ thin films. *J. Appl. Phys.* **112,** 52003 (2012).
74. Stolichnov, I. *et al.* Persistent conductive footprints of 109° domain walls in bismuth ferrite films. *Appl. Phys. Lett.* **104,** 1–5 (2014).
75. Crassous, A., Sluka, T., Tagantsev, A. K. & Setter, N. Polarization charge as a reconfigurable quasi-dopant in ferroelectric thin films. *Nat. Nanotechnol.* **10,** 614–8 (2015).
76. Seidel, J. *et al.* Domain wall conductivity in La-doped $BiFeO_3$. *Phys. Rev. Lett.* **105,** 2010–2012 (2010).
77. Rojac, T. *et al.* Domain-wall conduction in ferroelectric $BiFeO_3$ controlled by accumulation of charged defects. *Nat. Mater.* **16,** 3–5 (2016).
78. Vasudevan, R. K. *et al.* Domain wall geometry controls conduction in ferroelectrics. *Nano Lett.* **12,** 5524–5531 (2012).
79. Eliseev, E. A., Morozovska, A. N., Svechnikov, G. S., Gopalan, V. & Shur, V. Y. Static conductivity of charged domain walls in uniaxial ferroelectric semiconductors. *Phys. Rev. B - Condens. Matter Mater. Phys.* **83,** 235313 (2011).
80. Eliseev, E. A., Morozovska, A. N., Svechnikov, G. S., Maksymovych, P. & Kalinin, S. V. Domain wall conduction in multiaxial ferroelectrics. *Phys. Rev. B - Condens. Matter Mater. Phys.* **85,** 45312 (2012).
81. Guyonnet, J., Gaponenko, I., Gariglio, S. & Paruch, P. Conduction at domain walls in insulating $Pb(Zr_{0.2}Ti_{0.8})O_3$ thin films. *Adv. Mater.* **23,** 5377–5382 (2011).
82. Gaponenko, I., Tückmantel, P., Karthik, J., Martin, L. W. & Paruch, P. Towards reversible control of domain wall conduction in $Pb(Zr_{0.2}Ti_{0.8})O_3$ thin films. *Appl. Phys. Lett.* **106,** 162902 (2015).
83. Maksymovych, P. *et al.* Tunable metallic conductance in ferroelectric nanodomains. *Nano Lett.* **12,** 209–213 (2012).
84. Stolichnov, I. *et al.* Bent Ferroelectric Domain Walls as Reconfigurable Metallic-Like Channels. *Nano Lett.* **15,** 8049–8055 (2015).

85. Wei, X.-K. *et al.* Controlled Charging of Ferroelastic Domain Walls in Oxide Ferroelectrics. *ACS Appl. Mater. Interfaces* **9,** 6539–5646 (2017).
86. Faraji, N., Yan, Z. & Seidel, J. Electrical conduction at domain walls in lead titanate ($PbTiO_3$) single crystals. *Appl. Phys. Lett.* **110,** 213108 (2017).
87. Kokhanchik, L. & Irzhak, D. Investigation of Periodic Domain Structures in Lithium Niobate Crystals. *Ferroelectrics* **352,** 134–142 (2007).
88. Kugel, V. D. & Rosenman, G. Domain inversion in heat-treated $LiNbO_3$ crystals. *Appl. Phys. Lett.* **62,** 2902–2904 (1993).
89. Sheng, Y. *et al.* Three-dimensional ferroelectric domain visualization by Cerenkov-type second harmonic generation. *Opt. Express* **18,** 16539–16545 (2010).
90. Kämpfe, T. *et al.* Optical three-dimensional profiling of charged domain walls in ferroelectrics by Cherenkov second-harmonic generation. *Phys. Rev. B* **89,** 35314 (2014).
91. Volk, T. R., Gainutdinov, R. V. & Zhang, H. H. Domain-wall conduction in AFM-written domain patterns in ion-sliced $LiNbO_3$ films. *Appl. Phys. Lett.* **110,** 132905 (2017).
92. Kämpfe, T. Charged domain walls in ferroelectric single crystals. (Technical University Dresden, 2016).
93. Gonnissen, J. *et al.* Direct Observation of Ferroelectric Domain Walls in $LiNbO_3$: Wall-Meanders, Kinks, and Local Electric Charges. *Adv. Funct. Mater.* **26,** 7599–7604 (2016).
94. Wada, S. *et al.* Domain Wall Engineering in Lead-Free Piezoelectric Crystals. *Ferroelectrics* **355,** 11–21 (2007).
95. Sluka, T., Tagantsev, A. K., Bednyakov, P. & Setter, N. Free-electron gas at charged domain walls in insulating $BaTiO_3$. *Nat. Commun.* **4,** 1808 (2013).
96. Van Aken, B. B., Palstra, T. T. M., Filippetti, A. & Spaldin, N. A. The origin of ferroelectricity in magnetoelectric $YMnO_3$. *Nat. Mater.* **3,** 164–170 (2004).
97. Lorenz, B. Hexagonal Manganites—($RMnO_3$): Class (I) Multiferroics with Strong Coupling of Magnetism and Ferroelectricity. *ISRN Condens. Matter Phys.* **2013,** 1–43 (2013).
98. Fennie, C. J. & Rabe, K. M. Ferroelectric transition in $YMnO_3$ from first principles. *Phys. Rev. B - Condens. Matter Mater. Phys.* **72,** 100103 (2005).
99. Sim, H., Oh, J., Jeong, J., Le, M. D. & Park, J. G. Hexagonal $RMnO_3$: A model system for two-dimensional triangular lattice antiferromagnets. *Acta Crystallogr. Sect. B Struct. Sci. Cryst. Eng. Mater.* **72,** 3–19 (2016).
100. Artyukhin, S., Delaney, K. T., Spaldin, N. A. & Mostovoy, M. Landau theory of topological defects in multiferroic hexagonal manganites. *Nat. Mater.* **13,** 42–49

(2013).

101. Meier, Q. N. *et al.* Global Formation of Topological Defects in the Multiferroic Hexagonal Manganites. *Phys. Rev. X* **7,** 41014 (2017).
102. Lin, S.-Z. *et al.* Topological defects as relics of emergent continuous symmetry and Higgs condensation of disorder in ferroelectrics. *Nat. Phys.* **10,** 970–977 (2014).
103. Meier, D. Functional domain walls in multiferroics. *J. Phys. Condens. Matter* **27,** 463003 (2015).
104. Du, Y. *et al.* Domain wall conductivity in oxygen deficient multiferroic YMnO3 single crystals. *Appl. Phys. Lett.* **99,** 252107 (2011).
105. Schaab, J. *et al.* Imaging and characterization of conducting ferroelectric domain walls by photoemission electron microscopy. *Appl. Phys. Lett.* **104,** (2014).
106. Mundy, J. A. *et al.* Functional electronic inversion layers at ferroelectric domain walls. *Nat. Mater.* **16,** 622–627 (2017).
107. Zimmermann, A., Bollmann, W. & Schmid, H. Observations of ferroelectric domains in boracites. *Phys. Status Solidi* **3,** 707–720 (1970).
108. Schmid, H. & Pétermann, L. A. Dielectric constant and electric resistivity of copper chlorine boracite, $Cu_3B_7O_{13}Cl$ (Cu-Cl-B). *Phys. Status Solidi* **41,** K147–K150 (1977).
109. Benedek, N. A., Mulder, A. T. & Fennie, C. J. Polar octahedral rotations: A path to new multifunctional materials. *J. Solid State Chem.* **195,** 11–20 (2012).
110. Benedek, N. A. & Fennie, C. J. Hybrid improper ferroelectricity: A mechanism for controllable polarization-magnetization coupling. *Phys. Rev. Lett.* **106,** 3–6 (2011).

2 Atomic Force Microscopy

Atomic Force Microscopy (AFM) and variants thereof are the principle experimental techniques used in this body of work. An atomic force microscope facilitates non-destructive imaging of surface topography with nanometre resolution and with modifications to the central technique allows for further characterisation of the piezoelectric, structural and electrical properties of the material. Herein the theory behind the primary variants used for imaging ferroelectric domains and measuring domain wall conduction are presented, with detail on more specialised variants presented in following sections as relevant.

2.1 Contact mode Atomic Force Microscopy

In contact mode AFM a nanometre sharp probe, mounted on microscale cantilever, is lowered onto a material surface, as sketched in Figure 2.1a. As the probe tip comes within a few angstroms of the material surface the inter-atomic forces between tip and sample enter the repulsive regime, force as a function of tip to sample distance is sketched in Figure 2.1b, and the probe is said to be in contact. Further lowering against the repulsive regime causes deflection of cantilever. A laser is focused on the back of the cantilever, which reflects onto a quadrant photodiode, such that any deflection of the cantilever causes movement of the laser spot on the photodiode, leading to a change in voltage output. Contact force can be defined by lowering the probe until the initially centred laser spot deflects to a user-defined position on the photodiode, known as the deflection setpoint.

Topographical maps are obtained by rastering the probe across the material surface via piezoelectric actuators, allowing for movement in all axes with sub-micron precision[1]. Local variations in sample height lead to changes in the tip-sample separation and hence alter the repulsive forces on the probe, shifting the laser spot from the deflection setpoint. Resulting variations in voltage output are fed into feedback electronics which control the piezoelectric actuators to compensate and return the laser spot to the deflection setpoint. By recording the extension or retraction of the piezo actuators at a series of points across each scan line, the change in surface height along that line can be determined. Hence a 3-dimensional topography map (x, y, z) can be obtained from a raster scan where the resultant

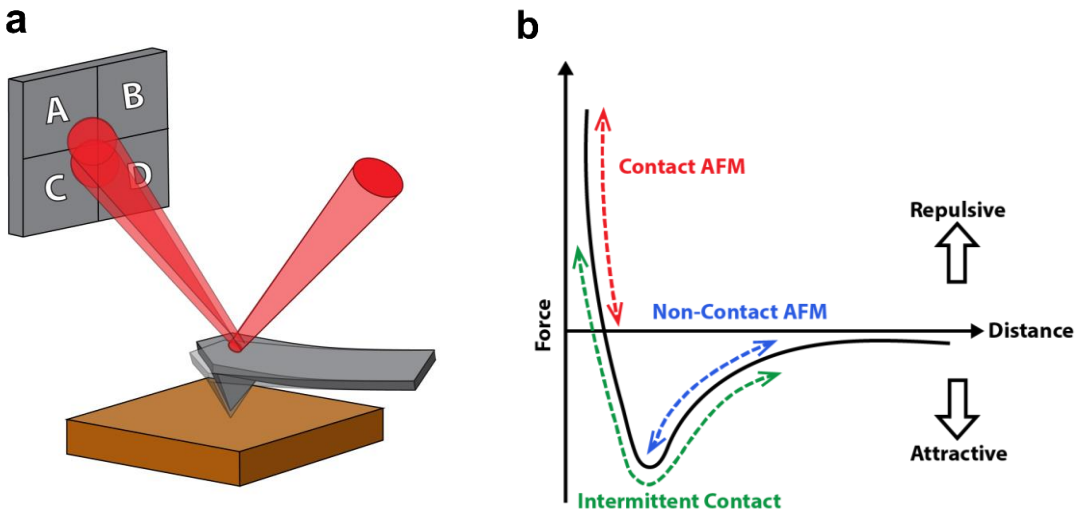

Figure 2.1 a Illustration of basic operation of atomic force microscope. A microscale probe, consisting of a cantilever with a nanometre sharp tip, is placed in contact with the sample. The probe is rastered across the sample where changes in the topography cause deflections of the cantilever. A laser beam incident on the back of the cantilever is reflected onto a quadrant photodiode. Deflection of the cantilever displaces the laser on the photodiode, allowing variations in the sample topography to be electronically recorded. **b** Typical form of a force distance curve, illustrating the different force regimes within which variants of atomic force microscopy operate. Figure **b** adapted from [2].

image resolution is determined by the number of sample points per line and the number of scan lines.

Cantilever deflection is quantified by the radial displacement of the laser beam position from the centre of the photodiode. Labelling the photodiode quadrants A to D, as shown in Figure 2.1, and defining the centre position as zero; vertical and lateral deflection may be calculated by (2.1) and (2.2) respectively.

$$\frac{(A+B)-(C+D)}{ABCD} \tag{2.1}$$

$$\frac{(B+D)-(A+C)}{ABCD} \tag{2.2}$$

From these expressions, the appropriate sign and magnitude of voltage can be determined and applied to the piezoactuator to return the laser beam to the deflection setpoint.

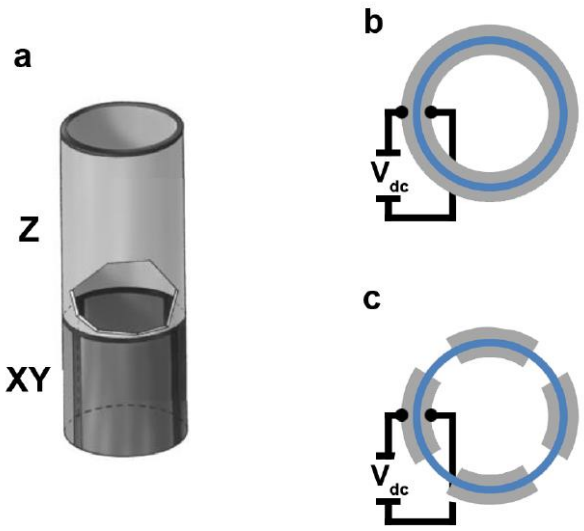

Figure 2.2 Schematic of typical piezo actuator construction. **a** The hollow piezotube is divided into two sections where the top controls the z-axis position and the bottom the position in the x-y plane. **b** Cross-sectional view of the z-actuator. Application of potential difference between the inner and outer electrodes, shown in grey, causes displacement of the piezoelectric material, shown in blue. **c** Cross-sectional view of the x-y actuators. Applying bias to a given quadrants causes displacement in that direction. Figure reprinted from [3].

The method of operation of the piezoactuator is conveyed in Figure 2.2. Typically cylindrical, the macroscopic piezoactuator is hollow to allow it to be positioned directly above the microscale probe without blocking the laser beam; leading to the common name piezotube. Application of a bias to the top section of the piezotube leads to extension or retraction in the z plane, depending on the voltage polarity. For lateral translation in the x,y plane, the bottom half is divided into four quadrants[4]. Application of a potential bias between inner and outer electrode layer of a given quadrant, causes bending in that direction.

Increased laser path length between cantilever and photodiode amplifies slight beam deflections which, coupled with the steep force gradient within the contact regime, enables z height resolution on the order of 0.1 nm. Lateral imaging resolution is dictated by the size of the tip-sample contact area, which depends on contact force, sample stiffness and tip radius[5]. Thus to maximise lateral resolution, probes with smaller tip radii can be used with decreasing contact force. However, a minimum contact force is required such that cantilever deflections are of sufficient magnitude

to generate an adequate signal to noise ratio. This lower limit on contact force establishes a corresponding limit on probe radius, as the contact pressure increases with decreasing contact area leading to deformation of both tip and sample. The functional limits of contact force and pressure vary with sample properties but considering a solid crystalline sample and a tip radius of ~ 50 nm; contact area diameters in ambient atmosphere are typically of the order of 10 nm[1,6]. Under ultra-high vacuum the contact force can be reduced by an order of magnitude to give nanometre resolution.

2.2 Piezoresponse Force Microscopy

Piezoresponse force microscopy (PFM) is a variant of contact AFM which exploits the converse piezoelectric effect to directly image ferroelectric domain patterns at a material surface. As described in section 1.1, all ferroelectric crystals are inherently piezoelectric. In PFM a conductive probe is used to locally apply a bias to the material surface, generating a mechanical displacement the sense of which is determined by the relative orientation of the local polarisation[7].

The converse piezoelectric effect is described by a linear relationship between applied electric field and induced strain. Expressed formally in Voight notation[8]:

$$S_m = d_{km} E_k \tag{2.1}$$

Where E_k is the applied field vector, S_m a second rank tensor representing the strain response and the coupling term d_{km}expresses the components of the piezoelectric tensor. In this notation, the index "k" denotes the electric field component along Cartesian axes, with 1, 2 and 3 corresponding to x, y and z. Similarly the index "m" denotes the direction of the strain response; ranging from 1 to 6, where 1 to 3 correspond to stresses along x, y and z while 4, 5 and 6 correspond to the shear strain components S_{zy}, S_{zx}, S_{yx}.

As a third rank tensor, d_{km}, could in theory have up to 3^3 independent components. However as stress and strain are symmetrical tensors, *i.e* $S_{ij} = S_{ji}$, the piezoelectric tensor exhibits symmetry with respect to the same indices, *i.e*. $d_{ijk} = d_{jik}$, and thus

can express a maximum of 18 independent piezoelectric coefficients[9]. This number is further reduced by geometrical symmetry of the crystal structure, with ferroelectric materials of higher crystallographic symmetry expressing fewer independent coefficients. For example in the hexagonal manganites, the principal material of study in this thesis, expressing point group 6mm[10], the piezoelectric tensor, shown (2.2), contains only three independent components[11].

$$\begin{pmatrix} 0 & 0 & 0 & 0 & d_{15} & 0 \\ 0 & 0 & 0 & d_{15} & 0 & 0 \\ d_{31} & d_{31} & d_{33} & 0 & 0 & 0 \end{pmatrix} \tag{2.2}$$

Transposing (2.2) and substituting into (2.1) we find:

$$\begin{pmatrix} S_1 \\ S_2 \\ S_3 \\ S_4 \\ S_5 \\ S_6 \end{pmatrix} = \begin{pmatrix} d_{31}E_3 \\ d_{31}E_3 \\ d_{33}E_3 \\ d_{15}E_2 \\ d_{15}E_1 \\ 0 \end{pmatrix} \tag{2.3}$$

Consequently, the nature of the resultant mechanical displacement is dependent on the directional components of applied electric field. For a unit cell with uniaxial polarisation, such as the hexagonal manganites, typically the z-axis is defined as the polar axis of the material. Considering only uniaxial fields for simplicity, an electric field applied along the polar axis will generate a tensile or compressive strain along that axis and the two orthogonal axes. This leads to a vertical deflection of the cantilever, as pictured in Figure 2.3. An electric field applied along x or y (orthogonal to the polar axis) will induce S_{zy} or S_{zx} shear strains respectively. In this case, the crystallographic shearing leads to a torsional force on the cantilever and a lateral deflection of the laser dot on the photodiode.

Hence, by applying a bias to the material surface and recording the sense of the cantilever deflection in vertical and lateral axes, intuitively referred to as vertical and lateral PFM respectively, the polar orientation can be determined. Rastering and sampling analogously to a topography map in contact AFM, the piezoresponse map

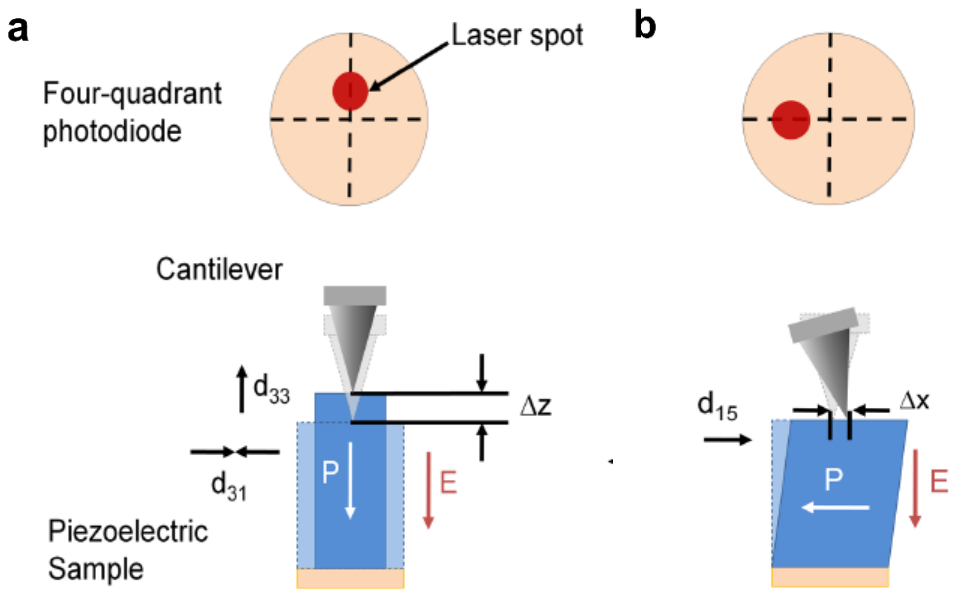

Figure 2.3 a Mechanism behind vertical piezoresponse force microscopy where application of electric field parallel to the polar axis leads to a tensile or compressive strain along that axis and the two orthogonal axes. Resultant vertical deflection of the cantilever and laser spot is recorded by photodiode. **b** Mechanism behind lateral piezoresponse force microscopy where application of electric field orthogonal to the polar axis induces a shear strain, tilting the cantilever and generating a lateral deflection of the laser spot. Figure reprinted from [3].

is obtained which displays the spatial variations in crystallographic orientation and by extension the ferroelectric domain pattern.

Not conveyed in Figure 2.3 is the case where the polarisation vector is parallel to the cantilever, such that the piezoelectric shearing causes the probe to bend along the axis of the cantilever. This flexural deflection generates a vertical displacement of the laser spot on the photodiode, typically smaller in magnitude than would be produced by a truly out of plane polarisation. Flexure can be falsely interpreted as a true vertical deflection and care must be taken to distinguish it from true vertical piezoresponse. This is most significant when the polar orientation of a sample is unknown.

2.2.1 The Lock-in Amplifier

In order to differentiate between topographic and piezoelectric signals, a lock-in technique is used, where an alternating voltage is applied to the tip. As the sign of the bias alternates so does the sense of the mechanical displacement, a tensile strain becomes a compressive stain and vice versa. If an AC bias of frequency ω and amplitude V_0 is applied to the tip:

$$V = V_0 \cos(\omega t) \tag{2.4}$$

This will result in mechanical oscillations on the material surface as given by (2.5).

$$\Delta d = d_0 + D \cos(\omega t + \varphi) \tag{2.5}$$

Where the mechanical oscillations Δd about the equilibrium position d_0, are of amplitude D and oscillate with a phase difference φ with respect to the applied voltage. The mechanical oscillations will either be in phase, φ = 0, or out of phase, φ = 180, depending on the polarisation direction, as depicted in Figure 2.4. To extract the oscillatory piezoelectric signal from the topographic, all signal from the photodiode is passed into an instrument called a lock-in amplifier.

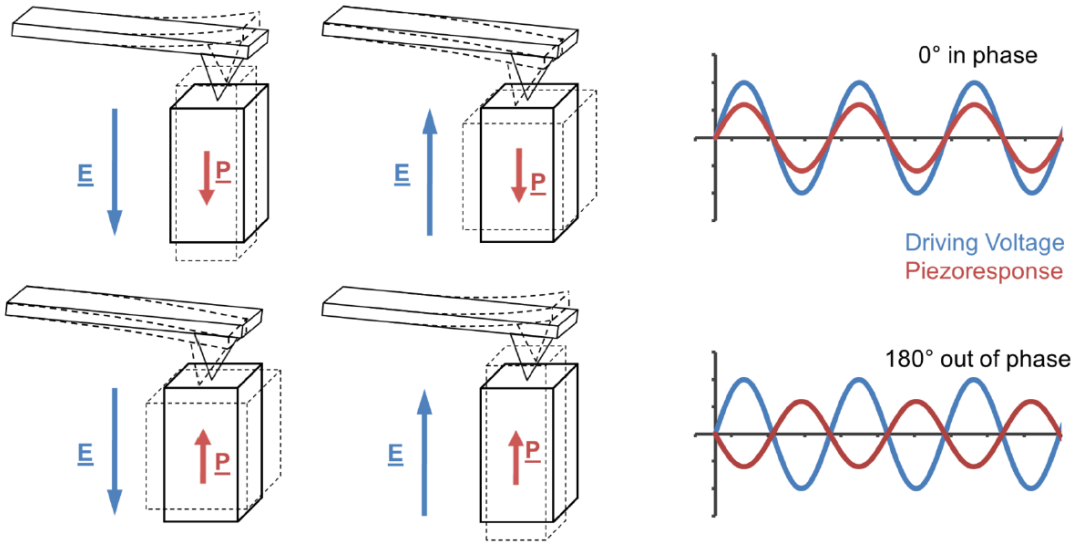

Figure 2.4 Schematic of vertical piezoresponse force microscopy. An AC bias is applied along the polarisation axis and the resulting cantilever deflection is in phase and out of phase with the applied bias for opposite polarisation directions. Figure reprinted from [12].

A lock-in amplifer (LiA) is essentially a phase discriminative low-pass filter. By comparing the input to a reference signal, in this case a sample of the external AC bias used to drive the oscillation, it extracts all components of the input signal that phase match the reference and uses a low-pass filter to remove the remainder[4]. This process of recovering a signal amongst noise, known as demodulation, can be conveyed neatly by carrying out the calculations in the complex plane[13]. The input signal $V_s(t)$, given by (2.6), can be represented as the sum of two vectors in the complex plane, (2.7).

$$V_s(t) = \sqrt{2}\,\mathrm{R}\cos(\omega_s t + \varphi) \tag{2.6}$$

$$V_s(t) = \frac{\mathrm{R}}{\sqrt{2}}\left(\mathrm{e}^{\mathrm{i}(\omega_s t+\varphi)} + \mathrm{e}^{-\mathrm{i}(\omega_s t+\varphi)}\right) \tag{2.7}$$

Where the amplitude of oscillating input is represented as $\sqrt{2}\mathrm{R}$ for convenience. The demodulation is a dual-phase process, wherein the input signal is split and each component multiplied separately with the reference signal and the reference signal phase shifted by 90°. Both the unaltered and phase shifted reference signal can be represented together as a single complex signal, $V_r(t)$:

$$V_r(t) = \sqrt{2}\cos(\omega_r t) + i\sqrt{2}\cos(\omega_r t + 90°) \tag{2.8}$$

$$V_r(t) = \sqrt{2}\cos(\omega_r t) - i\sqrt{2}\sin(\omega_r t) \tag{2.9}$$

$$V_r(t) = \sqrt{2}e^{-\omega_r t} \tag{2.10}$$

Multiplying (2.7) with (2.10) produces a complex signal, $Z(t)$:

$$Z(t) = R\left(\mathrm{e}^{\mathrm{i}((\omega_s-\omega_r)t+\varphi)} + \mathrm{e}^{-\mathrm{i}((\omega_s+\omega_r)t+\varphi)}\right) \tag{2.11}$$

The closer in value ω_r and ω_s, the greater the frequency difference between the two components of (2.11). If the input and reference frequencies are equal, then this simplifies to:

$$Z(t) = R\left(\mathrm{e}^{\mathrm{i}\varphi} + \mathrm{e}^{-\mathrm{i}(2\omega t+\varphi)}\right) \tag{2.12}$$

The combined signal $Z(t)$ now consists of an AC component at twice the reference frequency and a DC component dependent on the phase shift of the input signal. Passing the signal through a low pass filter with a sufficiently low cut-off, any AC signal components can be removed such that:

$$Z(t) = R\mathrm{e}^{\mathrm{i}\varphi} \tag{2.13}$$

Equation (2.13) is the demodulated signal, the noisy input signal reduced to a DC output that conveys the amplitude and phase shift of the photodiode signal. The amplitude and phase can be isolated by considering the signal as a vector in the complex plane and taking real and imaginary components, X and Y:

$$X = R\cos\varphi \tag{2.14}$$

$$Y = R\sin\varphi \tag{2.15}$$

Using trigonometry the phase, φ, and amplitude, R, can be found:

$$\varphi = \tan^{-1}\frac{Y}{X} \tag{2.16}$$

$$R = \sqrt{X^2 + Y^2} \tag{2.17}$$

This process facilitates simultaneous measurement of amplitude and phase of the piezoresponse; both are independently mapped to constitute a complete set of PFM data. The experimental importance of recording amplitude in PFM imaging is conveyed in the next section.

2.2.2 PFM Imaging

An example of a lateral PFM data set is presented in Figure 2.5, which shows amplitude and phase maps of two domains recorded on $LiNbO_3$ single crystal. In Figure 2.5a the recorded phase response changes across the domain wall and by applying a colour scale, with an appropriate range, the domain pattern is clearly imaged. In Figure 2.5b, the amplitude is approximately the same within each domain, as it is independent of polarisation direction and depends only on magnitude of

response. However, at the domain wall, amplitude is minimal, as the wall itself is characterised by a reduction through zero of the polarisation vector, *i.e.* ferroelectric walls exhibit Ising type behaviour[14]. Comparing the phase and amplitude maps, superficially we can see the former conveys the domain pattern and the latter the domain walls.

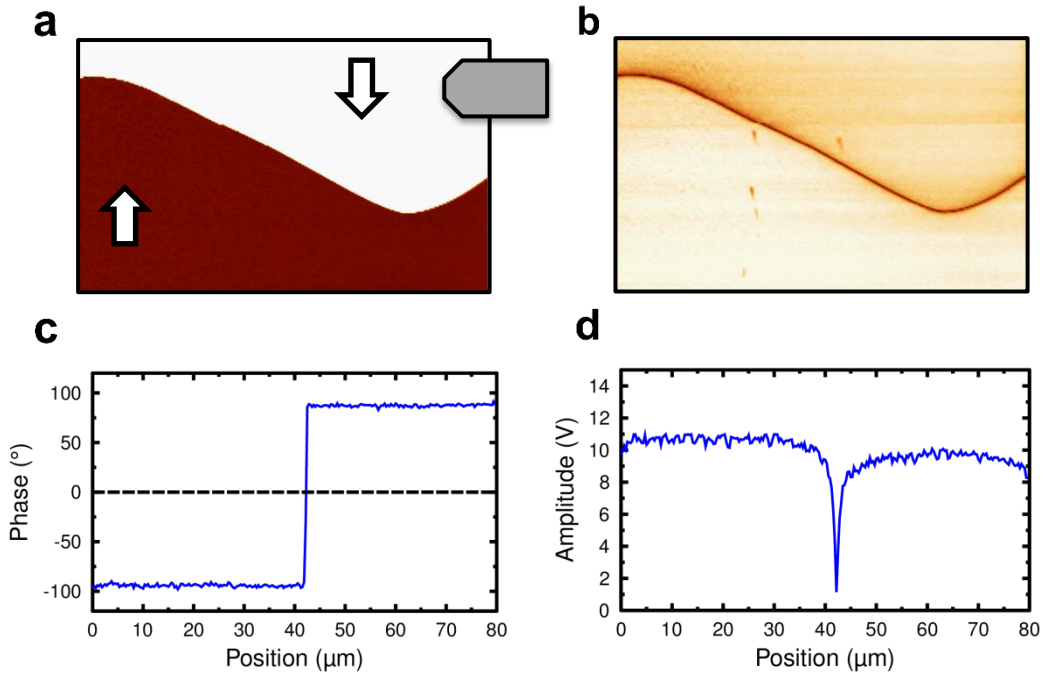

Figure 2.5 a Phase map from lateral PFM scan of lithium niobate crystal. Schematic cantilever is overlaid to convey scan orientation while block arrows convey direction of polarisation for each domain. **b** Corresponding amplitude map displaying the domain wall. **c** Plot of line profile across centre of phase map, displaying 180° inversion of phase angle. **d** Equivalent line profile of amplitude map, displaying dip in amplitude at the domain wall.

2.2.3 Microscope Specifications

All PFM measurements conveyed in this thesis were captured in-house at Queen's University Belfast (QUB), on one of two different systems. Images were predominately captured on a Bruker Dimension 5000 in conjunction with a Nanoscope V controller and a Stanford Research Systems SR830 LiA. The remainder were captured on a Veeco Dimension 3100 with a Nanoscope IIIa controller and an EG&G 7265 LiA. Referred to from here on as the 'Bruker' and 'Veeco' systems. Unless otherwise stated data presented was collected on the Bruker system, and the minority of data captured on Veeco will be identified in figure

captions. All measurements used Nanosensors PPP-EFM cantilever tips, which are silicon based with a platinum/iridium conductive coating. The cantilevers had a force constant of 2.8 Nm^{-1} and a resonant frequency of ~ 20 kHz.

2.3 Conductive Atomic Force Microscopy

Conductive atomic force microscopy, c-AFM, is variant of contact AFM where a conductive probe is used in combination with a current amplifier to map local transport properties. A typical experimental set-up is shown in Figure 2.6; a DC bias is applied to a bottom electrode and the probe grounded to establish a potential difference across the crystal. As the probe rasters in contact mode, the current flowing through the material and into the tip is sampled at regular intervals and a spatial current map is obtained.

The ability to image local variations in conductive properties of a material with nanometre resolution, combined with modern current amplifiers with measurement sensitivities in the femtoamp range, makes c-AFM ideal for investigation of conducting domain walls[15]. Indeed c-AFM is the principle investigative tool for study on domain wall conduction, with a spatial current map the classic verification of domain wall conductance[16,17]. By repeat imaging of the same area and incremental variation of the applied DC bias, basic current - voltage (IV) characteristics at the wall can be investigated. However, while c-AFM excels as a tool for imaging variations in conductance, exact quantitative measurements are difficult to obtain.

Cantilever tips are typically constructed of an insulating material with a conductive coating, which may be worn away with repeated scanning, causing variations in the contact resistance[18,19]. Structural degradation of the tip with repeated scans can also lead to significant contact variations as the nanometre scale of the tip apex amplifies minor deformations[20,21]. Degradation issues can be combated by the use of solid conducting cantilever tips such as doped diamond probes, which can also be used for larger scan times without worrying about tip deformation. Measurements can also be made under ultra-high vacuum, UHV, to reduce particulate build up at the surface, leading to enhanced current signals and longer tip life. Neither of the above are ideal solutions for ameliorating tip degradation however, as diamond probes are not-cost

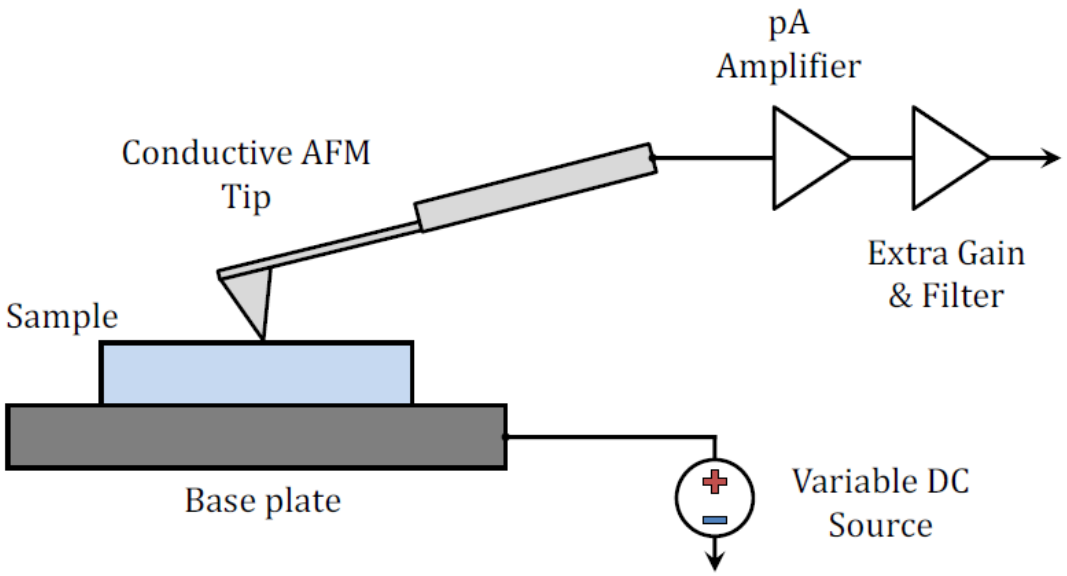

Figure 2.6 Typical experimental layout for c-AFM measurement. Sample is connected to a metallic base plate via conductive adhesive, such as silver paste, which in turn is connected to an external voltage source. A DC bias is applied to the sample while an earthed AFM probe is placed in contact with the top surface. Current at tip is sampled and passed through signal amplifier and basic filter to minimise the noise floor. Figure reprinted from [22]

effective for daily use and UHV systems impair sample access and significantly reduce the customisability of your experimental set up;

In addition c-AFM is unsuited to precise quantitative measurement as the feedback-loop-dictated tip-sample separation is inherently variant and can lead to significant variation of the metal-semiconductor contact between tip and sample. In general, when placing a c-AFM probe in contact with a ferroelectric surface, a rectifying Schottky barrier is to be expected and should be considered in any analysis of conductive behaviour[23,24]. The importance of metal-semiconductor contacts for electrical characterisation is discussed in more detail in section 4.2.

Precise quantification aside, c-AFM has been indispensable for advancing research into domain wall conductance, facilitating investigations into changing behaviour with varying voltage[25–28], temperature[26,27,29–33], dopant concentration[27,31,34] and growth conditions[35,36] in an array of materials. As a variant of AFM, current maps can be simultaneously captured with surface topography and, by changing the applied DC bias to an AC bias, alternating between piezoresponse and current

mapping is trivial. Together, this makes c-AFM a powerful tool in the characterisation of ferroelectric domain walls.

The c-AFM data presented in this thesis was obtained via a Bruker Tunnelling AFM (TUNA) current amplifier with a functional noise floor of 200 fA. For all measurements platinum/iridium coated silicon probes (Nanosensors model PPP-EFM) were used.

2.4 Non-contact and Intermittent contact AFM

Spatial resolution in AFM is limited by the diameter of the imaging probe. However, contact AFM requires a minimum deflection setpoint, such that reduction of the contact area results in larger applied pressures. Taking in-house system specifications as an example: achieving a spatial resolution in the tens of nanometres, with the minimum contact force of ~20 nN, results in typical applied pressures on the order of 10^8 Pa. Large required pressures make contact AFM unsuitable for softer samples, as the spatial resolution must be decreased to avoid sample damage. Applying said pressure while rastering also generates large lateral forces[37], which if the sample is not sufficiently massive, will lead to sample movement and poor measurements.

Martin *et al.*[38] overcame these limitations by pioneering non-contact topographic imaging. Herein, an AC bias is applied to the piezotube to oscillate the cantilever above the surface, and tip-sample interactions lead to changes in the vibrational properties of the cantilever. Variations in oscillating amplitude, resonant frequency, and phase shift between driving bias and cantilever response can all be monitored as sources of image contrast[15]. However, the two feedback modes most commonly used are amplitude modulated (AM-AFM) and frequency modulated (FM-AFM). The mechanisms behind each are conveyed in Figure 2.7.

In FM-AFM the cantilever is oscillated at resonance and kept at fixed amplitude throughout the scan. Local variations in topography change the mean tip-sample separation, as sketched in Figure 2.7a, changing the force gradient experienced by the cantilever, as sketched in Figure 2.7b, which causes a shift of the resonant frequency peak away from the setpoint value as sketched in Figure 2.7c. The

frequency shift is recorded and a feedback loop adjusts the mean tip-sample separation to return the system to free resonance. AM-FM is an off resonance technique where the cantilever oscillation is maintained at a fixed frequency and the equivalent movement of the resonance peak results in variations in the amplitude.

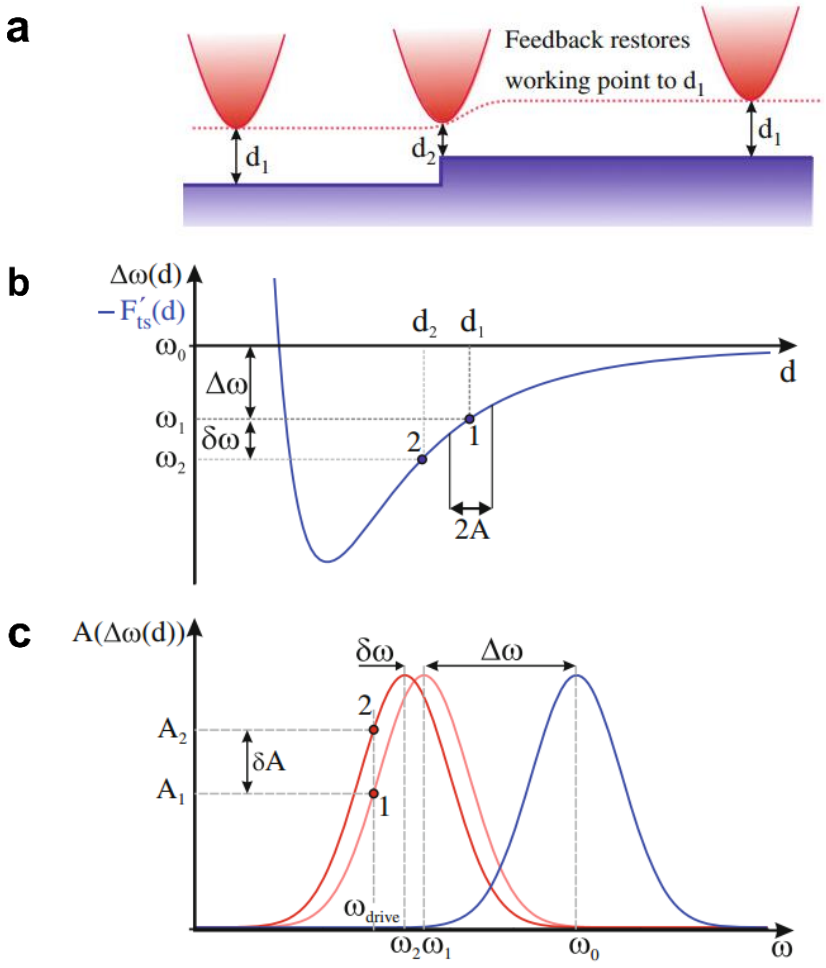

Figure 2.7 Mechanism behind non-contact AFM. **a** Variations in sample topography lead to a change in the tip-sample separation, d_1 to d_2. **b** Force experienced by the tip as a function of distance from sample, where a change of tip-sample separation leads to a change in the force gradient and corresponding shift in the resonant frequency, $\delta\omega$, from ω_1 to ω_2. **c** Cantilever oscillation amplitude, A, as a function of ω. In frequency modulated AFM, the change in resonant frequency is recorded whereas in amplitude modulated AFM the cantilever is driven at a fixed frequency, ω_{drive}, and the change in amplitude, δA, recorded. Figure adapted from [39]

Operation at the resonance peak grants FM-AFM enhanced measurement sensitivity over AM-AFM. However, in ambient conditions, maintaining a fixed amplitude is difficult due to frictional damping. Generally this mode is only applied in UHV, with cantilevers with high quality (commonly termed Q) factors, where damping is minimal and the resonance peak can be determined precisely. Conversely, for AM-AFM, low Q-factors are favoured as high Q-factors for the system would correspond to a slow changes in amplitude and a poor feedback response[40]. Hence, AM-AFM is typically chosen for ambient measurements.

Non-contact AFM is carried out within the attractive regime, as shown in Figure 2.1b, such that the response behaviour remains approximately linear[2]. To achieve this, small oscillation amplitudes are utilised so that the entirety of the oscillation falls within the net attractive regime. In addition, scanning is carried out as close to the sample surface as possible, without contacting the sample, to maximise lateral resolution, thus requiring high quality feedback control. Imperfect feedback control results in the tip contacting and sticking to the sample as the small oscillatory amplitude is insufficient to quickly overcome the adhesive forces.

Zhong *et al.*[41] proposed the use of large oscillation amplitudes (up to 100 nm) such that sample contact is made with every oscillation but no lag occurs from tip adhesion. This intermittent contact or "tapping" mode is a middle ground which eliminates the lateral forces of contact AFM while maintaining ease of use. Operating across the repulsive and attractive dominant force regimes, the highly non-linear tip-sample interactions make it difficult to obtain an analytical solution for the motion of the system. Several semi-analytical approaches[42–46] have been developed to describe tapping mode behaviour under set conditions. However, due to their complexity, observed interactions in tapping mode are more readily understood by empirical analysis.

Ideally, non-contact AFM is operated in frequency modulated mode as it favours small amplitudes and in general tapping mode AFM is operated in amplitude modulated mode as it favours large amplitudes and works effectively in ambient systems. This rule of thumb is prevalent to the point where the terms are interchangeable in literature[47].

2.5 References

1. Kruse, P. Scanning Probe Microscopy: The Lab on a Tip. *J. Electron Spectros. Relat. Phenomena* **135,** 83 (2004).
2. Howland, R. & Benatar, L. *A Practical Guide To Scanning Probe Microscopy*. (Park Scientific Instruments, 1996).
3. Whyte, J. R. Controlling ferroelectric domain wall injection and motion in mesoscale co-planar capacitor structures. (Queen's University Belfast, 2014).
4. Veeco, D. I. *Basic SPM Training Course (Manual)*. (2003).
5. Cappella, B. & Dietler, G. Force-distance curves by atomic force microscopy. *Surf. Sci. Rep.* **34,** 1–104 (1999).
6. Hertz, H. R., Jones, D. & Schott, G. in *Miscellaneous papers* **92,** 156–171 (Macmillan and Co. Ltd, 1896).
7. Lüthi, R. *et al.* Surface and domain structures of ferroelectric GASH crystals studied by scanning force microscopy. *Surf. Sci. Lett.* **285,** 7461–7471 (1993).
8. Safari, A. *Piezoelectric and Acoustic Materials for Transducer Applications*. (Springer US, 2008).
9. Alexe, M. & Gruverman, A. *Nanoscale Characterisation of Ferroelectric Materials*. (Springer Berlin Heidelberg, 2004).
10. Van Aken, B. B., Palstra, T. T. M., Filippetti, A. & Spaldin, N. A. The origin of ferroelectricity in magnetoelectric $YMnO_3$. *Nat. Mater.* **3,** 164–170 (2004).
11. de Jong, M., Chen, W., Geerlings, H., Asta, M. & Persson, K. A. A database to enable discovery and design of piezoelectric materials. *Sci. Data* **2,** 150053 (2015).
12. McGilly, L. J. Domain Topologies in Nanoscale Single-Crystal Ferroelectrics. (Queen's University Belfast, 2011).
13. Instruments, Z. *Principles of lock-in detection and the state of the art (White Paper)*. (2016).
14. Lee, D. *et al.* Mixed Bloch-Néel-Ising character of 180° ferroelectric domain walls. *Phys. Rev. B* **80,** 60102 (2009).
15. Kalinin, S. & Gruverman, A. *Scanning Probe Microscopy Electrical and Electromechanical Phenomena at the Nanoscale*. *Book* **II,** (2007).
16. Catalan, G., Seidel, J., Ramesh, R. & Scott, J. F. Domain wall nanoelectronics. *Rev. Mod. Phys.* **84,** 119–156 (2012).
17. Vasudevan, R. K. *et al.* Domain Wall Conduction and Polarization-Mediated Transport in Ferroelectrics. *Adv. Funct. Mater.* **23,** 2592–2616 (2013).
18. Guyonnet, J. *Ferroelectric Domain Walls: Statics, Dynamics, and Functionalities Revealed by Atomic Force Microscopy*. (Springer, 2014).

19. McQuaid, R. G. P., Campbell, M. P., Whatmore, R. W., Kumar, A. & Gregg, J. M. Injection and controlled motion of conducting domain walls in improper ferroelectric Cu-Cl boracite. *Nat. Commun.* **8,** 15105 (2017).
20. West, P. & Starostina, N. *A Guide to AFM Image Artifacts*. *Pacific Nanotechnology Training Manual* (2002).
21. Ricci, D. & Braga, P. C. Recognizing and avoiding artifacts in AFM imaging. *Methods Mol. Biol.* **242,** 25–37 (2004).
22. Douglas, A. M. Establishing the role of ferroelectric interfaces on nanoscale current and potential distributions. (Queen's University Belfast, 2016).
23. Kuntze, S. B. *et al.* Electrical Scanning Probe Microscopy: Investigating the Inner Workings of Electronic and Optoelectronic Devices. *Crit. Rev. Solid State Mater. Sci.* **30,** 71–124 (2005).
24. Bardeen, J. Surface states and rectification at a metal semi-conductor contact. *Phys. Rev.* **71,** 717–727 (1947).
25. Seidel, J. *et al.* Conduction at domain walls in oxide multiferroics. *Nat. Mater.* **8,** 229–34 (2009).
26. Guyonnet, J., Gaponenko, I., Gariglio, S. & Paruch, P. Conduction at domain walls in insulating $Pb(Zr_{0.2}Ti_{0.8})O_3$ thin films. *Adv. Mater.* **23,** 5377–5382 (2011).
27. Schröder, M. *et al.* Conducting domain walls in lithium niobate single crystals. *Adv. Funct. Mater.* **22,** 3936–3944 (2012).
28. Mundy, J. A. *et al.* Functional electronic inversion layers at ferroelectric domain walls. *Nat. Mater.* **16,** 622–627 (2017).
29. Farokhipoor, S. & Noheda, B. Conduction through 71° Domain Walls in $BiFeO_3$ Thin Films. *Phys. Rev. Lett.* **107,** 127601 (2011).
30. Crassous, A., Sluka, T., Tagantsev, A. K. & Setter, N. Polarization charge as a reconfigurable quasi-dopant in ferroelectric thin films. *Nat. Nanotechnol.* **10,** 614–8 (2015).
31. Seidel, J. *et al.* Domain wall conductivity in La-doped $BiFeO_3$. *Phys. Rev. Lett.* **105,** 2010–2012 (2010).
32. Maksymovych, P. *et al.* Tunable metallic conductance in ferroelectric nanodomains. *Nano Lett.* **12,** 209–213 (2012).
33. Stolichnov, I. *et al.* Bent Ferroelectric Domain Walls as Reconfigurable Metallic-Like Channels. *Nano Lett.* **15,** 8049–8055 (2015).
34. Schaab, J. *et al.* Optimization of Electronic Domain-Wall Properties by Aliovalent Cation Substitution. *Adv. Electron. Mater.* **2,** 1500195 (2016).
35. Oh, Y. S., Luo, X., Huang, F., Wang, Y. & Cheong, S. Experimental demonstration of hybrid improper ferroelectricity and the presence of abundant charged walls in

$(Ca,Sr)_3Ti_2O_7$ crystals. *Nat. Mater.* **14,** 1–7 (2015).

36. Gaponenko, I., Tückmantel, P., Karthik, J., Martin, L. W. & Paruch, P. Towards reversible control of domain wall conduction in $Pb(Zr_{0.2}Ti_{0.8})O_3$ thin films. *Appl. Phys. Lett.* **106,** 162902 (2015).
37. Den Boef, A. J. The influence of lateral forces in scanning force microscopy. *Rev. Sci. Instrum.* **62,** 88–92 (1991).
38. Martin, Y., Williams, C. C. & Wickramasinghe, H. K. Atomic force microscope-force mapping and profiling on a sub 100Å scale. *J. Appl. Phys.* **61,** 4723–4729 (1987).
39. Voigtländer, B. in *Scanning Probe microscopy, Atomic Force Microscopy and Scanning Tunnelling Microscopy* 187–204 (Springer Berlin Heidelberg, 2015).
40. García, R. & Pérez, R. *Dynamic atomic force microscopy methods*. *Surface Science Reports* **47,** (2002).
41. Zhong, Q., Inniss, D., Kjoller, K. & Elings, V. B. Fractured polymer/silica fiber surface studied by tapping mode atomic force microscopy. *Surf. Sci. Lett.* **290,** L688–L692 (1993).
42. Wang, L. Analytical descriptions of the tapping-mode atomic force microscopy response. *Appl. Phys. Lett.* **73,** 3781–3783 (1998).
43. Nony, L., Boisgard, R. & Aime, J. P. Nonlinear dynamical properties of an oscillating tip–cantilever system in the tapping mode. *J. Chem. Phys.* **111,** 1615 (1999).
44. Lee, S., Howell, S., Raman, A. & Reifenberger, R. Nonlinear dynamics of microcantilevers in tapping mode atomic force microscopy: A comparison between theory and experiment. *Phys. Rev. B* **66,** 115409 (2002).
45. Stark, R. W., Schitter, G. & Stemmer, A. Tuning the interaction forces in tapping mode atomic force microscopy. *Phys. Rev. B* **68,** 85401 (2003).
46. Zitzler, L., Herminghaus, S. & Mugele, F. Capillary forces in tapping mode atomic force microscopy. *Phys. Rev. B* **66,** 1–8 (2002).
47. Hölscher, H. & Schwarz, U. D. Theory of amplitude modulation atomic force microscopy with and without Q-Control. *Int. J. Non. Linear. Mech.* **42,** 608–625 (2007).

3 The Hall Effect

The major body of work presented in this thesis is the development and implementation of a novel scanning probe microscopy technique to spatially map Hall potentials with nanoscale resolution such that Hall effect characterisation may be carried out on conducting domain walls. To that end, an analysis of the theory behind the Hall effect, along with important considerations in making empirical measurements, are provided in the following section.

3.1 The Ideal Hall Effect

Upon observing the effect in 1879 Edwin Hall declared it "*a new action of the magnet on electric currents*"[1,2]. This was an accurate summary: the Hall effect is the generation of an electric potential within a material transverse to a driven current, upon exposure to an orthogonal magnetic field, as a direct manifestation of the Lorentz force acting the on charge carriers. At the time of Hall's experiments the Lorentz force itself was not widely known and yet to be formalised[3,4].

The Lorentz force, **F**, is the force experience by a charged particle moving in the presence of an electromagnetic field, formally defined by (3.1).

$$\mathbf{F} = q\mathbf{E} + q[\boldsymbol{\nu} \times \mathbf{B}] \tag{3.1}$$

Where q is the particle charge, **E** the electric field, $\boldsymbol{\nu}$ the carrier velocity and **B** the magnetic field. The first term is often referred to as the electrostatic force and the second term alone as the Lorentz force. To avoid confusion, in this work the first and second terms shall be referred to in full as the electric and magnetic Lorentz force components. Note, the magnetic force component is dependent on the cross product of the flux density and the carrier velocity *i.e.* a particle moving parallel to a magnetic field will not experience a magnetic Lorentz force.

Consider two strips of semiconducting material: one that is strongly p-type and the other strongly n-type, as shown Figure 3.1. A voltage is applied to each via electrical contacts on the end faces such that an electric field, $\mathbf{E}_x$, is established within the strip along the x-axis. If the samples are sufficiently long, (*i.e.* the length of the strip, l, is

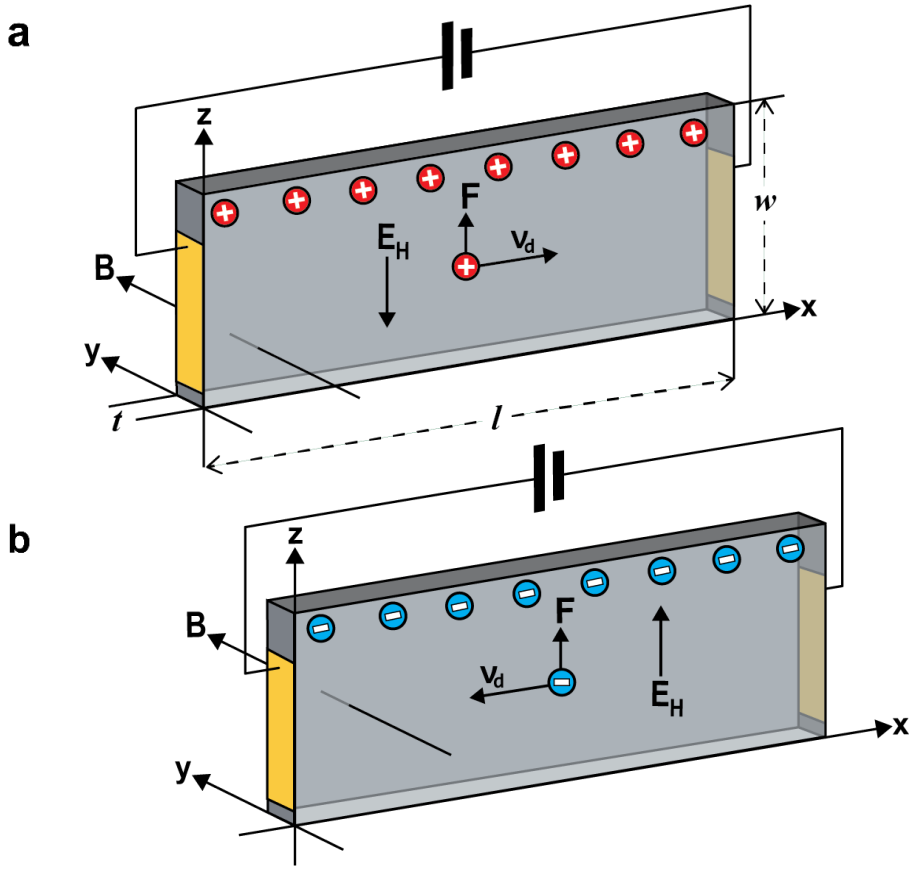

Figure 3.1 Illustration of the Hall effect in long semiconducting strips with majority p–type and n-type carriers for **a** and **b** respectively. A potential difference is applied to contacts, causing flow of charge carriers, with drift velocity, $\mathbf{v_d}$, perpendicular to a magnetic field, **B**. The magnetic Lorentz force deflects both p-type and n-type carriers upwards along *z* axis. Resultant potential difference between top and bottom edge generates Hall electric field, $\mathbf{E_H}$, which opposes the magnetic force for zero net force along *z* axis. The steady-state potential difference between top and bottom edges is the Hall voltage. Image adapted from [5].

much greater than its width, *w*) the influence of the current supplying contacts can be disregarded.

The charge carriers within the strip experience a force due to the electric component of Lorentz force, causing them to accelerate in a direction collinear with $\mathbf{E}_x$. However, free charge carriers moving within a semiconductor are subject to a range of scattering mechanisms. At room temperature the dominant mechanisms are ionized impurity scattering in doped samples and carrier-phonon interactions, *i.e.* lattice collisions due to thermal vibrations[6,7]. Under weak electric fields, the energy gained by the charge carriers is much less than their average thermal energy. Hence it

is assumed all the gained energy can transfer to the crystal lattice upon collision and after scattering the charge carrier begins acceleration again from zero initial velocity.

The velocity gained, $\delta\boldsymbol{\nu}$, by a carrier of charge, q, between collisions is given by:

$$\delta\boldsymbol{\nu} = \frac{q}{m^*}\mathbf{E}_x\tau \tag{3.2}$$

Where τ is the mean time between collisions and m^* is the effective mass of the charge carrier. Overall the charge carriers will travel through the strip with an averaged drift velocity, $\boldsymbol{\nu}_\mathbf{d} \approx \delta\boldsymbol{\nu}$. Rearranging (3.2):

$$\boldsymbol{\nu}_\mathbf{d} = \left(\frac{q}{m^*}\tau\right)\mathbf{E}_x = \mu\mathbf{E}_x \tag{3.3}$$

The drift velocity of carriers is linear in the applied electric field, where the strength of the response is quantified by the carrier mobility μ. Carrier mobility is by definition a positive quantity. The steady drift of carriers generates a steady current, **I**, flowing through the strip.

The resultant current density, **J**, can be calculated[8,9] from the dimensions of the strip and the charge carrier density, n:

$$\mathbf{J} = \frac{\mathbf{I}}{wt} = q\boldsymbol{\nu}_\boldsymbol{d}n \tag{3.4}$$

Where t is the thickness of the strip as labelled in Figure 3.1. The carrier density can also be expressed in terms of carrier mobility by substituting (3.3):

$$\mathbf{J} = \frac{\mathbf{I}}{wt} = q\mu n\mathbf{E}_x \tag{3.5}$$

From the form of the first component of (3.1), the electric field component of the Lorentz force acts along the same axis as the electric field, but the direction is dependent on the sign of both the field and carrier charge. Therefore for a given electric field direction, the oppositely charged carriers in the p-type and n-type strips will move in opposite directions.

Suppose a weak magnetic field is applied to the strip along the y axis, as shown Figure 3.1. Each carrier will now experience a magnetic Lorentz force component along the z-axis, orthogonal to both the drift velocity and magnetic field. Akin to the electric force component, the direction of the magnetic force component is dependent on the sign of the magnetic field and carrier charge with an additional dependence on the sign of the carrier velocity. As for a given electric field oppositely charged p-type and n-type carriers drift in opposite directions, the product of the signs cancel and the magnetic force component for each strip acts the same direction. Assuming electronic carriers:

$$\mathbf{F}_p = e[\boldsymbol{\nu}_\mathbf{d} \times \mathbf{B}] \tag{3.6}$$

$$\mathbf{F}_n = -e[-\boldsymbol{\nu}_\mathbf{d} \times \mathbf{B}] = e[\boldsymbol{\nu}_\mathbf{d} \times \mathbf{B}] \tag{3.7}$$

Where $\mathbf{F}_p$ and $\mathbf{F}_n$ are the magnetic Lorentz force components in the p-type and n-type strips and e is the electronic charge. For the field directions conveyed in Figure 3.1 the carriers are deflected towards the upper edge of the strip. The vertical displacement leads to an increased charge concentration at the top surface, a potential difference develops and a corresponding electrical field appears within the material. Known as the Hall electric field ($\mathbf{E_H}$) this in turn generates an electric Lorentz force acting to deflect the charge carriers along the z-axis. The sense of developed $\mathbf{E_H}$ reverses with the sign of deflected charge carrier thus the transverse electric Lorentz force always opposes the magnetic Lorentz force that generates it.

Eventually the forces reach equilibrium, resulting in zero net force along the z-axis, and the charge carriers drift through the strip as in zero magnetic field case. An expression for the Hall electric field can be found by equating the magnetic and electric Lorentz force components:

$$q[\boldsymbol{\nu}_\mathbf{d} \times \mathbf{B}] + q\mathbf{E_H} = 0 \tag{3.8}$$

$$[\boldsymbol{\nu}_\mathbf{d} \times \mathbf{B}] = -\mathbf{E_H} \tag{3.9}$$

Rearranging (3.4) and substituting for $\mathbf{v_d}$:

$$\frac{[\boldsymbol{J} \times \mathbf{B}]}{nq} = -\mathbf{E_H} \tag{3.10}$$

$$\mathbf{E_H} = -R_{\mathrm{H}}[\mathbf{J} \times \mathbf{B}] \tag{3.11}$$

Where R_{H}, known as the Hall coefficient, is a measure of the intensity and sign of the Hall effect of a material for fixed electric and magnetic field. While a convenient parameter for record and comparison of material properties, for empirical investigation it is useful to express (3.10) in terms of a directly measureable quantity. Assuming the magnetic field is applied perpendicular to the driven current, as in Figure 3.1, we can simplify the cross product:

$$\mathbf{E_H} = -\frac{\mathbf{JB}}{nq} \tag{3.12}$$

The Hall electric field develops from a potential difference (V_{H}) between the top and bottom edges of the material, which are separated by a distance w. Therefore:

$$-\frac{V_{\mathrm{H}}}{w} = -\frac{\mathbf{JB}}{nq} \tag{3.13}$$

Substituting for the current, **I**:

$$V_{\mathrm{H}} = \frac{\mathbf{IB}}{nqt} \tag{3.14}$$

Where potential difference developed (V_{H}) is known as the Hall voltage. The Hall voltage can also be expressed in terms of the carrier mobility, by rearranging (3.5) and substituting for **I**:

$$V_{\mathrm{H}} = \frac{wtq\mu \mathrm{n}\mathbf{E_x B}}{nqt} = w\mu \mathbf{E_x B} \tag{3.15}$$

We can separate (3.13) into specific expressions for the p-type and n-type strips by defining n as electron density and assign p as hole density:

$$V_{\mathrm{H}p} = \frac{\mathbf{IB}}{ept} = w\mu_p \mathbf{E_x B} \tag{3.16}$$

$$V_{\mathrm{H}n} = -\frac{\mathbf{IB}}{ent} = -w\mu_n \mathbf{E}_x \mathbf{B} \qquad (3.17)$$

Where μ_n and μ_p represent the electron and hole mobilities. $V_{\mathrm{H}p}$ and $V_{\mathrm{H}n}$ are the Hall voltages developed in the p-type and n-type strips respectively.

Equations (3.16) and (3.17) are the impetus behind the majority of work presented in this thesis. Together, they state that, if a fixed current is driven through a sample of known dimensions, with an orthogonal magnetic field applied; the Hall voltage will allow the dominant carrier sign, density and mobility to be determined.

Conceptually, the physics involved is simple, and measuring the Hall effect in macroscopic samples is often used in education as an introductory experiment to semiconductor physics[10]. This thesis focuses on overcoming the practical difficulties in translating the experiment to the nanoscale so that fundamental properties of charged domain walls can be revealed via transparent physics.

3.2 Limits of Ideal Model

Equation (3.15) was obtained under idealised conditions, which must be taken into account in designing an experiment. Non-ideal phenomena are discussed and their effect on the Hall voltage quantified, to verify that the investigative methods outlined in this thesis fall within pragmatic approximations of the ideal case and hence that all data obtained may be understood via expression (3.15).

3.2.1 Weak Magnetic Field

In section 3.1, a weak magnetic field was stipulated without proper definition. To explain the requirement for an upper limit on the applied magnetic field, we look in more detail at the path taken by a charged particle due to Lorentz force effects. Consider a charged particle moving in free space with velocity, **ν**, orthogonal to a magnetic field, **B**, without the action of an electric field. A Lorentz force acts perpendicular to **ν** and **B**, deflecting the particle and changing its direction of motion. As the Lorentz force continually changes the direction of **ν** and the force always acts

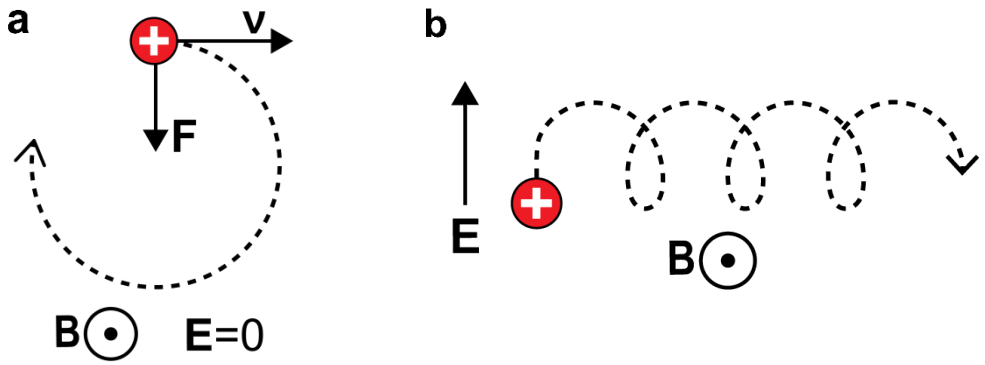

Figure 3.2 a Circular motion of a positive charged particle, with a drift velocity, **v**, orthogonal to a magnetic field. **b** Cycloidal motion of a positively charged particle in orthogonal electric and magnetic fields, **E** and **B**, where the particle rotates in the plane perpendicular to **B** and travels in the axis perpendicular to both **E** and **B.**

perpendicular to **v**, the particle gets trapped in a circular orbit in the plane orthogonal to the magnetic field, depicted in Figure 3.2a, with radius R given by:

$$R = \frac{m\mathbf{v}}{q\mathbf{B}} \tag{3.18}$$

Now consider a stationary charged particle, in orthogonal electric and magnetic fields[11]. The particle will accelerate in a direction collinear with E, due to the electric component of the Lorentz force, and at the same time will be deflected by the magnetic component of the Lorentz force. As the direction of **v** rotates, its magnitude increases or decreases depending on whether it is aligned or anti-aligned with the electric Lorentz force component. From (3.18) we can see the radius of an orbit is dependent on the particle velocity and hence the degree of curvature of the particle motion varies within each rotation. The resultant trajectory is a cycloid, depicted in Figure 3.2b, where the rotational motion occurs in the plane orthogonal to **B**, due to the magnetic Lorentz force component, and an overall particle motion occurs along the axis perpendicular to **B** and the accelerating electric field.

The charge carriers in a solid, under orthogonal electric and magnetic fields, behave between collisions as charger carriers in free space, beginning a cycloidal trajectory. The derivation of the ideal Hall voltage expression (3.15) does not account for cycloidal particle motion. However, a carrier will undergo a collision before completing a full rotation. After the collision, the particle has approximately zero

velocity and restarts the cycloidal trajectory from the initial conditions. If scattering events are sufficiently frequent, the charge carrier will never complete more than a small portion of an orbit and the ideal Hall assumptions will hold. We can quantify the limit of this condition by stating that if the period of a single orbit, T, is less than the mean free transit time between collisions, τ, the cycloidal motion will dominate[12]:

$$T = \frac{2\pi m^*}{q\mathbf{B}} < \tau \tag{3.19}$$

$$\frac{2\pi m^*}{q\mathbf{B}\tau} = \frac{2\pi}{\mu\mathbf{B}} < 1 \tag{3.20}$$

Rearranging, we find cycloidal motion can be disregarded until the limit:

$$\mathbf{B}\mu > 2\pi \tag{3.21}$$

Thus the limit of a weak magnetic field is dependent upon the carrier mobility within the sample. With regards to the Hall effect measurements in this thesis, the largest magnetic field applied was 0.35 T; the electromagnet utilised had manufacturer quoted upper limit of 0.4 T. Entering this value for **B** into (3.21) reveals that the applied magnetic field is considered "weak" so long as the carrier mobility within the conducting domain wall is below ~ 10^5 cm^2 $V^{-1}s^{-1}$. Hence, the assumption of a weak magnetic field for all measurements presented within this thesis is effectively an assumption of an upper limit for the carrier mobility within the domain wall.

This assumption is likely to hold true as the electron mobility for intrinsic silicon[13] at room temperature is on the order of ~ 10^3 cm^2 $V^{-1}s^{-1}$, however, it should be noted that room temperature mobilities of up to ~ 10^5 cm^2 $V^{-1}s^{-1}$ have been achieved within carbon nanotubes[14]. A rigorous determination of carrier mobility, independent of Hall potential measurement, would require geometric magnetoresistance measurements wherein a "short" sample geometry is utilised[15]. The mechanism behind this is explained in detail in section 3.2.2 and summarised by equation (3.24).

3.2.2 Sample Geometry

The importance of a long sample, where $l >> w$, is better understood by considering the extreme case of an infinitely short sample *i.e.* $w \approx \infty$. In this case the insulating boundaries at the top and bottom edge are infinitely far apart and as a result no Hall electric field can be established. Experimentally, this situation can be emulated[16,17] using a Corbino disc, sketched in Figure 3.3a. A disc of semiconducting material has circular electrodes placed at its centre and flanking the outer edge, such that there are no insulating boundaries present. The Corbino disc can be pictured as taking the standard Hall geometry of Figure 3.1 and bending the sample round until the top and bottom edges meet, effectively shorting the Hall potential.

When a potential difference is established between the inner and outer electrode a radial electric field is established. In the absence of an external magnetic field the current flows collinear with the electric field, intersecting the lines of equipotential at 90°. However, when a magnetic field is applied orthogonally to the plane of the disc, the charge carriers experience a magnetic Lorentz force component and are deflected off parallel from the electric field lines. As there are no insulating boundaries present, a Hall electric field cannot be established and the magnetic Lorentz force goes unbalanced. The magnitude of the current deflection is given by the deviation of the angle at which the current density intersects the equipotential lines away from the 90°, as labelled on Figure 3.3. Known as the Hall angle, θ_{H} can quantified by considering the relevant forces acting on the charge carriers.

The magnetic component of the Lorentz force acts perpendicular to the drift velocity, $\mathbf{v_d}$. If we consider this action to be the initial deflection of a carrier, the drift velocity is still parallel to the electric Lorentz force component, such that the resultant force is inclined at an angle θ_{H}, given by:

$$\tan\theta_{\mathrm{H}} = \frac{q[\mathbf{v_d} \times \mathbf{B}]}{q\mathbf{E}_{\mathrm{x}}} = \frac{\mathbf{v_d}\mathbf{B}}{\mathbf{E}_{\mathrm{x}}} \tag{3.22}$$

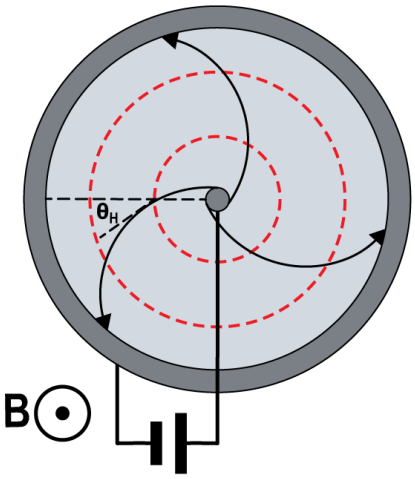

Figure 3.3 Schematic of a Corbino disc: a disc of semiconducting material with electrodes placed at its centre and along the outer edge. A potential is applied between the electrodes, dashed red lines represent lines of equipotential, generating current flow along the radial electric field. Upon application of an orthogonal magnetic field, **B**, a Lorentz force acts on the charger carriers causing a deflection of the radial current flow. The magnitude of deflection is given by the Hall angle, θ_{H}. Image adapted from [18].

Substituting for $\mathbf{E}_{\mathrm{x}}$ from (3.3):

$$\tan\theta_{\mathrm{H}} = \frac{\mathbf{v}_d \mathbf{B}\mu}{\mathbf{v}_d} = \mathbf{B}\mu \tag{3.23}$$

Somewhat intuitively, the Hall angle is proportional to the ease of movement of the carrier (the mobility) and the strength of the magnetic field inducing the Lorentz force. From inspection of Figure 3.3, it is clear that the inclination of the current density with respect to the electric field results in an increased path length for the current flow. This leads to an effective increase in sample resistivity, known as the geometric magnetoresistance effect, and follows the relationship[19]:

$$\frac{\Delta\rho}{\rho_0} = (\mathbf{B}\mu)^{\mathbf{2}} \tag{3.24}$$

Where $\Delta\rho$ is the change in resistivity due to the applied magnetic field and $\rho_0$the resistivity under zero magnetic field. This relationship can be used to determine carrier mobility and to determine the weak magnetic field limit, defined previously in

section 3.2.1, as once cycloidal motion dominates equation (3.24) no longer holds true.

While the Corbino disc is the extreme case wherein there is no insulating boundary present and zero Hall electric field develops, the current deflection effect scales depending on relative proximity of the current-providing electrodes and how effectively the $\mathbf{E}_{\mathrm{H}}$ is shorted.

The current density in a sample of intermediate geometry, $l = w$, is presented in Figure 3.4a. Directly at the electrical contacts, the Hall potential cannot develop and the current is fully deflected by the full Hall angle. Along the insulating boundaries the current travels parallel to the edge and a maximal Hall electric field is established. In the centre of the sample, intermediate behaviour occurs where the current is partially deflected and the Hall electric field is partially established with the ratio depending on the relative proximity of the electrical contacts and insulating edges[20].

In reality the Hall voltage generated by a finite sample will typically be less than that the predicted by the ideal expression (3.15). The degree from which a samples geometry deviates from ideal is known as the Hall geometrical factor, G_{H}, and is defined by[21]:

$$G_{\mathrm{H}} = \frac{V_{\mathrm{H}}}{V_{\mathrm{H}\infty}} \tag{3.25}$$

Where $V_{\mathrm{H}\infty}$is the Hall voltage of an infinitely long sample.

Determining G_{H} for a given sample geometry is arduous, as the relative contribution of non-ideal effects throughout the sample must be determined. From inspection of Figure 3.4a, this can become intensive if calculated by brute force. Typically, calculation requires finite element modelling or conformal mapping[15,22,23]. However, expressions for G_{H} have been determined for common geometries which may be used to apply a general correction factor to Hall voltage measurements[15,21].

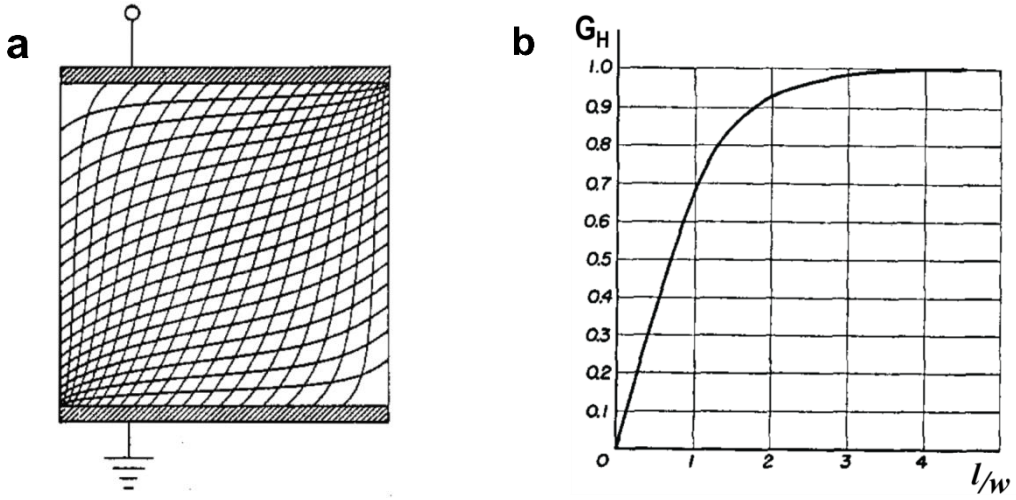

Figure 3.4 a Numerical modelling of a square Hall sample. Vertical lines linking the electrical contacts represent the lines of current flow and the horizontal represent equipotential. **b** Hall geometrical correction factor, G_H, calculated as a function of how long the sample is, determined by ratio of length to width, l / w. Data in **a** and **b** reprinted from [23] and [24].

Isenberg *et al.*[24] obtained an expression for G_{H} for the rectangular strip geometry we have been discussing. It was assumed that the sensing contacts on the top and bottom edges of the sample were small compared to the sample length and hence would not significantly influence the current path. Their results, presented in Figure 3.4b, indicate that above a length of $l / w \geq 3$ the geometrical factor approaches unity. Even in quite short samples of $l / w \approx 2$ the measured Hall voltage is over 90% of the ideal value.

Subsequent publications[25,26] take into account the additional influence of magnetic field strength wherein a larger Hall angle directs the current towards the insulating boundaries sooner, effectively increasing the G_{H} value for a fixed sample length. The results of these models are not presented as while the effect is noticeable at $l / w \leq 1$, the effect diminishes as the sample lengthens and for $l / w \geq 2$ the behaviour agrees with the predictions of Isenberg *et al.*

3.2.3 Weak Electric Field

The linear relationship between carrier drift velocity and applied electric field (3.3) was obtained under the stipulation of weak electric field. Above a critical field strength the linear relationship breaks down; $\mathbf{v_d}$ becomes less dependent on the electric field until, eventually, it is completely independent and plateaus at a maximum value. Experimental measurements are shown for a range of semiconductors in Figure 3.5.

From (3.15), the Hall voltage varies with $\mathbf{v_d}$ as:

$$V_{\mathrm{H}} = \mathbf{v}_{\boldsymbol{d}} w \mathbf{B} \tag{3.26}$$

Hence, for a constant magnetic field, the Hall voltage is directly proportional to the drift velocity and will exhibit the same behaviour; for a given magnetic field there is a maximum Hall voltage that may be generated.

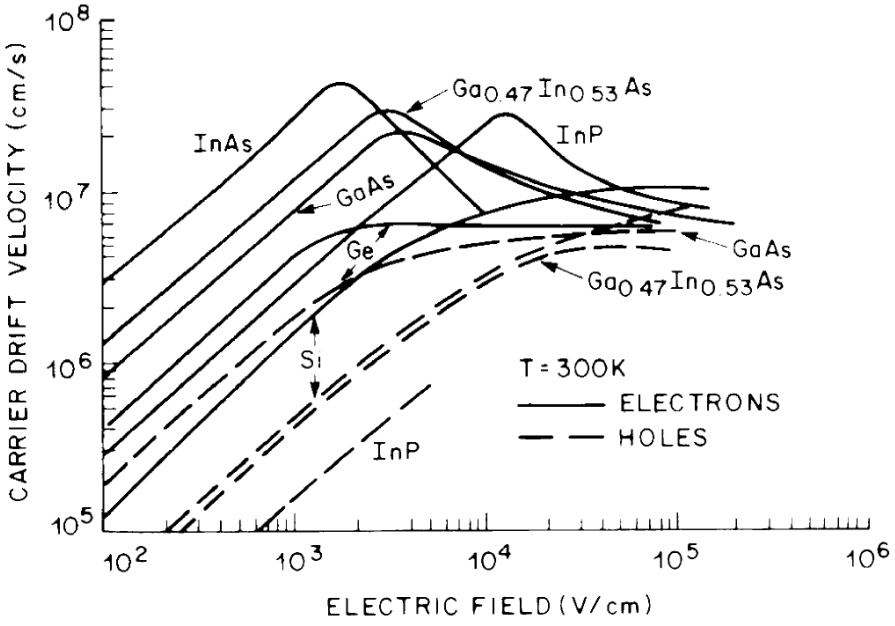

Figure 3.5 Carrier drift velocity behaviour for a range of commonly used semiconductor materials, depicting saturating of drift velocity at high electric fields. Graph reproduced from [27].

Referred to as velocity saturation[28,29], the plateauing of drift velocity is due to a change in the dominant scattering mechanism within the material. A weak electric field was described as imparting, on average, sufficiently little energy to the charge carriers so that upon collision all the energy gained can be transferred to the lattice. This limit can be quantified by modelling a lattice collision as the emission or absorption of a phonon by the charge carrier.

The maximum possible energy transfer corresponds to head-on elastic collision scattering the charge carrier directly backwards on itself[30]. In this case the change momentum of the carrier, $\Delta\mathbf{P}$, must be accounted for in the momentum of the emitted phonon.

$$\Delta\mathbf{P} = 2m^*\boldsymbol{\nu} = \hbar\mathbf{q}_{ph} \tag{3.27}$$

Where $\hbar$ is the reduced Planck constant, $\mathbf{q}_{ph}$ the wavevector of the phonon and their product gives the momentum of the phonon. The energy of a phonon can be expressed in terms of its momentum as:

$$\hbar\omega = \boldsymbol{\upsilon}(\hbar\boldsymbol{q}_{ph}) \tag{3.28}$$

Where ω and $\boldsymbol{\upsilon}$ are the frequency and velocity of the phonon respectively, and their product gives the phonon energy. Substituting (3.27) we find:

$$\hbar\omega = 2m^*\boldsymbol{\nu}\boldsymbol{\upsilon} \tag{3.29}$$

We can define a weak field by limiting the particle velocity, $\boldsymbol{\nu}$, to the average thermal velocity of the carriers, $\boldsymbol{\nu}_t$, such that the energy transferred to the lattice is on the order of that at thermal equilibrium[31].

$$E_{max} = 2m^*\boldsymbol{\nu}_t\boldsymbol{\upsilon} \tag{3.30}$$

The energy gain of the carriers due to the electric field, can be calculated from (3.3):

$$\Delta E = \frac{m^*}{2}(\mathbf{v_d})^2 = \frac{(q\tau \mathbf{E}_x)^2}{2m^*} \tag{3.31}$$

Setting $\Delta E < E_{max}$ we find the limit above which the material is no longer at equilibrium and the drift velocity ceases to respond linearly to applied field:

$$|\mathbf{E}_x| < \frac{2}{\mu}(\mathbf{v}_t \boldsymbol{\upsilon})^{\frac{1}{2}} \tag{3.32}$$

Above the limit defined in (3.32) after scattering, the charge carrier retains kinetic energy and hence can accelerate to a greater velocity before the next collision. Consequently in a strong electric field the mean free transit time decreases with increasing field and the mobility is no longer constant.

The energetic limit defined by (3.30) refers to low energy modes of lattice vibration where adjacent atoms oscillate in phase, termed longitudinal or acoustic modes[32]. In addition to these, transverse vibrational modes are possible in which adjacent atoms oscillate anti-phase such that their centre of mass remains stationary. They are referred to as optical modes, as they may be excited by incident light and hence are typically observed by absorption and transmission spectra[33]. Optical modes are of much higher energy than acoustic, as they must compete with the strong coupling between adjacent atoms. Correspondingly, in weak electric fields, charge carriers rarely avoid scattering long enough to gain sufficient energy to emit an optical phonon and thus only acoustic phonon interactions have been considered up to now.

Beyond the weak field limit, as carrier energy increases, the rate of scattering events increases accordingly. At energy equal to that of an optical phonon, the free transit time experienced by the carrier is massively reduced and little further energy can be gained before optical phonon scattering returns the carrier to approximately zero velocity. The large energetic cost required combined with the extreme scattering rate at this point makes optical phonon interactions an extremely effective energy consumption mechanism. The drift velocity eventually saturates at a value corresponding to the energy of optical phonons[34]:

$$\mathbf{v_{d,sat}} \cong \sqrt{\frac{\hbar\omega_O}{m^*}} \tag{3.33}$$

Exact calculation of the electric field at which saturation occurs is difficult as in the limit of $\mathbf{v_d} \rightarrow \mathbf{v_{d,sat}}$ the mobility tends towards zero and (3.5) is no longer an accurate expression. However, an approximate limiting value can be obtained by using the value of low field mobility[31]:

$$\boldsymbol{E_{x,sat}} \approx \frac{v_{d,sat}}{\mu} \tag{3.34}$$

Empirically determined values of saturation field are quoted in literature for the semiconducting compounds commonly used in industry[35], as shown in Figure 3.5. Taking n-type silicon as an example the limiting field is on the order of $\approx 10^6\ Vm^{-1}$. While typically not an issue for macroscopic measurements, upon scaling down to interelectrode geometries on the micron scale, equivalent field strengths can be easily achieved. Given the mobility for charge carriers along a conducting domain wall is an entirely unknown quantity, how relevant this limiting value is to domain wall conductance measurements is undetermined.

However caution should be taken in the experimental design, specifically in application of the lateral current as any basic Ohm's law assumptions may not hold true. The simplest method of ensuring an accurate value is through use of a constant current source wherein the instrument increases the driving potential until the minimum value required to drive the chosen current magnitude is reached. Operating in this fashion, the lateral field will not exceed the limiting case of (3.34). Field strengths within the non-linear region between the limits of (3.32) and (3.34) may be applied, however through a constant feedback loop an accurate current reading is maintained.

3.3 References

1. Hall, E. H. On the new action of magnetism on a permanent electric current. *Am. J. Sci.* **s3-20,** 161–186 (1880).

2. Hall, E. H. On a New Action of the Magnet on Electric Currents. **2,** 287–292 (1879).

3. Thomson, J. J. XXXIII. On the electric and magnetic effects produced by the motion of electrified bodies. *Philos. Mag. Ser. 5* **11,** 229–249 (1881).

4. Heaviside, O. XXXIX. On the electromagnetic effects due to the motion of electrification through a dielectric. *Philos. Mag. Ser. 5* **27,** 324–339 (1889).

5. Popovic, R. S. in *Hall Effect Devices* 65–67 (IOP Publishing, 2004).

6. Eisberg, R. & Resnick, R. Quantum Physics of Atoms, Molecules, Solids, Nuclei, and Particles, 2nd Edition. *Quantum Phys. Atoms, Mol. Solids, Nuclei, Part.* (1985).

7. Sze, S. M. in *Physics of Semiconductor Devices* 28–30 (John Wiley & Sons, Ltd, 2007).

8. Drude, P. Zur Elektronentheorie der Metalle; II. Teil. Galvanomagnetische und thermomagnetische Effecte. *Ann. Phys.* **308,** 369–402 (1900).

9. Halliday, D., Resnick, R. & Walker, J. in *Fundamentals of Physics* 682–689 (John Wiley & Sons, Ltd, 2008).

10. Halliday, D., Resnick, R. & Walker, J. in *Fundamentals of Physics* 741–742 (John Wiley & Sons, Ltd, 2008).

11. Bittencourt, J. A. in *Fundamentals of Plasma Physics* 33–58 (2004).

12. Popovic, R. S. in *Hall Effect Devices* 81–84 (IOP Publishing, 2004).

13. Pearson, G. L. & Bardeen, J. Electrical properties of pure silicon and silicon alloys containing boron and phosphorus. *Phys. Rev.* **75,** 865–883 (1949).

14. Dürkop, T., Getty, S. A., Cobas, E. & Fuhrer, M. S. Extraordinary Mobility in Semiconducting Carbon Nanotubes. *Nano Lett.* **4,** 35–39 (2004).

15. Putley, E. H. in *The Hall effect and Semi-conductor Physics* 42–55 (Dover, New York, 1960).

16. Corbino, O. M. Azioni Elettromagnetiche Doyute Agli Ioni dei Metalli Deviati Dalla Traiettoria Normale per Effetto di un Campo. *Nuovo Cim.* **1,** 397–420 (1911).

17. Carver, G. P. A Corbino Disk Apparatus to Measure Hall Mobilities in Amorphous Semiconductors. *Rev. Sci. Instrum.* **43,** 1257–1263 (1972).

18. Bechthold, P. S. Galvanomagnetic Transport : from Hall Effect to AMR (Lecture Series). (Max Planck Institut für Festkörperforschung).

19. Popovic, R. S. in *Hall Effect Devices* 74–76 (IOP Publishing, 2004).

20. Moelter, M. J. Electric potential in the classical Hall effect: An unusual boundary-

value problem. *Am. J. Phys.* **66,** 668 (1998).

21. Popovic, R. S. in *Hall Effect Devices* 175–204 (IOP Publishing, 2004).

22. Versnel, W. Analysis of symmetrical Hall plates with finite contacts. *J. Appl. Phys.* **52,** 4659–4666 (1981).

23. László, A., Henry, P., Nathan, A. & Schmidt-Weinmar, H. G. Numerical Modeling off Magnetic-Field-Sensitive Semiconductor Devices. *IEEE Trans. Electron Devices* 1224–1230 (1985).

24. Isenberg, I., Russell, B. R. & Greene, R. F. Improved method for measuring hall coefficients. *Rev. Sci. Instrum.* **19,** 685–688 (1948).

25. Hans-Joachim, L. & Friedrich, K. Der Geometrieeinfluss Auf Den Hall-Effekt Bei Rechteckigen Halbleiterplatten. *Zeitschrift fur Naturforsch. - Sect. A J. Phys. Sci.* **13,** 474–483 (1958).

26. Haeusler, J. Die Geometriefunktion vierelektrodiger Hallgeneratoren. *Arch. für Elektrotechnik* **52,** 11–19 (1968).

27. Brennan, K. F. & Brown, A. S. *Theory of Modern Electronic Semiconductor Devices*. (2003).

28. Sze, S. M. in *Physics of Semiconductor Devices* 35–40 (John Wiley & Sons, Ltd, 2007).

29. Brennan, K. & Brown, A. in *Theory of Modern Electronic Semiconductor Devices* 300 (John Wiley & Sons, Ltd, 2003).

30. Reggiani, L. in *Hot-Electron Transport in Semiconductors* 65–69 (Springer-Verlag, 1985).

31. Popovic, R. S. in *Hall Effect Devices* 38–53 (IOP Publishing, 2004).

32. Kittel, C. in *Introduction to Solid State Physics* 60–70 (John Wiley & Sons, Ltd, 1953).

33. Ruppin, R. & Englman, R. Optical phonons of small crystals. *Reports Prog. Phys.* **33,** 304 (1970).

34. Shockley, W. Hot Electrons in Germanium and Ohm's Law. *Bell System Technical Journal* **30,** 990–1034 (1951).

35. Reggiani, L. in *Hot-Electron Transport in Semiconductors* 99–111 (Springer-Verlag, 1985).

4 Contact Hall Effect Measurements

The exigency for fundamental characterisation of domain wall conduction was discussed in the introduction, and the Hall effect established as a powerful diagnostic tool, see section 3, revealing information on carrier type, density and mobility with a single voltage measurement. There is thus clear motivation for development of a technique which facilitates measurement of Hall potentials with the nanometre spatial resolution required to discern domain wall specific signals from that of the surrounding bulk. This chapter focuses on initial proof of concept investigations, wherein a scanning probe microscope was utilised to attempt Hall potential measurements in the simplest experimental geometry, contact mode atomic force microscopy (AFM).

Although this initial mode of operation proved to be flawed, unsuitable for the characteristically high resistivity of ferroelectric materials, the contact mode calibration experiments were pivotal in developing a pragmatic understanding of the practical limitation of the technique. It was these heuristic problems that, more so than the actual physics, ultimately dictated what could or could not be achieved.

4.1 Hall potential measurement via Scanning Voltage Microscopy

From inspection of the idealised Hall experiment, illustrated in Figure 3.1, the overt approach is to connect a voltmeter to a conducting AFM tip and initiate a contact mode scan so that the tip functions as a traditional voltage probe. Spatially mapping potential within a semiconductor using a repositionable metallic probe is a well-established imaging method; in 1952, Pearson *et al.* made the first direct measurements of the characteristic voltage profile across the depletion region of a p-n junction by manually dragging a sharpened tungsten probe across a doped crystal[1]. Known as scanning voltage microscopy (SVM) when referring specifically to modified SPM operation[2], the method is typically used to map potential across active semiconductor devices as a means of verifying correct operation.

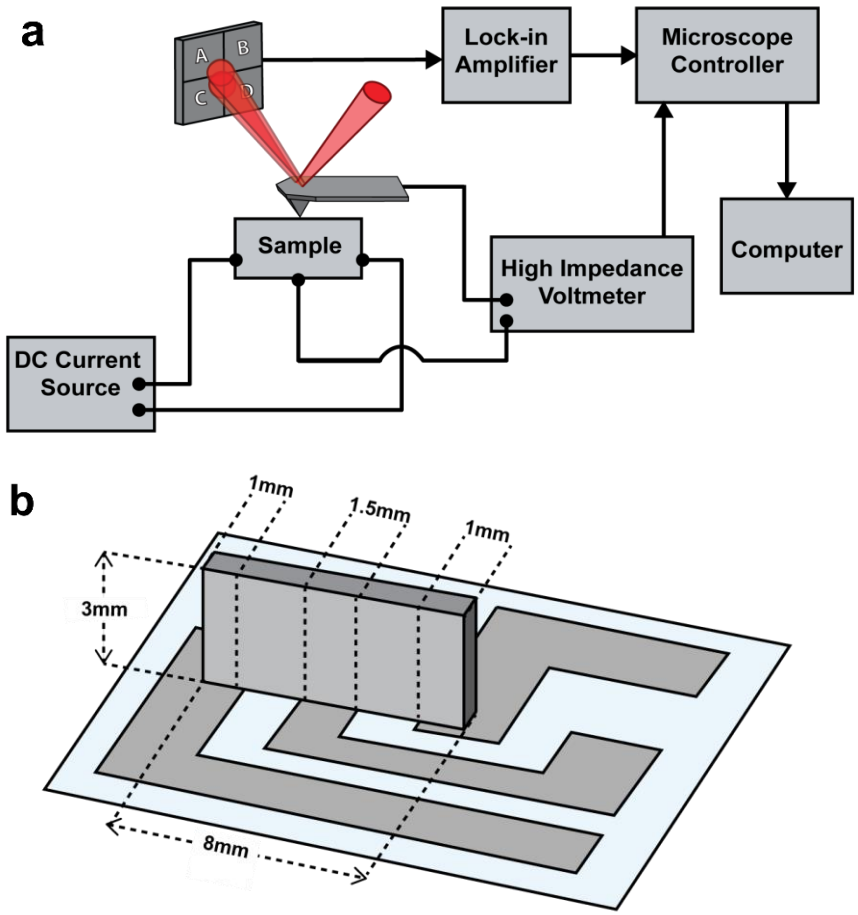

Figure 4.1 a Block diagram of the instrumentation used for scanning voltage microscopy. **b** Schematic of silicon strip, placed on edge and connected to three base platinum electrodes via silver dag. Current was driven between the outer two electrodes and the central pad connected to the voltmeter as shown in a. Dimensions are labelled, to verify that the sample was sufficiently long that the ideal Hall theory applies.

A schematic of the full experimental set up used in our case is shown in Figure 4.1a with the sample layout shown in detail in Figure 4.1b. All measurements were carried out on the Veeco system, with lateral current supplied by a Kiethley 6221 active DC source and the orthogonal magnetic field was applied by an in situ electromagnet. The resultant transverse Hall potential was measured between the tip and a fixed bottom electrode using a Kiethley 6514 electrometer as a high impedance voltmeter, ~ 200 TΩ. Herein direct electrical connection between the tip and external voltmeter was provided by a c-AFM cantilever holder, modified to fit between the electromagnet poles. Voltage readings where briefly stored in an internal buffer where the voltmeter interprets the value and generates a reference voltage at the analogue output, scaled between 0 – 2 V. By passing the analogue output signal

directly into a data channel on the controller, the measured potential could be recorded as a spatial map. Matching the buffer rate with the AFM scan speed and resolution ensured a direct correspondence with the topographic data.

For verification of the experimental method, a sample with known conductive properties was required such that measured carrier type and density could be compared. Both n and p-type materials were investigated to ensure the instrumentation can distinguish between, and function irrespective of, dominant carrier type. Boron (p-type) and phosphorous (n-type) doped silicon were chosen as the carrier properties as a function of dopant concentration are available in literature[3–5]. Single crystal silicon wafers were purchased with both p-type and n-type wafers having equal thickness, 280 μm, and the same quoted order of resistivity, 1-10 Ωcm^{-1}.

The sample layout was as shown in Figure 4.1b. Three platinum electrodes were sputtered onto a glass slide and a wire affixed to each with silver dag. Emulating the idealised Hall experiment, rectangular strips where cut from each wafer and orientated on their edges. They were held in place by silver dag, which also served as electrical contacts between the silicon and platinum electrodes. The size of the electrical contacts, ~ 1mm, was dictated by the minimum amount of silver dag which effectively stabilised the somewhat precariously orientated silicon strip. Thus, working with this lower limit, sample length and width of 8 mm and 3 mm were chosen respectively. With an gap of ~ 6 mm between the current driving electrodes this corresponds to a geometry ratio of $l / w \geq 2$.

Initial measurements recorded the same sign of potential at the tip, in both silicon strips, independent of magnetic field direction but this appeared to change sign with reversed current direction. Further investigation revealed a significant transverse voltage was recorded by the system in complete absence of an orthogonal magnetic field, solely due to the presence of a lateral current. Presence of a background voltage is common in commercial Hall effect devices; the offset is referred to as misalignment voltage and is chiefly due to positioning of the voltage sensing contacts[6]. Within an ideal, long sample of uniform resistivity, the equipotential lines

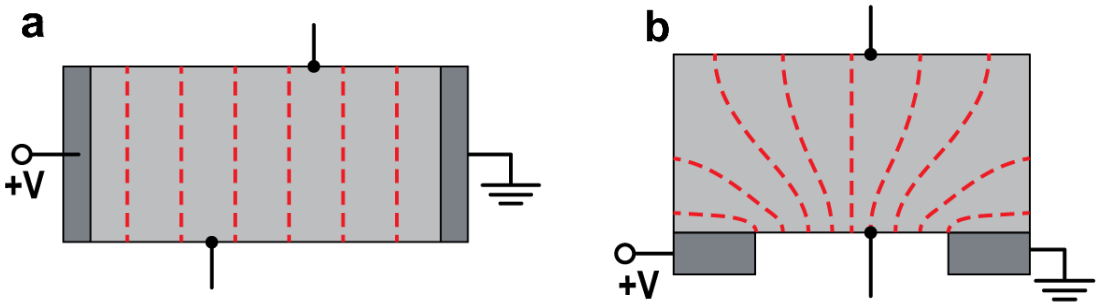

Figure 4.2 a Schematic of misalignment of voltage sensing contacts resulting in a offset voltage as contacts are within different equipotential regions, signified by red dashed equipotential lines. **b** Potential profile when source contacts are placed on the base of sample. If sense contacts are not centred between source contacts, even when both sense contacts are exactly aligned they will be at different values of lateral potential.

lie orthogonal to the top and bottom faces and the potential is dropped linearly across the sample, as shown Figure 4.2a. Hence, if one of the voltmeter electrodes is displaced across the samples length with respect to the other, then a potential difference will be measured in absence of a transverse Hall potential.

Equivalently, in a sample of non-uniform resistivity along the y-axis the equipotential lines lie angled to the top and bottom faces and thus even exact alignment of voltmeter electrodes results in a measured potential difference. Typically a combination of both effects is present in a commercial device.

Prime quality silicon wafers were purchased to ensure a high level of homogeneity in the dopant distribution and correspondingly in the sample resistivity. However, the model in Figure 4.2a assumes the current providing electrodes lie on the lateral faces of the sample and that they are sufficiently far away from the voltage sensing electrodes so as to not interact. For ease of contact, the driving electrodes on the investigated sample lie on the bottom face. Consequently, irrespective of sample uniformity, the asymmetry in the sample design results in an inhomogeneous potential profile across the sample, sketched in Figure 4.2b.

Commercial Hall devices nullify the misalignment voltage by connecting a potentiometer in series with one of the voltage sensing contacts. By varying the

resistance of, and concurrently the potential dropped across, the potentiometer, the transverse voltage measurement can be zeroed in the absence of a magnetic field. By this method the magnitude and accuracy of the offset reduction is limited by the range and resolution of the potentiometer. Additionally, if operating with a fixed current source, as opposed to a fixed voltage, a small non-zero offset will always persist, as intrinsic magnetoresistance effects[7] lead to a change in the lateral voltage dropped across the sample when the orthogonal magnetic field is applied.

High resolution Hall devices, designed for low magnetic fields, achieve superior offset reduction by using dynamic spinning-current technique[8,9] wherein the output signal appears as an alternating signal that is superimposed on a quasi-static Hall potential. Integrating the output over sufficient time periods allows for accurate demodulation of the Hall potential from the offset signal. However, this technique has severe geometrical restrictions, requiring the sample material to have at minimum 4-fold rotational symmetry.

Breaking the sophisticated spinning current technique down to its central idea, repeat measurements with alternating field conditions allows for cancellation of the offset voltage while retaining the contribution from the Hall potential. The sign of the offset voltage correlates with the sign of the lateral electric field $\mathbf{E}_x$, and is independent of the direction of the magnetic field $\mathbf{B}_z$ while, from (3.11), the sense of the Hall potential depends on the direction of both $\mathbf{E}_x$ and $\mathbf{B}_z$. The expressions in Table 4.1 present the behaviour of the Hall voltage,V_{H}, and the offset voltage, V_{off}, under each possible variant on field directions.

	$+\mathbf{B}_z$	$-\mathbf{B}_z$
$+\mathbf{E}_x$	$V_{\mathrm{H}} + V_{\mathrm{off}}$	$(-V_{\mathrm{H}}) + V_{\mathrm{off}}$
$-\mathbf{E}_x$	$(-V_{\mathrm{H}}) - V_{\mathrm{off}}$	$V_{\mathrm{H}} - V_{\mathrm{off}}$

Table 4.1 Total potential measured dependent on the direction of electric and magnetic field, $\mathbf{E}_x$ and $\mathbf{B}_z$**,** applied along the x and z axes of a right-hand coordinate system as defined in Figure 4.3. The signs are not representative of the sign of measured potential but are relative to that specific geometry.

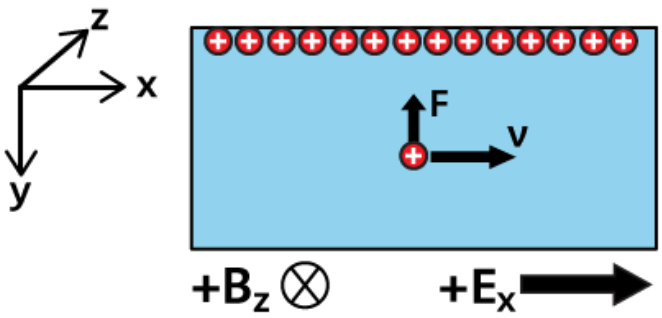

Figure 4.3 Schematic conveying sense of deflection a p-type carrier when both the electric and magnetic field, $\mathbf{E}_x$ and $\mathbf{B}_z$, are aligned positively along x and z directions as defined by the coordinate axis shown. The deflection of the p-type carriers upwards corresponds to a positive Hall voltage reading under scanning voltage microscopy. An n-type material under the same applied electric and magnetic field directions, would generate a negative voltage reading. Reversal of both fields maintains the same sense of deflection

The signs prefixed to each voltage are not representative of the sign of the measured potential but are relative to that measured under field directions of $+\mathbf{E}_x$ and $+\mathbf{B}_z$, as defined by the coordinate axis shown in Figure 4.3. This is the field geometry for which the measured Hall voltage would be positive and negative for p-type and n-type silicon respectively. By reversing both the electric and magnetic field directions, the sense of the offset voltage reverses while the sign of the Hall voltage remains unchanged. Summing the measured signal obtained under each field geometry, ($+\mathbf{E}_x$, $+\mathbf{B}_z$) and ($-\mathbf{E}_x$, $-\mathbf{B}_z$), cancels out the offset contribution and returns two times the Hall voltage.

SVM measurements were recorded at halfway along the length of each silicon strip for two field geometries; firstly with the electric and magnetic field directions of $+\mathbf{E}_x$ and $+\mathbf{B}_z$ and subsequently with both field directions antiparallel to the axis, $-\mathbf{E}_x$ and $-\mathbf{B}_z$. For all measurements a lateral current of 100 μA was maintained and the magnitude of magnetic field was fixed at 0.2 T. A complete set of SVM Hall measurements is presented in Figure 4.4.

Ideally the SVM maps should be featureless, as the silicon has a high degree of homogeneity. However, all the maps show banded behaviour, wherein the magnitude of measured potential changes abruptly after an arbitrary number of scan lines. This

behaviour is characteristic of rough sample topography: sudden variations in surface height, such as a crevice or ridge, correspond to changes in the tip contact. Sample dimensions and the on-edge orientation led to difficulties with mechanical polishing and topography could not be improved beyond a ~ 50 nm root mean square (RMS) surface roughness.

As verification that the instrumentation was indeed measuring the surface potential, line profiles were taken across the scan length to confirm that a linear drop in potential, changing sign and gradient with reversed lateral field, was imaged across the scan length. The magnitude of the potential drop in each scan was of the same order of magnitude as expected as the samples, having equal dimensions, were of the same order of magnitude in resistivity.

To obtain solely the V_{H} contribution measurements for each silicon strip, Figure 4.4a and 4.4b for n-type and Figures 4.4c and 4.4d for p-type, were summed directly using WSxM 5.0 software[10] and the values halved. The resultant Hall potential maps for the n-type and p-type silicon, Figure 4.4e and 4.4f, are majority negative and positive respectively, suggesting the data may discern the dominant carrier type. However, the banding effect present in the summands do not necessarily spatially align, as identical topography is no guarantee to identical tip behaviour, introducing errors in the direct pixel-to-pixel spatial summation. Consequently, the magnitude of the Hall voltage is known only to be less than or on the order of the variation between bands, ~ 10^2 mV.

Making approximations, the maximum possible Hall voltage within each silicon strip can be calculated from (3.14) and compared to contact measurements. Silicon resistivity as a function of carrier concentration has been well characterised in literature with a 1-10Ωcm resistivity range corresponding to carrier densities of 1x10^{15} to 1x10^{16} cm^{-3} and 5x10^{14} to 5x10^{15} cm^{-3} for boron and phosphorous dopants respectively[3–5]. Magnetic field strength (0.2 T), driven current (100 μA) and sample width (280 μm) are known. Hence, substituting into (3.14), maximum Hall voltages of $+\,0.9$ mV and $-\,0.4$ mV are obtained for p-type and n-type. Unfortunately, the theoretical Hall voltages for the silicon samples are a considerable three orders of

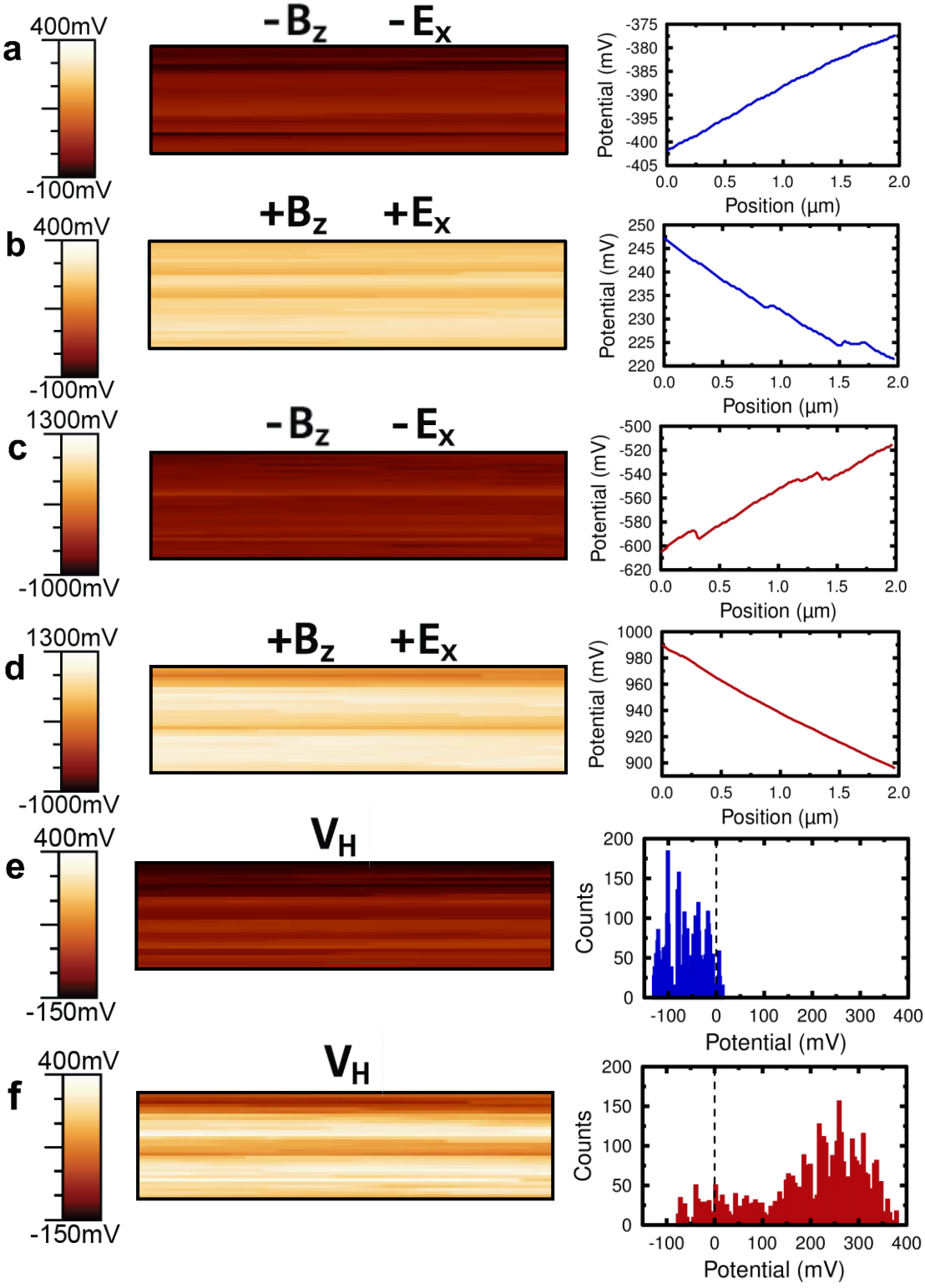

Figure 4.4 Scanning voltage microscopy maps of n-type silicon, **a** and **b,** and p-type silicon, **c** and **d,** under reversed field geometries wherein the sense of Hall voltage is unchanged but sign of offset is reversed. Line profiles, taken left to right, across each map verify lateral offset measurement. **e** and **f** maps of Hall voltage, $V_{H,}$ developed within n-type and p-type silicon respectively. Histograms display substantial spread of the data, ~10^2 mV, though majority negative and positive voltage readings are obtained for n-type and p-type samples.

magnitude below the error range introduced by the mismatch of topographical effects, and therefore no quantitative statements can be made from the investigation.
The silicon sample investigation confirmed that the experimental procedure operates at the most basic level, returning a map of the potential difference between tip and base electrode, as evidenced by the line profiles presented in Figure 4.4. However, it also revealed a strong dependence on sample topography that dominated the measurements, preventing determination of the measurement accuracy. Additionally, the spatial correspondence of the SVM maps had not yet been confirmed as, by design, the samples were featureless due to homogenous conductivity.

4.2 Calibration of Scanning Voltage Microscope

Moving forward, a new calibration experiment was designed. A multilayer ceramic capacitor was mechanically polished to reveal a cross section of alternating electrodes, spaced 20 μm apart, embedded in bulk polycrystalline $BaTiO_3$ dielectric, structure sketched in Figure 4.5a. The smaller dimensions of the capacitor, compared to the silicon strips, allowed for a micrometre adjustable tripod to be used to achieve a high grade polish. Contact AFM mapping, presented in Figure 4.5b, indicated no polish scratches in topography while clearly displaying the raised metallic electrodes adjacent to bulk dielectric. A 10 V bias was applied to one end of the capacitor and the opposite earthed such that each alternate electrode within the multilayer structure was fixed at 10 V and 0 V respectively. SVM measurements were carried out with the aim of imaging the boundaries of a live electrode and spatially mapping the potential drop across the granular $BaTiO_3$ towards the adjacent earth.

Figure 4.5 displays simultaneously captured topography and SVM maps (trace and retrace in Figure 4.5c and Figure 4.5d) of a biased electrode and the adjacent dielectric region. Both SVM maps show high potential in the region of the electrode. However, the electrode boundary appears poorly defined in the retrace scan, while distinct in the trace scan, with the shape of the electrode conveyed more clearly than in the topography scan. Comparing line profiles taken across the same region in each scan revealed that both trace and retrace map the edge of the electrode with equivalent precision, at 2.7 μm, in agreement with the topography profile, shown Figure 4.5e.

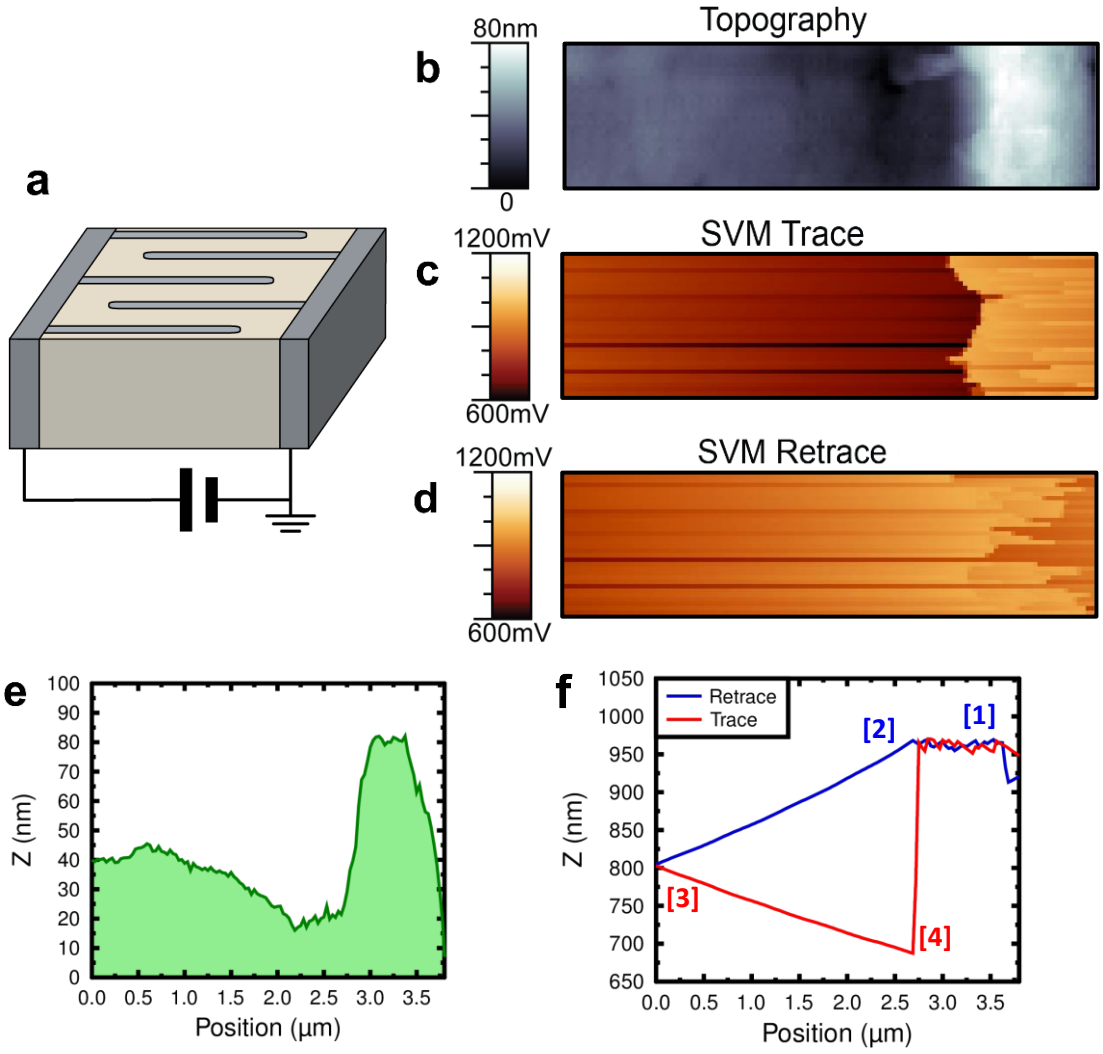

Figure 4.5a Illustration of multilayer capacitor structure, with polished top surface revealing metal electrodes in a bulk $BaTiO_3$ ceramic structure. **b** Topography and **c & d** corresponding scanning voltage microscopy maps of an electrode, biased at 10 V, and adjacent ceramic. **e** Line profile taken across the topography scan, conveying the electrode boundary. **f** Line profiles of trace and retrace scan, showing a 9.7 V reading at the electrode and a slow drop in potential at the ceramic, regardless of local potential.

The apparent distinction is due to the image contrast of the electrode voltage against the dielectric region. The potential at the metallic electrode is accurately imaged in both scans (the 9.7 V measured differs from the 10 V applied DC bias however the difference is attributed to the nonzero resistance of the electrodes) while the voltage profile across the dielectric region varies greatly for trace and retrace.

Plotting both trace and retrace line profiles on the same axes (shown in Figure 4.5f) the differing potential measurements are explained if the time taken for tip to match the ceramic potential is greater than the length of time the tip is in contact. Following the tip path in time, at point [1] the tip begins the retrace scan on the electrode making a low resistance metal-metal contact and the tip potential quickly equilibrates to the 9.7 V. At point [2] the tip has moved off the metal electrode onto the bulk ceramic forming a high resistance metal-semiconductor contact and the tip slowly discharges towards the lower potential of the dielectric. At point [3] the retrace scan has ended and the subsequent trace scan begun. The tip potential continues to decrease with the same behaviour, despite the increasing potential gradient along the sample; this suggests that the time constant needed to establish tip-ceramic equilibrium is significantly longer than the scan time. At point [4] the tip comes into contact with the electrode again and the low resistance metal-metal contact quickly equilibrates the tip and electrode potentials.

When the tip comes into contact with the sample, charge flows between tip and sample discharging / charging the tip until it matches the lower / higher potential of the contact. The contact behaves analogously to a capacitor plate structure and, as such, the rate of discharge decays exponentially, asymptotically approaching the sample potential with a time constant τ. As with a simple capacitor circuit:

$$\tau = RC \tag{4.1}$$

Where, in this case, R is the contact resistance and C is the capacitance of the measurement circuit (chiefly from parasitic capacitance of cabling between apparatus[11,12]). By convention the tip and sample potentials are stated to be equal after 5 τ, where the potentials are within less than 1% of each other[13].

The SVM maps in Figure 4.5 were captured at scan rate of 0.1 Hz, *i.e.* it took 10 s to capture both trace and retrace data for each spatial scan line; this was the same scan rate as used for the silicon data shown in Figure 4.4. To maximise the time available to the tip to reach equipotential with the sample, the scan rate was reduced to the

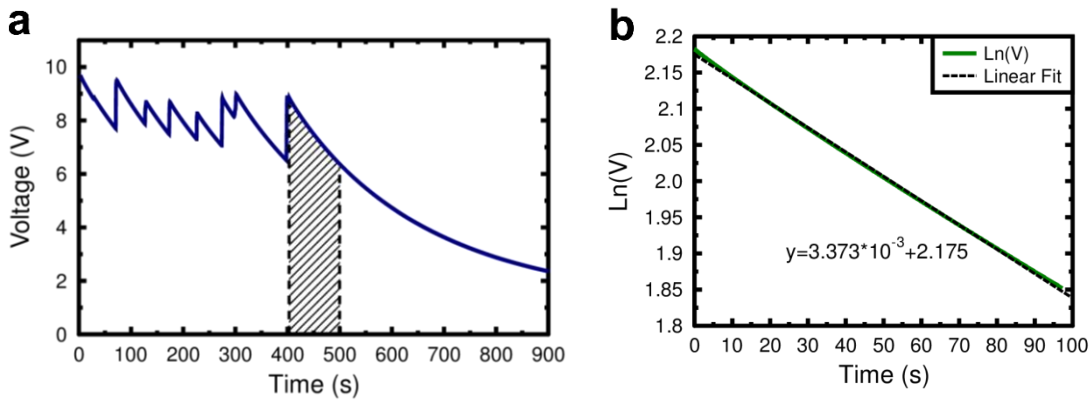

Figure 4.6a Measured voltage from the point where the tip moved off the electrode onto the ceramic, subsequent scan lines appended so as to plot the recorded potential over a large period of time. Jagged behaviour is due to tip making intermittent poor contact with the jagged electrode edge. Last contact with electrode is at 403s and the shaded area represents all subsequent measurements along the same spatial scan line. **b** The log of the voltage, within the shaded region, was plotted against time and a linear fit applied, so as to obtain the time constant for the tip-ceramic contact.

system minimum of 0.01 Hz and the scan direction set to 90° so that the tip rastered parallel to the electrode edge. The trace and retrace data for all scan lines was appended such that the measured potential could be plotted as a function of time. Potential as a function of time is shown in Figure 4.6a, beginning from where the tip moved off the electrode and made first contact with the $BaTiO_3$ ceramic. Due to the irregular electrode edge, for the initial scan lines on the ceramic the tip made intermittent poor contact with the electrode, causing the discernible spikes in measured potential.

The potential across a parallel plate capacitor, V, discharging from an initial voltage, V_0, for a time, t, is given by:

$$V = V_0 e^{-\frac{t}{RC}} \tag{4.2}$$

Taking the log of the potential we can find an expression for the time constant:

$$\ln V = -\frac{t}{RC} + \ln V_0 \tag{4.3}$$

Under the assumption that the ceramic was at equal potential across a single spatial scan line; the voltage measurements corresponding to the scan line after the last recorded contact with the metallic electrode were identified, conveyed by the shaded region in Figure 4.6a, the natural log taken and the result plotted as a function of scan time, plot presented in Figure 4.6b. A linear fit was applied and a value for the time constant of $\tau = 296s$ was obtained; three times the system's lowest scan rate.

For ideal operation, the time spent by the tip at each sample point should equal $5\,\tau$, so that the precise potential at each point is imaged[2,14]. In practice, the required accuracy depends on the gradient of the potential as, if the change in potential is negligible over a significant distance the steady state time may be divided amongst several sample points. This was likely the case with the silicon Hall measurements where there were no sharp potential features. Imaging the potential profile due to a conducting domain wall would require $5\,\tau$ to occur within the time taken to sample the spatial width of the conducting wall, on the order of ~10 nm. The local carrier density at a charged domain wall is predicted to increase by one or two orders of magnitude comparative to bulk[15], which may contribute to reduce the resistance element of the time constant. This combined with submicron scan sizes could in theory facilitate SVM imaging. However, for ambient AFM , the piezo-tube scanner experiences thermal drift over time at typical a rate of 1 to 2 nm per minute[16]. At a rate of 100 s per scan line, any submicron scan of decent resolution will experience significant drift.

The immense time constant of the $BaTiO_3$ contact compared to the responsive doped silicon may be understood by considering the origin of the contact resistance in a metal-semiconductor junction. Figure 4.7a shows the band structure of a high work function metal, such as platinum, and an intrinsic semiconductor. When the metal comes into contact, see Figure 4.7b, electrons will flow from the semiconductor into the metal until thermal equilibrium is reached and the Fermi levels of both materials are equal. As it approaches this steady-state potential, the accumulated electrons lead to a build-up of negative charge at the surface of the tip. Equivalently a region of positive charge develops in the semiconductor as it is locally depleted of electrons. The net positive charge is greatest at the junction and decreases with distance as the

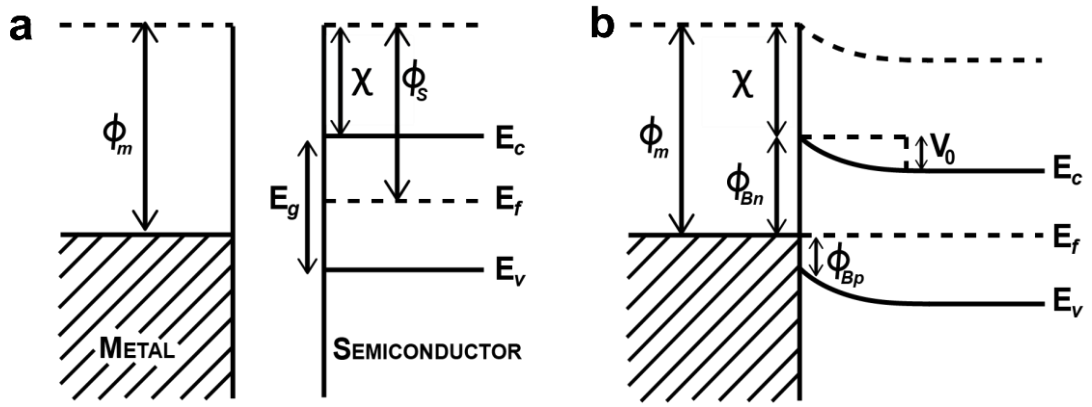

Figure 4.7 Band structure of intrinsic semiconductor and metal **a** as separate systems and **b** upon reaching equilibrium in contact. Where ϕ_m and ϕ_s are the work functions of the metal and semiconductor, E_g the band gap of the semiconductor, E_C the conduction band edge, E_V the valence band edge, E_f the fermi energy, χ the electron affinity, ϕ_{Bp} and ϕ_{Bn} the Schottky barriers for holes and electrons, V_0 the contact potential and e the electronic charge. Figure adapted from [17].

negative potential of the metal surface is effectively screened. The charge gradient leads to the development of an electric field within the depletion region, which causes bending of the conductance and valence bands.

It is the localised band bending which is the dominant source of contact resistance as potential barriers form which impede the motion of charge carriers across the interface. Two transport mechanisms, thermionic emission over the barrier and tunnelling through the barrier, operate in parallel with the resistance of both mechanisms increasing exponentially with the barrier height. Therefore the magnitude of the resistance for the tip-material contact can be predicted by calculating the expected barrier height[17].

From inspection of Figure 4.7b, diffusion of charge carriers from semiconductor to metal must overcome a barrier, eV_0:

$$eV_0 = \phi_m - \phi_s \qquad (4.4)$$

Where ϕ_m and ϕ_s are the work functions of the metal and semiconductor respectively and V_0 the contact potential established across the junction due to the difference in the workfunctions.

For diffusion of charge carriers from the metal to the semiconductor:

$$\phi_{Bn} = \phi_m - \chi \quad (4.5)$$

$$\phi_{Bp} = E_g - (\phi_m - \chi) \quad (4.6)$$

Where χ is the electron affinity of the semiconductor and ϕ_{Bn} and ϕ_{Bp} are the barriers impeding diffusion of electrons and holes respectively. The potential barrier for carrier diffusion in this direction is termed the Schottky barrier.

Substituting (4.5) into (4.4):

$$eV_0 = \phi_{Bn} - (E_c - E_f) \quad (4.7)$$

Where $(E_c - E_f)$ is the difference between the fermi energy and conduction band edge, effectively a measure of the dopant level in the semiconductor. It is clear that eV_0 is lower than, and scales with, the Schottky barrier height. Thus the Schottky barrier alone can be referred to as a qualitative measure of the contact resistance.

In practice the semiconductor band structure may have localised surface states due to termination of the periodic lattice at the surface, which contribute to the electric field at the interface[18]. Depending on the density of surface states, the resultant Schottky barrier may be partially or entirely independent of the metallic work function. While directly calculating the barrier height when accounting for surface states is significantly more complex, as (4.5) and (4.6) fail to hold[19,20], the general relationship between the barriers holds true[17]:

$$E_g = (\phi_{Bn} + \phi_{Bp}) \quad (4.8)$$

From (4.8), the upper limit on the height for a Schottky barrier is dictated by the band gap of the semiconductor. Hence, the barrier height typically increases with increasing sample band gap and, with it, the contact resistance at the tip increases exponentially.

Neglected here, the tunnelling resistance has an additional dependence on the barrier width with tunnelling probability increasing exponentially for decreasing width[21]. Therefore if the Schottky barrier is sufficiently narrow, the tunnelling mechanism will dominate and a low contact resistance can be achieved regardless of a large barrier height. The maximum width of a Schottky barrier is given by the length from the interface at which the depletion region ends, the semiconductor returns to neutral and there is zero electric field to bend the energy bands. In reality the charge density decreases with distance from the interface, however simplifying and modelling the carrier density within the depletion region as uniform we can quickly obtain an expression for the barrier width[22]. From Gauss' law:

$$\nabla \cdot E = \frac{\rho}{\varepsilon} \tag{4.9}$$

Where ρ is the charge density with the depletion region. Reducing it to one dimension and substituting for the potential drop, ϕ:

$$\frac{\partial^2 \phi}{\partial x^2} = \frac{Nq}{\varepsilon} \tag{4.10}$$

Where q is the free carrier charge and N is the density of ionised atoms due to depletion of charge carriers. Assuming complete removal of charge carriers, N equals the free carrier density of the bulk semiconductor, n. Solving for ϕ:

$$\phi = \frac{nq}{2\varepsilon} x^2 \tag{4.11}$$

Rearranging, for a Schottky barrier height of ϕ_B the barrier width W is given by:

$$W = \sqrt{\frac{2\phi_B \varepsilon}{nq}} \tag{4.12}$$

Where the barrier width is inversely proportional to the square root of the carrier density. This result is somewhat intuitive, as for a given total charge required to

equalise the Fermi levels, the greater the charge carrier density the smaller the spatial region which must be depleted of carriers.

Relating back to the SVM measurements, three major factors which affect the contact resistance are the band gap and carrier density of the semiconductor under contact and the work function of the conducting tip. $BaTiO_3$ is a wide band gap semiconductor with a band gap of 3.2 eV[23], in stark comparison to the 1.1 eV band gap of both the n-type and p-type silicon strips. For both investigations equivalent platinum iridium alloy (Pt / Ir) tips were used, which has a quoted work function of ~ 5.3 eV in literature[24,25]. With the silicon values for comparison, the band gap energies and bulk carrier densities are listed in Table 4.2 for single crystal ferroelectrics, which have been shown to express enhanced conductivity at domain walls.

Material	Carrier Density (cm^{-3})	Band Gap (eV)	Reference for Values
n type silicon	~10^{14} - 10^{15}	1.1	3, 26
$BaTiO_3$	~10^{18} - 10^{19}	3.2	23
Congruent $LiNbO_3$	~10^{19}*	3.78	27
$RMnO_3$ Family	⁂	1.5 - 1.7	28, 29,30
$Ca_{2.5}Sr_{0.5}Ti_2O_7$	⁂	3.9	31

⁂ Values could not be found in literature

*Theoretical estimate

Table 4.2 Bulk carrier densities and band gaps for a range of single crystal ferroelectric materials known to express domain wall conductance. Except for the family of hexagonal manganites ($RMnO_3$) the ferroelectric materials are wide band gap semiconductors in bulk. The carrier densities for $RMnO_3$ and $Ca_{2.5}Sr_{0.5}Ti_2O_7$ could not be found in literature.

The majority of the listed ferroelectric systems are wide band gap semiconductors in the bulk. $Cu_3B_7O_{13}Cl$ is absent as no values could be found in literature though band gaps for other members of the chloride boracite family were found to lie between 4 - 6.2 eV[32]. With exception of the comparatively narrow ~ 1.6 eV band gap of the

hexagonal manganites ($RMnO_3$), the bulk crystals have band gaps greater than that of $BaTiO_3$. Given the bulk carrier densities are also of the same order as $BaTiO_3$, the values suggest the steady state time will exceed the minimum scan rate for all but the $RMnO_3$ family.

While the technique appears incompatible with the majority of conducting domain wall materials, this is under the assumption of an equivalent work function of metallic tip. Optimisation of the tip material could allow a low resistance contact to be achieved as, from the expression for the Schottky barrier given in (4.5), in theory a sufficiently low metallic work function would result in a negligible Schottky barrier for n-type carriers. Note the barrier for p-type carriers, as expressed in (4.6), will be negligible under a sufficiently high metallic work function. Thus depending on the local carrier type, which in the case of conducting charged domain walls is dependent on whether the wall is of head-to-head or tail-to-tail orientation[15], opposite extremes of the tip work function are required.

The work functions of the various commercially available conducting AFM tips are listed in Table 4.3. Literature values for the work functions of conducting tip materials show wide variation due to differing measurement techniques used and depending on whether an actual tip or a deposited film of the material was investigated. In attempt to reduce variation, where available, values obtained from direct measurement of a tip are listed and all values were obtained using the same technique; termed kelvin probe microscopy this technique is described in detail in section 6.1.2.

From Table 4.3, conducting tips with work functions lower than Pt/Ir are available, though with the difference between the highest and lowest values less than 1 eV, as a whole conducting tips are made from high work function materials. Therefore, an acceptable contact resistance for the scanning voltage microscopy (SVM) technique is more likely to be achieved in contact of regions of p-type conductivity. Low work function metals, such as the alkaline earth metals, are chemically reactive and oxidise readily in ambient conditions making them impractical as a tip material. However, achieving low work function electrical contacts is crucial to the operation of organic

semiconductor devices[33]. To avoid the cost of device fabrication in in an inert atmosphere, a thin (1 -10 nm) layer of organic polymer is deposited onto a high work function metal or conductive metal oxide, substantially reducing the work function while maintaining electrical conductivity[34]. Using this approach the work function of a gold film was reduced from a measured 5.10 ± 0.10 eV to 3.90 ± 0.06 eV. While the robustness of such a polymer layer may not allow for contact AFM scanning, development of polymer coated conducting tips is a possible avenue for SVM measurement on n-type conductors, such as predicted at head-to-head conducting domain walls.

Material	Work Function (eV)	Reference for Value
Platinum - Iridium Alloy	5.2 - 5.4	23, 24
Platinum	5.0 - 5.5	24, 35, 36
Gold	4.95 - 5.25	24
Boron doped Diamond	4.65*	25
Titanium Nitride	4.58 - 4.78*	37

*Value obtained from a thin film of the material.

Table 4.3 Work function for different atomic force microscopy tip materials. Except where stated otherwise, all values were obtained from performing kelvin probe force microscopy with the tip on a calibration sample of known work function. All the commonly available tips use high work function materials.

4.3 Conclusions

Ultimately, scanning voltage microscopy (SVM), while a firmly established method for potential mapping of doped semiconductor devices, appears to be incompatible with measurement on bulk ferroelectrics. Ostensibly the technique appeared ideal, as in theory the measurement resolution is limited only by the noise floor of the voltmeter and the quality of the guarded connections. Calibration measurements carried out on a $BaTiO_3$ ceramic capacitor revealed a protracted time delay for the tip and sample potentials to equate, induced by the Schottky metal-semiconductor contact. The qualitative relationship between time constant, contact resistance and

sample band gap was known prior to investigation. However, without practical knowledge of the surface states and contact properties, the magnitude of the time constant could not be predicted.

Initial attempts at utilising SVM to image the Hall potential developed within silicon were promising. The lateral potential gradient due to the driven current was measured and of the expected order of magnitude. Unfortunately local variations in surface topography caused substantial variation in the recorded potentials. The overwhelming dependence on sample roughness was unexpected, as while dimensions made it difficult to obtain an optimal polish, an overall root mean square (RMS) surface roughness of ~ 50 nm was achieved. This degree of roughness is orders of magnitude below the micron sample roughness found in some conductive atomic force microscopy studies of ceramic and polymer materials[38–40]. From comparison of the band gaps of all single crystal ferroelectrics found to express enhanced conduction at domain walls, the $RMnO_3$ family alone showed promise with a narrow band gap only slightly larger than that of intrinsic silicon. In addition, as bulk conductivity in $RMnO_3$ is mediated by p-type carriers[41], the large work function of typical conducting AFM tips will promote a reduced Schottky barrier height.

Moving forward, while the approach was flawed, in carrying out the investigation a great deal was learned about the necessary sample preparation and the operation and limitations of the instrumentation. Knowledge of these provided a pragmatic boundary within which a new technique could be designed. The following chapters focus on development of a non-contact method for local mapping of the Hall potential with the aim of maintaining the spatial and measurement resolution of SVM while eliminating the issue of contact quality from the equation.

4.4 References

1. Pearson, G. L., Read, W. T. & Shockley, W. Probing the space-charge layer in a p-n junction. *Phys. Rev.* **85,** 1055–1057 (1952).

2. Kuntze, S. B. *et al.* Electrical Scanning Probe Microscopy: Investigating the Inner Workings of Electronic and Optoelectronic Devices. *Crit. Rev. Solid State Mater. Sci.* **30,** 71–124 (2005).

3. Li, S. S. & Thurber, W. R. The dopant density and temperature dependence of electron mobility and resistivity in n-type silicon. *Solid. State. Electron.* **20,** 609–616 (1977).

4. Li, S. S. The dopant density and temperature dependence of hole mobility and resistivity in boron doped silicon. *Solid. State. Electron.* **21,** 1109–1117 (1978).

5. Sze, S. M. in *Physics of Semiconductor Devices* 28–32 (John Wiley & Sons, Ltd, 2007).

6. Popovic, R. S. in *Hall Effect Devices* 204–218 (IOP Publishing, 2004).

7. Sze, S. M. in *Physics of Semiconductor Devices* 35–40 (John Wiley & Sons, Ltd, 2007).

8. Munter, P. J. A. A low-offset spinning-current hall plate. *Sensors Actuators A Phys.* **22,** 743–746 (1990).

9. Steiner, R., Maier, C., Häberli, A., Steiner, F. & Baltes, H. Offset reduction in Hall devices by continuous spinning current method. *Sensors Actuators A Phys.* **66,** 167–172 (1998).

10. Horcas, I. *et al.* WSXM: A software for scanning probe microscopy and a tool for nanotechnology. *Rev. Sci. Instrum.* **78,** 13705 (2007).

11. *Low Level Measurements Handbook: Precision DC Current, Voltage and Resistance Measurements*. (Keithley Instruments Inc., 2004).

12. *D257-14 Standard Test Methods for DC Resistance or Conductance of Insulating Materials (An American National Standard)*. (ASTM International, 2012).

13. Halliday, D., Resnick, R. & Walker, J. in *Fundamentals of Physics* 720–722 (John Wiley & Sons, Ltd, 2008).

14. Kuntze, S. B. *et al.* in *Scanning probe Microscopy: Electrical and Electromechanical Phenomena at the Nanoscale* 583–587 (Springer, 2007).

15. Eliseev, E. A., Morozovska, A. N., Svechnikov, G. S., Gopalan, V. & Shur, V. Y. Static conductivity of charged domain walls in uniaxial ferroelectric semiconductors. *Phys. Rev. B - Condens. Matter Mater. Phys.* **83,** 235313 (2011).

16. Marinello, F., Carmignato, S., Voltan, A., Savio, E. & De Chiffre, L. Error Sources in Atomic Force Microscopy for Dimensional Measurements: Taxonomy and Modeling. *J. Manuf. Sci. Eng.* **132,** 30903 (2010).

17. Sze, S. M. in *Physics of Semiconductor Devices* 134–136 (John Wiley & Sons, Ltd, 2007).

18. Bardeen, J. Surface states and rectification at a metal semi-conductor contact. *Phys. Rev.* **71,** 717–727 (1947).

19. Cowley, A. M. & Sze, S. M. Surface States and Barrier Height of Metal-Semiconductor Systems. *J. Appl. Phys.* **36,** 3212–3220 (1965).

20. Tersoff, J. Schottky barrier heights and the continuum of gap states. *Phys. Rev. Lett.* **52,** 465–468 (1984).

21. Eisberg, R. & Resnick, R. in *Quantum Physics of Atoms, Molecules, Solids, Nuclei, and Particles* 199–205 (John Wiley & Sons, Ltd, 1985).

22. Kittel, C. Theory of the structure of ferromagnetic domains in films and small particles. *Phys. Rev.* **70,** 965–971 (1946).

23. Lewis, G. & Catlow, C. Defect studies of doped and undoped barium titanate using computer simulation techniques. *J. Phys. Chem. Solids* **47,** 89–97 (1986).

24. Böhmisch, M. *et al.* Atomic Force Microscope Based Kelvin Probe Measurements: Application to an Electrochemical Reaction. *J. Phys. Chem. B* **101,** 10162–10165 (1997).

25. Bogdanowicz, R. *et al.* Fabrication and characterization of boron-doped nanocrystalline diamond-coated MEMS probes. *Appl. Phys. A Mater. Sci. Process.* **122,** 1–9 (2016).

26. Wagner, J. & del Alamo, J. A. Band-gap narrowing in heavily doped silicon: A comparison of optical and electrical data. *J. Appl. Phys.* **63,** 425–429 (1988).

27. Dhar, A. & Mansingh, A. Optical properties of reduced lithium niobate single crystals. *J. Appl. Phys.* **68,** 5804–5809 (1990).

28. Meier, D. *et al.* Anisotropic conductance at improper ferroelectric domain walls. *Nat. Mater.* **11,** 284–288 (2012).

29. Kalashnikova, A. M. & Pisarev, R. V. Electronic structure of hexagonal rare-earth manganites $RMnO_3$. *Jetp Lett.* **78,** 143–147 (2003).

30. Wu, W., Horibe, Y., Lee, N., Cheong, S. W. & Guest, J. R. Conduction of topologically protected charged ferroelectric domain walls. *Phys. Rev. Lett.* **108,** 77203 (2012).

31. Cherian, J. G. *et al.* Optical spectroscopy and band gap analysis of hybrid improper ferroelectric $Ca_3Ti_2O_7$. *Appl. Phys. Lett.* **108,** (2016).

32. Lifshits, V. G., Oura, K., Saranin, A. A. & Zotov, A. V. in *Adsorbed Layers on Surfaces. Part 1: Adsorption on Surfaces and Surface Diffusion of Adsorbates* 259–419 (2001).

33. Forrest, S., Burrows, P. & Thompson, M. The dawn of organic electronics. *IEEE Spectr.* **37,** 29–34 (2000).

34. Zhou, Y. *et al.* A Universal Method to Produce Low-Work Function Electrodes for Organic Electronics. *Science.* **336,** 327–332 (2012).

35. Peres, L., Bou, A., Cornille, C., Barakel, D. & Torchio, P. Work function measurement of multilayer electrodes using Kelvin probe force microscopy. *J. Phys. D. Appl. Phys.* **50,** (2017).

36. Kaushik, V., Varandani, D., Das, P. & Mehta, B. R. On the nature of AFM tip metal-MoS2contact; Effect of single layer character and tip force. *Appl. Phys. Lett.* **111,** 141601 (2017).

37. Enriquez-Flores, C. I. *et al.* Relation between work function, microstructural and mechanical properties of TiN-films. *Surf. Eng.* **844,** 1–7 (2017).

38. Alexeev, A., Loos, J. & Koetse, M. M. Nanoscale electrical characterization of semiconducting polymer blends by conductive atomic force microscopy (C-AFM). *Ultramicroscopy* **106,** 191–199 (2006).

39. Xi-Dong, D., Gang, F., Xiao-Min, X. & Jin-Xiu, Z. Characterization Method of Polycrystalline Materials Using Conductive Atomic Force Microscopy. *Chinese Phys. Lett.* **25,** 3597–3600 (2008).

40. Silva, M. S. *et al.* Conductive atomic force microscopy characterization of PTCR-BaTiO3 laser-sintered ceramics. *J. Eur. Ceram. Soc.* **36,** 1385–1389 (2016).

41. Subba Rao, G. V., Wanklyn, B. M. & Rao, C. N. R. Electrical transport in rare earth ortho-chromites, -manganites and -ferrites. *J. Phys. Chem. Solids* **32,** 345–358 (1971).

5 Intermittent Contact Hall Effect Measurements

Scanning voltage microscopy (SVM) proved to be unsuitable for the majority of ferroelectric systems, due to contact resistance at the tip-sample interface. This chapter discusses a novel technique utilising intermittent contact atomic force microscopy (AFM), wherein the local Hall potential is imaged by its influence on the topographic trace. Measurements were carried out on a sample of single crystal $YbMnO_3$, the domain structure of which is first introduced, so that the results may be readily understood. Calibration experiments were carried out to establish the absolute magnitude of the observed Hall voltage and from this the local carrier type, density and mobility were determined

Finally, following the conclusion in section 4 that SVM measurements on $YbMnO_3$ may be possible, direct contact measurement of the Hall potential was attempted.

5.1 Improper Ferroelectricity in the Hexagonal Manganites

In the high temperature phase the hexagonal manganites, $RMnO_3$ where R represents one of the following ions (Dy, Ho, Er, Tm, Yb, Lu, Y, Sc)[1], is paraelectric with the space group $P6_3/mmc$. The high symmetry structure, depicted in Figure 5.1a, consists of layers of corner sharing MnO_5 trigonal bipyramids (Mn^{3+} ions centred within O^{2-} polyhedra) intercalated with sheets of R^{3+} ions. Notably, the ionic layers are completely constrained within planes parallel to the ab plane, with the apical oxygen ions (O_T), the equatorial oxygen ions (O_E), the Mn^{3+} ions and the R^{3+} ions aligned at fixed positions along the c-axis[2].

Moving below T_C, the trigonal bipyramids tilt such that the O_E ion layer buckles with ions displaced oppositely along the c axis while Mn^{3+} and O_T ion layers each remain constrained within the ab planes. This, in turn, leads to a corresponding buckling of the R^{3+} ion layer such that the $R - O_E$ bond lengths remain unchanged across the phase transition[2–5]. Strictly, the symmetry reduction occurs via the freezing-in of a K_3 zone-boundary phonon mode reducing the symmetry to

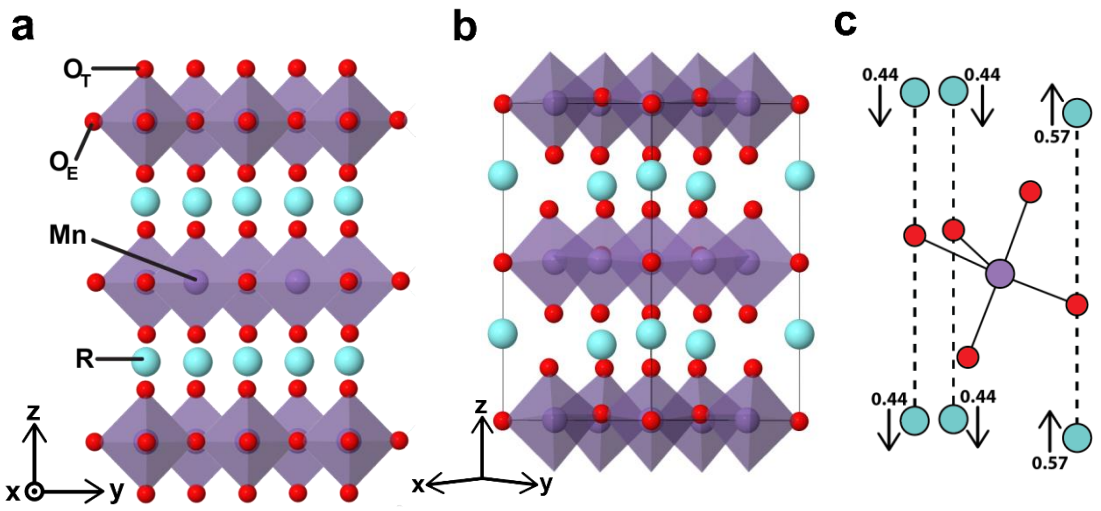

Figure 5.1 a High temperature structure of $RMnO_3$ in the paraelectric phase with layers of MnO_5 trigonal bipyramids intercalated with sheets of the R ion. **b** Unit cell for the ferroelectric phase. Moving below the transition temperature the symmetry is reduced with regards to structural order parameter, trimerisation. The oxygen polyhedral tilt such that equatorial ions, O_E, are displaced along the c-axis. The R ions buckle with the same '2 up, 1 down' configuration. **c** A net dipole moment is generated by the additional displacement of the R ions along the c-axis, such that the previously the O_E ions are no longer centred within the R - O_E - R bond, displaced according to the 2 up, 1 down tilt pattern. **a** and **b** modelled using data from [6] while **c** was adapted from [2].

$P6_3cm$ [7, 8]. This low symmetry phase is referred to as a trimerisation phase, partly due to the tripling of the unit cell volume. However, while the K_3 mode accounts for the complete reduction in symmetry, it alone does not result in a spontaneous polarisation[7,9].

The unit cell for the ferroelectric phase is depicted in Figure 5.1b. As shown, within a single unit cell there are a total of six R – O_E – R bonds: two centred within the unit cell and one along each corner. The tilting of the trigonal bipyramids results in the equal displacement of the two central R – O_E – R bonds in one direction along the c-axis and four corner R – O_E – R bonds in the opposite direction. Whereas the two central R – O_E – R bonds lie completely within the unit cell, each of the corner bonds is shared between 4 adjacent unit cells and thus each contributes only one quarter of its ionic volume to a single unit cell. Therefore, in terms of charge redistribution this equates to the displacement of two R – O_E – R bonds in opposite direction to one

complete R – O_E – R bond. Superficially, this "2 up, 1 down" displacement pattern would appear to lead to displacement of centres of positive and negative charge. However, measurements of the ionic displacement across T_C, both from experimental x-ray diffraction studies and density functional theory (DFT) calculations, determined that the displacement length of the central R – O_E – R bonds is half that of the corner bonds: resulting in zero net dipole moment[2–5].

The dipole moment comes about from the coupling of the K_3 mode with the low frequency, Γ_2 zone-centre mode[2,7,8]. Structurally this is realised by the additional displacement of the R^{3+} ions relative to O_E such that the O_E ions are no longer centred within the R – O_E – R bond. Crucially, this additional displacement is also of opposite direction for central and corner bonds but of equivalent magnitude.

The mechanism is conveyed for a single MnO_3 polyhedron in Figure 5.1c. Each polyhedron has three O_E ions (though not all lie within the same unit cell) and each of these is the midpoint of a R – O_E – R bond. Of these three bonds, two lie wholly within a unit cell and one is a 'corner bond' shared between four unit cells. Moving from the high temperature to the low temperature phase, the total R – O_E – R bond length is unchanged (for $YbMnO_3$ ~ 5.68 Å). However, in the high temperature phase, each component R – O_E bonds are of equal length (~ 2.84 Å) while in the low temperature phase each pair of R^{3+} ions are displaced such that the O_E ions of the 'whole' and 'corner' R – O_E – R bond are off centre by opposite directions (~ 0.57 Å and ~ 0.44 Å respectively for $YbMnO_3$) [2,4,6]. Summed across the unit cell, this results in a small net displacement of the centres of positive and negative charge, forming a spontaneous polarisation, P_s. A notable consequence of this somewhat complex interaction is that the local polarisation can be easily determined via high-angle annular dark-field imaging (HAADF) from the "2 up, 1 down" pattern of the large atomic number R^{3+} ions[10,11].

Magnitude of P_s is approximately equal across the $RMnO_3$ family[12] (~ 5.6 μCcm^{-2}), whereas the transition temperature (T_C) has been observed to increase with decreasing size of the R^{3+} ion[8] (ranging from 1373K to 1723K for $HoMnO_3$ to $LuMnO_3$)[13]. Note the values are approximate, as the determination of exact transition points are difficult due to the high temperatures involved.

Accounting for the full reduction in symmetry, the K_3 mode trimerisation is the primary order parameter for the transition, where a useful interpretation of the two components are the amplitude, Q, and relative angle, Φ, of the tilting bipyramids[7,14]. The secondary order parameter is given by the equilibrium amplitude of Γ_2, which is proportional to P_s. Artyukhin *et al.* [14], expanding on the work of Fennie *et al.*[7], used these parameters in DFT calculations to construct a quantitative description of the phase transition from LGD theory. Trimerisation may occur at one of three R^{3+} sites present in the high symmetry unit cell, leading to three possible trimerisation states in the low symmetry phase (denoted as α, β and γ). The three minima of the K_3 mode, coupled with the two possible polarisation states of the Γ_2 ($+$ and $-$) leads to six possible degenerate energetic minima for the free energy ($\alpha^{\pm}$, $\beta^{\pm}$ and $\gamma^{\pm}$). This somewhat convoluted relationship is concisely conveyed by the intuitive 'mexican-hat' free-energy plot calculated by Artyukhin and coworkers, presented in Figure 5.2a.

Each minimum in Figure 5.2a corresponds to a distinct domain, as energetic degeneracy means that all six domains form in the low symmetry phase, and neighbouring minima represent domains of opposite polarisation. The white dashed line outlines the lowest energy path from one domain to another and therefore represents the lowest-energy domain wall formation. Any other paths, such as between domains of same polarisation direction, must traverse a large energy gradient and are thus unstable. This restriction on adjacent domains leads to the formation of the characteristic 6-fold vertex domain pattern observed in the manganites. A vertical piezoresponse force microscopy (PFM) scan of $YbMnO_3$ single crystal, is presented in Figure 5.2b with an accompanying schematic, displayed in Figure 5.2c, to convey the relative structural and ferroelectric domain states. Note that while the domain walls must originate and terminate at a vertex, there is no requirement for all six walls to terminate at the same vertex.

Crucially, the trimerisation introduces a translational asymmetry such that the different trimerisation states are antiphase domains and thus the domain walls dividing them are antiphase boundaries[15–17]. This is significant as it means two adjacent domains cannot be merged under application of field (electric or strain) due

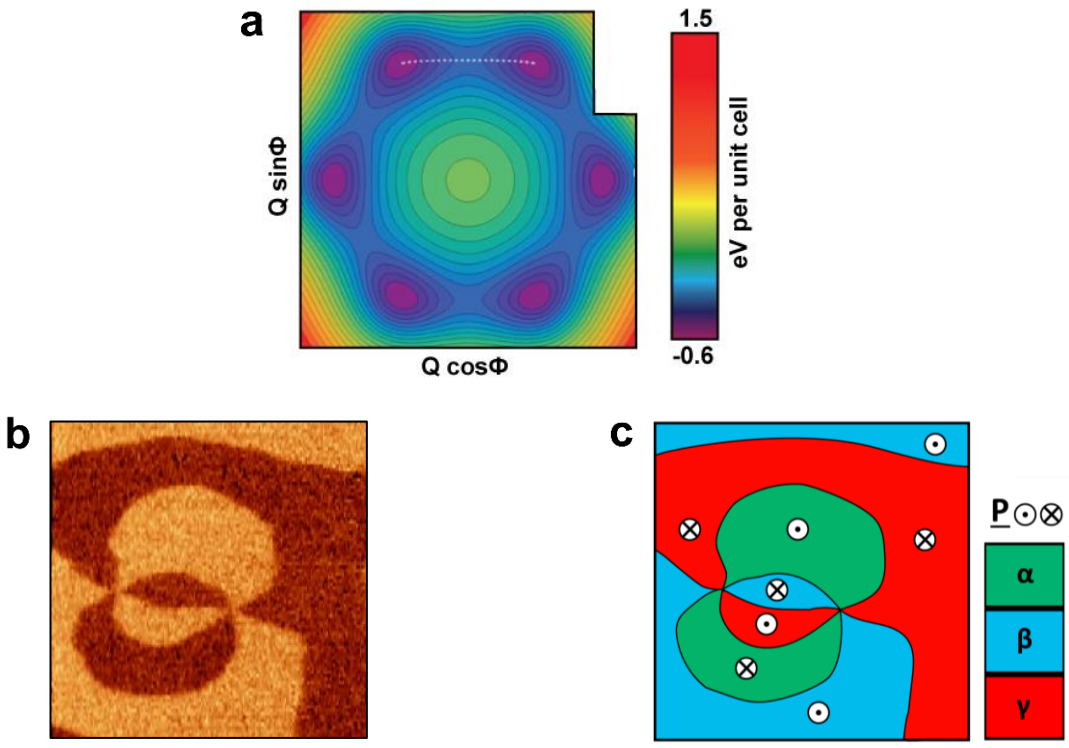

Figure 5.2 a Mexican-hat shaped free energy plot for the improper ferroelectric phase transition in $RMnO_3$. Minima represent the 6 degenerate domain states and the dashed line the favourable domain wall formation. **b** Vertical PFM phase map of $YbMnO_3$ single crystal conveying the typical domain structure with characteristic 6-fold vertices. **c** Structural schematic of b. Taking a circular path around each vertex it is seen that both the structural and corresponding polarization states alternate, so that no two equivalent structural or ferroelectric domains share a wall. Figure **a** adapted from [14].

to the relative lattice displacement. This accounts for robustness of the 6-fold vertex structures, remaining stationary and unreduced under large applied fields[16,18,19]. However, vertices have been observed to move under application of an in-plane shear strain[20].

In literature the 6-fold vertex structure is often erroneously referred to as a vortex, with the domain pattern shown in Figure 5.2 termed a vortex-antivortex pair[10,13,14,17,18,20–32]. The justification for the terminology is based upon representing the trimerisation parameter as a vector, where the magnitude and direction are given by Q and Φ respectively, as depicted in Figure 5.3a. Taking an anticlockwise path about the vertex and noting the orientation of the trimerisation at each point along the path, the trimerisation is found to complete one continuous anticlockwise rotation.

This is known as having a winding number of +1 and is a characteristic property of vortices[33]; an example of a vortex in a vector field is presented in Figure 5.3b for comparison.

However, while classification by winding number allows different topological patterns to be meaningfully grouped together, it cannot be used in isolation to define a vortex[34–36]. In addition to an integer winding number, for a vector field pattern to be a vortex it must have a non-zero curl. Indeed, in fluid dynamics the vorticity of a flow is found by representing the flow at as a vector field and calculating the curl about a point. From inspection of Figure 5.3a, it is clear the vector field represented by the trimerisation has zero curl, more closely matching the field pattern of a point source rather than a vortex.

Though distinction between vertex and vortex may appear somewhat pedantic, importantly it means that the 6-fold vertex domain patterns are not formed in vortex-antivortex pairs and thus need not exhibit any of the associated properties. Additionally, on a more simplistic note, the equivocal use of the term vortex when referencing a PFM phase map of the domain structure[13,22,32,37,38], an image which depicts solely the orientation of polarisation, can easily be misinterpreted as a declaration of a ferroelectric vortex. Indeed some authors have already mistakenly referred to the domain pattern as explicitly a ferroelectric or multiferroic vortex[10,25,26,32].

The vertices are not constrained to a particular crystallographic plane or axis[14], with investigations confirming that the vertex density is homogenous throughout the bulk[22]. This leads to a complex domain structure as domain walls proliferate the bulk in all directions interlinking a network of vertices. Superimposing the network of domain walls on a uniaxial polarisation guarantees native charged domain walls, head-to-head and tail-to-tail orientations, as walls intersect the polar axis at all angles.

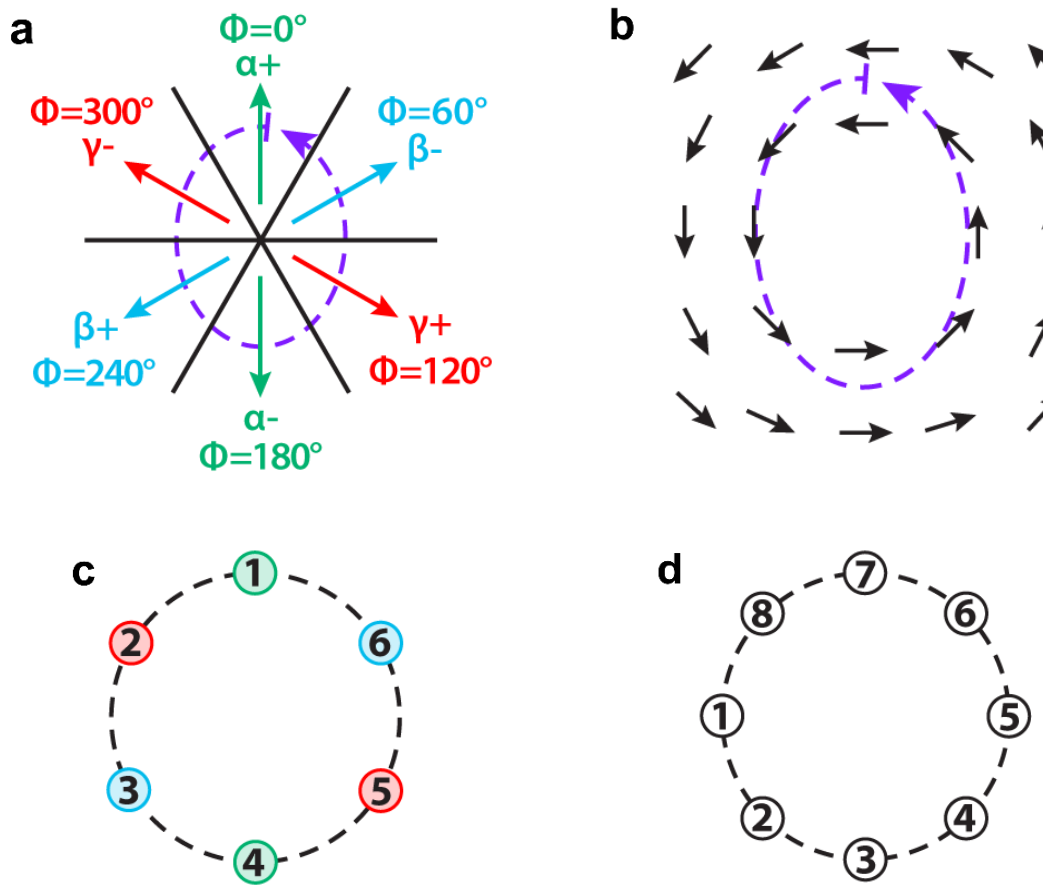

Figure 5.3 a Schematic of a 6-fold vertex structure with black lines representing domain boundaries. Thee coloured arrows represent the orientation of the trimerisation, Φ, within each domain type. **b** Schematic of a vortex pattern within a vector field. The dashed purple lines in **a** and **b** represent an arbitrary anticlockwise path taken through each vector field. **c** Following the anticlockwise path, the orientation of the vector field is plotted in order, verifying the trimerisation makes one full anticlockwise rotation for one anticlockwise loop about the vertex. *I.e.* the vector field has a winding number of +1. **d** Applying the same check to the vector field in **b,** confirming a winding number of +1.

5.2 Domain Wall Conductivity in $YbMnO_3$

The abundance of native charged domain walls, evidenced to exhibit distinct conductivity relative to the bulk[16,39–41], made the hexagonal manganites an attractive test material for developing a Hall effect imaging technique. Through collaboration with D. Prabhakaran at the University of Oxford, single crystal samples of stoichiometric $YbMnO_3$ were obtained. Charged domain walls within members of the $RMnO_3$ family are expected to display equivalent conductive behaviour as reported for in $ErMnO_3$: increased and decreased conductivity at tail-to-tail and head-to-head

walls respectively with activation of increased conductance at head-to-head walls under sufficient bias[39,41]. Nonetheless no direct observation of domain wall conductance had been reported for the specific case of $YbMnO_3$.

A $YbMnO_3$ sample was fractured to gain access to the undamaged interior faces of the as-grown crystal. The resultant crystal fragments had irregular surface topography due to a lack of cleavage planes, however, within small (sub 100 μm^2) regions the topography was smooth with root mean square (RMS) surface roughness of ~ 1 nm. This approach to sample preparation does not allow for controlled choice of crystallographic orientation and the fractured fragments of $YbMnO_3$ crystal had to be imaged repeatedly to find an appropriately aligned region. Additionally, when a suitably flat region has been found, the angle of approach for the cantilever has to be considered when mounting for AFM as the cantilever body may impact a higher region of topography during the engage stage. Regardless, whenever possible, native surfaces where preferred for characterisation as in general they were found to exhibit greater performance. Both in PFM with increased piezoresponse and less noisy phase mapping and for conduction measurements with more localised domain wall currents in comparison to polished samples. This was likely due to a damage layer introduced during chemo-mechanical polishing of the samples; polishing procedure was carried out with reducing roughness of diamond paper and finished with alkali silica slurry. Though it should be noted this may be a reflection of the efficacy of the specific polishing technique and not indicative of polishing $RMnO_3$ in general.

The unpolished surface of a $YbMnO_3$ sample was mapped repeatedly via PFM and a significant in-plane polarisation component confirmed, phase map presented in Figure 5.4a. A fixed DC bias was applied to a silver dag bottom electrode and local conductivity measurements were carried out in the same region using conductive atomic force microscopy (c-AFM). Focusing on variations in conductance at the vertex region, c-AFM map presented Figure 5.4, comparison with the polar map reveals increased and decreased conductance at tail-to-tail and head-to-head walls respectively. This conduction behaviour is in agreement with the previous observations by Meier *et al.* in $ErMnO_3$ [39]. In Figure 5.4c the locally measured conductance is plotted against the angle ϕ, wherein ϕ represents the angle between the normal to the wall and the polarisation axis, as sketched in Figure 5.4c, such that

ϕ = 0° and 180° correspond to tail-to-tail and head-to-head walls respectively. The extremes of conductance correspond to maximal divergence in the polarisation with measured conductance showing the same $G \propto 2P\cos\phi$ dependence as was shown in $ErMnO_3$. In contrast to recent reports[41] for $ErMnO_3$ the activation of a conductive state at head-to-head walls was not observed; with insulating head-to-head behaviour measured for c-AFM imaging biases of up to 12 V.

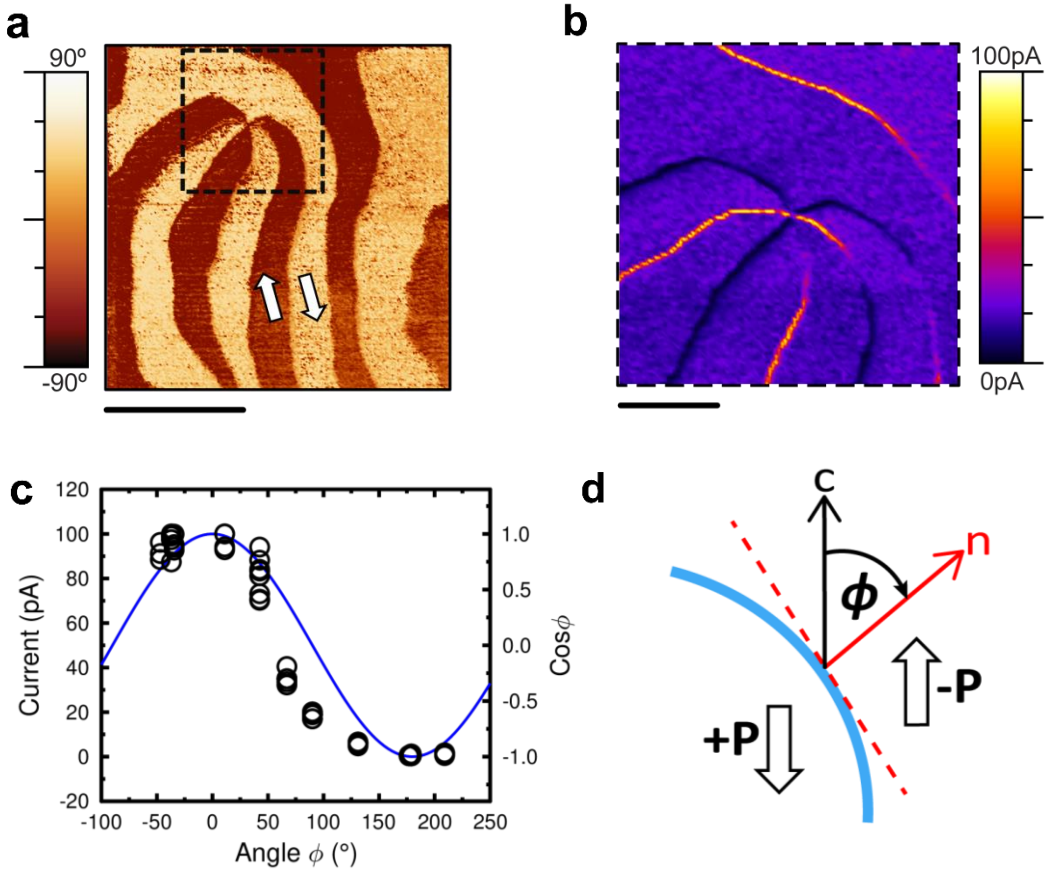

Figure 5.4 a Lateral PFM phase map, cantilever axis horizontal with respect to the image. Polarisation direction given by overlayed arrows. **b** c-AFM map, taken at 2.3 V, of the subset area showing increased and decreased conductance at oppositely charged domain walls. **c** Current measured along the domain walls in **b**, plotted as a function of wall angle, ϕ, verifying that conductance $G \propto 2P\cos\phi$. Cos ϕ function plotted in blue as a guide. **d** Definition of the domain wall angle ϕ. Scale bars for **a** and **b** are 2 μm and 1 μm. **d** adapted from [39]. Measurements performed on Vecco system.

5.3 Measurement of Hall potential within $YbMnO_3$

A schematic of the experimental set-up is shown in Figure 5.5a and the theory behind its operation is conveyed by Figure 5.5b and c. In terms of instrumentation, the experimental design is more simplistic than that used for contact Hall voltage measurements via SVM. A $YbMnO_3$ crystal was chemo-mechanically polished, through a combination of diamond paper and alkali silica slurry, to obtain a large smooth surface with maximal in-plane polarisation. Rectangular gold electrodes were sputtered on the crystal surface and silver dag tracks painted to macroscopic wires, facilitating connection of the electrodes to a Kiethley 6221 DC source. An electromagnet was positioned such that the applied magnetic field direction ran orthogonal to the expected lateral electric field, as shown in Figure 5.5a. As a constant current was driven across the inter-electrode gap, the charge carriers travelling through both the bulk and the conducting regions of domain wall were deflected vertically. The unidirectional displacement of carriers, and consequent charge accumulation, led to a variation in the local potential on the surface of the crystal.

An amplitude modulated intermittent-contact AFM topography scan is initiated within the inter-electrode region such that AFM tip rasters across the surface, oscillating at a fixed frequency. In this mode any change in the force-gradient experienced by the tip, typically due to variations in tip-sample separation, are recorded by the system as a local change in sample topography. The Pt/Ir AFM tip acts as an earthed electrode in a parallel plate structure wherein the tip experiences an attractive force due to the local potential difference. The Hall potential developed at the conducting domain walls differs from that within the bulk domains, due to differences in conductivity and dimensions, leading to a differing electrostatic force acting on the tip and the system records this as a local topographic contrast. The sense and magnitude of the topographic signal then correspond to the sign and magnitude of the Hall voltage within the domain wall.

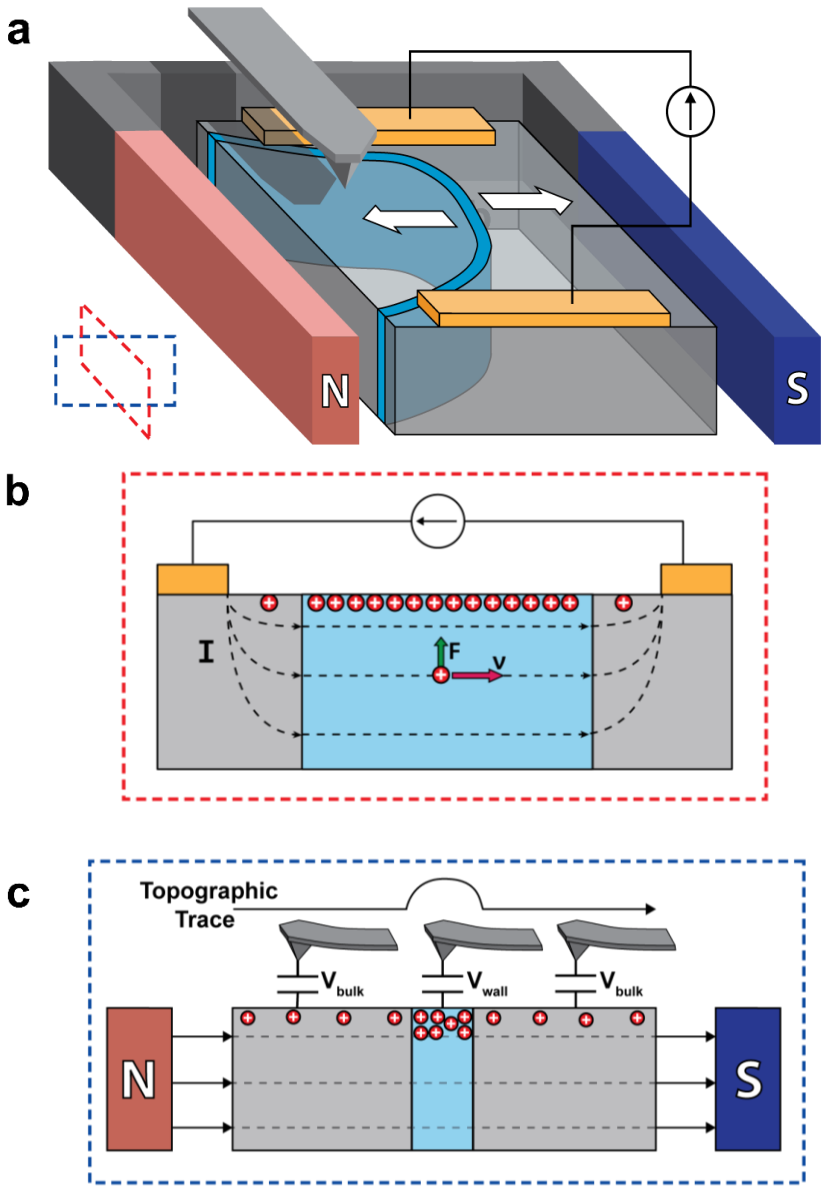

Figure 5.5 a Schematic of sample geometry. Gold surface electrodes sputtered on $YbMnO_3$ top surface, trapping a tail-to-tail domain wall, shown in blue. A constant current was driven through the surface electrodes and an in-plane magnetic field was applied to the sample, perpendicular to the driven current. Inset: red and blue dashed boxes indicate the relative orientations of the cross-sections shown in **b** & **c**. **b** Depiction of the Hall effect on a positive test charge, where symbols are as follows: carrier drift velocity **v**, magnetic Lorentz force **F**, current along the wall **I**. **c** The AFM tip is rastered across the sample surface in tapping mode. It acts as an earthed electrode in a capacitor structure, sensing spatial changes in force-gradients associated with variations in the potential difference between tip and sample surface (V_{bulk} within domains and V_{wall} at the domain wall). The Hall potential developed causes V_{wall} to be distinct from V_{bulk}, allowing domain wall contrast to appear in the topographic image.

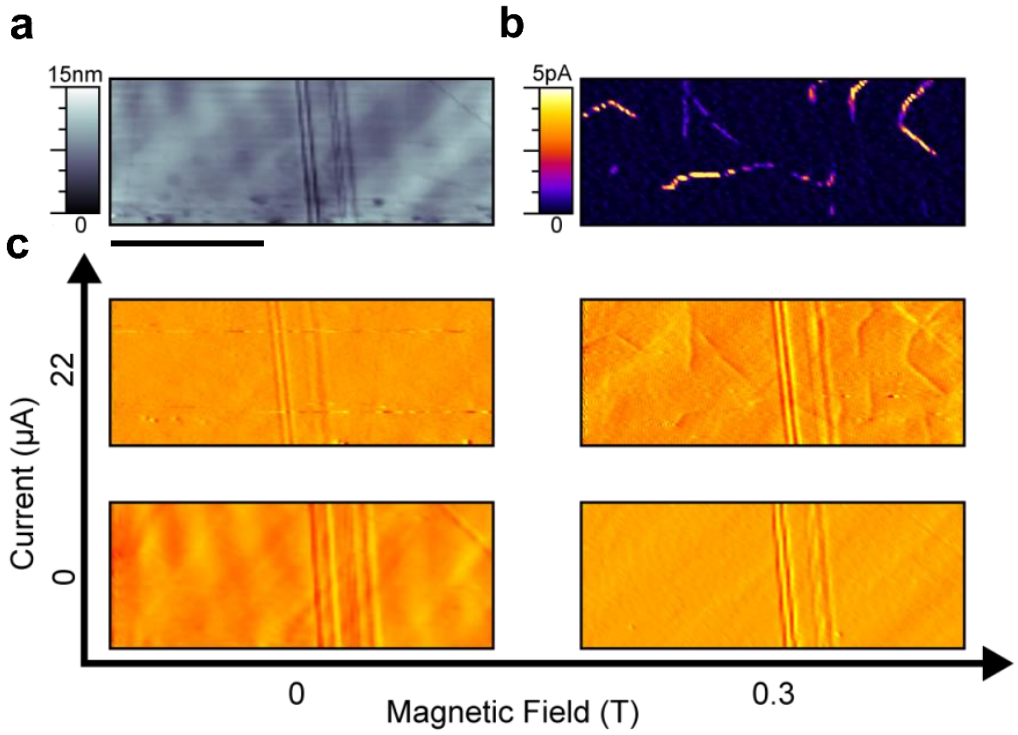

Figure 5.6 a Contact mode topography map and **b** associated current map taken within the interelectrode gap, showing a distinct pattern of conducting domain walls without any obvious topographic contrast. **c** Derivative of tapping mode AFM topography images taken under different conditions of magnetic field and source-drain current. Domain wall signals are only observed when both lateral current and a transverse magnetic field are applied, suggesting that the additional domain wall contrast is Lorentz-force mediated. Comparison with current map, **b**, confirms strong spatial correspondence. Scale bar in **a** is 5 μm. Data in **a** and **b** recorded on Veeco system.

Representative results from the technique are shown in Figure 5.5. An interelectrode region was mapped via c-AFM wherein the DC bias was applied to a lateral electrode. The resultant current map, shown Figure 5.5b, revealed multiple conducting segments of domain wall, corresponding to tail-to-tail orientated segments. Additionally the field geometry confirmed the existence of a percolating current pathway across the interelectrode gap. Contact AFM of the same region recorded simultaenoulsy with the c-AFM measurements (presented in Figure 5.5a) revealed distinctive scratches, which while prominent in topography do not exhibit conductive properties distinct from the bulk. This pattern of scratches later served as a useful topographic marker for the region and as verification that throughout various field geometries and optimisation of scan parameters, the tapping mode was continuing to operate correctly. Crucially, the scan verifies that there are no topographic features corresponding to the domain walls.

Tapping mode was engaged and a series of topographic maps recorded for a combination of electric and magnetic field states. As shown in Figure 5.5c, when either the laterally driven current (up to 22 μA) or orthogonal magnetic field (up to 0.3 T) were applied in absence of the other, the tapping mode topography map discerns only the vertical scratches with zero domain wall trace. However, when the current was driven in combination with an orthogonal magnetic field, additional topographic features were observed. Comparison with the c-AFM map of the same region reveals a direct spatial correspondence, positioning and shape, between the additional topographic contrast and the conducting segments of domain wall. While further sources of contrast cannot be entirely excluded, the requirement for simultaneous magnetic and electric fields is strongly indicative of a Lorentz force mediated effect. Hence the additional contrast is attributed solely to the establishment of a Hall potential within the domain wall.

5.4 Calibration of the Hall potential

Calibration experiments were carried out in order determine the sense and magnitude of the Hall potential that corresponded to the topographic trace observed along the conducting domain walls. A rectangular gold pad was sputtered on the surface of a polished $SrTiO_3$ single crystal and connected to a Kiethley 237 voltage source unit. A reference voltage, scaled between 0-2V, was connected to a data channel on the microscope controller, allowing the externally applied bias to be recorded within the Nanoscope software. A tapping mode topography map of an uncoated region of the crystal surface, immediately adjacent to the gold pad, was recorded while a constant DC bias was applied to the pad. This served to emulate the background potential within the middle of the interelectrode gap.

For the data presented in Figure 5.6c a potential difference between source and drain electrodes of ~100 V was required to drive the 22 μA lateral current. Quickfield software was used to generate a finite element model of the potential profile (shown Figure 5.7a) verifying Hall measurements recorded in the middle of

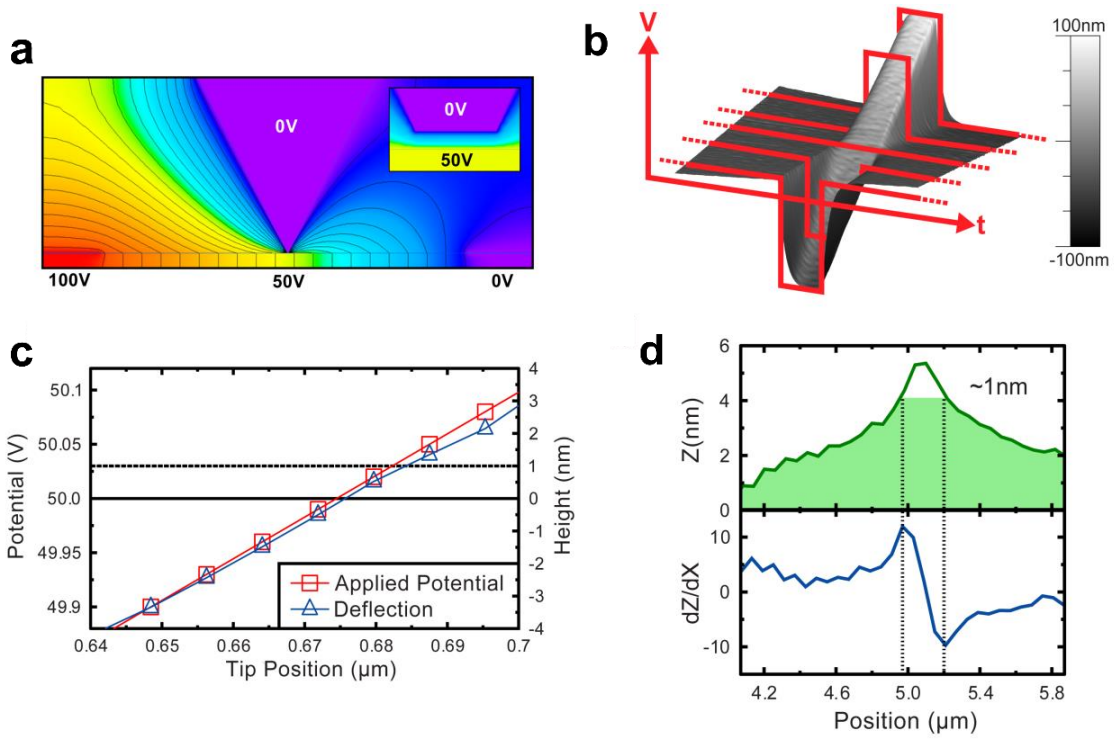

Figure 5.7 a Quickfield modelling of the tip and $YbMnO_3$ surface, with ~100 V potential difference between source and drain electrodes, verified that measurements of the Hall voltage were set against a DC potential background of around 50 V. **b** To calibrate the tip deflection associated with the Hall voltage measurements at domain walls, the topography of a gold-coated $SrTiO_3$ single crystal was monitored as negative and positive voltage pulses (schematically represented as red lines) were supplied to the crystal surface (schematically superimposed onto a background DC potential of 50 V). A smooth correlation between the applied voltage pulse and the topographic deflection was found. **c** A section of the measured topography associated with the ramp in **b** and the voltages responsible (voltage pulses plus 50 V DC background). **d** The topography signal, *Z*, across a conducting domain wall in which a Hall voltage has developed and the associated derivative, $^{dZ}/_{dX}$, show that the above background topographic peak is ~1 nm in height. This height corresponds to a voltage of about 30 mV from the calibration graph in **c** (dashed line).

the interelectrode gap were carried out against a background potential of around 50 V.

In order to simulate the additional Hall potential experienced at a conducting domain wall, a series of linearly increasing voltage pulses were superposed onto

the 50 V DC background and the associated change in the topographic trace observed. The intervals between pulses were timed such that they occurred at the same spatial point in each sequential AFM scan-line, producing the topographic ramp shown in Figure 5.7b.

Plotting topographic trace along the ramp and the total applied potential on the same spatial axis, see Figure 5.7c, there appeared to be a linear relationship between the magnitude of the voltage pulse and the magnitude of the resultant deflection. As such, an observed dip in topography at a conducting domain wall would indicate a negative Hall voltage, whereas an increase in the topographic height would indicate a positive Hall voltage. Taking a line profile across the topographic trace observed at $YbMnO_3$ domain walls, upon driving a lateral current under orthogonal magnetic field, revealed the local Hall potential resulted in an additional deflection of ~ 1 nm above the background, as shown Figure 5.7d.

Given the cross product dependence of the resultant magnetic Lorentz force on the relative directions of the applied electric and magnetic fields (discussed in section 3.1) for a fixed field geometry opposite surface potential will be observed for opposite carrier sign. A schematic of relative field directions associated with the data in Figure 5.6c is presented in Figure 5.8.

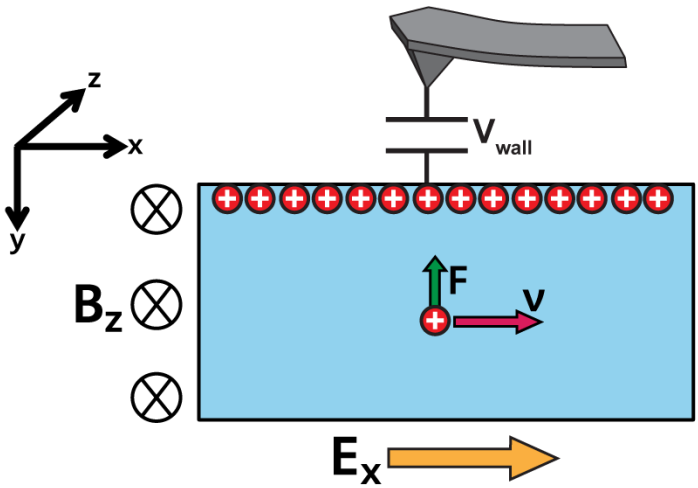

Figure 5.8 Schematic of the experimental geometry, illustrating the direction of the Hall potential for the tail-to-tail walls within $YbMnO_3$. The direction of the Lorentz force, **F**, is determined by considering the direction of the magnetic field, $\mathbf{B}_{\boldsymbol{Z}}$, and the direction of the carrier drift velocity, **v**, for given carrier type in the lateral electric field, $\mathbf{E}_{\boldsymbol{X}}$.

The magnetic Lorentz force, **F**, is given by:

$$\mathbf{F} = \pm q[\boldsymbol{\nu} \times \mathbf{B}] \tag{5.1}$$

Where $\boldsymbol{\nu}$ is the drift velocity, **B** the magnetic field strength and q is the charge of an individual carrier. Expanding:

$$\mathbf{F} = \pm q\left(\begin{pmatrix}\boldsymbol{\nu}_x\\ \boldsymbol{\nu}_y\\ \boldsymbol{\nu}_z\end{pmatrix} \times \begin{pmatrix}\mathbf{B}_x\\ \mathbf{B}_y\\ \mathbf{B}_z\end{pmatrix}\right) \tag{5.2}$$

Referring to the right hand coordinate system defined by the axis subset in Figure 5.8, the relevant vector components can be set to 0, 1 or -1. Given the direction of the conventional current, the direction of carrier drift is known (dependent on the sign of the carriers). As the resultant direction of the Lorentz force is the same regardless of carrier sign, either case can be considered. Choosing a test case of positive carriers:

$$\mathbf{F} = +q\left(\begin{pmatrix}1\\ 0\\ 0\end{pmatrix} \times \begin{pmatrix}0\\ 0\\ 1\end{pmatrix}\right) \tag{5.3}$$

Solving for the direction of the Lorentz force:

$$\mathbf{F} = +q\begin{pmatrix}0\\ -1\\ 0\end{pmatrix} \tag{5.4}$$

The magnetic Lorentz force deflects the charge carriers within the domain wall upwards, hence for a positive Hall potential to have developed at the top surface of the $YbMnO_3$ crystal the conduction with the domain wall must be mediated by p-type carriers.

The sign of the Hall voltage discerns only carrier type and does not allow for discrimination between whether conduction is mediated by holes or positive ions. However it has been shown[42,43], via temperature dependant measurements

originally carried out in 1970 and repeated in 2016 as part of a more detailed study on electronic structure, that bulk conduction in the hexagonal manganites is mediated by holes with calculations suggesting a small polaron nature is energetically favoured. Both studies conclude the ionic contribution to conduction is minor and n-type in nature, proposing cation vacancies or interstitial oxygen anions as the charge carriers. Therefore the increased conductance observed at tail-to-tail walls is most likely mediated by the large abundance of mobile holes which are freely available to aggregate at the wall and facilitate screening of the local divergence in polarisation. This is in agreement with suggestions made by Meier *et al.* for conductance at tail-to-tail walls in $ErMnO_3$ [39].

5.4.1 Quadratic Topographic Behaviour

It is important to note that when the equivalent calibration measurements are carried out in the absence of a constant background potential, an approximately quadratic relationship is observed between applied voltage and topographic response (shown Figure 5.9a). Plotting the topographic deflection against applied potential, Figure 5.9b clearly conveys that, regardless of the sign of potential, a local increase in topography is recorded such that a positive and negative Hall potential would be indistinguishable. The significance of the background potential and the apparent change from a linear to a quadratic relationship, may be rationalised by comparing the tip-sample interaction to the force between two charged parallel plates.

This comparison is a substantial oversimplification of the situation, disregarding a number of factors, such as additional forces experienced due to tip-sample distance and the oscillatory motion of the tip, and is by no means an attempt to explicitly model the interaction. However, this simple example is useful to consider as it provides an understanding of the fundamental mechanism underlying the topographic response.

The force between two parallel plates, F, is related to their potential difference, V, by[44]:

$$F \propto V^2 \tag{5.5}$$

Therefore, the force experienced by the cantilever will be given by:

$$F \propto \left(V_{tip} - V_{sample}\right)^2 \tag{5.6}$$

Where V_{tip} and V_{sample} represent the potential at the AFM tip and the sample respectively. Note the order of both potentials has been assigned arbitrarily as the resulted is squared.

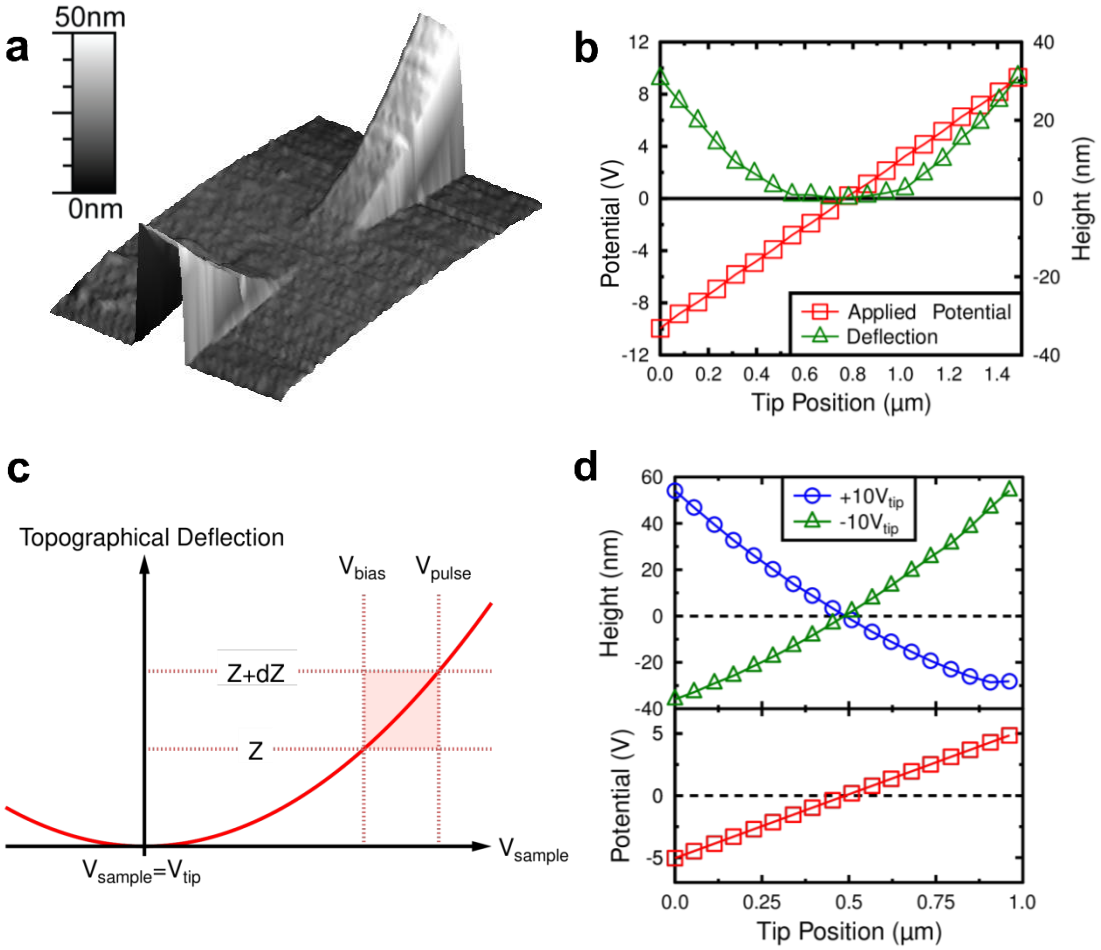

Figure 5.9 a Tapping mode topography map showing recorded deflection as linearly increasing voltage pulses, -10 V to 10 V, were applied in absence of a DC background. **b** Plotting the topographic deflection and applied potential on the same spatial axis conveys a quadratic topographic response to the linear potential. **c** Schematic of relationship between measured topographic deflection and applied potential, wherein V_{sample} represents the sample potential, V_{tip} the tip potential, V_{bias} the DC background, Z the measured topographic height , V_{pulse} the increase in potential on application of a voltage pulse and dZ the corresponding increase in measured height.

At a conducting domain wall the term V_{sample} will be the sum of the locally generated Hall potential and the background potential applied by the lateral current source, represented in the calibration experiment by the voltage pulse (V_{pulse}) and the application of a fixed DC bias (V_{bias}).

$$F \propto \left(V_{tip} - (V_{pulse} + V_{bias})\right)^2 \tag{5.7}$$

As the AFM tip was shorted to earth, $V_{tip} = 0$, therefore:

$$F \propto \left(V_{pulse} + V_{bias}\right)^2 \tag{5.8}$$

Significantly the force experienced by the tip due to the sample potential is always attractive. As depicted in Figure 2.7, increasing force corresponds to an increase in height as recorded in the topographic trace. Assuming a direct relationship between the force on the tip and the resultant deflection, the behaviour of the system can be understood and is depicted by the qualitative plot in Figure 5.9c.

From (5.6), the response is quadratic about a minimum centred on $V_{tip} = V_{sample}$, so that any increase in the magnitude of V_{sample} corresponds to an increase in the topography. This is the case when V_{pulse} is varied with a zero background. Application of a fixed DC offset, V_{bias}, moves the response up a branch of the curve, away from the minimum. Now an increase or decrease in V_{sample} is dependent on the sign of V_{pulse} and causes an increase or decrease in the attractive force and a corresponding increase or decrease in the topographic deflection. As shown by the shaded box in Figure 5.9c, sufficiently far from the minimum, or for a sufficiently small range in potential, movement within the subsection of the parabolic curve is approximately linear.

A quadratic relationship between topographic deformation and an applied potential is one of the defining characteristics of electrostriction and the $SrTiO_3$ substrate used in the calibration experiments, chosen due to availability, is an electrostrictive material.

To exclude electrostrictive effects and verify the capacitive origin of the topographic contrast, the influence of tip potential was demonstrated.

Calibration measurements were repeated with identical voltage profiles applied to the substrate (V_{bias} = 0, V_{pulse} ranging from – 5 V to 5 V) and differing bias applied to the tip (V_{tip}= 10 V and -10 V). Plotting topographic deflection from both scans on the same axis, as shown in Figure 5.9d, it is clear that in both cases the response is approximately linear, with the slope inverting with the sign of the tip potential. This behaviour is in agreement with (5.7) as for V_{tip}= 10 V and -10 V, the magnitude of the sum decreases and increases respectively as V_{sample} increases. Equivalently, Figure 5.9d can be viewed as the subsection of two parabolas with minima centred on 10 V and -10 V, where $V_{sample} = V_{tip}$.

5.5 Calculation of Carrier Density and Mobility

Using the calibration experiment as a basis, from Figure 5.7c, a 1 nm increase in the topography indicates a positive Hall potential of ~ 30 mV. Having obtained an approximate value for the Hall potential, some basic calculations can be made as to the carrier density and mobility along the conducting domain wall. Taking the ideal Hall expression, (3.16), and rearranging in terms of the carrier density (p):

$$p = \frac{\mathbf{IB}}{V_{\mathrm{H}} q d} \tag{5.9}$$

Where **I** is the lateral current driven along the domain wall, **B** is the strength of the orthogonal magnetic field, V_{H} is the Hall potential, q is the charge of a single carrier and d is the width the conducting domain wall. The majority of the terms are easily determined; V_{H} ~ 30 mV, the applied magnetic field strength was measured with a commercial Hall sensor to confirm **B** ~ 0.3 T, and assuming the carriers are singly charged, q is the electron charge. The remaining terms though are not precisely known and require some approximation.

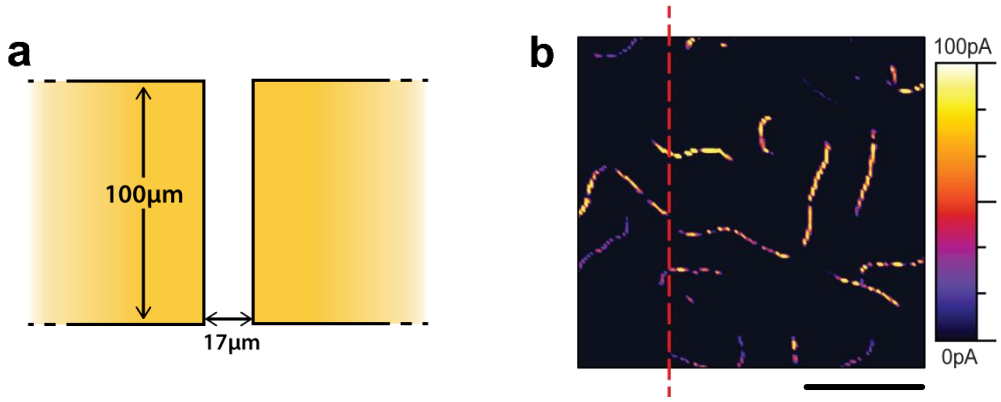

Figure 5.10 a Schematic displaying the dimensions of the interelectrode gap. **b** A 15 µm^2 c-AFM map, recorded with 2 V applied to one of the electrodes, conveying the density of conducting domain walls within the interelectrode region. Taking a vertical cross-section, red dashed line, 3 – 4 conducting walls are intersected across the 15 µm length. Scale bar, 5 µm.

The term **I** represents the current within a single domain wall however the 22 µA lateral current was driven across the entirety of the interelectrode gap; the dimensions of which are presented by the schematic in Figure 5.10a. A 15 x 15 µm c-AFM scan, taken within the interelectrode region, is also shown. The 6-fold vertex domain pattern results in curved segments of conducting domain wall, of various length, scattered throughout interelectrode gap. Due to the complexity of the domain wall network, the current within an individual domain wall cannot be precisely determined. Accepting this, we limit the calculation to a broad order of magnitude approximation. Depending on the position along the horizontal axis, taking a vertical cross section, represented by the dashed line overlaying the scan, intersects three or four conducting domain walls across the 15 µm length.

Scaling up across the full 100 µm length of the gold electrodes, gives a value of ~ 20-30 domain walls straddling the interelectrode gap. While this is an extremely general figure, making the safe assumption of no extreme variations in the domain density, the number of domain walls acting in parallel is on the order of tens, not hundreds. Thus, it is assumed the 22 µA is shared among ~ 10 domain walls and for the carrier density a value of **I** ~ 2.2 µA per domain wall is used.

To obtain an estimate for the width of a conducting domain wall, d, the distinction must be made between structural domain wall width, as defined by the length across which the order parameter reorients, and the width of the region of increased conductivity. In the case of proper ferroelectrics the distinction is somewhat pedantic as the Ising structure mitigates the energetic cost of greater divergence in polarisation at the wall by gradually reducing the polarisation over a greater number of unit cells[45–47], i.*e.* the more highly charged the wall, the greater the structural wall width. In the hexagonal manganites, however, the wall structure is dictated by the orientation of the trimerisation on each side of the wall, independent of polarisation.

The domain wall structure of the hexagonal manganites has been imaged with atomic resolution in a series of scanning transmission electron microscopy (STEM) studies using high angle annular dark field imaging (HAADF), revealing three distinct wall types resulting from the translational asymmetry of the adjacent trimerisation domains[10,11,15]. HAADF imaging of each wall type within $YMnO_3$ is presented in Figure 5.11a, 5.11b, and 5.11c. Viewed down the [010] direction, the characteristic "2 up, 1 down" pattern of the Y^{3+} ions, depicted previously in section 5.1, is clearly visible and may be used to define both the unit cell boundaries and the orientation of the polarisation vector. Figures 5.11a and 5.11b convey neutral domain walls aligned with the polarisation axis and, using disruption of the “2 up, 1 down” pattern to determine where the unit cell periodicity breaks down, they convey structural wall widths of one third and four thirds of a unit cell width respectively.

For a charged domain wall inclined at an angle to the polarisation axis, as imaged in Figure 5.11c, considering a discrete unit cell model results in a stepped wall formed by a combination of neutral and maximally charged wall segments. In Figure 5.11c, neutral wall segments depict the third wall type with a width of two thirds of a unit cell, while the maximally charged segments show the top of an upward polarised unit cell meeting the base of a downward polarised unit cell without any intermediate gap, for an effective structural wall width of zero. However, the straightforward method of defining the domain wall by unit cell boundaries is a poor fit to charged walls as the spatial separation of deviations from bulk symmetry is not fixed at a

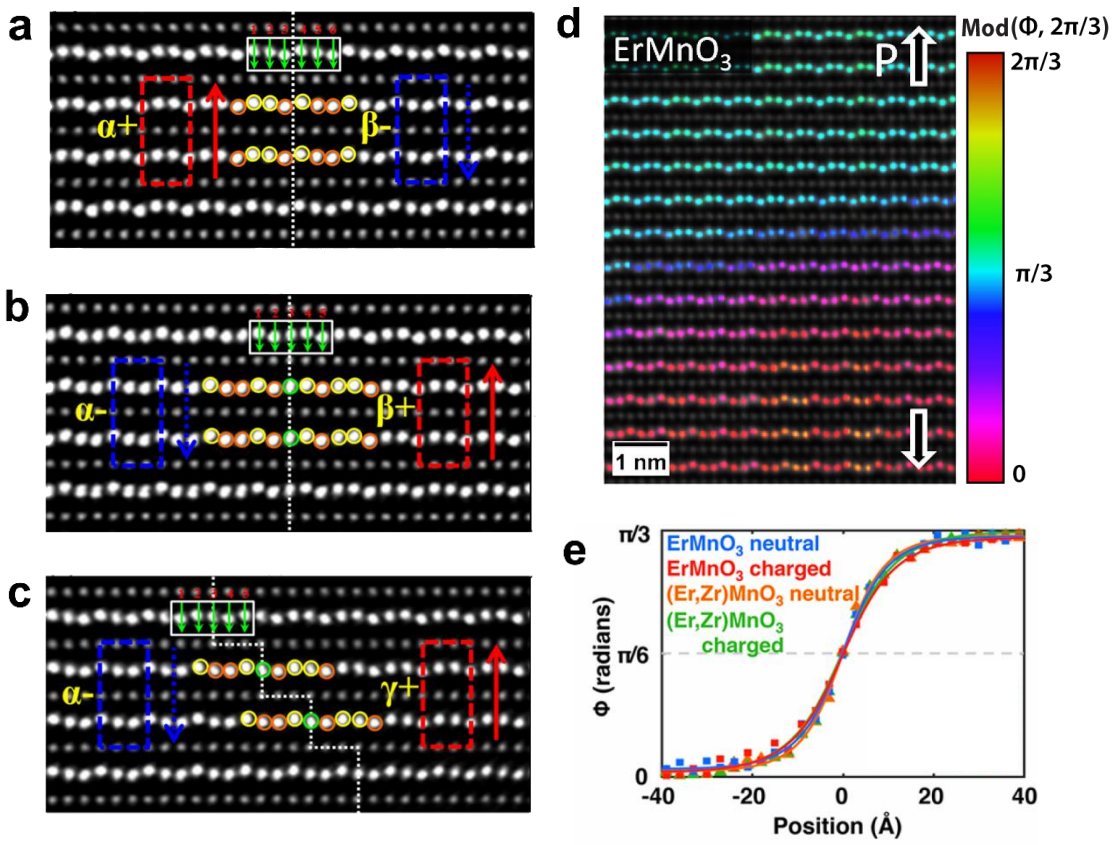

Figure 5.11 a b and c HAADF imaging of $YMnO_3$ viewed down [010] revealing the three distinct domain wall structural types. The white dotted line marks the centre of the domain wall. The large bright circles are the Y^{3+} ions and the smaller dull circles the Mn^{3+} ions. Upward and downward displaced Y^{3+} ions are marked by yellow and orange rings respectively, to emphasise the characteristic "2 up, 1 down" pattern. The green rings denote ions found to be are centred on the non-polar undisplaced position. **d** HAADF imaging of $ErMnO_3$ viewed down $[1\bar{1}0]$ with the Er^{3+} ions coloured to represent the calculated value of trimerisation phase, Φ. **e** Change in Φ with position for different wall types. Data points correspond to empirical values and the solid lines to predictions made via free energy calculations. Figures **a, b** and **c** reprinted from [11] and **d** and **e** reprinted from [48].

multiple of the unit cell dimensions. This is shown in Figure 5.11c as the demarked step height is less than a unit cell height.

This issue of a discontinuous model is avoided by Holtz *et al.*[48] in their HAADF imaging and analysis of the domain wall structure in $ErMnO_3$. Here the authors define a relation between the local displacement of Er^{3+} ions from their idealised position in the high symmetry phase and the local trimerisation amplitude (Q) and angle (Φ). Thus by measuring the displacement of each Er^{3+} ion relative to its two

neighbouring ions and calculating the corresponding trimerisation state, the orientation of the order parameter was assigned with atomic resolution; resulting in an effectively continuous model of the domain wall structure. An example of a charged domain wall is presented in Figure 5.11d, where each Er^{3+} ion is coloured to represent the calculated value of Φ, conveying an approximate $\pi/3$ rotation between the upward and downward polarised domains. Calculating the trimerisation across a range of maximally charged and neutral domain walls, with an allowed 5° variance in wall angle for each, and plotting as a function of position revealed the structural width of charged and neutral walls to be within angstroms of each other. Presented in Figure 5.11e, the data points correspond to empirical values and the solid lines to free energy calculations, the continuous model results in a structural wall width of ~ 4nm.

The conclusion that can be made from various HAADF studies on $RMnO_3$ is that the structural domain wall width is unaltered by the local divergence in polarisation and, while the absolute value depends on how the data is interpreted, it is at most 4 nm and possibly as narrow as to have zero effective width. Given the minute dimensions, it is unreasonable to assume the region of increased conductivity lies within the structural domain wall width.

Following theory, the increased conductance at charged domain walls is due to the local aggregation of screening charges, hence the width of the conducting region through which the domain wall current **I** was driven is determined by the length from the wall for which local free carrier density is increased relative to the bulk. Assuming charged domain walls in the hexagonal manganites are screened by a classical gas of free carriers, given the small value of spontaneous polarisation, the conductive region can be approximated by twice the Debye screening length[49]. The Debye screening length for the domain wall is difficult to calculate directly as the model outlined by Gureev *et al.*[49] is obtained assuming a proper ferroelectric system with typical Ising wall behaviour. Nonetheless, Schaab *et al.*[50] modelled the Debye screening length for a maximally charged tail-to-tail wall in $Er_{1-x}Ca_xMnO_3$ as a function of Ca^{2+} dopant concentration. For an undoped system Schaab *et al.* report

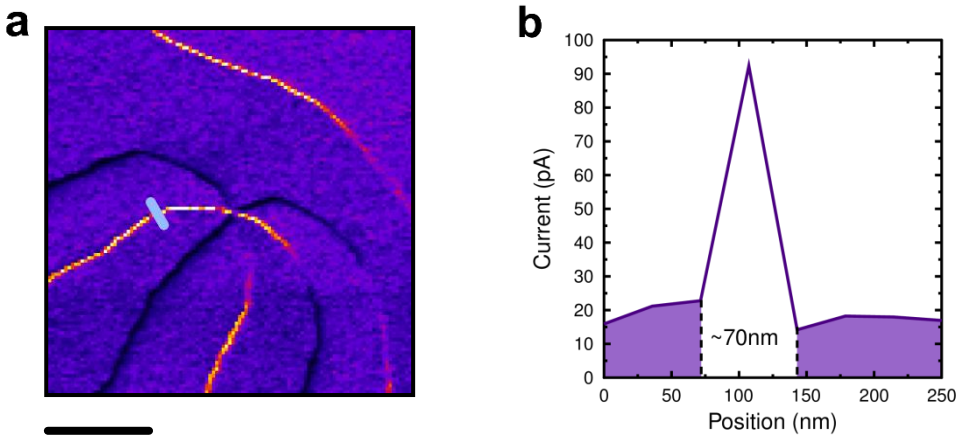

Figure 5.12 a High resolution c-AFM map of a 6-fold vertex in $YbMnO_3$, taken at 2.3V DC shown line profile position. Scale bar 1 μm. **b** The current profile of the wall marked in **a**, showing the region of increased conductance at a domain wall has a maximum width of 71 nm. For comparison the c-AFM map was recorded with a 50 nm radius tip.

a wall width of ~70 nm though the expressions used to calculate the Debye screening length is not presented

An empirical value for the conducting wall width in $YbMnO_3$ can be obtained from c-AFM measurements. Taking line profiles across a conducting domain wall in the c-AFM map presented in Figure 5.3 returned a maximum width of 71 nm as shown in Figures 5.12a and 5.12b. At just under twice the resolution limit, one pixel is $31nm^2$, this value represents an extreme upper limit. In addition, when the earthed tip is in contact with a region of bulk conductivity sufficiently close to the conductive domain wall, the reduced series resistance will result in current leakage from the wall through the bulk to the tip[50]. This leads to broadening of the measured current profile in comparison to the true width of the conductive region.

To summarise, the length scales for each method of defining the domain wall width are listed in Table 5.1. The structural width of a charged domain wall is wholly independent of the width of the region of increased conductivity, which following theory is determined by the screening length of accumulated charge carriers. However, developing a model for the screening length of charged domain walls within the hexagonal manganites, akin to the work of Gureev *et al.*[49] for proper ferroelectrics, is a significant undertaking and any quantitative calculation

would likely require approximation of further unknown variables. The current trace recorded under c-AFM is useful as it provides an empirical measurement of conducting width. The 71 nm current trace measured by c-AFM is certain to be an exaggeration of the conducting channel, due to a combination of current leakage near the wall and convolution by the 50 nm radius tip, and thus provides an upper limit. Knowing the conducting region to be less than the trace width and considering the 70 nm width calculated for $ErMnO_{3,}$ the available information suggests the conducting region is more likely to be on the order of 10s of nanometres rather than unit nanometres. Hence, in the same vein as the estimate for domain wall current, we use a value of d ~ 10nm.

	Measurement Method	**Width (nm)**
Structural Width	HAADF	≤ 4
Twice the Debye Screening Length	Theoretical Model	~ 70
Width of Conductive Trace	c-AFM	< 71

Table 5.1 The different approaches by which the width of a conducting domain wall within the hexagonal manganites may be defined. The width of the conducting region is independent of the structural width and is defined by the Debye length for free carriers screening the divergence in polarisation at the charged domain wall. However, modelling the screening length is non trivial and thus the conductive trace observed under c-AFM provides a useful upper limit.

Inserting all the values into the expression for carrier density, (5.9), a local carrier density on the order of p ~ 10^{16} cm^{-3} is obtained for the maximally charged domain wall, as shown in (5.10).

$$p = \frac{(2.2\text{x}10^{-6})(0.3)}{(30\text{x}10^{-3})(1.60\text{x}10^{-19})(10\text{x}10^{-9})} \qquad (5.10)$$

$$p = 1.37\ \text{x}10^{16}\ \text{cm}^{-3}$$

To put this value into perspective, the charge density required to screen the divergence in polarisation may calculated using expression (1.34). The bound charge density is dependent on the magnitude of polarisation, ~ 5.6 μCcm^{-2}, and the distance across which the polarisation reverses. An approximate value for the latter can be obtained from the HAADF imaging by Holtz *et. al*[48], presented in Figure 5.13, which has been coloured to depict the measured displacement of Er^{3+} ions across a charged wall. Without the quantitative data the reorientation distance was approximated from the colour overlay. Counting pixels and scaling returns values ranging from 2.3 nm to 2.78nm and an approximate distance range of 2 to 3 nm was chosen. Hence, the charge density required to screen the divergence in polarisation is on the order of 10^{20} cm^{-3}, four orders of magnitude higher than the carrier density associated with the Hall voltage. Hence, if the tail-to-tail walls within $YbMnO_3$ are fully screened then only one in every ten thousand screening charges contributes towards conduction.

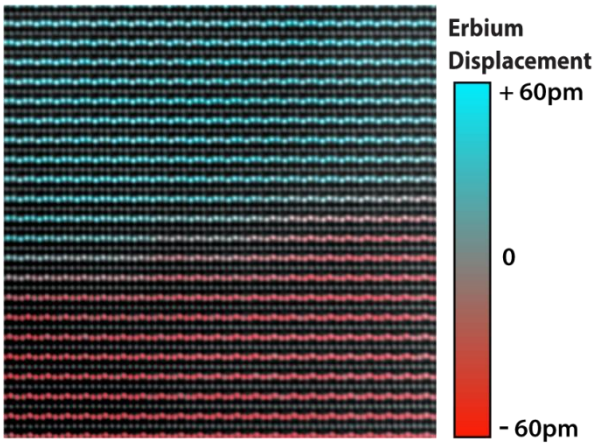

Figure 5.13 HAADF imaging of a tail-to-tail domain wall in $ErMnO_3$, where overlaid colour represents the measured net displacement of the Er^{3+} ions from their position in the non-polar phase. Imaged area is 12.2 nm^2 and thus the polarisation reorientation region is between 2 to 3 nm in width. Figure reprinted from [48].

Given the disparity between values, the accuracy of the estimate for local carrier density is considered. The measurement error in the values for magnetic field and Hall voltage can be disregarded in comparison to the breadth of possible values introduced by the rudimentary estimations of domain wall current, **I**, and conducting width, d. The value of **I** ~ 2.2 μA was obtained from an estimated 20 to 30 parallel

conducting domain walls within the interelectrode gap, which was approximated to ~ 10 walls and divided into the total 22 μA of driven current. A lower limit on **I** can be taken from the upper estimate of 30 parallel walls, and an maximum for **I** obtained from assuming the 4 parallel conducting domain walls imaged under c-AFM, presented Figure 5.10b, are the only conducting walls within the entirety of the interelectrode gap. These upper and lower bounds correspond to a domain wall current of 4.4 μA and 0.7 μA respectively.

The dominant source of imprecision in the calculation of local carrier density is the width of the region of increased conductivity, d, strictly known only to be less than the 71nm width of the c-AFM trace. To convey the influence of the rudimentary estimation of **I** and d; Figure 5.14 plots the calculated carrier density as a function of the conducting width, down to $d = 1$ Å, for the full range of domain wall current. It's clear from inspection that even leveraging the substantial uncertainty in *d*, the measured Hall voltage still reveals a disparity between the local free carrier density and the required screening density. Taking the maximum current value, which corresponds to the implausible assumption of four parallel conducting domain walls within 15 μm and zero for the remaining 85 μm length, and assuming an atomically sharp screening length, $d = 1$ Å, the calculated carrier density, $p \sim 10^{18}$ cm^{-3}, is still two orders of magnitude below the density required for screening. Restricting to a more reasonable regime, for **I** ~ 2.2 μA, the original calculated estimate of $p \sim 10^{16}$ cm^{-3} corresponds to the approximate interval $3\ nm < d < 30\ nm$.

A direct consequence of the disparity in carrier densities is that, taking $p \sim 10^{16}$ cm^{-3}, if the tail-to-tail walls within $YbMnO_3$ are fully screened then only one in every ten thousand screening charges contributes towards conduction. Furthermore, since the laterally driven current is not entirely restricted to the conducting domain walls, the obtained values for carrier density are likely to be a significant overestimate. As an improper ferroelectric, the charged domain walls may be stabilised with incomplete screening. However at 0.01% of the required density, a contribution to screening from immobile charges which do not contribution to conductivity seems likely.

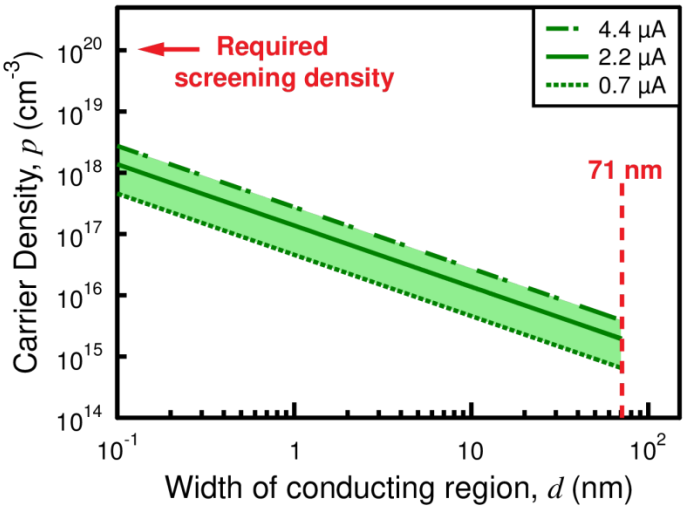

Figure 5.14 Plot of the resulting value of local carrier density as a function of the approximated value for the width of the region of increased conductance at the wall. The carrier density calculated is plotted for both the estimated value of domain wall current (2.2 μA) in and the maximum and minimum current values that could be justified (4.4 μA and 0.7 μA respectively) to portray full uncertainty of the estimate. The significant result that even at implausibly sharp wall widths, the measured Hall voltage still reveals a two order of magnitude deficit between the local carrier density and the required screening density.

This result is in agreement with the greatly increased domain wall conductance observed by Schaab *et al.*[50] upon acceptor (Ca^{2+}) doping of $ErMnO_3$. Assuming the charged domain walls in the native undoped system were fully screened by mobile carriers, there would be no justification for the observed enhancement with doping. Additionally the large scale of the enhancement indicates a substantial percentage deficit in the mobile carrier density at the wall as a comparatively small increase in the available mobile carriers, a 1% dopant, resulted in a ten-fold increase in conductance.

The ideal Hall equation can also be expressed in terms of carrier mobility, μ, as follows:

$$\mu = \frac{V_{\mathrm{H}}}{\mathbf{E}w\mathbf{B}} \tag{5.11}$$

Where **E** is the applied electric field driving the lateral current and w, in this geometry, represents the depth of the conducting domain wall from the top surface.

A potential difference of 100 V was required to drive the 22 μA current, as shown in Figure 5.6a, which with an interelectrode separation of 17 μm corresponds to an electric field strength of ~ 5.9×10^7 Vm^{-1}.

To obtain an estimate for the domain wall depth, we refer to the Landua-Ginzburg-Devonshire theoretical models[14] for domain formation in $RMnO_3$. Assuming the entirety of the crystal bulk cooled from the high temperature phase at an equivalent rate[13,27], the domain density should be homogenous throughout the bulk with the only energetic preference for elongated domain walls aligned parallel to the polar axis. This assumption of through-depth homogeneity is supported by work of Lin *et al.* wherein a $LuMnO_3$ crystal was consecutively polished and imaged via PFM to investigate bulk domain structure[22]. Additionally, in-house experience with repeated sample polishing has observed equivalent domain density through bulk. Therefore, the domain wall depth w is taken to be the same as the conducting domain wall length on the top surface, *i.e.* on the order of a few microns, taken to be ~ 3 μm.

Substituting the values into (5.11), a carrier mobility of ~ 60 $cm^2V^{-1}s^{-1}$ is obtained for the charge carriers mediating conduction along the wall. Compared to the estimate for domain wall density, the estimated mobility isn't as imprecise, with the principal source of error from the approximation of wall depth, w. Taking maximum and minimum conducting wall depths of 10 μm and 1 μm, returns a possible carrier mobility range of $17 < \mu < 170$ $cm^2V^{-1}s^{-1}$. For comparison the estimated carrier mobility is about an order of magnitude lower than the ~ 500 $cm^2V^{-1}s^{-1}$ typical of p-type silicon with a similar carrier density[51]. However, it is several orders of magnitude higher than mobilities typical of small polarons in oxides[52,53] and at the high end of that typical of large polarons[54]. It is therefore possible that transport along the walls does not involve significant lattice coupling, but categorical statements will require further measurements.

5.6 Sample Degradation

In order to generate the ~1 nm topographical deflection at maximally charged domain walls, a constant 22 μA current had to be driven between the electrodes, requiring the current source to operate near its maximum compliance voltage. To

obtain the necessary resolution, such that the domain wall contrast could be clearly distinguished, high resolution scans, typically 256 samples by 256 lines, had to be carried out with signals collected over long scan times (scan rate ~0.1Hz) to minimise noise. The protracted time scales, coupled with the unavoidable repeat imaging for optimisation of the scan parameters, necessitated the continuous application of the lateral current, and the large electric field, for hours at a time in order to capture an individual scan. With extended operation, the current source was no longer able to maintain the 22 μA with the apparent interelectrode resistance increasing the longer the lateral electric field was applied.

This was initially assumed to be due to some degree of Joule heating effect, occurring either at the sample or along the electrical pathway to the current source. However, the conductance did not recover. Suspecting degradation of the gold electrodes, the crystal surface was polished, as no suitable gold etchant had been determined at the time, and an identical electrode geometry sputtered. Despite an equivalent domain density in the interelectrode region, the conductance did not recover to previous levels and, with continued attempts at Hall effect measurements, the resistance increased further.

The reduction in sample conductance inhibited the measurement of the Hall effect at a full range of electric and magnetic field directions. An intermittent contact mode topography scan conveying Hall potential contrast is shown in Figure 5.15a wherein both the magnetic field and current directions have been reversed with respect to Figure 5.7. From comparison with a c-AFM map of the same region, presented in Figure 5.15b, it is clear that the topographic signal corresponds to the conducting domain walls. With a current magnitude of only 4 μA, the domain wall signal is on the same scale as the background noise such that taking the derivative (as with Figure 5.6c) does not help distinguish the wall from the background. Instead the colour scale of the image shown has been manipulated to magnify the contrast. It was mainly due to the distinct pattern of the c-AFM map that the domain wall contrast was noticed in the original topography at all.

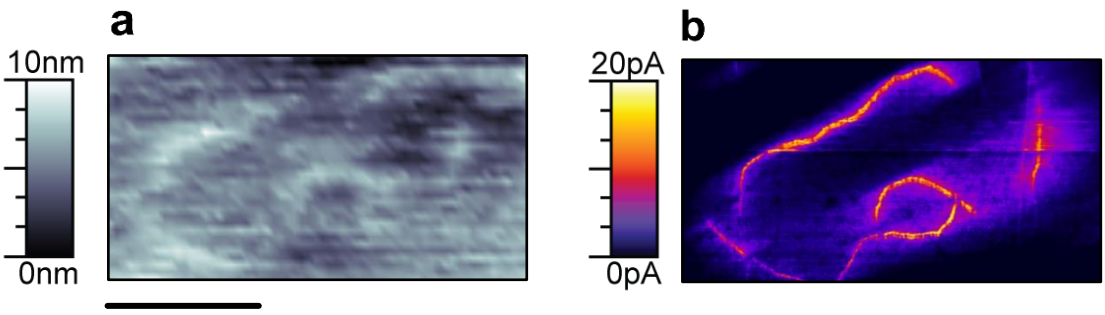

Figure 5.15 a Tapping mode topography map, recorded with 4 μA current and 0.3 T applied in the opposite directions as to Figure 5.7, showing faint domain wall contrast. **b** A current map, recorded with 2 V DC, of the same region showing conducting domain wall structure, matching the signal in **a**. Scale bar, 1.5 μm.

5.7 Contact SVM measurements on $YbMnO_3$

With the maximum current and corresponding Hall potential falling below the measurement resolution of the intermittent contact method, contact measurements were attempted using the scanning voltage microscopy methodology outlined in section 4. In theory the measurement resolution of technique was limited only by the guarding of the connections and the noise floor of the voltmeter, on the order of microvolts.

A distinctive conducting domain wall was identified within the interelectrode gap, via c-AFM, and a 5 x 5 μm^2 SVM map was centred on its position. Contact topography and SVM maps were recorded continuously with a 0.3 T magnetic field and the current source operating at maximum compliance. Initially data was collected at a scan rate of 0.1 Hz, which was sequentially reduced to the minimum of 0.01 Hz, but the SVM map remained featureless throughout. The contact topography, however, varied, showing increased signs of topographic damage with each passing scan. Initial and final topography maps are shown in Figures 5.16a and 5.16b respectively. Removing the lateral bias and magnetic field, traditional contact scans were taken at a large scale to assess the change in topography. These revealed a positive step deformation, 8 μm in height, that at ~ 5 μm^2 corresponded to where the SVM measurements had occurred, shown Figure 5.16c. Contact and tapping mode scans were repeated a week later to verify this was a true surface deformation and not an electrostatic effect.

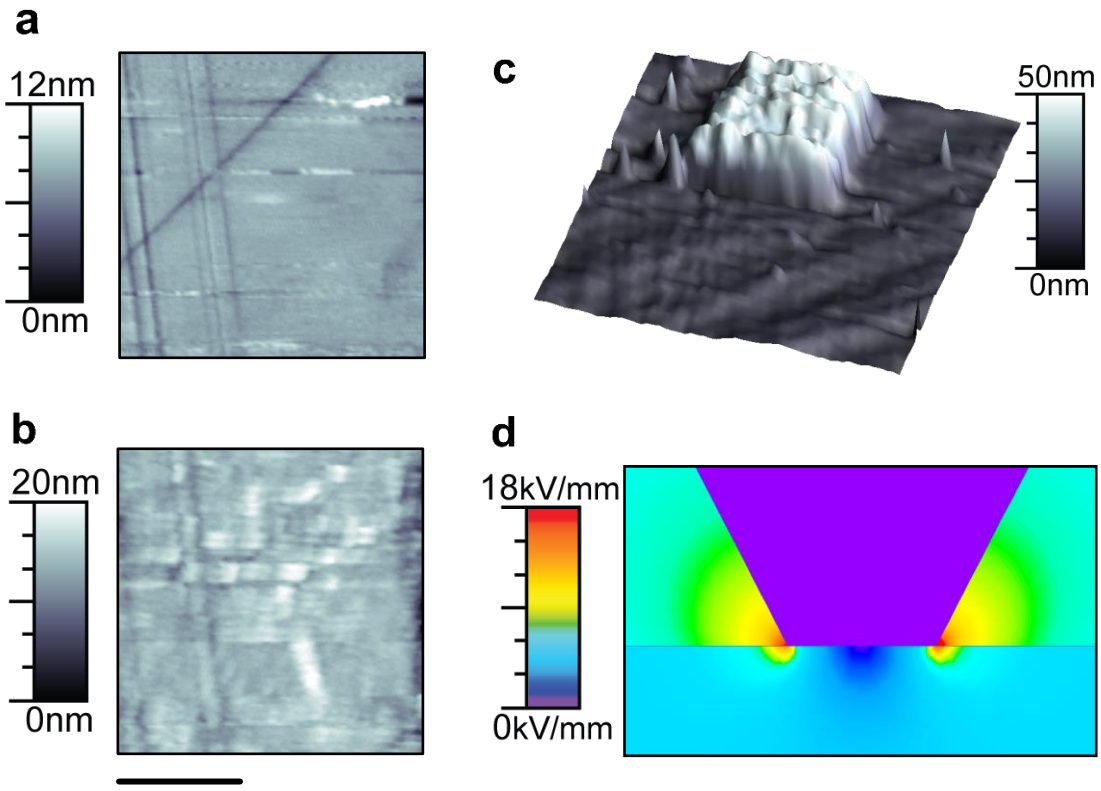

Figure 5.16 a, b Contact mode topography at the beginning and end of several hours of SVM scanning of a 5 μm region, showing topographic deformation over time. **c** Larger scale topography map showing raised step deformation, 8 μm in height, cooresponding to the region in a and b. **d** Quickfield modelling of the tip in contact with the $YbMnO_3$ surface, with ~100 V potential difference between source and drain electrodes (not shown), revealing an intense electric field at the tip-contact equivalent to a locally applied bias. Scale bar 2 μm.

Focusing in on the tip-sample contact area, finite element modelling (presented in Figure 5.16d) revealed an intense electric field at the tip contact in comparison to the bulk. This local field profile is equivalent to the profile observed when applying a large bias to the tip, in absence of a lateral electrical field. Thus, the raised topography may be due to local accumulation of carbon. Contamination via carbon deposition at the tip is a known phenomenon for scanning tunnelling microscopy (STM) where the highly localised electric field can dissociate contaminant gases present in the vacuum chamber[55,56]. An equivalent mechanism seems plausible considering carbon deposition has been observed in STM under high vacuum while the Hall measurements were recorded in ambient.

5.8 Conclusions

A scanning probe microscopy technique has been demonstrated to image the Hall potential developed within a ferroelectric domain wall, with a spatial resolution on the order of tens of nanometres, realising one of the fundamental aims of this thesis. Intermittent contact topography scans were carried out on a sample, to which orthogonal electric and magnetic fields were applied, and the tip-sample interaction found to mimic a charged parallel plate capacitor wherein the Hall potential was recorded as the increase or decrease in the attractive force.

Measurements on $YbMnO_3$ revealed the increased conductance at tail-to-tail walls is mediated by p-type carriers that, from bulk characterisation studies[42,43], are likely to be holes. Calibrations experiments allowed for quantitative interpretation of the domain wall signal and, from these, order of magnitude estimations have been made for the local carrier mobility and density. Interestingly, the estimated carrier density, ~ $1x10^{16}$ cm^{-3}, was a substantial four orders of magnitude lower than the charge density required to screen the divergence in polarisation. This result of incomplete screening by mobile carriers is supported by the observations of increased domain wall conductance in $RMnO_3$ crystals upon increase in bulk p-type carrier density by acceptor dopant[50]. The sheer scale of the deficit suggests there is significant promise for extensive enhancement of the conductivity at the $YbMnO_3$ domain walls as, for the currents presently measured, only one ten-thousandth of the permissible local charge density is contributing to transport. The estimated carrier mobility, ~ 60 $cm^2V^{-1}s^{-1}$, while lower than that of equivalent doped p-type silicon[51] is sufficiently large to suggest that the domain wall transport may occur without significant lattice coupling[52–54]. This is in contrast to the polaronic transport proposed both for p-type conduction in bulk[42] and recently for the minority-carrier conduction state[41] observed at head-to-head walls in $ErMnO_3$.

The large lateral bias and corresponding electric field required to obtain the domain wall contrast led to the unrecoverable degradation of the conductive properties of the sample. This, however, was a fault of the sample design and not of the experimental technique. The relatively small domain density and correspondingly short conducting

segments of domain wall required a substantial portion of the current path to pass through the strongly insulating bulk, leading to a large total resistance. As a result a substantial and ultimately harmful electric field was required to generate the minimal requisite current density within the conducting domain walls. The length scales of conducting domain walls in $RMnO_3$ crystals can be controlled by the cooling-rate of the crystal across the phase transition[13,27]. Therefore samples with tailored domain density could be prepared. Equivalently, for systems where in the conducting wall length cannot be easily increased the interelectrode geometry can be scaled down. The ~ 10^{-8} m spatial resolution would facilitate measurement in sub-micron interelectrode distances, at which point typical thermal drift of ambient AFM is the main consideration.

$ErMnO_3$ crystals with tailored large scale domain structure were prepared through collaboration with D. Meier and J. Schaab at ETH Zurich and used for the development of a more quantitative measurement technique. Progress made in mapping of the Hall potential via Kelvin probe force microscopy (KPFM) is discussed in the section 6.

5.9 References

1. Abrahams, S. C. Ferroelectricity and structure in the $YMnO_3$ family. *Acta Crystallogr. Sect. B Struct. Sci.* **57,** 485–490 (2001).

2. Van Aken, B. B., Palstra, T. T. M., Filippetti, A. & Spaldin, N. A. The origin of ferroelectricity in magnetoelectric $YMnO_3$. *Nat. Mater.* **3,** 164–170 (2004).

3. Van Aken, B. B., Meetsma, A. & Palstra, T. T. M. Hexagonal $ErMnO_3$. *Acta Crystallogr. Sect. E Struct. Reports Online* **57,** i38–i40 (2001).

4. Van Aken, B. B., Meetsma, A. & Palstra, T. T. M. Hexagonal $YbMnO_3$ revisited. *Acta Crystallogr. Sect. E Struct. Reports Online* **57,** i87–i89 (2001).

5. Katsufuji, T. *et al.* Crystal structure and magnetic properties of hexagonal $RMnO_3$ (R = Y, Lu, and Sc) and the effect of doping. *Phys. Rev. B* **66,** 134434 (2002).

6. Jeong, I. K., Hur, N. & Proffen, T. High-temperature structural evolution of hexagonal multiferroic $YMnO_3$ and $YbMnO_3$. *J. Appl. Crystallogr.* **40,** 730–734 (2007).

7. Fennie, C. J. & Rabe, K. M. Ferroelectric transition in $YMnO_3$ from first principles. *Phys. Rev. B - Condens. Matter Mater. Phys.* **72,** 100103 (2005).

8. Sim, H., Oh, J., Jeong, J., Le, M. D. & Park, J. G. Hexagonal $RMnO_3$: A model system for two-dimensional triangular lattice antiferromagnets. *Acta Crystallogr. Sect. B Struct. Sci. Cryst. Eng. Mater.* **72,** 3–19 (2016).

9. Lines, M. E. & Glass, A. M. in *Principles and Applications of Ferroelectrics and Related Materials* 8–15 (Oxford University Press, 2004).

10. Zhang, Q. *et al.* Direct observation of multiferroic vortex domains in $YMnO_3$. *Sci. Rep.* **3,** 2741 (2013).

11. Tian, L., Wang, Y., Ge, B., Zhang, X. & Zhang, Z. Direct observation of interlocked domain walls and topological four-state vortex-like domain patterns in multiferroic $YMnO_3$ single crystal. *Appl. Phys. Lett.* **106,** 112903 (2015).

12. Fujimura, N., Ishida, T., Yoshimura, T. & Ito, T. Epitaxially grown $YMnO_3$ film: New candidate for nonvolatile memory devices. *Appl. Phys. Lett.* **69,** 1011–1013 (1996).

13. Chae, S. C. *et al.* Direct observation of the proliferation of ferroelectric loop domains and vortex-antivortex pairs. *Phys. Rev. Lett.* **108,** 1–5 (2012).

14. Artyukhin, S., Delaney, K. T., Spaldin, N. A. & Mostovoy, M. Landau theory of topological defects in multiferroic hexagonal manganites. *Nat. Mater.* **13,** 42–49 (2013).

15. Zhang, Q. H. *et al.* Direct observation of interlocked domain walls in hexagonal $RMnO_3$ (R=Tm, Lu). *Phys. Rev. B - Condens. Matter Mater. Phys.* **85,** 20102 (2012).

16. Choi, T. *et al.* Insulating interlocked ferroelectric and structural antiphase domain walls in multiferroic $YMnO_3$. *Nat. Mater.* **9,** 253–8 (2010).

17. Kumagai, Y. & Spaldin, N. A. Structural domain walls in polar hexagonal manganites. *Nat. Commun.* **4,** 1–8 (2013).

18. Jungk, T., Hoffmann, Á., Fiebig, M. & Soergel, E. Electrostatic topology of ferroelectric domains in $YMnO_3$. *Appl. Phys. Lett.* **97,** 12904 (2010).

19. Han, M. G. *et al.* Ferroelectric switching dynamics of topological vortex domains in a hexagonal manganite. *Adv. Mater.* **25,** 2415–2421 (2013).

20. Wang, X. *et al.* Unfolding of vortices into topological stripes in a multiferroic material. *Phys. Rev. Lett.* **112,** 247601 (2014).

21. Mostovoy, M. Multiferroics: A whirlwind of opportunities. *Nat. Mater.* **9,** 188–190 (2010).

22. Lin, S.-Z. *et al.* Topological defects as relics of emergent continuous symmetry and Higgs condensation of disorder in ferroelectrics. *Nat. Phys.* **10,** 970–977 (2014).

23. Das, H., Wysocki, A. L., Geng, Y., Wu, W. & Fennie, C. J. Bulk magnetoelectricity in the hexagonal manganites and ferrites. *Nat. Commun.* **5,** 2998 (2014).

24. Geng, Y. *et al.* Direct visualization of magnetoelectric domains. *Nat. Mater.* **13,** 163–7 (2014).

25. Huang, F. T. *et al.* Duality of topological defects in hexagonal manganites. *Phys. Rev. Lett.* **113,** 267602 (2014).

26. Cheng, S., Zhao, Y., Sun, X. & Zhu, J. Polarization structures of topological domains in multiferroic hexagonal manganites. *J. Am. Ceram. Soc.* **97,** 3371–3373 (2014).

27. Meier, Q. N. *et al.* Global Formation of Topological Defects in the Multiferroic Hexagonal Manganites. *Phys. Rev. X* **7,** 41014 (2017).

28. Li, J. *et al.* Scanning secondary-electron microscopy on ferroelectric domains and domain walls in $YMnO_3$. *Appl. Phys. Lett.* **100,** 152903 (2012).

29. Vasudevan, R. K. *et al.* Domain Wall Conduction and Polarization-Mediated Transport in Ferroelectrics. *Adv. Funct. Mater.* **23,** 2592–2616 (2013).

30. Zhang, Q. H. *et al.* Topology breaking of the vortex in multiferroic $Y_{0.67}Lu_{0.33}MnO_3$. *Appl. Phys. Lett.* **105,** 12902 (2014).

31. Geng, Y., Lee, N., Choi, Y. J., Cheong, S. & Wu, W. Collective Magnetism at Multiferroic Vortex Domain Walls. *Nano Lett.* **12,** 6055–6059 (2012).

32. Lilienblum, M., Soergel, E. & Fiebig, M. Manipulation of ferroelectric vortex domains in hexagonal manganites. *J. Appl. Phys.* **110,** (2011).

33. Mermin, N. D. The topological theory of defects in ordered media. *Rev. Mod. Phys.* **51,** 591–648 (1979).

34. Scott, J. F., Schilling, A., Rowley, S. E. & Gregg, J. M. Some current problems in perovskite nano-ferroelectrics and multiferroics: kinetically-limited systems of finite lateral size. *Sci. Technol. Adv. Mater.* **16,** 36001 (2015).

35. Prosandeev, S. *et al.* in *Nanoscale Ferroelectrics and Multiferroics* 700–728 (John Wiley & Sons, Ltd, 2016).

36. Hong, J., Catalan, G., Fang, D. N., Artacho, E. & Scott, J. F. Topology of the polarization field in ferroelectric nanowires from first principles. *Phys. Rev. B - Condens. Matter Mater. Phys.* **81,** 172101 (2010).

37. Vasudevan, R. K. *et al.* Domain Wall Conduction and Polarization-Mediated Transport in Ferroelectrics. *Adv. Funct. Mater.* **23,** 2592–2616 (2013).

38. Du, Y. *et al.* Domain wall conductivity in oxygen deficient multiferroic $YMnO_3$ single crystals. *Appl. Phys. Lett.* **99,** 252107 (2011).

39. Meier, D. *et al.* Anisotropic conductance at improper ferroelectric domain walls. *Nat. Mater.* **11,** 284–288 (2012).

40. Wu, W., Horibe, Y., Lee, N., Cheong, S. W. & Guest, J. R. Conduction of topologically protected charged ferroelectric domain walls. *Phys. Rev. Lett.* **108,** 77203 (2012).

41. Mundy, J. A. *et al.* Functional electronic inversion layers at ferroelectric domain walls. *Nat. Mater.* **16,** 622–627 (2017).

42. Subba Rao, G. V., Wanklyn, B. M. & Rao, C. N. R. Electrical transport in rare earth ortho-chromites, -manganites and -ferrites. *J. Phys. Chem. Solids* **32,** 345–358 (1971).

43. Skjærvø, S. H. *et al.* Interstitial oxygen as a source of p-type conductivity in hexagonal manganites. *Nat. Commun.* **7,** 13745 (2016).

44. Halliday, D., Resnick, R. & Walker, J. in *Fundamentals of Physics* 656–668 (John Wiley & Sons, Ltd, 2008).

45. Sluka, T., Tagantsev, A. K., Damjanovic, D., Gureev, M. & Setter, N. Enhanced electromechanical response of ferroelectrics due to charged domain walls. *Nat. Commun.* **3,** 1–7 (2012).

46. Yudin, P. V., Gureev, M. Y., Sluka, T., Tagantsev, A. K. & Setter, N. Anomalously thick domain walls in ferroelectrics. *Phys. Rev. B - Condens. Matter Mater. Phys.* **91,** 60102 (2015).

47. Jia, C.-L. *et al.* Atomic-scale study of electric dipoles near charged and uncharged domain walls in ferroelectric films. *Nat. Mater.* **7,** 57–61 (2008).

48. Holtz, M. E. *et al.* Topological Defects in Hexagonal Manganites: Inner Structure and Emergent Electrostatics. *Nano Lett.* **17,** 5883–5890 (2017).

49. Gureev, M. Y., Tagantsev, A. K. & Setter, N. Head-to-head and tail-to-tail 180° domain walls in an isolated ferroelectric. *Phys. Rev. B - Condens. Matter Mater. Phys.* **83,** 184104 (2011).

50. Schaab, J. *et al.* Optimization of Electronic Domain-Wall Properties by Aliovalent Cation Substitution. *Adv. Electron. Mater.* **2,** 1500195 (2016).

51. Jacoboni, C., Canali, C., Ottaviani, G. & Alberigi Quaranta, A. A review of some charge transport properties of silicon. *Solid. State. Electron.* **20,** 77–89 (1977).

52. Naik, I. K. & Tien, T. Y. Small-polaron mobility in nonstoichiometric cerium dioxide. *J. Phys. Chem. Solids* **39,** 311–315 (1978).

53. Rettie, A. J. E., Chemelewski, W. D., Emin, D. & Mullins, C. B. Unravelling Small-Polaron Transport in Metal Oxide Photoelectrodes. *J. Phys. Chem. Lett.* **7,** 471–479 (2016).

54. Biaggio, I., Hellwarth, R. W. & Partanen, J. P. Band Mobility of Photoexcited

Electrons in $Bi_{12}SiO_{20}$. *Phys. Rev. Lett.* **78,** 891–894 (1997).

55. Stöffler, D., Löhneysen, H. V & Hoffmann, R. STM-induced surface aggregates on metals and oxidized silicon. *Nanoscale* **3,** 3391–4 (2011).

56. Baba, M. & Matsui, S. Nanostructure Fabrication by Scanning Tunneling Microscope. *Jpn. J. Appl. Phys.* **29,** 2854–2857 (1990).

6 Hall Measurements via Kelvin Probe Force Microscopy

In section 5, it was demonstrated that the Hall potential developed within a conducting domain wall may be imaged by its influence on the topographic trace recorded via intermittent contact mode atomic force microscopy (AFM). Kelvin probe force microscopy (KPFM) is a variant of AFM in which a double-pass technique is used to record the topographic and electrostatic signal contributions in isolation, facilitating direct measurement of local potential[1–5]. While unmistakeably an applicable technique for Hall effect measurement, the increased quantitative accuracy is offset by the imposition of an upper limit on the potential available to drive current. KPFM is typically carried out in the low voltage regime, with the Bruker system in-house, described in section 2.2.3, designed to operate within a maximum potential of 10 V.

To compensate for the order of magnitude reduction in the driving potential, relative to the 100 V used for mapping via intermittent contact AFM, an $ErMnO_3$ crystal with a large scale domain structure was obtained. Exhibiting conducting domain wall lengths of ~ 20 μm, in comparison to the ~ 3 μm of the previously studied $YbMnO_3$ sample, the longer conducting domain walls will more effectively bridge an interelectrode gap of equivalent width.

This chapter discusses the advancement of the Hall effect methodology by using KPFM to facilitate direct quantitative mapping of the local Hall potential. As the focus is on the development of the experimental technique, the theory behind KPFM is expounded, along with a discussion of the more pragmatic considerations that may affect quantitative accuracy. A brief analysis of the domain structure and conductive behaviour of the $ErMnO_3$ sample is then presented, before outlining the progress made to date in implementing the technique.

6.1 Kelvin Probe Force Microscopy

6.1.1 The Macroscopic Kelvin Probe

KPFM is an extension of a macroscopic technique devised in 1898 by Lord Kelvin for measurement of surface potentials[6]. Herein, a metal plate is suspended over a flat sample of the material under investigation so that the opposing faces form a parallel plate structure, with the two plates separated by a distance z. The two differing materials have differing work functions and upon making an electrical connection, as shown in Figure 6.1, charge flows from the material of higher work function to the lower until the Fermi levels are aligned and thermodynamic equilibrium is established[4]. The resultant charge on each plate (Q) is given by:

$$Q = CV_0 \tag{6.1}$$

Where, C is the capacitance between the plates and V_0 the potential difference driving the charge flow, referred to as the contact potential difference[5,7,8] and given by:

$$V_0 = \left(\frac{\phi_{sample}}{e} - \frac{\phi_{ref}}{e}\right) \tag{6.2}$$

Where e is the elementary charge and ϕ_{sample} and ϕ_{ref} are the work functions of the sample and reference material respectively.

Vertical displacement of the suspended plate (Δz) causes a change in capacitance (ΔC) and a corresponding charge (ΔQ) to flow between the plates. Placing a large resistor in series with the plates, the typically small ΔQ signal can be magnified by measuring the potential drop across the resistor[9]. If a DC bias, V_{DC}, is applied to the reference plate, the total potential difference is given by:

$$V = \frac{\phi_{sample}}{e} - \left(\frac{\phi_{ref}}{e} + V_{DC}\right) \tag{6.3}$$

$$V = V_0 - V_{DC} \tag{6.4}$$

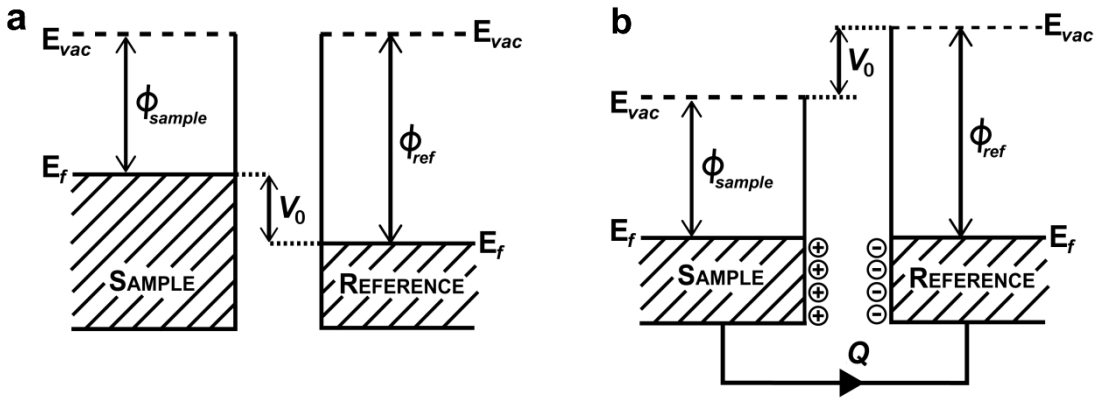

Figure 6.1 a A sample and reference plate in isolation with differing work functions, ϕ_{sample} and ϕ_{ref}. **b** On connection, charge Q flows driven by the contact potential difference, V_0, until the fermi levels equate and equilibrium is reached. Here E_{vac} is the vacuum energy and E_f the fermi energy. Figure adapted from [10]

From (6.4), it is clear that the potential between the plates will be zero when V_{DC} = V_0. Therefore, by continually adjusting V_{DC} until change in z generates zero charge flow, the contact potential difference can be determined and hence ϕ_{sample} is known in relation to ϕ_{ref}. This is the central concept behind the Kelvin probe technique, that by application of a DC bias the capacitive effect can be nullified and the contact potential difference recorded.

The technique went relatively unchanged until 1932 when Zisman[11] significantly improved both response time and accuracy by mechanically oscillating the reference plate at a known frequency. Thus measuring the potential across the resistor returned an alternating voltage of the same frequency as the oscillation, facilitating amplification of the signal and use of phase sensitive detection[9].

6.1.2 Theory of Kelvin Probe Force Microscopy

First developed by Nonenmacher *et al.*[1], KPFM applies the methodology of Zisman to non-contact AFM. Herein, an oscillating AFM tip acts as a microscale reference plate that can be moved across the sample to spatially map the surface potential. (A complete description of non-contact AFM is given in section 2.3). However, the microscopic dimensions of the 'plates' in KPFM corresponds to an equivalent reduction in the capacitance such that measuring the charge flow results in minute

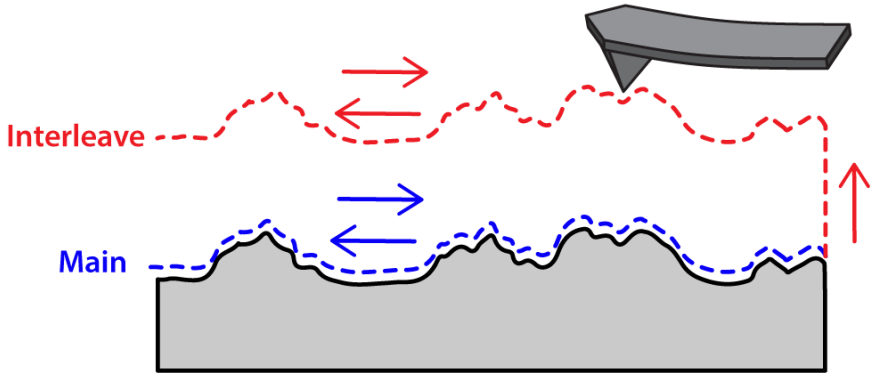

Figure 6.2 Schematic of interleave mode. First the topographic profile is recorded, trace and retrace, commonly referred to as the main trace. Subsequently the tip moves to the designated lift height and scans the sample, using the topographic profile recorded in the main trace to maintain a constant separation from the sample. This is repeated for each scan line, thus interleave operation doubles the total scan time.

absolute signal and poor measurement accuracy. Instead, KPFM measures the effect of the electrostatic force acting on the tip.

In order to separate the electrostatic signal from the topographic, an AC bias is applied to the tip (V_{ac}) at a frequency ω, generating an oscillating electrostatic force on the tip. This electrostatic oscillation is superimposed on the mechanical oscillating force applied by the piezotube. By setting ω to be distinct from the setpoint frequency of the non-contact AFM scan, a dual channel lock-in amplifier can be used to isolate the electrostatic and topographic signals independently[1,12]. To further separate the electrostatic signal, a double pass scan technique is commonly used to record the topographic and electrostatic surface profiles at different points in time.[2,12]

Here, each scan line of the image is recorded twice. First, in the main mode, an intermittent contact scan records the topography, trace and retrace, as shown Figure 6.2. Upon finishing the retrace measurement, the interleave mode scan is initiated and the tip raises to a user defined height, termed the lift height. Now, as trace and retrace are carried out, the tip path mimics the topographic profile recorded in the main mode so that the tip-sample distance is fixed at the lift height[3]. By maintaining a constant tip-sample separation, the topographic force on the tip should remain constant and any change in the dynamics of the probe may be attributed to

electrostatic forces. The oscillating tip generates an AC signal on the photodiode, which is used as the input signal in a feedback loop that applies a DC offset (V_{DC}) to the tip in order to nullify the oscillation and, thus, zero the input.

The electrostatic force between the tip and sample, F_{el}, at a distance z from the surface is given by[2,3,13]:

$$F_{el} = -\frac{1}{2}\frac{\partial C}{\partial z}V^2 \tag{6.5}$$

Where V is the total potential difference between tip and surface:

$$V = V_0 - V_{DC} + V_{AC}\sin(\omega t) \tag{6.6}$$

Substituting (6.6) into (6.5) and multiplying through, F_{el} can be broken into three frequency components:

$$F_{dc} = -\frac{1}{2}\frac{\partial C}{\partial z}\left((V_0 - V_{DC})^2 + \frac{1}{4}{V_{ac}}^2\right) \tag{6.7}$$

$$F_{\omega} = -\frac{\partial C}{\partial z}(V_0 - V_{DC})V_{AC}\sin(\omega t) \tag{6.8}$$

$$F_{2\omega} = \frac{\partial C}{\partial z}\frac{1}{4}{V_{AC}}^2\cos(2\omega t) \tag{6.9}$$

Using V_{ac} as the reference signal for a lock-in amplifier, the ω force component, F_{ω}, can be isolated and from inspection of (6.8), it is clear that the signal will be zero when $V_{DC} = V_0$. Feedback electronics are used to continuously monitor F_{ω}, apply the necessary V_{DC} to nullify the oscillation and hence map the contact potential difference as the tip is rastered across the sample. This detection method directly monitors electrostatic force, and is known as amplitude-modulated detection (AM-KPFM).

Frequency-modulated detection, (FM-KPFM), first presented by Kitamura *et al.*[14], monitors the electrostatic force gradient. Herein, the cantilever is mechanically oscillated at the resonant frequency of the system, f_0, and an AC bias of frequency ω

is applied to the tip, resulting in an oscillating shift of the resonant frequency. The shift in resonant frequency, Δf_0, can be approximated by[15,16] :

$$\Delta f_0 = -\frac{f_0}{2k}\frac{\partial F_{el}}{\partial z} \tag{6.10}$$

Where k is the spring constant of the system. Hence, Δf_0 is proportional to the electrostatic force gradient. Substituting (6.5) into (6.10) and separating out the different frequency components as before, the ω component of the oscillating frequency shift, $\Delta f_0(\omega)$ is given by:

$$\Delta f_0(\omega) \propto \frac{\partial F_\omega}{\partial z} = -\frac{\partial^2 C}{\partial z^2}(V_0 - V_{DC})V_{AC}\sin(\omega t) \tag{6.11}$$

Analogous to AM-KPFM, where the ω force component was nullified via feedback loop, in FM-KPFM the the ω component of the frequency shift is isolated from the resulting oscillating signal and used as the input for the feedback electronics. It is clear from (6.11) that the ω component of the frequency shift will be zero when $V_{DC} = V_0$.

6.1.3 Comparison of Amplitude and Frequency Modulated KPFM

The principal difference between AM and FM detection modes is the long and short range nature of the electrostatic force and force gradient respectively. The practical significance of this can be conveyed by a simplistic calculation of the relative contributions from the tip and the cantilever to the total signal[17,18]. Consider an AFM probe orientated parallel to the sample surface with a lift height of 15 nm, as shown in the schematic in Figure 6.3.

Continuing to use the parallel plate model, the capacitance of the tip (C_1) and cantilever (C_2) is given by:

$$C_1 = \frac{A_1\varepsilon_0}{z_1} \qquad \& \qquad C_2 = \frac{A_2\varepsilon_0}{z_2} \tag{6.12}$$

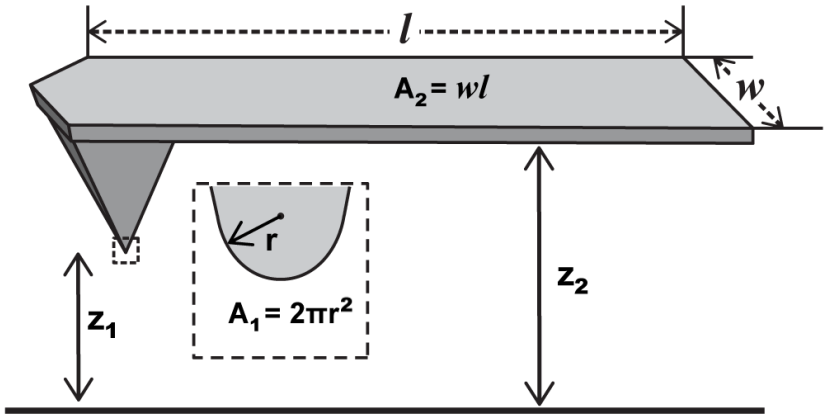

Figure 6.3 Schematic of relative cantilever dimensions for calculation of cantilever contribution to signal. The tip area is approximated by the surface area of a hemisphere with radius r equal to the tip radius.

Where ε_0 is the permittivity of free space and A is the area of the plate. For AM-KPFM, the relative contributions to the total signal can found from (6.8). Setting the potential terms equal to one:

$$F_\omega \approx \frac{2\pi r^2 \varepsilon_0}{{z_1}^2} + \frac{lw\varepsilon_0}{{z_2}^2} \tag{6.13}$$

Taking the dimensions of the AFM probes used for all measurements in this thesis, Nanosensor brand PPP-EFM probes, (r = 25 nm, w = 28 μm, l = 225 μm, z_1 = 15 nm , z_2 = 12 μm) and solving:

$$F_\omega \approx 15.5nN + 38.7nN \tag{6.14}$$

The measured signal is dominated by the signal contribution from the micron scale cantilever, with roughly 40% of the signal collected at the tip apex. Using (6.11) to make the equivalent calculation for FM-KPFM:

$$\frac{\partial F_\omega}{\partial z} \approx \frac{4\pi r^2 \varepsilon_0}{{z_1}^3} + \frac{2lw\varepsilon_0}{{z_2}^3} \tag{6.15}$$

$$\frac{\partial F_\omega}{\partial z} \approx 20.6\text{x}10^{-3} Nm^{-1} + 64.6\text{x}10^{-6} Nm^{-1} \tag{6.16}$$

For the same experimental geometry in FM-KPFM, over 99% of the total signal is collected at the apex of the tip.

This worked example is clearly an over-simplification, however, it agrees qualitatively with more rigorous theoretical models[18–21] and experimental comparisons of AM and FM-KPFM on standardized samples[16,22,23]. Figure 6.4a is taken from a study by Zerweck *et al.*[22] and compares the potential profile measured by AM and FM-KPFM when scanning off the edge of a monolayer of potassium chloride onto a gold coated substrate. The sharp step in contact potential difference at the edge is more accurately imaged by FM-KPFM, as in AM-KPFM when the tip passes the monolayer edge the signal is convoluted by the cantilever, resulting in reduced spatial resolution. Notably, this results in a quantitative difference in the measured potential. Nonetheless, the relative influence of the cantilever in AM-KPFM can be reduced with decreased lift height[19,21], as can be shown from varying z_1 in (6.13), and atomic scale resolution has been achieved using AM detection[24].

An additional consideration is operation in air in comparison to under vacuum. The data presented in Figure 6.4a was collected under vacuum where the quality factor, Q, of the system was maximal (up to $Q \approx 10^5$) in comparison to the $Q \approx 10^2$ typical of a cantilever in air[3,22,25]. However, the settling time for the change in amplitude is linearly proportional to Q, and thus under vacuum the response time for AM detection is orders of magnitude greater then FM-KPFM[25]. Conversely, the low Q factor in air corresponds to a broad ill-defined resonance peak, leading to an increase in the minimum discernible frequency shift and an overall reduction in sensitivity. Zeigler *et al.*[26] compared AM and FM detection in air by mapping a sample of gold islands embedded in a titanium bulk. Figure 6.4c shows the potential profile measured across a Au-TiO_2-Au interface at a range of lift heights. The spatial resolution of the AM-KPFM increases with reduced lift height: accurately mapping the sharp Au-TiO_2 interface for lift heights below 20 nm. By comparison, the FM-KPFM measurement shows substantially increased noise levels, with the Au boundary poorly discerned.

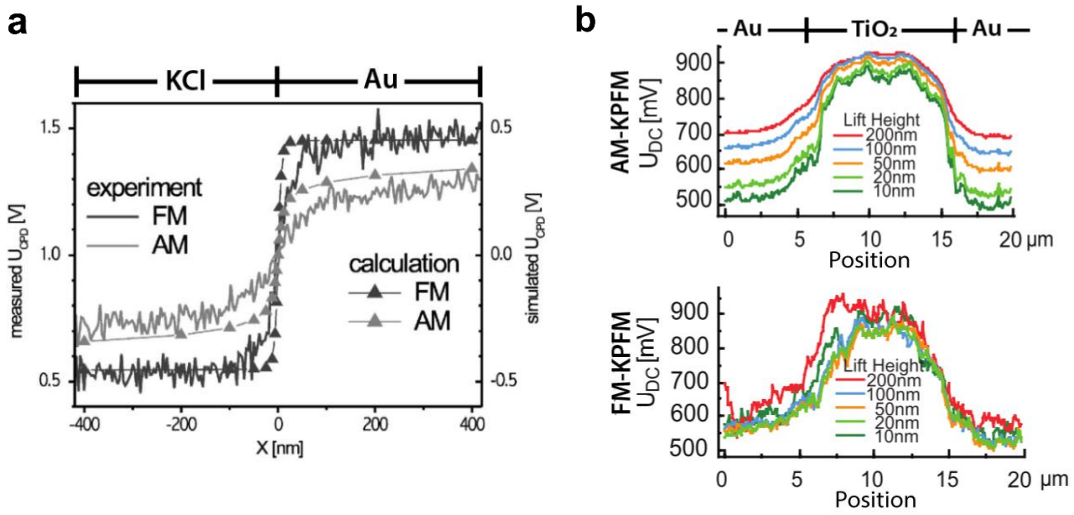

Figure 6.4 a Comparison of the contact potential difference measured by frequency modulated (FM) and amplitude modulated (AM) KPFM while scanning across a monolayer of KCl and onto sputtered gold. **b** Plot of the contact potential difference measured across a TiO_2 island embedded in gold, for both AM-KPFM and FM-KPFM at a range of lift heights. Measurements in both **a** and **b** were recorded in vacuum. Figures **a** and **b** reprinted from [18] and [20] respectively.

Crucially, to facilitate detection in air via FM mode, the authors applied a V_{AC} of 5 V, magnifying the frequency shift associated with a given contact potential difference. This is significant as, to facilitate autonomous feedback, both the V_{AC} and V_{DC} applied to the tip are regulated by microscope controller, which prevents the use of an external voltage source. Consequently, the total applied voltage ($V_{AC} + V_{DC}$), is limited to the typically low bias limit of the microscope. For example, the Bruker system in-house has a bias limit of 10 V. Therefore, with V_{AC} = 5 V the maximum surface potential that could be measured is halved. By comparison, AM-KPFM achieves a sufficient signal to noise ratio in air with $V_{AC} \approx 10^{-1}$ V [27].

6.1.4 KPFM Measurement in Practice

The exact potential measurement is affected by a number of experimental variables. As stated previously, the lift height significantly affects the measured potential in AM-KPFM and to a lesser degree FM detection, with values converging with reducing lift height[28,29]. Both theoretical[19,21,30] and experimental[16,22,31] studies have shown the shape of the tip is significant. Below a critical limit, dependent on the lift height and cantilever dimensions, a smaller tip radius leads to a reduction in spatial

resolution as the absolute signal collected at the tip apex decreases. Similarly, the tip length and volume affect the magnitude of signal collected.

Another trade-off is found for the magnitude of the oscillation amplitude, as large amplitudes magnify small variations in the contact potential difference, while also decreasing system response time. Additionally, KPFM operates on the basis of the electrostatic oscillations remaining within a region of equivalent force gradient on the topographic force-distance curve (sketched in Figure 2.1b). Large oscillation amplitudes expose the tip to varying topographic force-gradient, influencing the cantilever motion. Optimal amplitude is dependent on quality factor and spring constant of cantilever, as well as the bandwidth of the detector[15].

Futhermore, care must be taken to fine-tune the parameters controlling the feedback electronics. The magnitude of signal output by the lock-in amplifier is dependent on the optimal choice of reference phase[31]. The phase difference between excitation by V_{AC} and the AC signal output by the photo-diode varies depending on cantilever properties. Poor phase matching introduces system lag affecting the response rate to sudden variations potential. Calibration of gains is crucial as they dictate how effectively the feedback loop can nullify the capacitive force component, essentially determining the error bar on $V_{DC} = V_0$.

Given the litany of system variables which influence the potential measured, accurate quantitative measurement cannot be assumed. Initial calibration against a reference sample, operating with minimal scan speeds at the lowest permissible lift height, is required to verify the degree of quantitative accuracy achievable given the fixed variables of the system.

6.2 Conduction at Head-to-Head Domain Walls in $ErMnO_3$

The large domain $ErMnO_3$ sample was obtained through collaboration with D. Meier at ETH Zurich. Recently Meier and co-workers reported[32] the inversion of local behaviour at head-to-head walls, from decreased to increased conductance relative to bulk upon sufficient applied bias ($\sim$ 4.8V). This represents the first observation of increased conduction at charged domain walls at which, following theory,

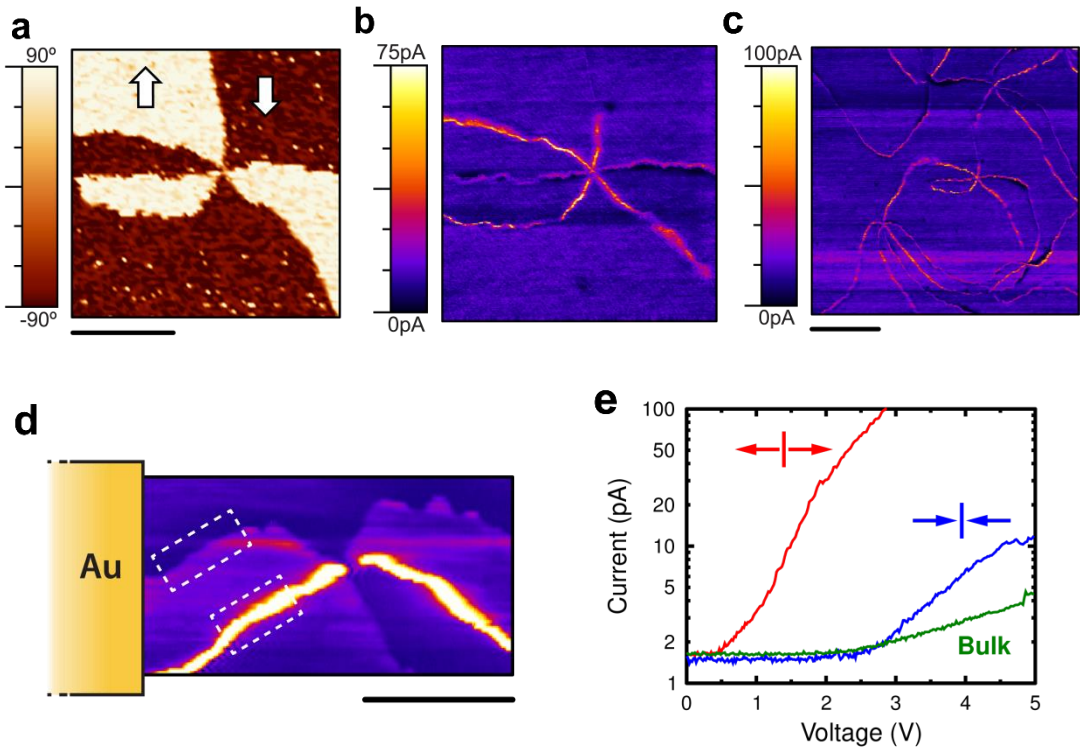

Figure 6.5 a and **b** Lateral PFM phase and c-AFM map, recorded with 2 V bias, of a six-fold vertex in $ErMnO_3$ with all six domain walls exhibiting increased conductance over the bulk. Arrows overlayed on **a** convey polarisation direction and verify both tail-to-tail and head-to-head walls show conductance in **b**. **c** Larger c-AFM map of the same area, bias 2 V, showing increased conductance for the majority of domain wall angles. **d** Schematic of the electrode geometry used for lateral current versus voltage (IV) measurements. The region shown in the c-AFM map was divided into a grid (50 x 25) and an IV curve from 0 V to 5 V performed at each point. Data from the parallel segments of head-to-head and tail-to-tail walls, marked by the white dashed boxes, was isolated and the largest current values for each voltage recorded. **e** Maximal current response of the head-to-head and tail-to-tail wall marked in **d** (blue and red respectively) plotted alongside maximal bulk response (green). Scale bars in **a**, **b** and **d** are 2 μm, 5 μm and 2μm respectively.

aggregation of the majority carrier type in bulk is disfavoured and thus the conduction is likely mediated by minority carriers.

The local screening mechanism was investigated via electron energy-loss spectroscopy (EELS), revealing an increased concentration of the lower valence Mn^{2+} state, compared to the predominant Mn^{3+}, at the head-to-head wall suggesting a locally increased electron density[32]. Further measurements observed no anomaly in the oxygen spectrum at the wall, refuting the presence of local oxygen vacancies.

The authors propose that due to the strong columbic repulsion experienced by the relevant manganese orbitals, coupling of the electrons with the lattice is energetically favourable and hence suggest the observed increased conductance is mediated by n-type polarons. The sample we received exhibited similar minority carrier behaviour with increased conductance measured at both wall types at 2 V, as shown by comparison of piezoresponse force microscopy (PFM) and conductive atomic force microscopy (c-AFM) maps of a 6-fold vertex (presented in Figures 6.5a and 6.5b respectively).

Mapping over a larger 20 μm^2 area, approximately the width of the interelectrode gap for the previous Hall investigation, it is clear that the domain walls exhibit enhanced conductance for almost all wall angles. Current map presented in Figure 6.5c. Following the same convention for defining wall angle as described in Figure 5.3d, with an applied 2 V bias bulk conductance was observed only for domain walls within the narrow range of $79° < \phi < 101°$. Thus, in contrast to the ~ 3μm long conducting segments observed in the $YbMnO_3$ sample, the domain walls may form an almost continuous current pathway across an equivalently sized interelectrode gap. This corresponds to a substantial increase in the percentage of the total lateral current driven along the walls, as opposed to through bulk.

Under repeat c-AFM measurements the threshold voltage required for inversion of the conductive state at head-to-head walls varied significantly across different regions of the sample, with conductive behaviour observed as low as 1.5 V and insulating behaviour as high as 4.5 V. Possible explanations for this were variations in quality of the tip-contact, spatial variation in the quality of the silver dag bottom electrode or variation in the conductive pathway from the bottom electrode to the grounded AFM tip.

To perform more direct measurements of local current as function of voltage, (IV measurements), a gold electrode was sputtered on the top surface, overlaying a pair of head-to-head and tail-to-tail walls. With bias applied to the electrode and an earthed tip, lateral IV measurements were performed by moving the tip in a grid pattern over a 5 x 2.5 μm region encompassing the walls, as displayed by the c-AFM map in Figure 6.5d. Each individual IV curve was recorded by incrementing the

electrode potential from 0 V to 5 V in 256 equal steps. Measurements from parallel segments of the head-to-head and tail-to-tail walls, marked on Figure 6.5d, were isolated and for each region (approximately 20 curves) the largest current reading at each voltage step was extracted. Values for bulk IV characterisation were taken from a region equidistant from the electrode.

Operating under the reasoning that variation in tip contact serves only to reduce, and not erroneously contribute to, the measured current, this method allowed for determination of maximal current response of each wall. IV behaviour of both wall types and the bulk are plotted in Figure 6.5e for comparison. The head-to-head wall was locally more insulating than bulk up until a threshold bias of 2.8 V, beyond which there was a sharp increase in conductance to a maximum measured current of 12 pA at 5 V bias (~ 2.5 times the bulk conductance).

In comparison, the tail-to-tail wall exhibited an order of magnitude greater conductance than the head-to-head wall; saturating the 100 pA limit of the current amplifier at 2.9 V (~ 50 times bulk conductance at the same voltage). This behaviour contrasts somewhat with the results of Mundy *et al.*[32], who reported the head-to-head wall conductance approaching that of the tail-to-tail wall upon inversion from the insulating to conducting state.

6.3 Hall Potential Mapping at $ErMnO_3$ Domain Walls

All KPFM measurements presented were recorded in air on the Bruker system (described in full in section 2.2.3) using amplitude modulated detection in interleave mode. For the initial aim of verifying the efficacy of the technique, large gold electrodes were deposited with a 120 μm long interelectrode edge. While the large network of interelectrode domain wall pathways prevents precise determination of domain wall current, the greater number of domain walls available for imaging was advantageous for troubleshooting during the optimisation of the scan parameters. The current driving potential was applied directly by the microscope, with a Kiethely 6517b electrometer placed in series as an ammeter to monitor the driven current. To generate the Hall potential, an electromagnet was positioned such that the direction of applied magnetic field ran orthogonal to the lateral electric field.

Representative results are shown in Figure 6.6 with KPFM mapping performed over the same interelectrode region for a combination of applied electric and magnetic field states. PFM imaging of the region, lateral phase presented in Figure 6.6a, conveyed a distinctive branched 'Y' pattern of charged domain walls.

KPFM maps of the same region are presented (Figure 6.6b through 6.5e) with the magnitude and sense of the current and magnetic fields as labelled. The 10 V upper limit on the electrode bias equated to a lateral current of 25 nA and a maximum magnetic field of 0.35 T was applied. Positive and negative field directions follow the same convention as used for intermittent contact Hall investigation, outlined in section 5.4 and depicted in Figure 5.7. To reverse the direction of driven current, the high and low electrode contacts were exchanged and thus a positive 10 V bias was consistently applied. KPFM data presented in Figure 6.6 has been flattened within WSxM software[33] so that domain wall contrast may be viewed more clearly.

Comparing the KPFM map in Figure 6.6b, recorded with orthogonal electric and magnetic fields applied, with the PFM phase map, it is clear that the observed surface potential contrast has direct spatial correspondence with the charged domain walls. However, on inspection, the contrast at tail-to-tail and head-to-head walls is of the same sign. Fixing the magnetic field direction and reversing the direction of driven current, the domain wall potential appears unchanged, see Figure 6.6c, in conflict with the cross product dependence of the Hall potential. This apparent indifference to directionality is due to a substantial offset signal measured at the charged domain walls, wholly due to the applied bias. Figure 6.6d displays the potential contrast measured with bias applied in absence of magnetic field and Figure 6.6e the lack of domain wall contrast in absence of both lateral potential and magnetic field.

Surface potential measurements, under zero applied bias and magnetic field, were attempted on $ErMnO_3$, $YbMnO_3$, $LiNbO_3$ and Cu-Cl boracite as part of an independent investigation to establish whether charged domain walls natively provided measureable potential contrast. No native domain wall contrast was observed in-house, for any material, without application of external bias to the sample. Thus, the KPFM contrast observed under bias in absence of magnetic field is

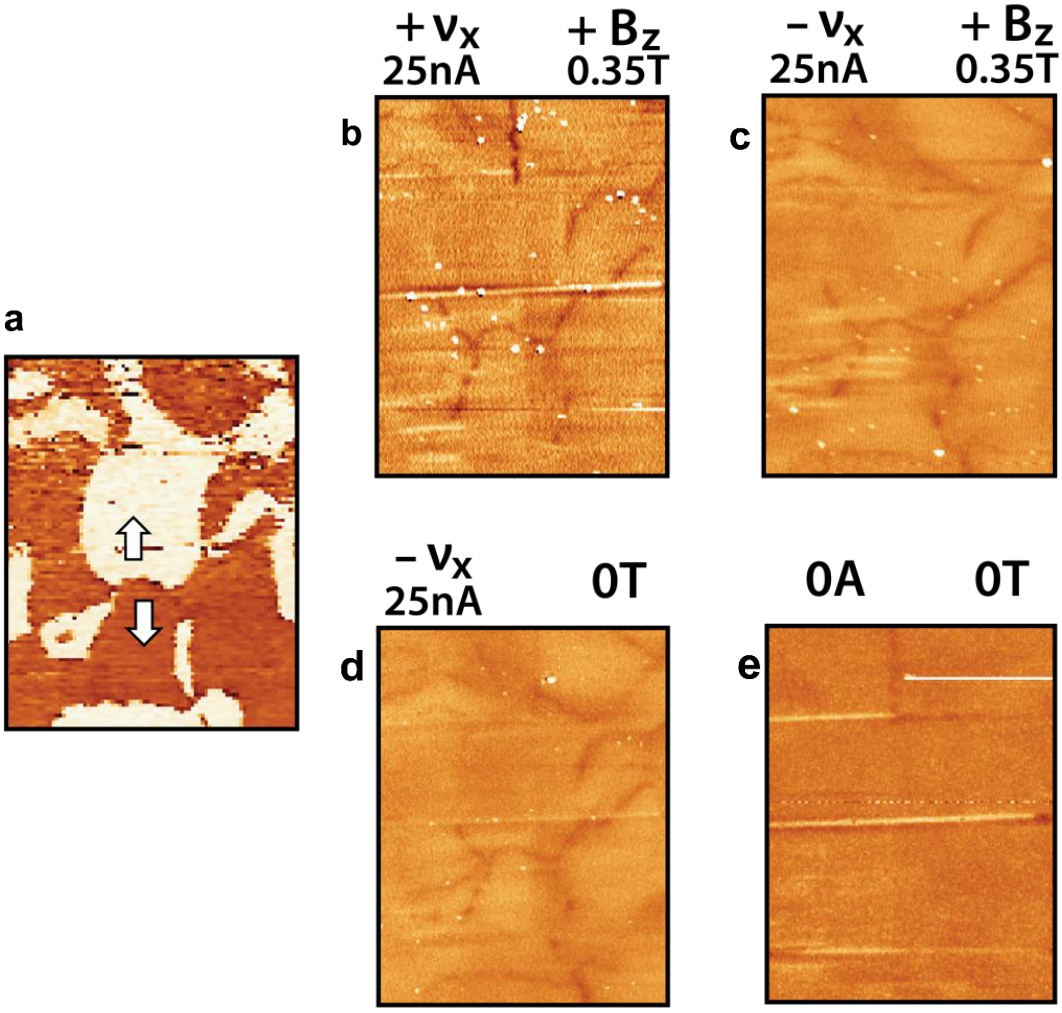

Figure 6.6 a Lateral PFM of an interelectrode region, displaying charged domain walls. Overlaid arrows convey local polarisation. **b**, **c**, **d** and **e** KPFM measurements of the region in a, displaying the same distinctive 'Y' pattern of the charged domain walls, recorded under different conditions of magnetic field and driven current. $\mathbf{B}_Z$ and $\boldsymbol{v}_x$ represent direction of applied magnetic field and driven current respectively. Field geometry with respect to sample is as defined in section 5.4.

attributed to local variations in the lateral potential dropped across the interelectrode gap. Possibly due to the comparative resistance of bulk and conducting domain wall pathways.

By mapping the domain wall potential, under lateral bias and orthogonal magnetic field, and reversing the magnetic field direction, the local potential will increase or decrease by an amount equal to twice the Hall voltage. Therefore, the local Hall potential may be measured despite presence of the offset potential. However, due to time constraints, the initial investigation concerned only the development and

calibration of the experimental method to reach a state where consistent domain wall imaging was achieved. Unfortunately sufficient data was not collected to explicitly verify the presence of the Hall potential. During the preparation of this thesis, the investigation was continued independently by P. Turner, who performed a quantitative analysis of the domain wall potential measured under various field geometries. Data from this investigation is presented, Figure 6.7, as verification that the Hall potential may be measured using this methodology.

Herein the lateral potential was kept constant, and current observed to remain constant, while the magnetic field was varied between KPFM measurements. Thus, the interelectrode potential profile remained constant throughout and any measured variation in the potential at domain walls was attributed to the application of orthogonal magnetic field. Figure 6.7 displays the potential profile measured across a tail-to-tail charged domain wall with a magnetic field of 0.35 T applied along + $\mathbf{B_Z}$ and – $\mathbf{B_Z}$ directions respectively. When the magnetic field was reversed the potential measured at the domain wall changed, as would be expected if the locally generated Hall potential was being measured.

As the current direction was fixed along $-\boldsymbol{\nu_X}$ direction and from the Lorentz force expression (5.1), the positive and negative Hall potential observed for magnetic field directions of + $\mathbf{B_Z}$ and – $\mathbf{B_Z}$ respectively corresponds to conduction mediated by positive charge carriers. The determination of p-type conduction at tail-to-tail domain walls in $ErMnO_3$ is in agreement with the observations made for tail-to-tail walls in $YbMnO_3$ using the intermittent contact methodology for imaging local Hall potential.

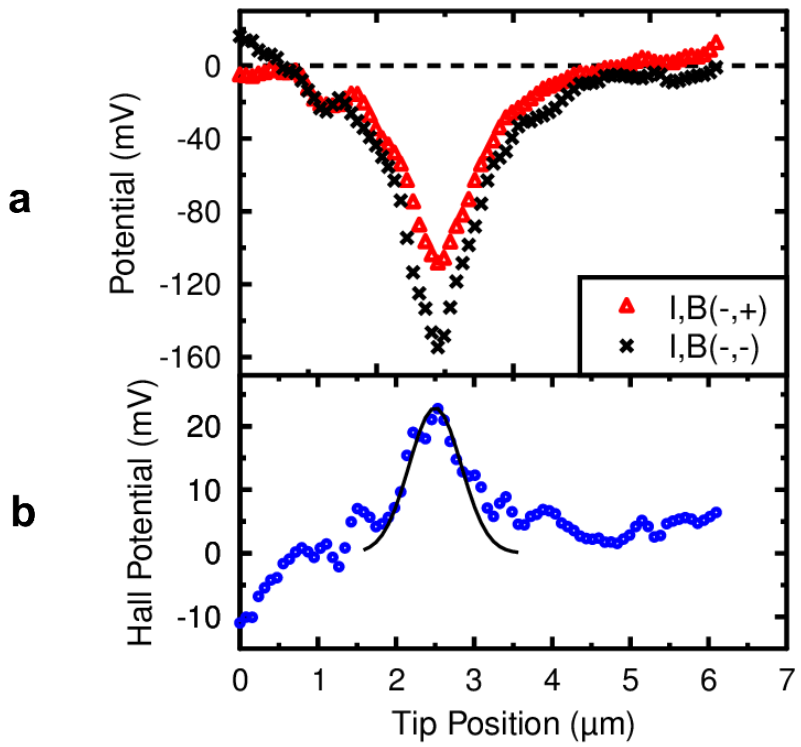

Figure 6.7 a Potential profile measured across a tail-to-tail domain wall in the interelectrode region. Current direction was fixed and magnetic field direction reversed between measurements. Data plotted is an average potential profile from multiple line profiles. The difference between the two peaks is attributed to the reversed sign of Hall potential developed at the wall. **b** Difference between measured potentials is taken and halved to reveal local Hall potential. A solid black is overlaid to emphasise the domain wall profile amongst the data. Resulting positive potential peak conveys p-type conductivity, in agreement with previous investigation.

6.4 Calibration of the Quantitative Accuracy

The KPFM measurements in Figure 6.6 represent the maximal domain wall contrast that could be repeatedly achieved using scan parameters that facilitated stable measurement. As discussed in section 6.1, it is not sufficient to utilise parameters that provide image clarity, but rather the quantitative accuracy of the chosen parameters must be established. For calibration a rectangular gold pad was sputtered onto a polished $SrTiO_3$ single crystal and connected to a Keithley 237 voltage source. A Keithley 6514 electrometer was used as to monitor the voltage applied to the calibration sample and a reference signal for the measured voltage, scaled between 0 and 2V, was passed to a data channel on the microscope controller. This allowed for

the applied bias and measured potential to be recorded simultaneously within the Nanoscope software.

An interleave mode AM-KPFM scan was engaged, mapping the potential of the gold electrode, while a 0.35 T magnetic field was applied to the sample. To simulate sharp variations in surface potential, such as experienced at a conducting domain wall, a series of linearly increasing voltage pulses were applied to the electrode and timed such that they occurred at the same point within each interleave retrace scanline. Figure 6.8a plots the applied bias and measured potential on the same spatial axis for a pulse ramp increasing from -5V to 5 V in 50 mV steps. The main figure focuses within the narrow -0.1 V to 0.1 V range to show agreement while a plot of agreement over the full range is inset. To determine the change in potential due to applied bias, separate from the contact potential difference measured under zero bias, the potential profile recorded in interleave trace was subtracted from the retrace data.

The difference between the measured and applied potential for each pulse is plotted in Figure 6.8b, revealing a strong linear relationship between absolute error and the applied bias. Plotting the residual about a linear trendline reveals a steady noise level of approximately $\pm$ 25 mV. The linear trend is indicative of a significant cantilever contribution to the overall capacitive force at this lift height. During scanning the main body of the cantilever was not above the gold but rather was positioned above the lower magnitude potential of the crystal surface. At larger applied bias, the increased weighting of the low surface potential far from the gold, reduced the overall change in potential measured by the tip. Despite the increasing absolute error the percentage error is unaffected, plotted Figure 6.8d, remaining below 2% for bias greater than 1 V. As the bias approaches the noise floor the percentage error increases, peaking at a maximum of 30%.

Overall the calibration confirms that the optimised scan parameters are providing a high degree of quantitative accuracy, with the caveat of ensuring the surface potential under the length of the cantilever is not disparate to that under the tip. Practically this relates to taking care in design of the electrode geometry so the cantilever body is not suspended over an earthed electrode during scanning (as was the case for the data presented in Figure 6.6). On inspection the $\pm$ 25 mV

noise floor appears substantial given the 30 mV magnitude of the Hall potential measured for a charged domain wall in $YbMnO_3$ using intermittent contact AFM. However, the noise level measured under calibration was inflated by the use of external voltage source and voltmeter. In comparison the bias and measurement for the Hall measurements were performed internally by the microscope and controller, substantially reducing line noise and external cabling. Thus, the $\pm$ 25 mV noise represents an upper limit.

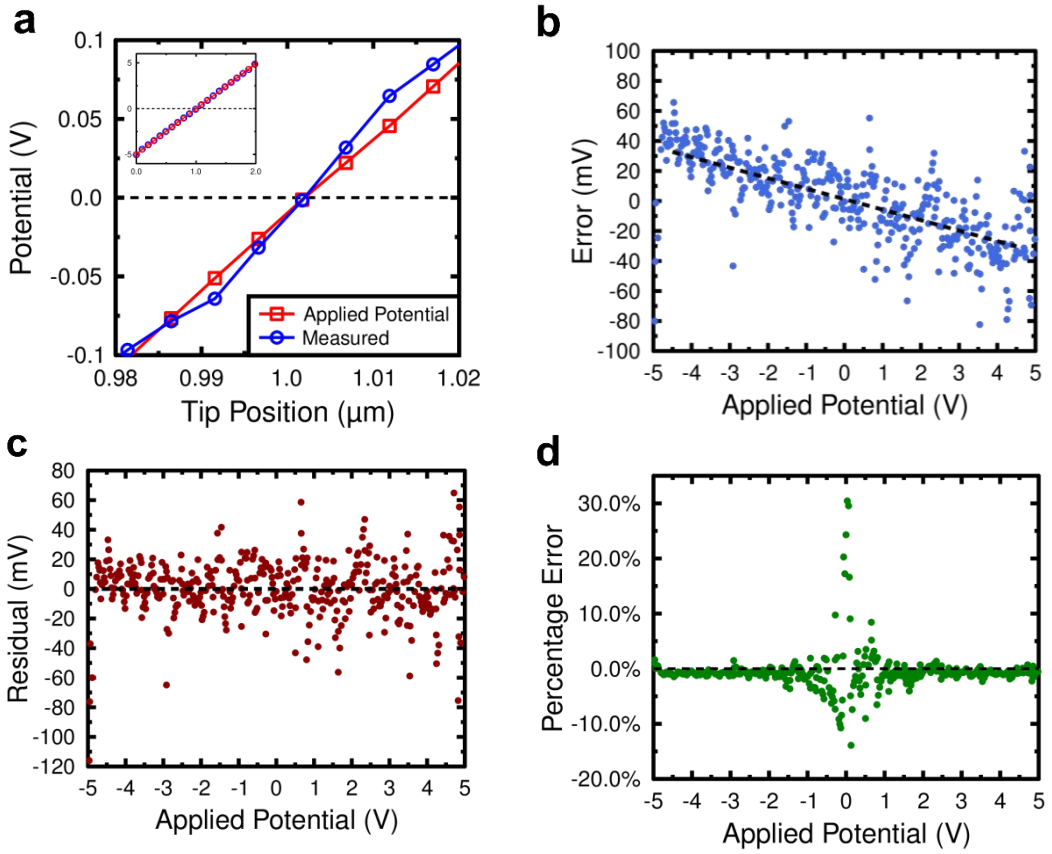

Figure 6.8 a The surface potential of a gold-coated $SrTiO_3$ single crystal was measured via AM-KPFM in interleave while a series of voltage pulses were applied, increasing from -5 V to 5 V in 256 steps. To account for the contact potential difference, the potential measured under zero bias was subtracted. **b** The measured potential was subtracted from the applied potential for each voltage step to determine measurement error, and plotted against applied potential. Dashed trendline shows linear relationship between error and potential, caused by convolution of signal by cantilever. **c** Residual of error from trendline in **b**, revealing a $\pm$ 25 mV noise level. **d** Plot of percentage error, with a peak error of 30%.

6.5 Optimised Scan Parameters for Quantitative Measurement

The weighting of the cantilever to the total signal is dependent on the lift height, as shown in Figure 6.4b, and the noise level affected by a multitude of scan parameters such as scan size, rate and resolution. Herein, the chosen scan parameters are presented along with justification for their values.

For data presented in Figure 6.6 and Figure 6.8, KPFM measurements were carried out with V_{AC} = 500mV, at a lift height of 15 nm and a scan rate of 0.1 Hz. Domain wall contrast was successfully imaged for lift heights as low as 9 nm without reduction of V_{AC}, however the significantly reduced margin of error for the feedback loop corresponded to more frequent tip-sample crashes, particularly over the long operation times. A lift height of 15 nm was chosen as facilitating potential mapping with sufficient spatial resolution while allowing tip crashes to be avoided with conscientious operation.

Slower scan rates were observed to reduce noise and increase system stability. Operating in interleave mode, however, doubles the time taken to complete each scan line. For a typical image resolution of 256 scan lines, 0.1 Hz with interleave corresponds to 85 minutes per scan. This was chosen as the lower limit compromise between system stability and ease of use. Additionally, while scanner drift is generally only a concern at small (unit micron) scan sizes, in interleave mode protracted scan times can lead to sufficient drift between main and interleave trace such that the topographic profile followed by the tip in interleave is no longer accurate[34].

Scanning resolution had an unexpectedly significant effect on stability, as despite smooth sample topography (~ 1.2 nm root mean square roughness) a low number of samples per line resulted in inconsistent potential mapping. A more detailed topographic trace was required for smooth imaging of the majorly flat surface potential of the bulk crystal. To maximise stability a rectangular image resolution was chosen of 256 lines with 512 samples per line.

The resonant frequency is determined by the Nanoscope software, however the user should ensure to tune the tip in the presence of the maximum lateral potential and magnetic field and as close to the surface as possible. While the values for resonant frequency and drive amplitude obtained by tuning in this manner provided accurate topography mapping with or without applied field, tuning in zero field resulted in poor topography under field and an unstable lift height.

6.6 Conclusions

Employing KPFM represents a significant advancement over the indirect method of imaging the Hall potential via intermittent contact AFM. Directly mapping the local surface potential allows the resultant data to be intuitively understood without consideration for the quadratic behaviour of the topographic trace (discussed in section 5.4.1).

Measurements were performed in air necessitating the use of amplitude modulated detection, which is generally disfavoured for quantitative measurement due to increased convolution of the signal collected at the tip by the cantilever. In spite of this, calibration measurements on a reference sample confirmed good quantitative accuracy with the principal error introduced by an appreciable ± 25 mV noise. The measured noise level was amplified due to external instrumentation used in calibration. Regardless, the impact of the noise is reduced on analysis as rather than considering points in isolation, the full Gaussian profile of potential across the wall is plotted and averaged over multiple scan lines for each wall.

Effective operation in air is advantageous due to the higher prevalence of ambient atomic force microscopes, attributable to the lower equipment cost and increased ease of use in comparison to vacuum AFM. Equivalently though, the methodology can be employed under vacuum using frequency modulated KPFM, without requiring any modification of the procedure or the recommended scan parameters. This would effectively eliminate the signal convolution due to the cantilever while, due to the increased Q factor from operating in vacuum, increasing measurement resolution and reducing the noise floor.

Nonetheless, despite its quantitative superiority, the KPFM method is inherentely restricted in that the maximum potential available for driving the lateral current is dictated by the typically low compliance voltage of the feedback electronics, 10 V for the in-house system. The benefit of the indirect approach of intermittent contact AFM is that, in theory, there is no limitation on the lateral potential. The only requirement is establishing a stable topographic trace. Considering the successful imaging of domain wall potential with a 100 V applied bias was achieved with a nominal 2 V deflection setpoint, the robustness of the microscale electrode geometry under high bias is likely a more pragmatic limiting factor.

Now equipped with two complementary techniques for measuring the Hall potential along a conducting domain wall, the carrier properties of each single crystal system known to exhibit domain wall conduction await analysis. In the more immediate future, a smaller electrode geometry is to be sputtered on the large domain $ErMnO_3$ sample so that the current can be directed along individual conducting domain walls. Thus, allowing the carrier density and mobility at both head-to-head and tail-to-tail walls to be calculated with greater accuracy.

6.7 References

1. Nonnenmacher, M., O'Boyle, M. P. & Wickramasinghe, H. K. Kelvin probe force microscopy. *Appl. Phys. Lett.* **58,** 2921–2923 (1991).

2. Thierry, M., Zdrojek, M. & Brunel, D. Electrostatic Force Microscopy and Kelvin Force Microscopy as a Probe of the Electrostatic and Electronic Properties of Carbon Nanotubes. *Scanning Probe Microsc. Nanosci. Nanotechnol.* 89–128 (2010).

3. Melitz, W., Shen, J., Kummel, A. C. & Lee, S. Kelvin probe force microscopy and its application. *Surf. Sci. Rep.* **66,** 1–27 (2011).

4. Glatzel, T., Lux-Steiner, M. C., Strassburg, E., Boag, A. & Rosenwaks, Y. in *Scanning Probe Microscopy* 113–131 (Springer New York).

5. Sadewasser, S. in *Kelvin Probe Force Microscopy* 12–14 (Springer, 2012).

6. Kelvin, Lord. Contact electricity of metals. *Philos. Mag. Ser. 5* **46,** 82–120 (1898).

7. Mélin, T., Zdrojek, M. & Brunel, D. in *Scanning Probe microscopy in Nanoscience and Nanotechnology* 89–128 (2010).

8. Sze, S. M. in *Physics of Semiconductor Devices* 134–136 (John Wiley & Sons, Ltd, 2007).

9. Surplice, N. A. & D'Arcy, R. J. A critique of the Kelvin method of measuring work functions. *J. Phys. E.* **37,** 477–482 (1970).

10. Glatzel, T., Lux-Steiner, M. C., Strassburg, E., Boag, A. & Rosenwaks, Y. in *Scanning probe Microscopy: Electrical and Electromechanical Phenomena at the Nanoscale* 115 (Springer, 2007).

11. Zisman, W. A. A new method of measuring contact potential differences in metals. *Rev. Sci. Instrum.* **3,** 367–370 (1932).

12. Sadewasser, S. in *Kelvin Probe Force Microscopy* 19–21 (Springer, 2012).

13. Glatzel, T., Lux-Steiner, M. C., Strassburg, E., Boag, A. & Rosenwaks, Y. in *Scanning probe Microscopy: Electrical and Electromechanical Phenomena at the Nanoscale* 115–118 (2007).

14. Kitamura, S. & Iwatsuki, M. High-resolution imaging of contact potential difference with ultrahigh vacuum noncontact atomic force microscope. *Appl. Phys. Lett.* **72,** 3154–3156 (1998).

15. Giessibl, F. J., Bielefeldt, H., Hembacher, S. & Mannhart, J. Calculation of the optimal imaging parameters for frequency modulation atomic force microscopy. *Appl. Surf. Sci.* **140,** 352–357 (1999).

16. Glatzel, T., Sadewasser, S. & Lux-Steiner, M. C. Amplitude or frequency modulation-detection in Kelvin probe force microscopy. *Appl. Surf. Sci.* **210,** 84–89 (2003).

17. Girard, P. Electrostatic force microscopy: principles and some applications to semiconductors. *Nanotechnology* **12,** 485–490 (2001).

18. Belaidi, S., Girard, P. & Leveque, G. Electrostatic forces acting on the tip in atomic force microscopy: Modelization and comparison with analytic expressions. *J. Appl. Phys.* **81,** 1023–1030 (1997).

19. Elias, G. *et al.* The role of the cantilever in Kelvin probe force: Microscopy measurements. *Beilstein J. Nanotechnol.* **2,** 252–260 (2011).

20. Hochwitz, T., Henning, A. K., Levey, C. & Daghlian, C. Capacitive effects on quantitative dopant profiling with scanned electrostatic force microscopes. *J. Vac. Sci. Technol. B Microelectron. Nanom. Struct.* **14,** 1–9 (1996).

21. Koley, G., Spencer, M. G. & Bhangale, H. R. Cantilever effects on the measurement of electrostatic potentials by scanning Kelvin probe microscopy. *Appl. Phys. Lett.* **79,** 545–547 (2001).

22. Zerweck, U., Loppacher, C., Otto, T., Grafström, S. & Eng, L. M. Accuracy and resolution limits of Kelvin probe force microscopy. *Phys. Rev. B - Condens. Matter Mater. Phys.* **71,** 125424 (2005).

23. Panchal, V., Pearce, R., Yakimova, R., Tzalenchuk, A. & Kazakova, O. Standardization of surface potential measurements of graphene domains. *Sci. Rep.* **3,** 2597 (2013).

24. Enevoldsen, G. H., Glatzel, T., Christensen, M. C., Lauritsen, J. V. & Besenbacher, F. Atomic scale Kelvin probe force microscopy studies of the surface potential variations on the TiO2(110) surface. *Phys. Rev. Lett.* **100,** 236104 (2008).

25. Albrecht, T. R., Grütter, P., Horne, D. & Rugar, D. Frequency modulation detection using high-Q cantilevers for enhanced force microscope sensitivity. *J. Appl. Phys.* **69,** 668–673 (1991).

26. Ziegler, D. & Stemmer, A. Force gradient sensitive detection in lift-mode Kelvin probe force microscopy. *Nanotechnology* **22,** 75501 (2011).

27. Glatzel, T., Lux-Steiner, M. C., Strassburg, E., Boag, A. & Rosenwaks, Y. in *Scanning probe Microscopy: Electrical and Electromechanical Phenomena at the Nanoscale* 118–119 (Springer, 2007).

28. Polak, L. & Wijngaarden, R. J. Preventing probe induced topography correlated artifacts in Kelvin Probe Force Microscopy. *Ultramicroscopy* **171,** 158–165 (2016).

29. Cohen, G. *et al.* Reconstruction of surface potential from Kelvin probe force microscopy images. *Nanotechnology* **24,** 295702 (2013).

30. Nony, L., Bocquet, F., Loppacher, C. & Glatzel, T. On the relevance of the atomic-scale contact potential difference by amplitude-modulation and frequency-modulation Kelvin probe force microscopy. *Nanotechnology* **20,** 264014 (2009).

31. Jacobs, H. O., Knapp, H. F. & Stemmer, A. Practical aspects of Kelvin probe force microscopy. **70,** 1756–1760 (1999).

32. Mundy, J. A. *et al.* Functional electronic inversion layers at ferroelectric domain walls. *Nat. Mater.* **16,** 622–627 (2017).

33. Horcas, I. *et al.* WSXM: A software for scanning probe microscopy and a tool for

nanotechnology. *Rev. Sci. Instrum.* **78,** 13705 (2007).

34. Sadewasser, S. in *Kelvin Probe Force Microscopy* 20–21 (Springer, 2012).

7 Two Probe Measurement of Domain Wall Conductance

The thesis so far has concerned the development of a technique to measure the Hall Effect within a conducting domain wall, as the resultant potential grants a comprehensive analysis of the conductive properties by revealing local carrier density and mobility. This chapter details an improved method for the more basic measurement of conductance at an individual domain wall.

Collating studies on conducting ferroelectric domain walls, for a full summary see section 1.6, reveals conductive atomic force microscopy (c-AFM) to be by far the most prevalent technique for measuring domain wall conductance. The utility of c-AFM cannot be understated and the field of domain wall nanoelectronics would not have progressed as rapidly without the ease with which c-AFM facilitates spatial mapping of current on the nanoscale. However the repositionable nature of the submicron AFM tip which enables high-resolution mapping carries a characteristic uncertainty in the consistency of the electrical contact.

During spatial mapping the tip-sample contact is inherently variable, dependent on the feedback electronics' ability to maintain a constant deflection set point[1–3]. Additionally, rastering in contact with the sample wears the tip over time, deforming the shape and size of the contact made with the sample and may, in the case of coated silicon probes, remove conductive coating[4,5]. These issues can be combated by use of conductive diamond probes or low contact forces, though the latter exacerbates feedback stability issues and the former comes at considerable expense.

These issues pervade into spectroscopic c-AFM, wherein an IV curve is recorded for a fixed spatial point, as the formation of a Schottky barrier between tip and sample[6–8] (discussed in section 4.2) requires current measurement over protracted timescales to ensure steady-state has been reached. Thermal drift, which is minimal when mapping a large area[9], becomes substantial when attempting a stationary measurement, more-so when recording an array of IV curves across a sample. The quantitative

shortcomings of c-AFM are widely recognized[2,4,10–12], which has catalysed the application of alternative techniques for local measurement of conductance on the nanoscale[10,13–17].

In this chapter a traditional pair of deposited electrodes is used to measure the conductance of an individual domain wall. Commonly used for bulk measurements over multiple domain walls[18–23], the basic technique does not readily scale to a single wall; due to the typically (but not universally[24]) high resistance of the nanoscale conducting channel and correspondingly minute driven current available for measurement. Herein we employ a technique developed by Keithley Instruments[25], were by applying bias in a low frequency square wave and using a low pass filter, extraneous signal can be eliminated and the driven current measured. A benefit of this traditional electrode geometry, beyond ease of use, is the facility to optimise the electrode material and deposition procedure to minimise the Schottky barrier and achieve an ohmic metal-semiconductor contact[7,8,26].

The work presented in this chapter was motivated by collaboration with E. Soergel at Bonn University who provided single crystal samples of congruent $LiNbO_3$, engineered to express maximally charged head-to-head domain walls of millimetre length scales, with the aim of accurately measuring the domain wall conductance. Using the improved two probe methodology the conductance of an individual conducting head-to-head domain wall is precisely measured. Additionally conductance is measured as a function of temperature to determine whether the walls express metallic or semiconducting behaviour.

7.1 Crystal Structure of Lithium Niobate

7.1.1 The Ferroelectric Phase

At room temperature $LiNbO_3$ is a proper ferroelectric with rhombohedral point group 3m (space group R3c) [27–29] and a uniaxial spontaneous polarisation. The high temperature paraelectric phase is also rhombohedral with point group -3m, however the Curie temperature ($T_C \approx$ 1479K) is marginally higher than the melting point of

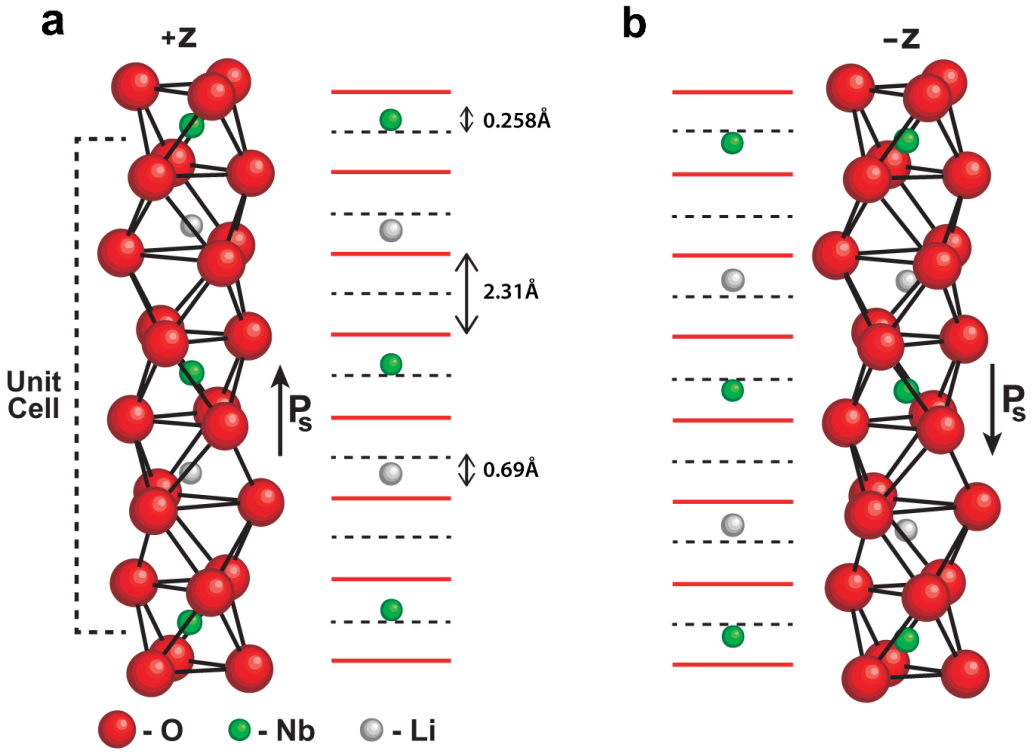

Figure 7.1 a Structure of stoichiometric lithium niobate in the ferroelectric phase, depicted with orthohexagonal axes for clarity. Oxygen ions form stacked, alternately tiled octahedra with the oxygen ions lying in planes normal to the *z*-axis. Octahedra are occupied by a single ion with the sequence, Nb^{5+} - Li^{+} - □ - Nb^{5+} - Li^{+} - □ …, where □ represents a vacant octahedron. Spontaneous polarisation P_s arises from the displacement of the Li^{+} and Nb^{5+} ions along the *z*-axis, by 0.690 Å and 0.258 Å respectively. **b** Oppositely polarised structure depicting ion displacements. Figure adapted from [30,31] and atomic values taken from [27]

1475K[32,33]. The melting point increases and T_C decreases for increasingly non-stoichiometric samples. Significance of stoichiometry is discussed in more detail in section 7.1.2.

The unit cell of the ferroelectric phase is typically depicted using orthohexagonal axes[31,34] as the crystal structure is more readily understood when each ion position is defined by its displacement from an idealised hexagonal structure[35]. Within the unit cell, depicted in Figure 7.1a, the oxygen ions form stacked octahedra, tilted such that the oxygen ions lie in parallel sheets regularly spaced along the z-axis. Moving along the z-axis the octahedra are each filled with an ion with the sequence (Nb^{5+} - Li^{+} - □ - Nb^{5+} - Li^{+} - □ …) where □ denotes an empty octahedron. Both the Li^{+} and Nb^{5+} ions

are positioned off-centre within the octahedra, by 0.690 Å and 0.258 Å respectively[27], which leads to a relative displacement of the centres of negative and positive charge. The polarisation direction is determined by the positioning of the Li^+ and Nb^{5+} along the c-axis and polarisation reversal is facilitated by motion of Li^+ into the adjacent vacant octahedron and reversal of the direction of off-centre displacement of Nb^{5+} [31], as depicted in Figure 7.1b.

7.1.2 Stoichiometric and Congruent Lithium Niobate

$LiNbO_3$ single crystals are commonly produced by the Czochralski process wherein a seed crystal is placed in the melt to promote nucleation and then slowly removed to produce a long single crystal[36,37]. The relative molar concentration of Li and Nb ions in the melt will determine the composition of the grown crystal, as seen from the phase diagram in Figure 7.2. Equal molar concentrations of Li and Nb in the nucleated crystal corresponds to a stoichiometric composition, whereas any deviation from this represents a congruent composition. The phase range for homogenous nucleation of $LiNbO_3$, marked in blue, lies entirely within the Li deficient region, with the ideal stoichiometric composition aligned at the boundary. In practice the instability of the homogenous nucleation at the stoichiometric point results in variation of the crystal composition throughout growth[38]. To obtain large-scale uniform crystals with a high degree of homogeneity, a Li deficient congruent melt ratio is commonly used, with a possible Li deficiency of down to 48.5% [39].

A 48.5% Li concentration corresponds to a vacancy at ~ 6% of Li^+ ion sites, consequently within congruent $LiNbO_3$ point defects form as local restructuring occurs in an attempt to compensate for the charge imbalance. The defective structure of congruent $LiNbO_3$ is not explicitly known, with several models proposed in literature[31,40–42]. However, there are some general statements which can be made. For increasingly Li deficient compositions, the density of $LiNbO_3$ has been shown to increase[43]. This supports the partial occupation of Li^+ sites by Nb^{5+} ions, termed a niobium antisite, as Nb^{5+} has a smaller ionic radius (64 pm versus 76 pm for Li^+)[44]. Structural analysis[45,46] via x-ray and neutron diffraction reports minimal evidence for presence of oxygen vacancies and theoretical modelling[47] predicts that oxygen vacancies

are energetically unfavourable. Calculations also show that formation of a Nb^{5+} vacancy is energetically unfavourable in comparison to a Li^{+} vacancy[31,40].

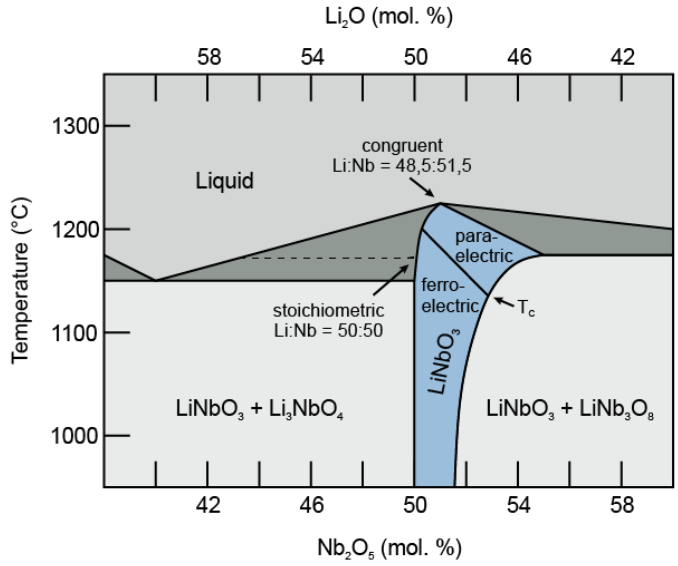

Figure 7.2 Phase diagram for the Li_2O - Nb_2O_5 system. Shaded blue region corresponds to homogenous growth of $LiNbO_3$ with stoichiometric $LiNbO_3$ corresponding to the line at 50:50 molar ratio. In practice stoichiometry is not achieved and lithium deficient congruent samples are grown. Figure adapted from [38].

7.2 Dark Conductance of Head-to-Head Domain Walls in $LiNbO_3$

The congruent $LiNbO_3$ samples received were rectangular in dimension, with the polarisation direction perpendicular to the long axis, and each expressed a single maximally charged head-to-head domain wall permeating through the 500 μm depth and along the full 5 mm length of the crystal, as sketched in Figure 7.3a. Both x-cut and y-cut samples were received, defined by the y-axis and x-axis parallel to the long side of the crystal respectively, though throughout the investigation no significant difference was observed in the domain structure or domain wall conductance of each orientation.

Mapping the domain wall structure via piezoresponse force microscopy (PFM), representative data presented in Figure 7.3b, the wall meanders significantly occasionally turning back on itself to form tail-to-tail wall segments and providing a

full range of domain wall angles. Nonetheless, uncharged wall segments are in the minority with the clear majority of the domain wall intersecting the polarisation axis in defiance of the increased energetic cost of local divergence in polarisation. Additionally, smaller domains were observed either side of the wall. PFM mapping of opposite faces suggested these smaller domains are enclosed, not extending to the bottom face. This was corroborated by the head-to-head walls of the smaller domains exhibiting conductance with lateral electrode configuration but not through depth.

Given the apparently stable yet typically unfavourable domain configuration, vector PFM was performed to verify the polarisation axis ran orthogonal to the length of crystal. Herein the crystal was rotated through 360° in 45° intervals and for each rotation lateral PFM was recorded on the same segment of the domain wall, with cantilever parallel and perpendicular to the long edge of the crystal corresponding to 0° and 90° respectively. The phase map recorded at 90° rotation is displayed in Figure 7.3c. The amplitude of the piezoresponse in lateral operation is maximal when the polarisation axis is perpendicular to the cantilever (see section 2.2 for detail on operation of PFM). Therefore, by plotting the measured amplitude against the rotation angle the polarisation axis can be determined to within the resolution of the rotation interval. For each recorded amplitude map the distribution of amplitude measurements was plotted, a curve fitted and the voltage taken from the peak of the curve. The full range of collected PFM maps, phase and amplitude, are presented in appendix A1 along with plots of the raw amplitude distributions.

The amplitude signal is plotted as a function of sample rotation in Figure 7.3e. A guide line, shown in blue, is overlaid to highlight the two peaks at 90° and 270° which verify the polarisation axis was perpendicular to the long edge of the crystal. The significantly diminished response for all scans beyond 180° was due tip wear degrading the electrical contact and reducing how effectively the AC bias could be applied to the sample.

Through depth c-AFM was performed across the same wall segment, current map presented in Figure 7.3d, with bias applied to a gold bottom electrode and current measured with an earthed tip. Notably, unlike the principal study of Schröder *et al.*[20]

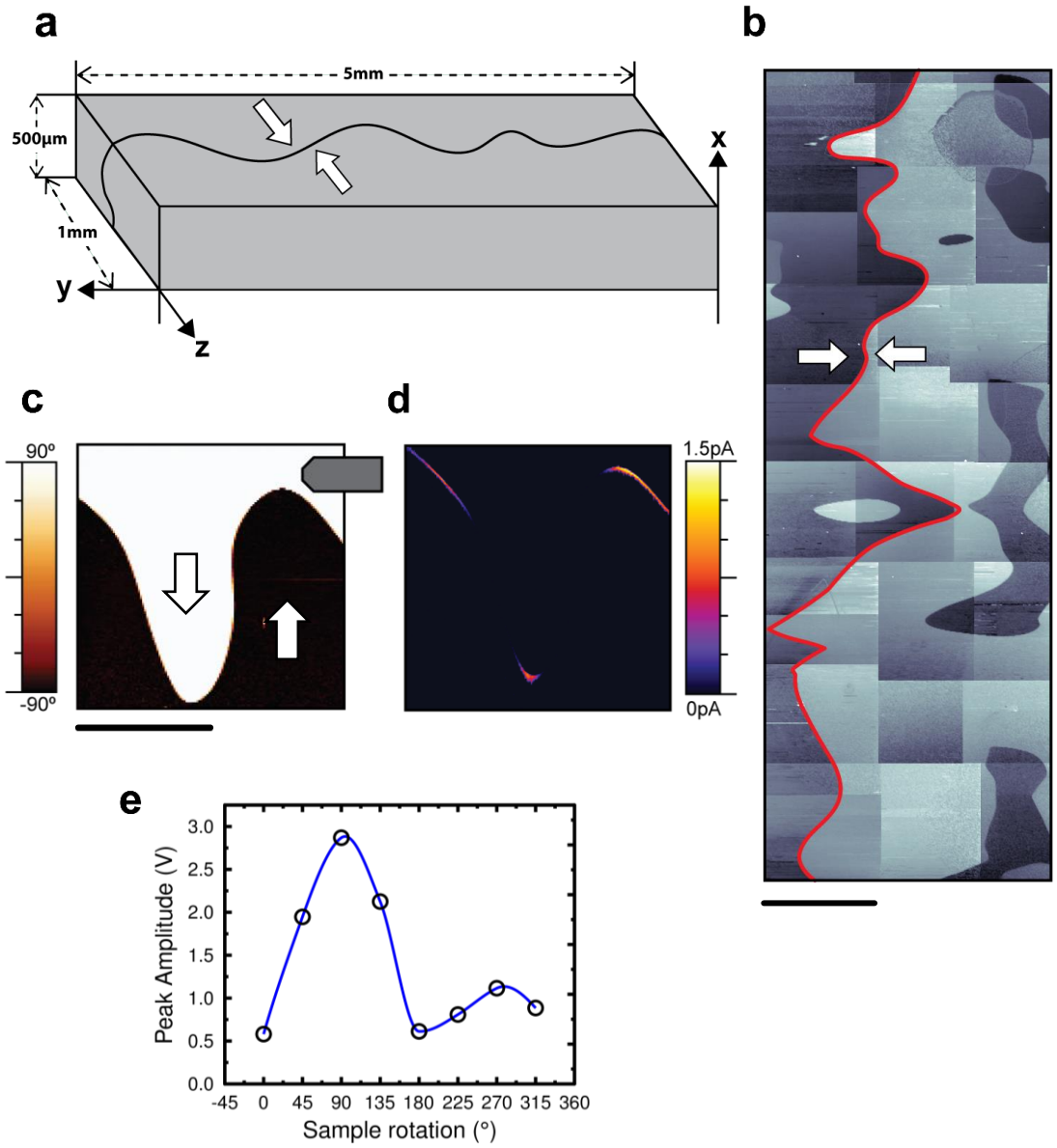

Figure 7.3 a Schematic of the congruent $LiNbO_3$ single crystal samples, conveying the central head-to-head domain wall. Labelled axes correspond to x-cut sample. **b** Section of the central head-to-head domain wall of x-cut $LiNbO_3$ sample, conveying curved meandering wall structure. Imaged via a series of lateral PFM phase maps. Red guide line overlaid to mark central wall. Scale bar 20 µm. **c & e** Vector PFM was performed on a section of the domain wall image in **b**, sample rotated from 360° and imaged in 45° intervals. **c** Phase for 90°, cantilever parallel to the long edge of the crystal, conveying full 180° phase inversion. **e** Central peak of histogram of measured amplitudes plotted against angle. Blue line overlaid as guide, showing two peaks at 90° and 270° verifying polarisation axis is orthogonal to long edge of crystal. **d** c-AFM map of the domain wall segment in **c**, recorded at - 8V, showing maximal conductance for maximal divergence in the polarisation. Scale bar for **b** is 100 µm and for **c**, **d** 40 µm.

that originally reported increased conductance at head-to-head domain walls in $LiNbO_3$, these measurements were performed without super-band gap illumination, *i.e.* generation of photo-carriers was not required.

On visual comparison of the c-AFM and PFM maps, it is apparent that the regions of greatest conductance correspond to maximally charged head-to-head orientation with the measured current decreasing as wall angle approaches parallel with polarisation axis. The absolute current measured was low with a maximum of 1.6 pA measured for a -8 V sample bias, corresponding to a conductance of $2x10^{-13}$ S. At the equivalent domain wall angle Schröder *et al.* reported, after scaling the measured currents to a 500 μm sample thickness, a significantly greater conductance of $8x10^{-13}$ S under ultraviolet (UV) illumination. However, given the small unit picoamp currents, variations in the experimental procedure that causes a minor variation in absolute current measured, such as decreased scan rate, will have a substantial effect on the relative conductance.

Conduction mapping of a tail-to-tail wall segment is not presented as the domain wall conductance was indiscernible from the bulk, with the signal for both below the noise floor of c-AFM. The zero current measured for the ferroelectric bulk is unsurprising given a maximum conductivity of ~ 10^{-15} Sm^{-1} reported in literature[48]. Consequently it could not be determined whether the local conductance at tail-to-tail domain walls is equivalent to or lower than bulk.

Of note, in order to measure domain wall conductance, a gold bottom electrode had to be sputtered onto the crystal in lieu of solely silver dag, as used in-house for measurements on the hexagonal manganites and Cu-Cl boracite. No discernible current was measured with a silver dag electrode despite application of biases of up to - 40 V.

7.3 Problems in IV Measurement of High Resistance Samples

The experimental layout is depicted in the schematic in Figure 7.4a. An array of gold stripe electrodes was sputtered on to an x-cut $LiNbO_3$ crystal, orientated parallel to z-axis and covering the full width of the face, trapping independent segments of the central charged domain wall within 30 μm inter-electrode gaps. PFM and c-AFM mapping was performed within the interelectrode regions to determine which electrodes were connected by a continuously conducting domain wall pathway, with some found to be linked by up to three conducting walls due to bubble domains. The sample was placed under a Semiprobe brand ambient probe station which incorporated an optical microscope to facilitate the manual contacting of electrodes with Micromanipulator probes, model 7B-100. Electrical characterisation was carried out with a Kiethley 237 source-measure unit chosen for its large 10^{14} Ω input impedance and high current resolution of 20 fA.

Initial conductance measurements were promising with the trapped segments of conducting domain wall exhibiting a linear current response symmetric about zero, indicative of an ohmic metal-semiconductor contact[7,49,50]. An example data set is presented in Figure 7.4b, displaying current measured across a single domain wall from -10 V to 10 V. The linear response is in stark contrast to the pronounced Schottky behaviour characteristic of c-AFM measurements, see section 1.6 for examples from literature, wherein conductance is dominated by the current transport past the potential barrier formed between tip and sample, masking the bulk behaviour. The overt indicator of a reduced Schottky barrier in comparison to c-AFM was the symmetrical conductance profile, as for c-AFM mapping of $LiNbO_3$ domain wall current could only be imaged under negative bias.

A linear response between current and voltage is necessary but not sufficient to confirm the absence of a Schottky barrier[51], the Simmons emission mechanism is noted where the current transport through the Schottky barrier is approximately linear under low voltage[52]. Nonetheless, the possibility of an ohmic contact is an improvement over the non-ohmic contact conveyed by the Schottky curves typically recorded with c-AFM.

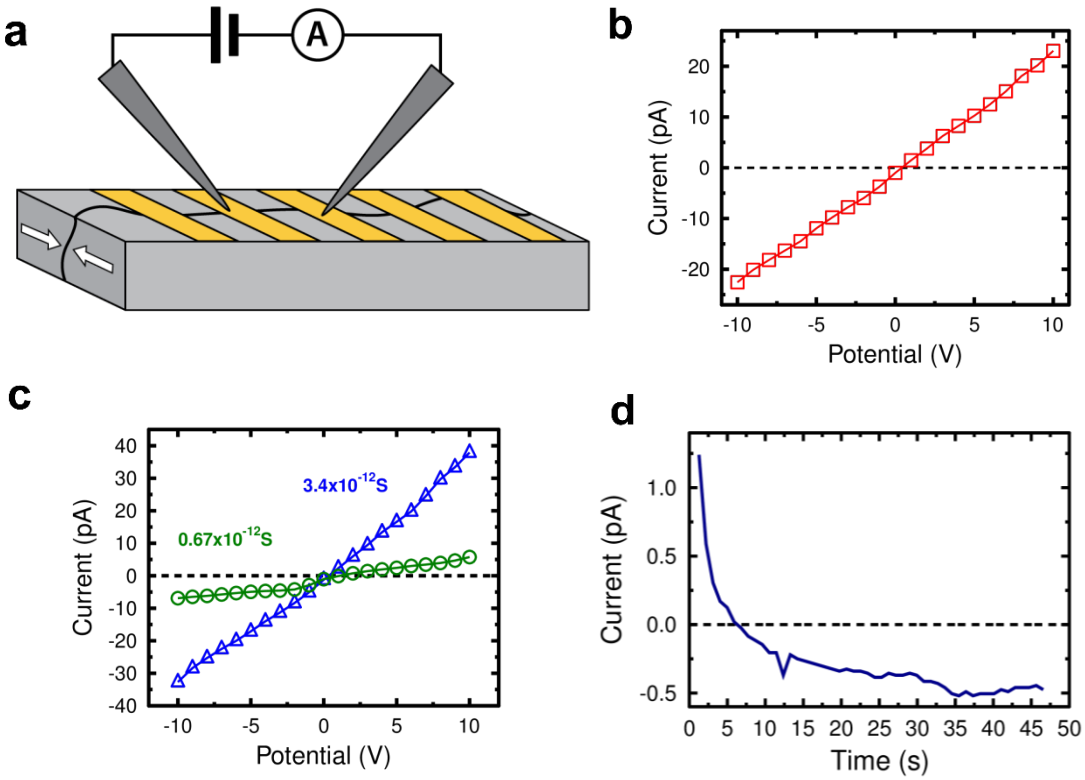

Figure 7.4 a Schematic of experimental set up. An array of gold electrodes was sputtered on x cut $LiNbO_3$, trapping segments of central head-to-head within 30 μm inter-electrode gaps. **b** IV profile recoded across a single domain wall, conveying a strongly ohmic response. **c** Repeat measurements across the wall in b returned linear profiles but with consistently varying conductance. Maximum and minimum measured conductance is plotted. **d** Current measured over time, under 10 V bias, exhibiting a capacitive decay through zero and indicating the driven current is masked by extraneous background currents.

The limitations of the traditional IV methodology, wherein a DC bias is applied and the current measured, became apparent when attempting to reproduce measurements. Repeated IV measurements, performed same on the wall as in Fig 7.4b, returned consistently varying resistances. The profiles corresponding to the maximum and minimum recorded conductance are plotted in Figure 7.4c. Despite the large spread of conductance values, the individual IV profiles exhibited strong linearity with minimal scattering, suggesting negligible measurement noise.

Applying a fixed bias and measuring the change in conductance over time, the characteristic decaying current of a charging capacitor was observed with a short time constant on the order of 10 s (variable dependent on interelectrode structure). In

contrast to resistor capacitor (RC) circuit behaviour previously discussed in section 4.2 which indicated a large contact resistance, the current profile was due to the inter-electrode region exhibiting dielectric absorption[53–56]. In addition to the driven current due to drift of free charge carriers there is a polarisation current due to the slower response of the bound ions displacing under electric field[57]. This polarisation current is transient and approaches zero as the dielectric approaches the maximally polarised state for the applied electric field. Therefore upon reaching a steady state the measured current should represent the true inter-electrode resistance.

However in the case of measurements with comparatively low current, such as under low bias or for domain wall segments of greater resistance, the measured current decayed through zero (as shown Figure 7.4e) indicating a negative resistance. A negative current under positive bias is clearly erroneous and suggests the presence of further background currents of sufficient magnitude to mask the driven current.

Additional background currents may be extrinsic or intrinsic in origin. Dependent on crystal structure, the dielectric absorption can be a combinative process as substructures of differing polarisability generate distinct polarisations currents on differing time scales[53,56,58]. Such as localised space-charges within the crystal, which form at regions of conductive inhomogeneity[59]. At a more tangible level, background current may be induced by ambient conditions during testing as, given the reduced signal level, ordinarily negligible pyroelectric, piezoelectric and photoelectric currents can be substantial. A criterion for high resistivity measurements in industry is that the sample be enclosed in a guarded housing to minimise ambient variance[60–62]. During characterisation of $LiNbO_3$, the measured current was found to dependent on the ambient light level as steps in the current profile were generated by blocking light from the crystal.

Instrumentation can also generate background currents in the form of stray impedance due to low amplitude AC voltages offset upon the applied DC bias. Stray impedance may stem from capacitive coupling along cables, vibrational noise, inductance from ambient electromagnetic signals and earth noise from other electronics sharing the ground line.

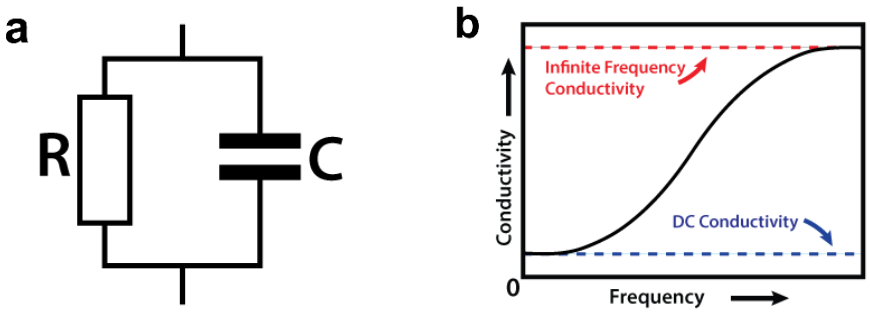

Figure 7.5 a Diagram of a simple RC circuit element, with a resistor (R) and capacitor (C) in parallel. **b** Conductivity of a dielectric as a function of frequency of an applied bias. Figure **b** adapted from [56].

As stated previously dielectric materials exhibit capacitive behaviour and equivalent circuit modelling has shown they behave analogously to a complex network of resistors and capacitors in parallel[53,54,63]. Simplifying for discussion, the materials behaviour may be modelled as a single RC element, as shown Figure 7.5a. The impedance, Z, is a complex quantity given by the sum of resistance, R, and reactance, X, as shown in (7.1).

$$Z = R + iX \tag{7.1}$$

An ideal resistor has zero reactance while an ideal capacitor has zero resistance, thus the magnitude of net impedance (Z_T) for the circuit is given by:

$$\left|\frac{1}{Z_T}\right| = \frac{1}{R} + \frac{1}{X_C} \tag{7.2}$$

Where R is the resistance of the resistor and X_c the reactance of the capacitor. The reactance of the capacitor, X_c is given by:

$$X_c = \frac{1}{2\pi f C} \tag{7.3}$$

Where C represents the capacitance and f the frequency of the applied voltage. For an ideal DC signal of zero frequency, the capacitor reactance is infinite. Therefore

from (7.2) the measured impedance is equal to the static resistance of the system. If an additional AC signal is offset on the DC bias, however, the AC potential will experience a finite reactance and generate a current corresponding to the lower net impedance.

A schematic of the conductivity of a dielectric material as a function of frequency is presented in Figure 7.5b. In typical operation the AC offset is orders of magnitude lower than the applied DC potential and the currents corresponding to stray impedance can be disregarded[60,62]. In the case of large resistance, dependent on the frequency of the AC offset the alternating current corresponding to the stray impedances may be on the order of the static current from the DC potential.

7.4 Alternating Polarity Method for Improved High Resistance Measurement

Observing the negative resistance conveyed by Figure 7.4d, it is evident that the resistance along an individual head-to-head domain wall in $LiNbO_3$ is sufficiently great that under basic DC measurement the signal is dominated by background currents, regardless of their origin. The "alternating polarity method", as described in a white paper by Keithley Instruments[25], uses a square wave potential with a protracted period to measure the impedance at a very low frequency where it is equivalent to the static DC resistance. The measured current profile, a convolution of driven current and background currents, is sampled with the periodicity of the applied square wave potential and the sample data filtered using a moving average weighted by the binomial coefficients. In effect this acts as a Gaussian filter, centred upon the sampling frequency, removing or reducing signal components of differing frequency.

It would be an egregious error to imply that the methodology outlined here, precise impedance measurement by way of a frequency filter, is a novel one. Difference bridge circuits have been used for the analogue filtering of stray impedance since their development by Christie and Wheatstone in the mid 1800s[64–66]. Digital signal demodulation via frequency-response-analysers, operating on the same principle as the lock-in amplifier discussed in section 2.2.1, has been a staple of impedance

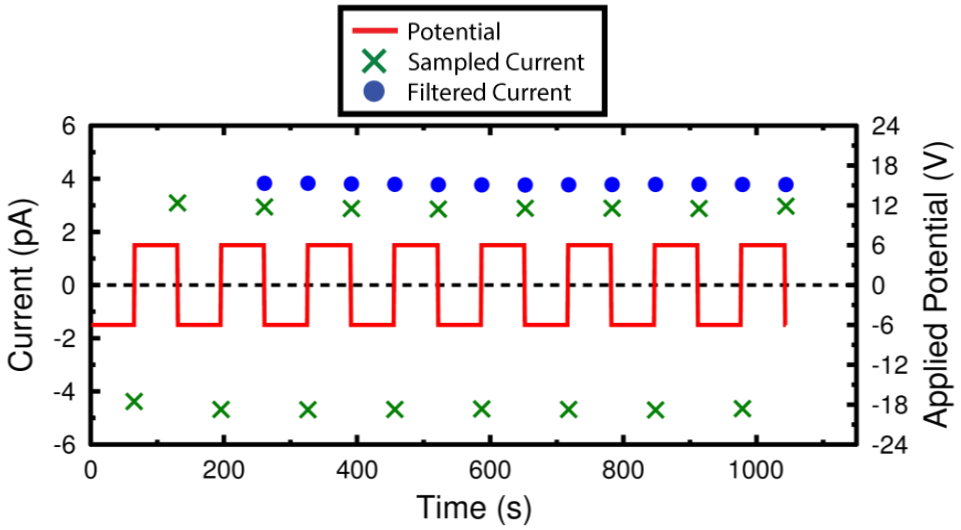

Figure 7.6 Diagram of the alternating polarity method. A low frequency square wave potential is applied with pulse length 65 s, and the current recorded at the trailing edge of each peak, marked by green cross. A binomial filter, 4 point moving average weighted by the 3rd order binomial coefficients, is applied to sampled current values to produce filtered current values, marked by blue circles. The binomial filter removes signal components of differing frequency to the sampling frequency. By applying bias with sufficiently low frequency, the DC impedance is measured in absence of background currents.

spectroscopy since their widespread commercial availability in the 1970s[63]. Even within the narrow field of conducting ferroelectric domain walls, frequency-response-analyzers have been successfully used to measure the AC conductivity across bulk domain wall networks[18,23]. The chief advantage of the alternating polarity method is the simplicity of its operation and the transparency of the demodulation process, with the binomial filter calculable by hand.

Figure 7.6 plots the application of a 6 V square wave, across a single domain wall, with a pulse width of 65 s corresponding to measuring the impedance at 15 mHz. This length was chosen as it was the maximum programmable delay between bias and measurement on the Kiethley 237. Current measurements were synchronised with the bias frequency and also recorded at intervals of 65 s, corresponding to the falling edge of each pulse. The lower the frequency of the square wave potential, the greater the time allowed for the dielectric to reach a steady-state and additionally the lesser the significance of any latency between applied bias and measured current.

A nth order binomial filter is then applied by taking a weighted moving average of the sampled current with the weighting factors corresponding to the binomial coefficients of the nth row of Pascal's triangle[67,68]. For example sampled data corresponding to the measurements in Figure 7.6 are listed in Table 7.1.

Applied Potential (V)	Recorded Current (pA)
-6	-4.38
6	3.09
-6	-4.68
6	2.94
-6	-4.69
6	2.88

Table 7.1 The raw recorded current values which where sampled at 65 s intervals, corresponding to the sampled current values plotted in Figure 7.6, listed alongside the potential applied during each measurement.

A 3rd order binomial filter was applied to the data thus from inspection of Pascal's triangle shown in Figure 7.7a a 4 point moving average was taken with the weighting of (1/8, 3/8, 3/8, 1/8) as demonstrated for first two values in (7.4) and (7.5).

$$\left(\frac{(-)(-4.38)+(3)(3.09)+(-3)(-4.68)+(2.94)}{8}\right)=3.829 \qquad (7.4)$$

$$\left(\frac{(3.09)+(-3)(-4.68)+(3)(2.94)+(-)(-4.69)}{8}\right)=3.830 \qquad (7.5)$$

Note the measured current is multiplied by the sign of the applied bias as it is the impedance response which is filtered and a negative current under negative bias corresponds to positive impedance. If a positive current were measured under negative bias, akin to Figure 7.4e, the resultant negative term in the moving average would signify the negative impedance. Continuing the moving average for the full data set, the filtered current values are plotted on Figure 7.6 for comparison. It is clear from inspection that the filtered current shows minimal fluctuation, with the

difference between largest and lowest magnitude current equal to 0.06 pA in comparison to 1.84 pA for of the unfiltered current.

To convey the operation of the binomial filter, the sample weighting of the 2nd, 4th and 16th orders are plotted as a function of time in Figure 7.7b. The binomial coefficients approximate the shape of a Gaussian, with the higher order filters representing a closer approximation. The significance of this is taking the Fourier transform of a Gaussian response over time reveals a Gaussian distribution in the frequency domain, as shown Figure 7.7c, with a higher order binomial filter corresponding to a more narrow range of unattenuated frequencies[69,70]. Therefore, by sampling with the bias period and weighting the data by the binomial coefficients, any currents of differing frequency to the applied potential are attenuated or nullified dependent on their proximity to sample frequency and the order of the binomial filter.

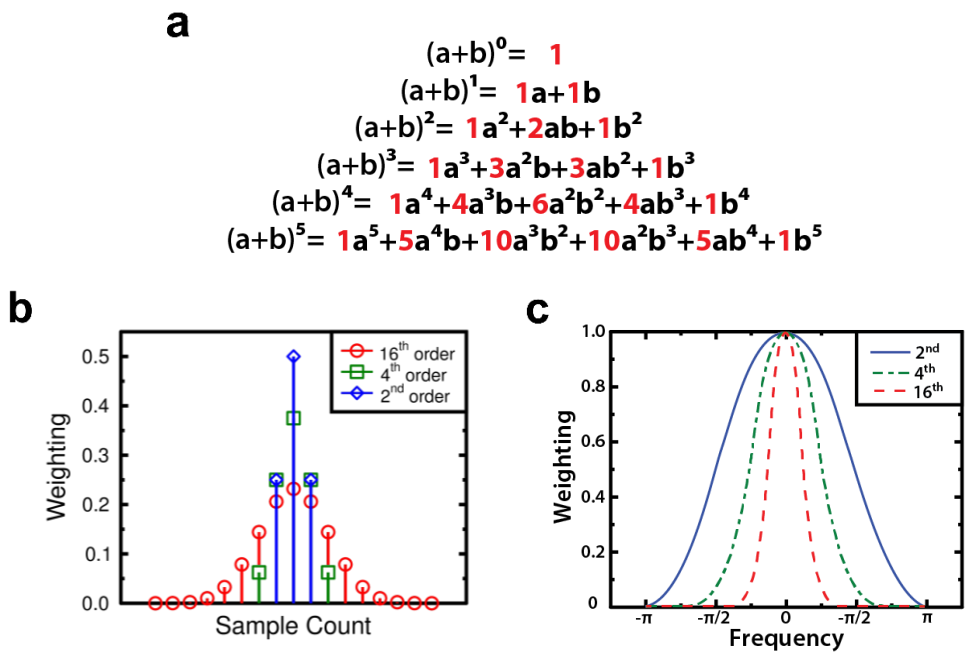

Figure 7.7 a Illustration of how the factors of the *nth* row of Pascal's triangle, marked in red, correspond to the coefficients of an *nth* order binomial expansion. **b** Weighting of 2nd, 4th and 16th order binomial filters for each sample, conveying how the response is a discrete approximation of a Gaussian. As samples are recorded at regular intervals, this equates to the response of each filter over time. **c** Frequency response of each filter, obtained from the fourier transform of the response in **b**. The binomial filter has an approximately Gaussian response, centred on the sampling frequency. Figures **b** and **c** adapted from [71].

7.5 Two Probe Conductance Measurement of a $LiNbO_3$ Head-to-Head Domain wall

Conductance measurements were performed across a 30 μm inter-electrode gap that PFM mapping revealed was bridged by a single continuous conducting domain wall, lateral phase presented in Figure 7.8a. Visible adjacent to the domain wall is a series of parallel needle domains which, assuming they are orientated to minimise energetic cost, can be used to precisely determine polarisation axis. From this, the peak resistance along the wall corresponds to a minimum domain wall angle of 47° off parallel with the polar axis. The alternating polarity method was used to measure conductance from 1 V to 10 V in 1 V steps. At each voltage the maximum pulse width of 65 s was applied and 16 current samples recorded, which with a 3rd order binomial filter provided 13 filtered data points at each bias. For increased accuracy, the initial filtered value for each voltage was disregarded to account for the finite time taken for a RC circuit to respond to an applied AC frequency[72]. This lag is somewhat visible in the measurements presented in Figure 7.6 but was more prevalent at higher voltages.

The resultant IV profile, shown Figure 7.8b, exhibits the same strong linearity as with the traditional 2 probe method, presented in Figure 7.4b, however there is a pronounced improvement in the stability of the measured conductance with the 12 values plotted at each bias showing minimal scatter. A least squares fit was applied and a value for inter-electrode conductance of 6.25x10^{-13} S was obtained.

Equivalent measurements were attempted across an inter-electrode gap without a continuously conducting domain wall in order to determine the bulk contribution. An erratic current profile, of magnitude below the 20 fA noise floor of the Keithely 237, was recorded and on further investigation the behaviour was identical to that of an open circuit. Recalling the 10^{15} Ωm resistivity[48] previously stated for congruent $LiNbO_3$ in bulk, the failed measurements are unsurprising. A lower limit for the bulk resistance can be estimated by assuming current flow through the full cross-sectional area of the crystal:

$$R_B = \rho_B \frac{l}{A} \tag{7.6}$$

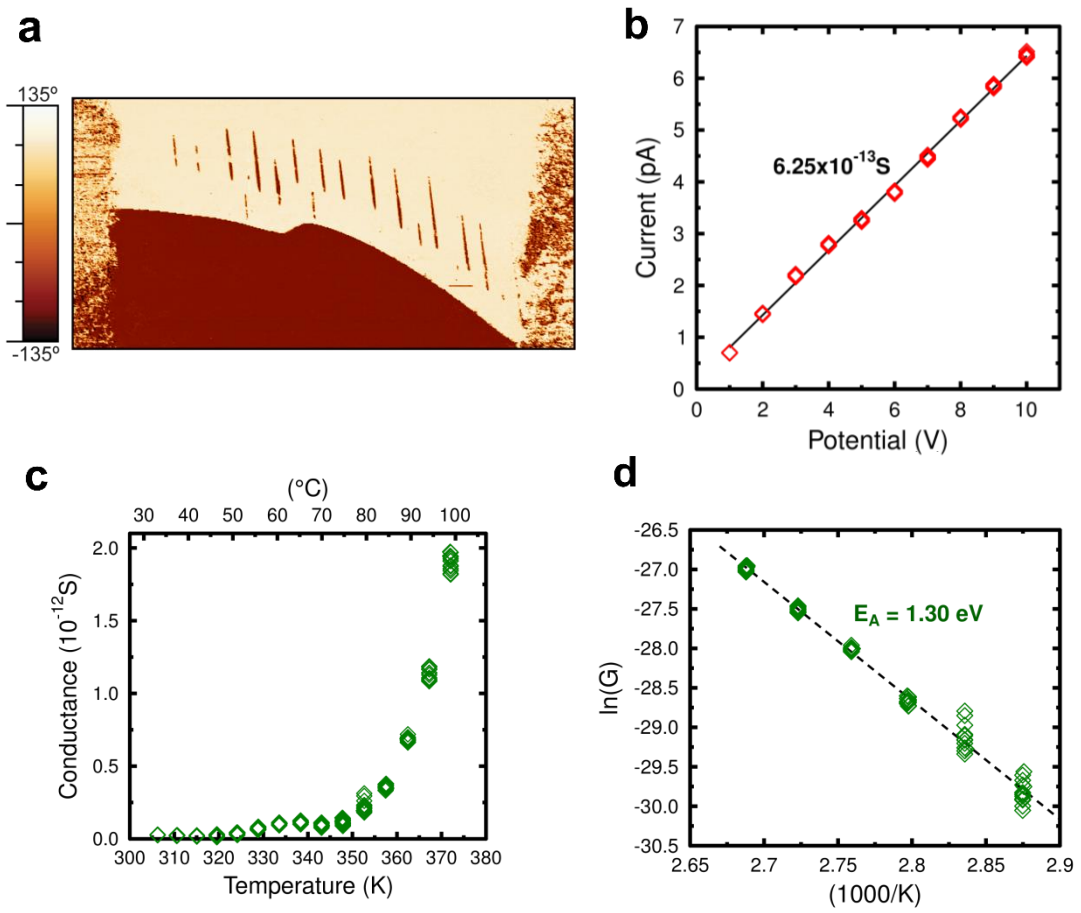

Figure 7.8 a PFM phase map of a head-to-head domain wall between gold electrodes, visible by noisy phase at edges of map. Scale bar is 10 μm. **b** IV measurement of domain wall in a displaying a ohmic response with conductance of 6.25×10^{-13} S. Measurements performed via alternating polarity method, with the 12 current values plotted for each potential showing high level of stability. **c** Conductance as a function of temperature, measured under 10 V bias from 30 °C to 100 °C in 5 °C steps, conveying clear semiconducting behaviour. **d** Plotting natural log of the conductance, lnG, against reciprocal temperature, between 75 to 100 °C, confirms Arrhenius behaviour with an activation energy (E_A) of 1.30 eV.

$$R_B = (10^{15})\left(\frac{30 \times 10^{-6}}{(1000 \times 10^{-6})(500 \times 10^{-6})}\right) = 6 \times 10^{16}\ \Omega \qquad (7.7)$$

Where l is the length of inter-electrode gap and R_B and ρ_B are the bulk resistance and resistivity respectively. Despite the extreme geometry, the inter-electrode bulk resistance is still a substantial $6 \times 10^{16}\ \Omega$. Comparing this result to Figure 7.8b, the

nanoscale current pathway provided by the single domain wall has reduced the inter-electrode resistance by, at minimum, over 4 orders of magnitude.

Having established a stable method of measurement, temperature dependent studies were carried out to determine whether the domain wall behaves metallically or as a semiconductor. The observed ohmic behaviour is not unique to metallic conductors and is exhibited by undoped semiconducting crystals, particularly in the low voltage regime[51,73].

The sample was affixed to a glass slide with silver dag and placed on a ceramic heater, which was controlled by a Thor Labs TC200 temperature controller. Temperature was monitored via a calibrated k-type thermocouple attached to the ceramic block. Conductance was measured at a 10 V bias, from 30 °C to 100 °C in steps of 5 °C. At each temperature a square wave voltage with a 65 s pulse length was applied and 20 current samples recorded and analysed with a 3rd order binomial filter. The number of calculated current values varied as for each temperature level differing temperature stability was observed. Requiring subsequent measurements within 0.1 °C of each other, the minimum number of calculated values for a given temperature was 7 at 30 °C. After each step in temperature a minimum delay of one hour was allotted to allow the $LiNbO_3$ to approach the ceramic temperature and avoid measurement of any pyroelectric currents generated by the sudden change in temperature. Minor pyroelectric currents generated due to temperature fluctuations during measurement were removed or attenuated by the binomial filter.

Calculating the conductance corresponding to each filtered current value and plotting as a function of temperature, as shown in Figure 7.8c, reveals semiconducting behaviour with the conductance increasing slowly beyond 50 °C until activation of a secondary conduction mechanism at 75 °C, with a sharp increase in conductance to a maximum of 1.9×10^{-11} S at 100 °C. Looking to temperature-dependent studies on congruent $LiNbO_3$ in literature[48,74], we find a reported bulk resistivity on the order of 10^{13} Ωm at 100 °C. Taking a lower limit estimate for the bulk inter-electrode resistance, as performed in (7.7), results in a minimum of 6×10^{14} Ω. At four orders of magnitude greater than the measured resistance of 5.26×10^{10} Ω, the observed

semiconducting behaviour is attributed wholly to conduction along the head-to-head domain wall.

Taking the natural log of the conductance from 75 °C to 100 °C and plotting against the reciprocal temperature, as shown Figure 7.8d, we see it follows an Arrhenius behaviour with temperature, *i.e.*

$$\sigma \propto \exp\left(\frac{-E_A}{k_B T}\right) \tag{7.8}$$

Where σ is the conductivity, T the temperature, k_B the Boltzmann constant and E_A the activation energy. Fitting the Arrhenius plot returns an activation energy of 1.30 eV. Literature values for bulk congruent $LiNbO_3$ at equivalent temperatures fall within the large range of 1.0 eV to 1.5 eV[31,74–77]. The inconsistency in measured values is likely due to varying stoichiometry between samples, with the dominant diffusion mechanism shown to depend on the relative abundance of lithium[78]. Our observed thermal activation behaviour closely matches that recorded for strongly lithium deficient crystals. Here Bollmann and Gernand[76] measured bulk conductance in the range of 20 °C to 900 °C and observed a thermally activated conduction mechanism beginning at 75 °C and proceeding up to 700 °C, with activation energy of 1.28 eV. The authors suggest the activation of oxygen vacancies, however subsequent studies have established that, barring directed effort at their creation, oxygen vacancies are present in $LiNbO_3$ in negligible concentrations[79,80]. Precluding external dopants, diffusion of lithium vacancies or hydrogen impurities, with activation energies in the range 1.1 eV to 1.23 eV, is likely to dominate at the given temperature range[31,75,77,78].

While the specific procedure used in preparation of the sample under study is not known, all the methods found in literature for producing equivalent domain wall structures in $LiNbO_3$ entailed domain nucleation under extreme temperatures, greater than 950 °C [81–85]. Assuming formation at high temperature, the negatively charged lithium vacancies may facilitate screening of the local divergence in polarisation at the head-to-head domain wall. Upon cooling to room temperature the effectively immobile vacancies, while contributing to the density of screening carriers, contribute negligibly to local conduction. This screening model would

account for the observed thermal activation as the increasingly mobile ionic screening charges contribute to the local conductivity.

Further support stems from the original study of domain wall conduction in $LiNbO_3$ under super-band gap illumination. Schroder *et al.*[20] poled z-cut $LiNbO_3$ crystals to 180° domains with walls inclined with angles ranging from 0.006° to 0.225° off the polar axis. In addition they produced a maximally charged domain wall by "radical heat treatment" suggesting wall formation at high temperatures. For the domain walls formed by electrical poling, they observed increased conductance with increasing angle, from 10^{-14} S to 10^{-12} S. Despite necessitating a substantially larger local carrier density for screening, at the maximally charged wall they measured a reduced conductance of 10^{-13} S. By assuming the conductance scales solely with local carrier density, *i.e.* that carrier mobility remains constant, the estimated conductance for the maximally charged wall should have been on the order of 10^{-10} S.

During the writing of this thesis, Werner *et al.*[19] published an independent study on the dark conductivity of head-to-head domain walls in $LiNbO_3$. An array of 180° striped domains were written into the z face of a MgO doped $LiNbO_3$ single crystal, with domain walls inclined at an angle of 1° off the polar axis. IV measurements were performed through depth in a parallel plate geometry, maximising conductance across the array of 732 walls and negating the need for current filtering. Authors observed a strongly linear response in agreement with our measurements on a single wall, though pronounced diode behaviour was observed dependent on the choice of electrode material.

Temperature dependent measurements revealed an exponential decay of the conductance over time for temperatures above 75 °C. The current decay for a range of temperatures, as measured by Werner *et al.*, is presented in Figure 7.9a. Taking an Arrhenius plot of the lifetime of the conductance at each temperature, *i.e.* the time taken for measured current to decay to zero, revealed an activation energy of 1.2 ± 0.1 eV, as shown Figure 7.9b. The temperature and activation energy are in direct correspondence with the thermal activated conductance measured for a single domain wall. Decaying conductance was observed for $LiNbO_3$ samples in-house, with repeated heating of samples resulting in diminishing domain wall currents,

though no formal investigation of the thermal decay was carried out. Notably samples stored at ambient temperatures exhibited decaying domain wall conductance over a period of months.

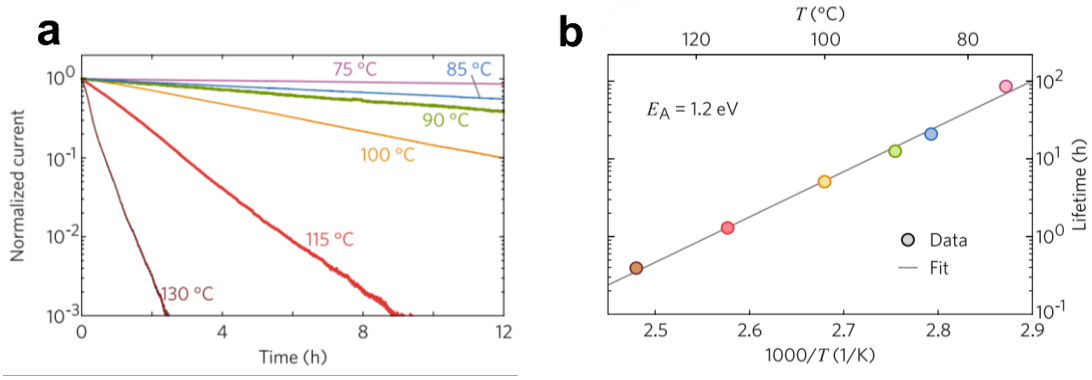

Figure 7.9 a Plot of domain wall current decaying exponentially upon heating. **b** Lifetime of conductance follows an Arrhenius behaviour with temperature, with a thermal activation energy, E_A, of 1.2 eV. Figures reprinted from [19].

7.6 Conclusions

A conductive atomic force microscopy map has been the quintessential depiction of domain wall conduction since the seminal study by Seidel *et al*[11,12,86,87]. Nonetheless, the characteristic formation of a Schottky barrier between tip and sample limits the ability of c-AFM to measure conductive behaviour without convolution by barrier transport. In this chapter, the alternating polarity method[25] was established as a basic implementation of an impedance filter, which facilitates the reliable conductance measurement of an individual domain wall with a simple two probe geometry. The need for some form of signal demodulation was demonstrated by measurement of the dark conductance, *i.e.*in absence of super band gap illumination, of a head-to-head domain wall in congruent $LiNbO_3$. Due to the high resistance inherent to a nanoscale channel width, the current driven under applied bias may be suppressed by background currents of both internal and external origin.

Alternating polarity conductance measurement revealed a strongly ohmic response from the charged wall, suggesting the marginal influence of any Schottky barrier present at the interface between the sputtered electrodes and the $LiNbO_3$. Investigating conductance as a function of temperature, distinct semiconducting

behaviour was observed with pronounced thermal activation beginning at 75°C and persisting to the maximum recorded temperature of 100 °C. An activation energy of 1.30 eV was measured, with the recorded behaviour matching that observed for lithium deficient $LiNbO_3$ [76]. The activation energy correlates with the diffusion of lithium vacancies and hydrogen ions measured for $LiNbO_3$ in bulk, 1.1 - 1.23eV, at this temperature range[75,77].

The form of maximally charged domain wall studied is typically prepared by domain inversion under extreme thermal treatment, > 900 °C [81–85]. On comparison with conductance measurements for head-to-head domain walls formed in $LiNbO_3$ by electrical poling at room temperature, the measured conductance was orders of magnitude below what was expected. In agreement with theory and charged domain wall behaviour observed for other ferroelectric crystals (see sections 1.5.1 and 1.6) the domain wall conductance should scale with the domain wall angle as the local carrier density necessary to screen the divergence in polarisation increases. Formed under extreme temperatures, the maximally charged domain wall may have been stabilised in part by mobile lithium vacancies, which, upon cooling to room temperature, become immobile and cannot contribute to local conduction. This screening model would account for the observed thermal activation as the ionic screening carriers become mobile upon reheating.

7.7 References

1. Cappella, B. & Dietler, G. Force-distance curves by atomic force microscopy. *Surf. Sci. Rep.* **34,** 1–104 (1999).

2. Kruse, P. Scanning Probe Microscopy: The Lab on a Tip. *J. Electron Spectros. Relat. Phenomena* **135,** 83 (2004).

3. Hertz, H. R., Jones, D. & Schott, G. in *Miscellaneous papers* **92,** 156–171 (Macmillan and Co. Ltd, 1896).

4. Guyonnet, J. in *Ferroelectric Domain Walls: Statics, Dynamics, and Functionalities Revealed by Atomic Force Microscopy* 38–39 (Springer, 2014).

5. McQuaid, R. G. P., Campbell, M. P., Whatmore, R. W., Kumar, A. & Gregg, J. M. Injection and controlled motion of conducting domain walls in improper ferroelectric Cu-Cl boracite. *Nat. Commun.* **8,** 15105 (2017).

6. Kuntze, S. B. *et al.* Electrical Scanning Probe Microscopy: Investigating the Inner Workings of Electronic and Optoelectronic Devices. *Crit. Rev. Solid State Mater. Sci.* **30,** 71–124 (2005).

7. Bardeen, J. Surface states and rectification at a metal semi-conductor contact. *Phys. Rev.* **71,** 717–727 (1947).

8. Cowley, A. M. & Sze, S. M. Surface States and Barrier Height of Metal-Semiconductor Systems. *J. Appl. Phys.* **36,** 3212–3220 (1965).

9. Marinello, F., Carmignato, S., Voltan, A., Savio, E. & De Chiffre, L. Error Sources in Atomic Force Microscopy for Dimensional Measurements: Taxonomy and Modeling. *J. Manuf. Sci. Eng.* **132,** 30903 (2010).

10. Ho, G., Ven, L. G. J. Van Der & With, G. De. Quantitative Conductive Atomic Force Microscopy on Single-Walled Carbon Nanotube-Based Polymer Composites. *ACS Appl. Mater. Interfaces* **8,** 19701–19708 (2016).

11. Catalan, G., Seidel, J., Ramesh, R. & Scott, J. F. Domain wall nanoelectronics. *Rev. Mod. Phys.* **84,** 119–156 (2012).

12. Vasudevan, R. K. *et al.* Domain Wall Conduction and Polarization-Mediated Transport in Ferroelectrics. *Adv. Funct. Mater.* **23,** 2592–2616 (2013).

13. Ju, B.-F., Ju, Y. & Saka, M. Quantitative measurement of submicrometre electrical conductivity. *J. Phys. D. Appl. Phys.* **40,** 7467–7470 (2007).

14. Chiu, Y. P. *et al.* Atomic-scale evolution of local electronic structure across multiferroic domain walls. *Adv. Mater.* **23,** 1530–1534 (2011).

15. Schaab, J. *et al.* Contact-Free Mapping of Electronic Transport Phenomena of Polar Domains in $SrMnO_3$ Films. *Phys. Rev. Appl.* **5,** 54009 (2016).

16. Pawlik, A.-S. *et al.* Polarization driven conductance variations at charged ferroelectric domain walls. *Nanoscale* 10933–10939 (2017).

17. Mundy, J. A. *et al.* Functional electronic inversion layers at ferroelectric domain

walls. *Nat. Mater.* **16,** 622–627 (2017).

18. Ruff, E. *et al.* Conductivity Contrast and Tunneling Charge Transport in the Vortexlike Ferroelectric Domain Patterns of Multiferroic Hexagonal $YMnO_3$. *Phys. Rev. Lett.* **118,** 1–5 (2017).

19. Werner, C. S. *et al.* Large and accessible conductivity of charged domain walls in lithium niobate. *Sci. Rep.* 9862 (2017).

20. Schröder, M. *et al.* Conducting domain walls in lithium niobate single crystals. *Adv. Funct. Mater.* **22,** 3936–3944 (2012).

21. Shur, V. Y., Baturin, I. S., Akhmatkhanov, A. R., Chezganov, D. S. & Esin, A. A. Time-dependent conduction current in lithium niobate crystals with charged domain walls. *Appl. Phys. Lett.* **103,** (2013).

22. Shur, V. Y., Rumyantsev, E. L., Nikolaeva, E. V. & Shishkin, E. I. Formation and evolution of charged domain walls in congruent lithium niobate. *Appl. Phys. Lett.* **77,** 3636–3638 (2000).

23. Schröder, M. *et al.* Nanoscale and macroscopic electrical ac transport along conductive domain walls in lithium niobate single crystals. *Mater. Res. Express* **1,** 35012 (2014).

24. Sluka, T., Tagantsev, A. K., Bednyakov, P. & Setter, N. Free-electron gas at charged domain walls in insulating $BaTiO_3$. *Nat. Commun.* **4,** 1808 (2013).

25. Daire, A. *Improving the Repeatability of Ultra-High Resistance and Resistivity Measurements (White Paper)*. (Keithley Instruments, 2001).

26. Li, S. S. in *Semiconductor Physical Electronics* 247–286 (Springer, 1993).

27. Abrahams, S. C., Reddy, J. M. & Bernstein, J. L. Ferroelectric lithium niobate. 3. Single crystal X-ray diffraction study at 24°C. *J. Phys. Chem. Solids* **27,** 997–1012 (1966).

28. Abrahams, S. C., Hamilton, W. C. & Reddy, J. M. Ferroelectric lithium niobate. 4. Single crystal neutron diffraction study at 24°C. *J. Phys. Chem. Solids* **27,** 1013–1018 (1966).

29. Jundt, D. H. & Foulon, G. in *Properties of Lithium Niobate* 8–9 (INSPEC, 2002).

30. Kämpfe, T. Charged Domain Walls in Ferroelectric Single Crystals. (Technische Universität Dresden, 2016).

31. Gopalan, V., Dierolf, V. & Scrymgeour, D. a. Defect–Domain Wall Interactions in Trigonal Ferroelectrics. *Annu. Rev. Mater. Res.* **37,** 449–489 (2007).

32. Nikogosyan, D. N. in *Nonlinear Optical Crystals: A Complete Survey* 36 (Springer New York, 2005).

33. Volk, T. R., Gainutdinov, R. V, Bodnarchuk, Y. V & Ivleva, L. I. Creation of domains and domain patterns on the nonpolar surface of $Sr_xBa_{1-x}Nb_2O_6$ crystals by atomic force microscopy. *JETP Lett.* **97,** 483–489 (2013).

34. Schröder, M. Conductive Domain Walls in Ferroelectric Bulk Single Crystals.

(Technische Universität Dresden, 2013).

35. Megaw, H. D. A note on the structure of lithium niobate, $LiNbO_3$. *Acta Crystallogr. Sect. A* **24,** 583–588 (1968).

36. Czochralski, J. Ein neues Verfahren zur Messung der Kristallisationsgeschwindigkeit der Metalle. *Zeitschrift für Phys. Chemie* **92U,** (1918).

37. Ballman, A. Growth of Piezoelectric and Ferroelectric Materials by the CzochraIski Technique. *J. Am. Ceram. Soc.* **48,** 112–113 (1965).

38. Volk, T. & Wöhlecke, M. in *Lithium Niobate* 1–8 (Springer, 2008).

39. Abrahams, S. C. in *Properties of Lithium Niobate* (ed. Wong, K. K.) 3–7 (INSPEC, 2002).

40. Donnerberg, H., Schirmer, O. F., Catlow, C. R. A. & Tomlinson, S. M. Computer simulation of extrinsic defects in $LiNbO_3$ crystals. *Radiat. Eff. Defects Solids* **119–121,** 957–962 (1991).

41. Abrahams, S. C. & Marsh, P. Defect structure dependence on composition in lithium niobate. *Acta Crystallogr. Sect. B* **42,** 61–68 (1986).

42. Lerner, P., Legras, C. & Dumas, J. P. Stoechiométrie des monocristaux de métaniobate de lithium. *J. Cryst. Growth* **3–4,** 231–235 (1968).

43. Young, W. M., Feigelson, R. S., Jundt, D. H. & Fejer, M. M. Influence of composition of MgO-doped lithium niobate on phase-matching temperature for frequency doubling in the visible. *J. Appl. Phys.* **69,** 7372–7374 (1991).

44. Volk, T. & Wöhlecke, M. in *Lithium Niobate* 10–14 (Springer, 2008).

45. Iyi, N. *et al.* Comparative study of defect structures in lithium niobate with different compositions. *J. Solid State Chem.* **101,** 340–352 (1992).

46. Wilkinson, A. P., Cheetham, A. K. & Jarman, R. H. The defect structure of congruently melting lithium niobate. *J. Appl. Phys.* **74,** 3080–3083 (1993).

47. DeLeo, G. G., Dobson, J. L., Masters, M. F. & Bonjack, L. H. Electronic structure of an oxygen vacancy in lithium niobate. *Phys. Rev. B* **37,** 8394–8400 (1988).

48. Staebler, D. L. & Amodei, J. J. Thermally fixed holograms in $LiNbO_3$. *Ferroelectrics* **3,** 107–113 (1972).

49. Kolaklieva, L. & Kakanakov, R. in *Micro Electronic and Mechanical Systems* 293–318 (InTech, 2009).

50. Yu, A. Y. C. Electron tunneling and contact resistance of metal-silicon contact barriers. *Solid. State. Electron.* **13,** 239–247 (1970).

51. Scott, J. F. There's no place like Ohm: conduction in oxide thin films. *J. Phys. Condens. Matter* **26,** 142202 (2014).

52. Simmons, J. G. Potential barriers and emission-limited current flow between closely spaced parallel metal electrodes. *J. Appl. Phys.* **35,** 2472–2481 (1964).

53. Murphy, E. J., Morgan, S. O. & . The dielectric properties of insulating materials. *Bell Syst. Tech. Journal* **640,** 20 (1937).

54. Dow, P. C. An Analysis of Certain Errors in Electronic Differential Analyzers II-Capacitor Dielectric Absorption. *Electron. Comput. IRE Trans.* **EC-7,** 17–22 (1958).

55. Cole, K. S. & Cole, R. H. Dispersion and Absorption in Dielectrics I. Alternating Current Characteristics. *J. Chem. Phys.* **9,** 341 (1941).

56. Cole, K. S. & Cole, R. H. Dispersion and Absorption in Dielectrics II. Direct Current Characteristics. *J. Chem. Phys.* **10,** 98–105 (1942).

57. Joffé, A. in *The Physics of Crystals* 81–90 (McGraw-Hill Book Company, Inc., 1928).

58. Fang, P. H. Cole—Cole Diagram and the Distribution of Relaxation Times. *J. Chem. Phys.* **42,** 3411 (1965).

59. Macdonald, J. R. Theory of space-charge polarization and electrode-discharge effects. *J. Chem. Phys.* **58,** 4982 (1973).

60. *Introduction to Resistance Measurement (Technical Report)*. (HIOKI E.E Corporation).

61. *D257-14 Standard Test Methods for DC Resistance or Conductance of Insulating Materials (An American National Standard)*. (ASTM International, 2012).

62. *Low Level Measurements Handbook: Precision DC Current, Voltage and Resistance Measurements*. (Keithley Instruments Inc., 2004).

63. Macdonald, J. R. Impedance Spectroscopy. *Ann. Biomed. Eng.* **20,** 289–305 (1992).

64. Christie, S. H. The Bakerian Lecture: Experimental Determination of the Laws of Magneto-Electric Induction in Different Masses of the Same Metal, and of Its Intensity in Different Metals. *Philos. Trans. R. Soc. London* **123,** 95–142 (1833).

65. Heaviside, O. in *Electrical Papers Volume II* 102–111 (MacMillan and Co., 1894).

66. Wheatstone, C. The Bakerian Lecture: An Account of Several New Instruments and Processes for Determining the Constants of a Voltaic Circuit. *Philos. Trans. R. Soc. London* **133,** 303–327 (1843).

67. Smith, S. in *Digital Signal Processing* 277–284 (Newnes, 2003).

68. Kupče, E. in *Data Handling in Science and Technology* **18,** 145–163 (1996).

69. Smith, S. in *Digital Signal Processing* 209–224 (Newnes, 2003).

70. Crowley, J., Riff, O. & Piater, J. Fast computation of characteristic scale using a half octave pyramid. *Int. Conf. Scale-sp. Theor. Comput. Vis.* 1–8 (2002).

71. Derpanis, K. G. Overview of binomial filters (Lecture Series). (York University, 2005).

72. Horowitz, P. & Winfield, H. in *The Art of Electronics* 263–268 (Cambridge University Press, 1990).

73. Shockley, W. Hot Electrons in Germanium and Ohm's Law. *Bell System Technical Journal* **30,** 990–1034 (1951).

74. Kovacs, L., Polgar, K. & Florea, C. in *Lithium Niobate* 91–96 (Springer, 2002).

75. Staebler, D. L. & Amodei, J. J. Thermally fixed holograms in $LiNbO_3$. *IEEE Trans. Sonics Ultrason.* **19,** 107–114 (1972).

76. Bollmann, W. & Gernand, M. On the Disorder of $LiNbO_3$Crystals. **9,** 301–308 (1972).

77. Yariv, A., Orlov, S. S. & Rakuljic, G. a. Holographic storage dynamics in lithium niobate: theory and experiment. *J. Opt. Soc. Am. B* **13,** 2513 (1996).

78. Birnie III, D. P. Review Analysis of diffusion in lithium niobate. *J. Mater. Sci.* **28,** 302–315 (1993).

79. Schirmer, O. F., Thiemann, O. & Wöhlecke, M. Defects in $LiNbO_3$-I. experimental aspects. *J. Phys. Chem. Solids* **52,** 185–200 (1991).

80. Smyth, D. M. Defects and transport in $LiNbO_3$. *Ferroelectrics* **50,** 93–102 (1983).

81. Kugel, V. D. & Rosenman, G. Domain inversion in heat-treated $LiNbO_3$ crystals. *Appl. Phys. Lett.* **62,** 2902–2904 (1993).

82. Nakamura, K. & Shimizu, H. Local domain inversion in ferroelectric crystals and its application to piezoelectric devices. *Proceedings, IEEE Ultrason. Symp.* 309–318 (1989).

83. Nakamura, K., Ando, H. & Shimizu, H. Ferroelectric domain inversion caused in $LiNbO_3$ plates by heat treatment. *Appl. Phys. Lett.* **50,** 1413–1414 (1987).

84. Huang, L. & Jaeger, N. A. F. Discussion of domain inversion in $LiNbO_3$. *Appl. Phys. Lett.* **65,** 1763–1765 (1994).

85. Miyazawa, S. Ferroelectric domain inversion in Ti-diffused $LiNbO_3$ optical waveguide. *J. Appl. Phys.* **50,** 4599–4603 (1979).

86. Seidel, J. *et al.* Conduction at domain walls in oxide multiferroics. *Nat. Mater.* **8,** 229–34 (2009).

87. Meier, D. Functional domain walls in multiferroics. *J. Phys. Condens. Matter* **27,** 463003 (2015).

8 Conclusions and Further Work

8.1 Conclusions

Conducting domain walls have the potential to revolutionise solid state electronics as they offer the enticing possibility of reconfigurable circuit design, with devices written and erased as trivially as bits on a hard drive. The viability of such domain wall devices is uncertain, however, as currently the most fundamental aspects of conduction, carrier types, densities and mobilities, have not been determined. This thesis details the development of a novel scanning probe technique for local measurement of the Hall effect within conducting domain walls. While optimisation is ongoing, the initial measurements presented here represent the first explicit characterisation of the mobile carriers mediating domain wall conduction.

The original approach emulated that of traditional Hall measurement on bulk materials, where potential is measured between fixed electrodes deposited on opposing faces of the crystal. Here an atomic force microscopy (AFM) tip was substituted for an electrode, acting as a repositionable voltage probe with nanometre spatial resolution. Contact potential measurement by this method is a long established technique, known as scanning voltage microscopy (SVM), used in industry for verification of semiconductor device operation[1,2], lending credence to the approach. Concurrently, preliminary measurements on doped silicon were promising with the lateral potential clearly imaged and n-type and p-type silicon samples returning negative and positive Hall voltages respectively.

The limitations of contact potentiometry became apparent as attempts to measure the potential dropped across a $BaTiO_3$ ceramic capacitor revealed a protracted time constant (τ) for the equilibration of tip potential in response to a variation in sample potential. With 5 τ roughly 24 minutes, the response time of SVM for a single point was an order of magnitude greater than the maximum 100 second duration for a single scan line. The delayed response was due to the formation of a high resistance

Schottky barrier between tip and ceramic, the height of which scales with the wide band gap of $BaTiO_3$. Reviewing the band structures for single crystal ferroelectrics known to express conducting domain walls, with the exception of the hexagonal manganites ($RMnO_3$ where R = Dy, Ho, Er, Tm, Yb, Lu, Y, Sc)[3], all possess band gaps greater than $BaTiO_3$. Ultimately, the overt approach of contact potential measurement is infeasible given the characteristically high resistivity of ferroelectric materials.

Moving forward, a technique based upon intermittent contact AFM was developed where, unfettered by issues of contact resistance, the local Hall potential at domain walls was successfully imaged by its influence on the topographic trace. The test piece material chosen for study was single crystal $YbMnO_3$ as, owing to its improper ferroelectric order[4], the material natively expresses a high density of stable charged domain walls. Studies on other members of the $RMnO_3$ family have established the charged domain walls exhibit distinct conduction from the bulk[5,6]. A combination of piezoresponse force microscope (PFM) and conductive atomic force microscopy (c-AFM) confirmed increased and decreased conduction relative to bulk at tail-to-tail and head-to-head charged domain walls respectively, in agreement with previous studies on the analogous $ErMnO_3$[5].

Herein, a pair of gold electrodes were deposited onto the in-plane polarised surface of the crystal and a constant current driven through the conducting domain wall segments trapped within the inter-electrode gap. An orthogonal magnetic field was applied via an electromagnet and an intermittent contact mode topography scan was engaged within the interelectrode gap. Under perpendicular electric and magnetic fields, a Hall potential developed which, owing to their increased conductance and the inversely proportional dependence on the width of the conducting channel, was greater within the domain walls than the surrounding bulk. The local variations in surface potential at the conducting domain walls corresponded to variations in the electrostatic force acting on the oscillating AFM tip, which was recorded as a change in the topographic trace.

Calibration measurements on a sample of known potential allowed for quantitative interpretation of the domain wall contrast. From the sense of the developed Hall

potential, the charge carriers mediating conduction along tail-to-tail walls were found to be p-type. Thus confirming the widely accepted but previously unverified predictions in literature[5,6]. The sense of the Hall potential cannot distinguish between holes and positive ionic carriers, however temperature dependent studies on $YbMnO_3$ have established bulk conduction is mediated by holes, with the ionic contribution minor and n-type in nature[7,8]. Therefore, as conduction is only observed at the tail-to-tail walls, the large abundance of mobile holes would be the most likely to facilitate to screening of the local divergence in polarisation and contribute to local conduction.

Quantitative estimates were calculated for the carrier mobilities and densities by making order of magnitude approximations for the domain wall geometry. Notably, the estimated carrier density of ~ 10^{16} cm^{-3}, was a substantial four orders of magnitude below the ~ 10^{20} cm^{-3} required to screen the local divergence in polarisation. Even exploiting the error introduced by the estimated values used in calculation, by considering the increased conduction at the domain wall occurs within single angstrom in width, the calculated ~ 10^{18} cm^{-3}, is still two orders of magnitude below the density required for screening. This suggests the potential for substantial enhancement of the domain wall conductance as, assuming complete screening, the measured conduction is mediated by merely one in every ten thousand of the local screening carriers. Steps towards exploiting this severe deficit can already be found in literature as Schaab *et al.* observed increased conductance at tail-to-tail walls for acceptor doped $ErMnO_3$ samples with a greater availability of mobile carriers in bulk to contribute to screening[9].

On comparison the value for carrier mobility was not as revelatory as, at ~ 60 $cm^2V^{-1}s^{-1}$, the result is is about an order of magnitude lower than the ~ 500 $cm^2V^{-1}s^{-1}$ typical of p-type silicon with a similar carrier density[10]. In this case the principal error was in estimation of the conducting domain wall depth, with maximum and minimum depths of 10 μm and 1 μm returning a possible carrier mobility range of $17 < \mu < 170$ $cm^2V^{-1}s^{-1}$. At several orders of magnitude higher than that typical of small polarons in oxides[11,12] and at the upper limit of that typical of large polarons[13], the range of mobility values suggests domain wall transport occurs without significant lattice coupling. This contrasts with the polaronic transport proposed both for p-

type conduction in bulk[7] and recently for the minority-carrier conduction state observed at head-to-head walls in $ErMnO_3$ [14].

Building on the success of intermittent contact Hall measurement, steps were made to advance the technique by employing Kelvin probe force microscopy (KPFM): a double pass technique in which the topographic and electrostatic signal contributions are collected in isolation. Thus, under ideal operation, KPFM directly returns a quantitative map of the surface potential. A shortcoming of the KPFM approach, however, is the restriction of the lateral potential to the typically low maximum bias that can be controlled via the microscope feedback. In-house, the microscope was limited to a maximum current driving potential of 10 V an order of magnitude lower than the 100 V used for intermittent contact measurements on $YbMnO_3$.

To account for this, a bespoke $ErMnO_3$ sample with a large scale domain structure was obtained through collaboration with D. Meier and J. Schaab of ETH Zurich. In addition to longer conducting domain wall segments this sample exhibited, under sufficient bias, enhanced conduction at the usually insulating head-to-head walls as reported by Mundy *et al.*[14] Following theory[15,16], and the previous observation of p-type carriers at tail-to-tail walls, the conduction at head-to-head walls is likely facilitated by minority n-type carriers which screen the local positive bound charge density. Consequently, expressing a continuous variation from majority to minority carrier conduction within a single curved domain wall, $ErMnO_3$ is an excellent test-piece material for demonstrating the utility of the Hall effect technique.

Practical considerations for ensuring quantitative accuracy of KPFM were discussed and as measurements were performed in air, amplitude modulated detection (AM-KPFM) was used. Hall potential measurements were successful, exhibiting high stability and low noise within the magnetic field and, upon flattening the lateral potential gradient, images conveyed improved domain wall contrast in comparison to the intermittent contact method. Calibration measurements verified the quantitative accuracy of the imaged surface potential

while highlighting the importance of electrode geometry due to the unwanted signal contribution from the cantilever body.

In contrast with to the lower resolution intermittent contact technique, potential trace was observed at conducting domain walls solely due to an applied electric field, in absence of an magnetic field. To isolate the Hall potential from this background offset, the lateral potential and current were fixed and measurements performed under varying magnetic field. Under equal and opposite magnetic fields, the offset remains fixed while the Hall potential is of equal and opposite magnitude. Thus recording the potential profile of a domain wall under both field geometries, subtracting and halving the result returns a profile of the local Hall potential. Unfortunately, while the calibration and development of the experimental procedure which facilitated such measurements was completed, due to time constraints the Hall potential was not determined during this project. Subsequent quantitative measurement and analysis was performed in-house by P. Turner. As they were independently obtained, the results are not discussed in full but are presented briefly as verification of the efficacy of the technique.

The final chapter moves away from the Hall technique and focuses on the more basic measurement of domain wall conductance. Conductive AFM is the predominant technique in literature, with the repositionable AFM probe facilitating high resolution spatial mapping of conductance[17,18]. However, current against voltage (IV) profiles recorded via c-AFM typically exhibit pronounced Schottky behaviour as the domain wall transport is obscured by the poor metal-semiconductor contact.

Investigation into the dark conductance of a maximally charged head-to-head wall in congruent $LiNbO_3$, sample received through collaboration with E. Soergel at Bonn University, reiterated this as pronounced rectification was observed via c-AFM, with zero current measured under positive bias. Fixed electrodes were deposited to provide greater contact stability and IV measurements conveyed a strongly linear response, suggesting ohmic contact. However repeat measurements, despite minimal noise, returned varying values for resistance and, significantly, measuring the current profile under fixed bias revealed a decay

through the origin, signifying a negative wall resistance. The nonsensical results indicated the resistance of the single domain wall was sufficiently high that background currents, both external and internal in origin, were masking the minute driven current.

Here the alternating polarity method[19] was implemented, wherein bias is applied in a low frequency square wave and a weighted moving average applied to the sampled current, acting as a basic impedance filter and isolating the driven current. The modified IV technique displayed markedly increased stability over repeat measurement, confirming the ohmic domain response with a conductance of 6.25×10^{-13} S for a ~ 30 μm curved head-to-head wall with a minimum angle of 47° off the polar axis. Investigating the conductance as a function of temperature, pronounced thermal activation was observed above 75°C, with an activation energy of 1.30 eV, closely matching behaviour reported for strongly lithium deficient $LiNbO_3$ [20]. The observed thermal activation is in accordance with the diffusion of lithium vacancies in bulk at the equivalent temperature range[21,22]. As the measured conductance (1.9×10^{-11} S at 100°C) was four orders of magnitude greater than the upper limit for bulk conductance, estimated with resistivity values obtained from temperature dependent studies on bulk $LiNbO_3$ [23,24], the observed semiconducting behaviour is attributed solely to domain wall transport.

A proposed rationalisation of the results is that the highly charged head-to-head domain wall, which was likely nucleated via extreme thermal treatment[25,26], is partially screened by lithium ion vacancies. At room temperature the immobile lithium vacancies do not contribute to domain wall transport but upon heating become increasingly immobile, resulting in an Arrhenius conductance behaviour with temperature. This is in agreement with the observation by Schröder *et al.* of diminished conductance at ~ 90° domain walls formed under high temperatures, in comparison to 0.225° walls formed at room temperature, despite an expected three orders of magnitude increase in the screening charge density[27].

The central aim of this thesis is to communicate the methodology behind the technique for localised Hall measurement, and the complementary alternating polarity method, as their widespread implementation has the potential to define

our understanding of domain wall conduction. Already the results of the initial proof of concept measurements have possible implications for the capabilities of future domain wall devices as they suggest the conductance measured at both domain wall systems are orders of magnitude lower than their full potential, as currently local screening appears to be partially facilitated by immobile carriers.

8.2 Further Work

Now equipped with a means of locally measuring the Hall potential developed within conducting domain walls, the carrier properties for every permutation of wall (*i.e.* head-to-head, tail-to-tail and neutral), within each bulk material and formed by various techniques, await measurement and comparison. As with any experimental technique, the quickest path to optimisation is through use. Limitations of the initial methodology, and the corresponding solutions, will become apparent as the technique is applied to a wider range of experimental situations.

Alongside Hall potential mapping, implementing the alternating polarity method[19] will aid precise measurement of local conductivity which, in conjunction with the carrier mobility and density, will provide a complete analysis of the domain wall conduction. A major empirical advantage is the alternating polarity method utilises the same fixed electrode geometry as the Hall measurement and, thus, performing the additional conductance measurements requires zero additional sample preparation.

In the immediate future, quantitative Hall measurements on $ErMnO_3$ are to be repeated with greatly reduced electrode dimensions to allow for more directed current flow along select domain walls. This will minimise the number of possible current pathways and allow more precise calculation of carrier properties. However, despite offering a complete selection domain wall charge states within a single system, the uniquely complex domain structure of the hexagonal manganites impedes quantitative measurement. Future measurements on the predominantly linear domain walls of other conducting domain wall systems will be comparatively straightforward.

Moving towards more simplistic geometries, particularly samples wherein the conducting domain walls permeate entirely through depth, will allow for electrical contact to both the long edges of the domain wall. Driving current along this axis will flip the geometry to make an extremely short Hall sample and maximise the effective geometric magnetoresistance, allowing for independent verification of the carrier mobility. In theory magnetoresistance measurements can be performed with the same electrode geometry as the Hall and alternating polarity measurements, however, in practice the long sample geometry will result in, barring extreme carrier mobility, negligible magnetoresistance for achievable magnetic fields.

Electrical poling techniques for generating through depth conducting walls have been demonstrated in single crystal $BaTiO_3$ and $LiNbO_3$ but no others, and are certainly inapplicable to the improper ferroelectric systems[27–30]. In these systems ideal wall geometry could be obtained using focused ion beam (FIB) milling to remove a single crystal lamella containing an individual wall. Preparation of lamellae without destruction of the ferroelectric properties has been demonstrated previously and proven to be a valuable technique for isolated analysis of domain wall formation without convolution from a macroscopic bulk[31–34].

Adaption of the ferroelectric milling procedures outlined in literature could allow for conductive functionality to be maintained and hence bespoke wall geometries prepared for Hall voltage mapping, with the precisely defined wall dimensions resulting in quantitative analysis with optimal precision. FIB systems commonly use scanning electron microscopy (SEM) to image the crystal surface and determine milling location. Typically ferroelectric domain walls are not visible under SEM, however, conducting domain walls may be imaged by what is referred to as the passive voltage contrast[35], commonly used for fault analysis of printed circuits in industry. Originally demonstrated by Aristov *et al.*[36,37] for $BaTiO_3$ and $LiNbO_3$ and repeated in-house for $RMnO_3$ and $Cu_3B_7O_{13}Cl$, providing there is a sufficient density of conducting domain walls to prevent excessive charge build up, an uncoated crystal may be imaged under SEM with the conducting domain walls visible against the insulating bulk.

It is a poor tradesman who blames his tools, however, the measurements presented in this thesis were limited by the capabilities of the instrumentation. In an ideal scenario, all potential measurements would be performed under ultra high vacuum facilitating the use of frequency modulated KPFM (FM-KPFM) and negating the issue of convolution of tip signal by the cantilever. Similarly, use of a higher strength electromagnet, commercially available modules for MFM are capable of 0.8 T [38], would reduce the minimum domain wall current required to develop a measureable Hall potential. The principal restriction on the use of KPFM for quantitative potential measurement was the 10 V potential maximum available for driving current though the domain walls, necessitating a sufficient domain wall conductance. Bruker have demonstrated surface potential mapping via a high-voltage detection mode, which they give the acronym KPFM-HV, wherein detection is no longer based upon nullification of the force acting on tip and instead a dual channel lock-in amplifier is used, with the contact potential difference calculated from the varying ω and 2ω force components[39]. With this technique, Bruker claim successful operation within $\pm$ 200 V. While no peer-reviewed evidence for KPFM-HV was found, it presents a promising avenue for expanding the scope for quantitative Hall measurement on minimally conducting domain walls.

Recording the domain wall conductance and Hall potential over a full range of temperatures, operating temperatures for KPFM in literature range from ~ 10^{-1} to 10^{3} K [40–42], and under lateral bias of up to the coercive field, the complete conductive profile of the domain wall can be catalogued across a wide range of transport regimes. Such measurement would help elucidate the inconsistent metallic and semiconducting behaviour currently reported for equivalent domain wall systems. A key example is the increased conductance upon increased temperature observed for charged domain walls in lead zirconate titanate despite the inherently metallic conductivity observed at 4 K [43]. Crucially, this allows for the carrier properties of differing domain walls to now be determined with the same exhaustive rigor as that of silicon and germanium. Such meticulous analysis is required if conducting domain walls are to emulate the extreme versatility of modern semiconductor devices.

At the extreme limits of what can be achieved with modern instrumentation, scanning probe systems have been demonstrated with insitu electromagnetic fields of 27 T [44] and ambient temperatures of down to 10 mK [45]. Consequently, the basic KPFM methodology described herein could be used to potentially image the quantum Hall effect[46] within domain walls, explicitly verifying them as reconfigurable two-dimensional conductors. In an analogous experiment KPFM has already been used, at a temperature of 1.4 K and up to 10 T, to successfully measure the quantised Hall resistance of a two dimensional electron gas within a GaAs / $Al_{0.33}Ga_{0.67}As$ heterostructure[47].

Looking forward, while domain walls where the impetus behind its development, the Hall measurement technique demonstrated herein is not limited to analysis of interface phenomena. Increased sample width can be offset by minimising sample depth or by maximising the applied electric and magnetic fields. Hence the Hall technique allows for quantitative mapping of variations in the local carrier mobility and density across a sample. One potential application is providing a more direct method of imaging dopant profiles under AFM, with the quantitative carrier density obtained directly from local Hall potential without need for comparative modelling as with scanning capacitance microscopy[1,48,49] and traditional KPFM[50,51]. Further, given the relative ease of use, Hall potential mapping may be a convenient tool for broad investigation into changes in local electronic structure, complementing the high precision but considerably more intricate procedure of electron energy loss spectroscopy[52,53].

8.3 References

1. Kuntze, S. B. *et al.* Electrical Scanning Probe Microscopy: Investigating the Inner Workings of Electronic and Optoelectronic Devices. *Crit. Rev. Solid State Mater. Sci.* **30,** 71–124 (2005).

2. Pearson, G. L., Read, W. T. & Shockley, W. Probing the space-charge layer in a p-n junction. *Phys. Rev.* **85,** 1055–1057 (1952).

3. Abrahams, S. C. Ferroelectricity and structure in the $YMnO_3$ family. *Acta Crystallogr. Sect. B Struct. Sci.* **57,** 485–490 (2001).

4. Artyukhin, S., Delaney, K. T., Spaldin, N. A. & Mostovoy, M. Landau theory of topological defects in multiferroic hexagonal manganites. *Nat. Mater.* **13,** 42–49 (2013).

5. Meier, D. *et al.* Anisotropic conductance at improper ferroelectric domain walls. *Nat. Mater.* **11,** 284–288 (2012).

6. Wu, W., Horibe, Y., Lee, N., Cheong, S. W. & Guest, J. R. Conduction of topologically protected charged ferroelectric domain walls. *Phys. Rev. Lett.* **108,** 77203 (2012).

7. Subba Rao, G. V., Wanklyn, B. M. & Rao, C. N. R. Electrical transport in rare earth ortho-chromites, -manganites and -ferrites. *J. Phys. Chem. Solids* **32,** 345–358 (1971).

8. Skjærvø, S. H. *et al.* Interstitial oxygen as a source of p-type conductivity in hexagonal manganites. *Nat. Commun.* **7,** 13745 (2016).

9. Schaab, J. *et al.* Optimization of Electronic Domain-Wall Properties by Aliovalent Cation Substitution. *Adv. Electron. Mater.* **2,** 1500195 (2016).

10. Jacoboni, C., Canali, C., Ottaviani, G. & Alberigi Quaranta, A. A review of some charge transport properties of silicon. *Solid. State. Electron.* **20,** 77–89 (1977).

11. Naik, I. K. & Tien, T. Y. Small-polaron mobility in nonstoichiometric cerium dioxide. *J. Phys. Chem. Solids* **39,** 311–315 (1978).

12. Rettie, A. J. E., Chemelewski, W. D., Emin, D. & Mullins, C. B. Unravelling Small-Polaron Transport in Metal Oxide Photoelectrodes. *J. Phys. Chem. Lett.* **7,** 471–479 (2016).

13. Biaggio, I., Hellwarth, R. W. & Partanen, J. P. Band Mobility of Photoexcited Electrons in $Bi_{12}SiO_{20}$. *Phys. Rev. Lett.* **78,** 891–894 (1997).

14. Mundy, J. A. *et al.* Functional electronic inversion layers at ferroelectric domain walls. *Nat. Mater.* **16,** 622–627 (2017).

15. Gureev, M. Y., Tagantsev, A. K. & Setter, N. Head-to-head and tail-to-tail 180° domain walls in an isolated ferroelectric. *Phys. Rev. B - Condens. Matter Mater. Phys.* **83,** 184104 (2011).

16. Eliseev, E. A., Morozovska, A. N., Svechnikov, G. S., Gopalan, V. & Shur, V. Y.

Static conductivity of charged domain walls in uniaxial ferroelectric semiconductors. *Phys. Rev. B - Condens. Matter Mater. Phys.* **83,** 235313 (2011).

17. Catalan, G., Seidel, J., Ramesh, R. & Scott, J. F. Domain wall nanoelectronics. *Rev. Mod. Phys.* **84,** 119–156 (2012).

18. Vasudevan, R. K. *et al.* Domain Wall Conduction and Polarization-Mediated Transport in Ferroelectrics. *Adv. Funct. Mater.* **23,** 2592–2616 (2013).

19. Daire, A. *Improving the Repeatability of Ultra-High Resistance and Resistivity Measurements (White Paper)*. (Keithley Instruments, 2001).

20. Bollmann, W. & Gernand, M. On the Disorder of $LiNbO_3$Crystals. **9,** 301–308 (1972).

21. Birnie III, D. P. Review Analysis of diffusion in lithium niobate. *J. Mater. Sci.* **28,** 302–315 (1993).

22. Gopalan, V., Dierolf, V. & Scrymgeour, D. Defect–Domain Wall Interactions in Trigonal Ferroelectrics. *Annu. Rev. Mater. Res.* **37,** 449–489 (2007).

23. Staebler, D. L. & Amodei, J. J. Thermally fixed holograms in $LiNbO_3$. *IEEE Trans. Sonics Ultrason.* **19,** 107–114 (1972).

24. Kovacs, L., Polgar, K. & Florea, C. in *Lithium Niobate* 91–96 (Springer, 2002).

25. Nakamura, K., Ando, H. & Shimizu, H. Ferroelectric domain inversion caused in $LiNbO_3$ plates by heat treatment. *Appl. Phys. Lett.* **50,** 1413–1414 (1987).

26. Kugel, V. D. & Rosenman, G. Domain inversion in heat-treated $LiNbO_3$ crystals. *Appl. Phys. Lett.* **62,** 2902–2904 (1993).

27. Schröder, M. *et al.* Conducting domain walls in lithium niobate single crystals. *Adv. Funct. Mater.* **22,** 3936–3944 (2012).

28. Sluka, T., Tagantsev, A. K., Bednyakov, P. & Setter, N. Free-electron gas at charged domain walls in insulating $BaTiO_3$. *Nat. Commun.* **4,** 1808 (2013).

29. Volk, T. R., Gainutdinov, R. V. & Zhang, H. H. Domain-wall conduction in AFM-written domain patterns in ion-sliced $LiNbO_3$ films. *Appl. Phys. Lett.* **110,** 132905 (2017).

30. Sheng, Y. *et al.* Three-dimensional ferroelectric domain visualization by Cerenkov-type second harmonic generation. *Opt. Express* **18,** 16539–16545 (2010).

31. Schilling, A. *et al.* Shape-induced phase transition of domain patterns in ferroelectric platelets. *Phys. Rev. B* **84,** 64110 (2011).

32. McQuaid, R. G. P., McGilly, L. J., Sharma, P., Gruverman, A. & Gregg, J. M. Mesoscale flux-closure domain formation in single-crystal $BaTiO_3$. *Nat. Commun.* **2,** 404 (2011).

33. Whyte, J. R. *et al.* Sequential injection of domain walls into ferroelectrics at different bias voltages: Paving the way for 'domain wall memristors'. *J. Appl. Phys.* **116,** 66813 (2014).

34. Whyte, J. R. & Gregg, J. M. A diode for ferroelectric domain-wall motion. *Nat. Commun.* **6,** 7361 (2015).

35. Rosenkranz, R. Failure localization with active and passive voltage contrast in FIB and SEM. *J. Mater. Sci. Mater. Electron.* **22,** 1523–1535 (2011).

36. Aristov, V. V., Kokhanchik, L. S., Meyer, K. P. & Blumtritt, H. Scanning electron microscopic investigations of peculiarities of the $BaTiO_3$ ferroelectric domain contrast. *Phys. Status Solidi* **78,** 229–236 (1983).

37. Aristov, V. V., Kokhanchik, L. S. & Voronovskii, Y. I. Voltage contrast of ferroelectric domains of lithium niobate in SEM. *Phys. Status Solidi* **86,** 133–141 (1984).

38. VFM2^{TM} Variable Field Module from Asylum Research.

39. *PeakForce Kelvin Probe Force Microscopy (Application Note #140)*. (Bruker Nano Surfaces Devision).

40. Vančura, T. *et al.* Kelvin probe spectroscopy of a two-dimensional electron gas below 300 mK. *Appl. Phys. Lett.* **83,** 2602–2604 (2003).

41. Ligowski, M. *et al.* Observation of individual dopants in a thin silicon layer by low temperature Kelvin Probe Force Microscope. *Appl. Phys. Lett.* **93,** 1–4 (2008).

42. Hansen, K. V., Wu, Y., Jacobsen, T., Mogensen, M. B. & Theil Kuhn, L. Improved controlled atmosphere high temperature scanning probe microscope. *Rev. Sci. Instrum.* **84,** 73701 (2013).

43. Stolichnov, I. *et al.* Bent Ferroelectric Domain Walls as Reconfigurable Metallic-Like Channels. *Nano Lett.* **15,** 8049–8055 (2015).

44. Meng, W., Guo, Y., Hou, Y. & Lu, Q. Atomic resolution scanning tunneling microscope imaging up to 27 T in a water-cooled magnet. *Nano Res.* **8,** 3898–3904 (2015).

45. Song, Y. J. *et al.* Invited Review Article: A 10 mK scanning probe microscopy facility. *Rev. Sci. Instrum.* **81,** 121101 (2010).

46. Von Klitzing, K. The quantized Hall effect. *Rev. Mod. Phys.* **58,** 519–531 (1986).

47. Weitz, P., Ahlswede, E., Weis, J., Von Klitzing, K. & Eberl, K. A low-temperature scanning force microscope for investigating buried two-dimensional electron systems under quantum Hall conditions. *Appl. Surf. Sci.* **157,** 349–354 (2000).

48. Williams, C. C., Slinkman, J., Hough, W. P. & Wickramasinghe, H. K. Lateral dopant profiling with 200 nm resolution by scanning capacitance microscopy. *Appl. Phys. Lett.* **55,** 1662–1664 (1989).

49. Marchiando, J. F. Model database for determining dopant profiles from scanning capacitance microscope measurements. *J. Vac. Sci. Technol. B Microelectron. Nanom. Struct.* **16,** 463 (1998).

50. Kikukawa, A., Hosaka, S. & Imura, R. Silicon pn junction imaging and characterizations using sensitivity enhanced Kelvin probe force microscopy. *Appl.*

Phys. Lett. **66,** 3510–3512 (1995).

51. Baumgart, C., Helm, M. & Schmidt, H. Quantitative dopant profiling in semiconductors: A Kelvin probe force microscopy model. *Phys. Rev. B* **80,** 85305 (2009).

52. Oxley, M. P., Lupini, A. R. & Pennycook, S. J. Ultra-high resolution electron microscopy. *Reports Prog. Phys.* **80,** 26101 (2017).

53. Egerton, R. F. Electron energy-loss spectroscopy in the TEM. *Reports Prog. Phys.* **72,** 16502 (2009).

A1 Vector PFM on $LiNbO_3$

In section 7.2, vector piezoresponse force microscopy (PFM) measurements were presented to establish the polarisation direction within a congruent $LiNbO_3$ crystal, relative to both the sample axes and the central domain wall present throughout its length. Lateral PFM mapping was performed across the same domain wall segment, with the sample sequentially rotated with respect to the cantilever in increments of 45°, from 0° to 315°. However, only a single PFM phase map was presented (Figure 7.3c) along with a graph of the relative PFM amplitude measured at each angle (Figure 7.3e). Herein, the lateral phase and amplitude scans for each angle are shown, Figure A1.2 and Figure A1.3 respectively, along with the distribution of amplitude measurements at each angle (Figure A1.4).

The schematics shown in Figure A1.1a and Figure A1.1b convey the sample and domain wall orientation relative to the PFM cantilever, for 0° and 90° scan orientations respectively.

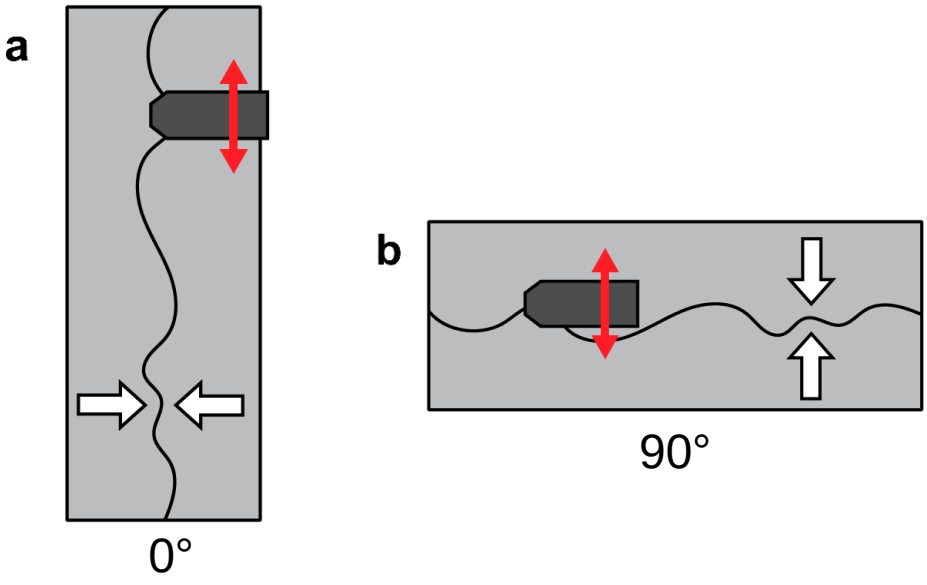

Figure A1.1 Schematic of the $LiNbO_3$ crystal orientation with respect to fixed cantilever position. Overlaid arrows convey local polarisation. **a** and **b** correspond 0° and 90° scan orientations respectively.

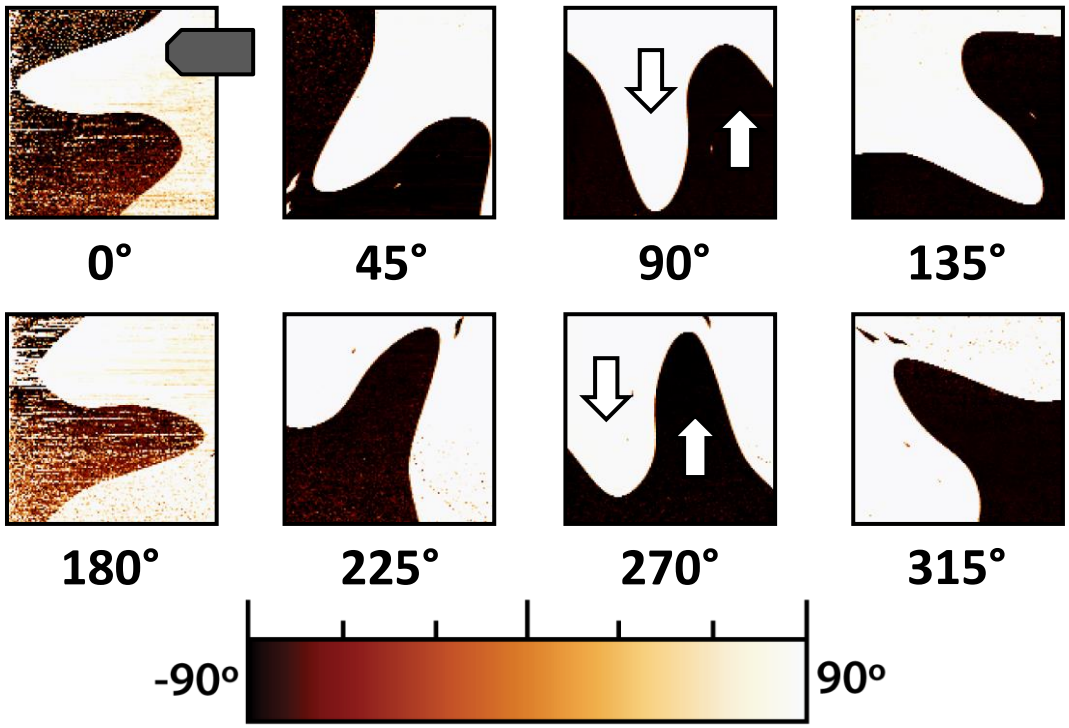

Figure A1.2 Lateral PFM phase maps recorded across a domain wall in $LiNbO_3$ at a range of sample angles. Cantilever position was fixed across all scans. Overlaid arrows portray local polarisation direction.

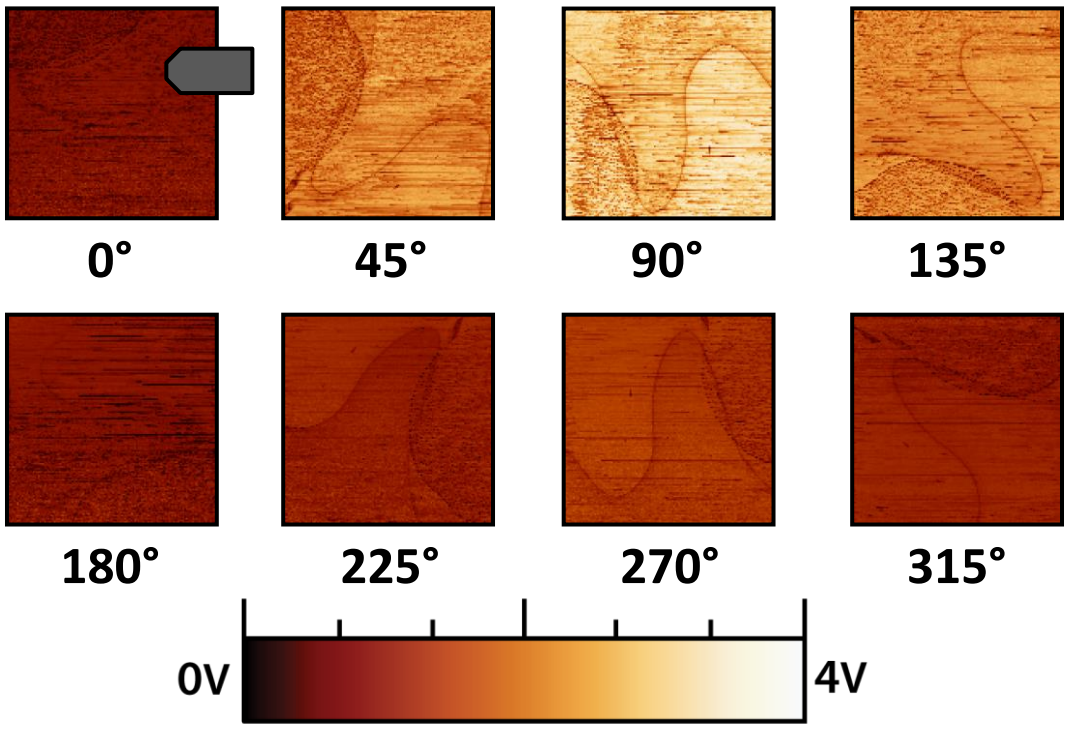

Figure A1.3 Lateral PFM amplitude scans recorded across a domain wall in $LiNbO_3$. Cantilever position was fixed across all scans.

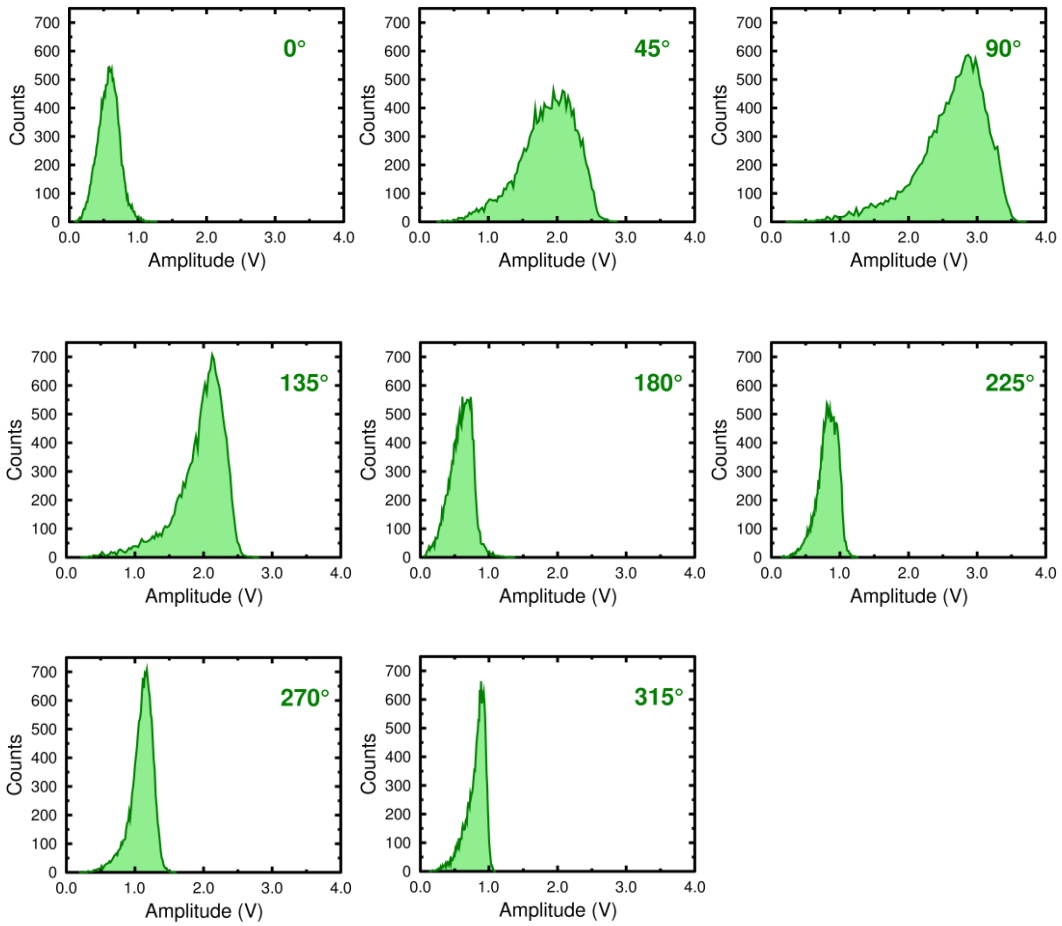

Figure A1.4 Line profiles of the measured amplitude distribution for each of the lateral PFM maps presented in Figure A1.3. Measurements show greatest signal was recorded for a 90° angle.